Probing Amyloid-beta Aggregation Using Paramagnetic Complexes

Julius Adamson

A thesis submitted in fulfilment of the requirements for the degree of Doctor of Philosophy

The University of Sydney

School of Chemistry, Faculty of Science

2024

This research reported in this thesis was supported by the award of a Research Training Program scholarship to the PhD Candidate.

Abstract

Alzheimer's disease is the leading cause of dementia and is creating a growing economic and social burden on the aging global population. The drugs approved for the treatment of Alzheimer's disease are only able to slow the onset of the disease. Attempts to develop treatments which halt, or reverse, cognitive decline have proven unsuccessful.

Amyloid-β is a neuronally-derived peptide which has been implicated in Alzheimer's disease for over three decades. Amyloid-β aggregates to form fibrils which eventually deposit as amyloid plaques in the brain and has remained a popular target for the treatment of Alzheimer's disease. Treatments that inhibit the production of amyloid-β, or remove the end-stage aggregates have not been able to ameliorate the symptoms of the disease. The demonstrated toxicity of intermediate oligomers of amyloid-β has caused research to shift towards understanding and disrupting the aggregation process itself.

This thesis focuses on the synthesis of bis-perphenazine cyclam conjugates and their complexes, which were identified in a screen of compounds that inhibit the aggregation of amyloid-β. Chapter 2 describes the development of a scalable synthesis of these compounds and further characterises their biological activity. It was found that these compounds inhibited aggregation by interacting with monomeric Aβ and that they could reduce the toxicity of Aβ towards cultured neuronal cells.

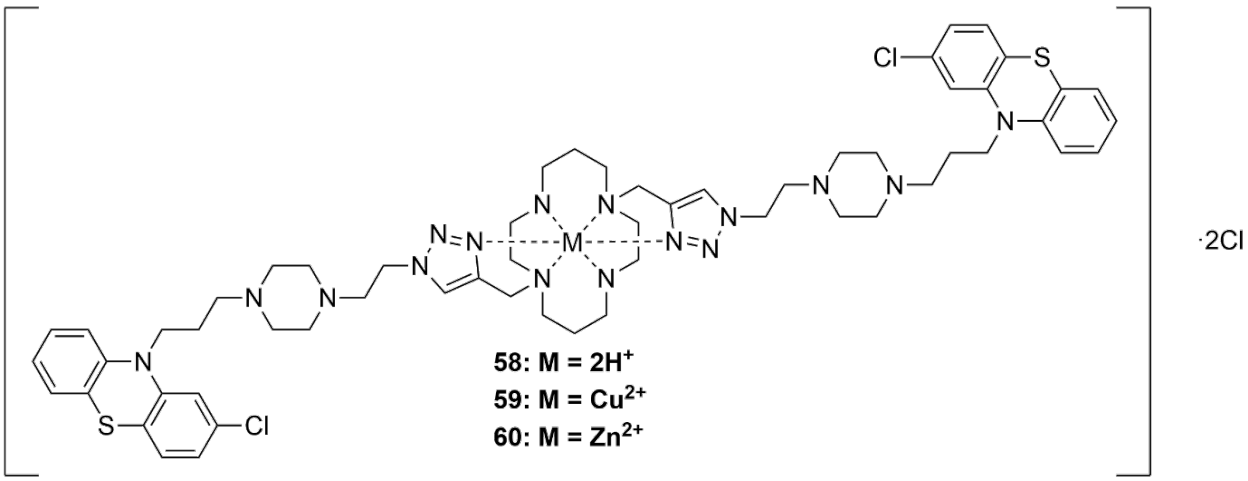

58: M = $2H^+$
59: M = Cu^{2+}
60: M = Zn^{2+}

Chapters 3 and 4 describe the development of a series of probe compounds which can act as paramagnetic NMR probes to investigate how the compounds bind to amyloid-β. Attempts at synthesising bis-perphenazine lanthanide probes are described in Chapter 3. Chapter 4 describes the synthesis of a series of lanthanide probes containing one perphenazine pendant. The compounds were shown to disrupt the aggregation of Aβ *in vitro* but attempts to identify how the probes interacted with monomeric Aβ using paramagnetic relaxation enhancement were unsuccessful.

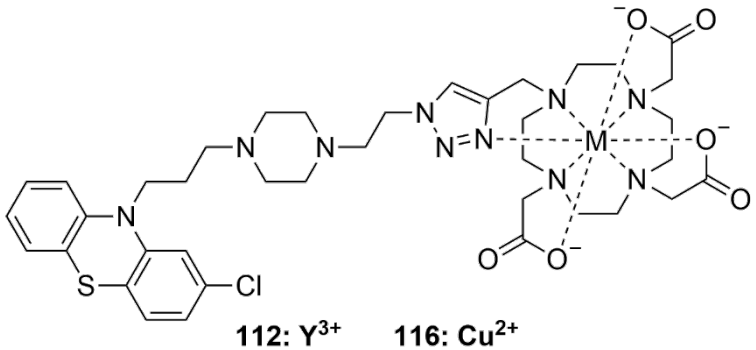

112: Y^{3+} **116: Cu^{2+}**
114: Eu^{3+} **117: Zn^{2+}**
115: Gd^{3+} **118: Mn^{2+}**

Declaration

The work described in this thesis was conducted by the author at the University of Sydney in the School of Chemistry under the supervision of Prof. Peter Rutledge. This thesis has not been submitted for any other degree.

High-resolution mass spectrometry data were acquired by Dr. Nicholas Proschogo and his staff at the Mass Spectrometry Facility in the School of Chemistry. High-field ^{1}H and ^{13}C NMR spectra were acquired by Dr. Ian Luck and his staff at the Magnetic Resonance Facility at Sydney Analytical.

Thioflavin T experiments described in Chapter 2 were performed by Sarah Ball (University of Sydney). NMR titrations against amyloid-β and concentration-response curve fitting described in Chapter 2 were performed by Sarah Ball and A/Prof. Ann Kwan (University of Sydney). Kinetic modelling of amyloid-β aggregation described in Chapter 2 was performed by Manuela Zimmerman (University of Cambridge). Electron microscopy described in Chapter 2 was performed by Dr. Victor Lo (University of Sydney). Cell toxicity assays described in Chapter 2 were performed by Michael Sullivan (University of Sydney), André McKenzie (University of Sydney) and Dr. Eryn Werry (University of Sydney). The compounds from the initial screen first described in Chapter 1 were first synthesised by Frank Jiang. NMR titrations performed in Chapter 4 were performed by myself with assistance from A/Prof. Ann Kwan.

All other work described in this thesis was my own. I certify that the intellectual content of this thesis is the product of my own work and that all the assistance received in preparing this thesis and sources have been acknowledged.

Julius Stephen Peter Adamson

2023

Author Attribution Statement

Chapter 2 of this thesis is published as:

Ball S.R., **Adamson J.S.P**., Sullivan M.A., Zimmermann M.R., Lo V., Sanz-Hernandez M., Jiang X., Kwan A.H., McKenzie A.D.J., Werry E.L., Knowles T.P.J., Kassiou M., Meisl G., Todd M.H., Rutledge P.J., Sunde M. Perphenazine-Macrocycle Conjugates Rapidly Sequester the Aβ42 Monomer and Prevent Formation of Toxic Oligomers and Amyloid *ACS Chem. Neurosci.*, **2023** 14 (1), 87 – 98.

I am second author of this publication and synthesised and characterised the compounds used in the main body of the paper, excluding the compounds synthesised for the initial screen which are shown in the supporting information.

In addition to the statements above, in cases where I am not the corresponding author of a published item, permission to include the published material has been granted by the corresponding author.

Julius Stephen Peter Adamson

2023

As supervisor for the candidature upon which this thesis is based, I can confirm that the authorship attribution statements above are correct.

Peter Rutledge, Supervisor

2023

Acknowledgements

What a wild couple of years. I had no idea four (and a half) years would turn out the way they did. First and foremost, I'd like to thank my supervisor Professor Peter Rutledge for giving me the opportunity to take on such a challenging and interesting project, and for being such a generous and patient supervisor. I can't think of anyone I would rather have done a PhD with.

I'd like to thank Professor Margaret Sunde, my auxiliary supervisor, Dr. Sarah Ball, Dr. Caitlin Johnston, and Ann Kwan for being excellent collaborators. Thanks in particular go to Margie, Caitlin, Ann, and Biswa in G08 for helping me learn and perform thioflavin-T assays and protein NMR over the course of about six weeks right before submission- this thesis wouldn't be possible without your help!

I'd like to thank the technical staff in the School of Chemistry, in particular Dennis and Carlo for putting up with my constant whinging and supplying me with the latest gossip in the school. Thanks also to Roberto and the team at Forum for the hundreds of free coffees I've received over the past four years.

A special thanks goes out to the past and present members of the Rutledge and SCOPE groups. To Marat, thank you for all the encouragement you gave me throughout my PhD and making sure I was giving things my best efforts. To Nick, who started at the same time as me (and looks like we'll finish at the same time), thanks for being a sympathetic ear. Kym, thank you for encouraging my curiosity and being excellent company at the pub! Thanks to Nicole and Paul for always enjoying a whinge or gossip session.

I'd also like to thank all the friends both from outside and within the School of Chemistry who helped me along the way. Leila, for being an excellent friend, and teaching me everything I needed to know about lanthanide chemistry- this thesis would look a lot different without you! Tom, Olivia, Ciara, and Andrew, thank you for always being keen

for coffee or the pub. Thanks to Dan, Krupa and Al for being excellent conversation, and for never bringing up chemistry. Especially thank you to my darling Klementine, whose love kept me going throughout this time.

Finally, I'd like to thank my family for being supportive of my studies, and always lending an ear to my grievances and successes; Dad, Georgie, Joe and Aunty Lorna, thank you so much. Lachlan, thank you for being someone I could lean on, as you were going through the same thing. To Mum, who taught me kindness and curiosity, and my Uncle Peter, who taught me to always be looking for fun, thank you so much; I wish you were around to see me finish this.

Table of Contents

Abbreviations

A_{280}	Absorbance at 280 nm
Aβ	Amyloid beta
AD	Alzheimer's disease
ANOVA	Analysis of variance
APP	Amyloid precursor protein
Asp	Asparagine
AFM	Atomic force microscopy
ATR	Attenuated total reflectance
Boc	*tert*-Butoxycarbonyl
BSE	Bovine spongiform encephalopathy
Cbz	Carboxybenzyl
CEST	Chemical exchange saturation transfer
COSY	Correlation spectroscopy
CPMG	Carr-Purcell-Meiboom-Gill relaxation
Cryo-EM	Cryogenic electron microscopy
CSGA	Major curlin subunit
CuAAC	Cu(I)-catalysed azide-alkyne cycloaddition
d	Doublet
DBU	Diazabicyclo(5.4.0)undec-7-ene
DCM	Dichloromethane
DET	Dexter energy transfer
DIPEA	Diisopropylethylamine
DMF	Dimethylformamide
DOTA	1,4,7,10-Tetraazacyclododecane-1,4,7,10-tetraacetic acid
DO2A	1,4,7,10-Tetraazacyclododence-1,7-diacetic acid
DO3A	1,4,7,10-Tetraazacyclododecane-1,4,7-triacetic acid
DTPA	Diethylenetriaminepentaacetic acid
DPA	Di(2-picolyl)amine
DPPA	Diphenylphosphoryl azide

EDTA	Ethylenediamine tetraacetic acid
EGCG	Epigallocatechin gallate
EM	Electron microscopy
ESI	Electrospray ionisation
Et_3N	Triethylamine
FRET	Förster resonance energy transfer
g	Grams
Glu	Glutamic acid
h	hours
HCl	Hydrochloric acid
HRMS	High resolution mass spectrometry
HSQC	Heteronuclear single quantum coherence spectroscopy
K_d	Equilibrium dissociated constant
Lys	Lysine
LRMS	Low resolution mass spectrometry
M	Molar
m	Multiplet
M^{x+}	Metal
M+	Molecular ion
mAbs	Monoclonal antibodies
min	Minutes
MeCN	Acetonitrile
MRI	Magnetic resonance imaging
nm	Nanometre
NMR	Nuclear magnetic resonance
NOE	Nuclear Overhauser effect
NOESY	Nuclear Overhauser effect spectroscopy
NOTA	1,4,7-Triazacyclononane-1,4,7-triacetic acid
OTf	Triflate
P	Pentuplet
ParaCEST	Paramagnetic chemical exchange saturation transfer

PCS	Pseudocontact shift
PDB	Protein Data Bank
Pd/C	Palladium on carbon
PET	Photoinduced electron transfer
PRE	Paramagnetic relaxation enhancement
q	Quadruplet
RDC	Residual dipolar coupling
rt	Room temperature
s	Singlet
SAXS	Small-angle X-ray scattering
SFX	Serial femtosecond crystallography
t	Triplet
T_1	Longitudinal relaxation time
T_2	Transverse relaxation time
TACN	1,4,7-Triazacyclononane
TBTA	Tris(benzyltriazolylmethyl)amine
TEM	Transmission electron microscopy
TETA	1,4,8,11-Tetraazacyclotetradecane-1,4,8,11-tetraacetic acid
TFA	Trifluoroacetic acid
THF	Tetrahydrofuran
TMEDA	Tetramethylethylenediamine
ThT	Thioflavin-T
TOCSY	Total correlation spectroscopy
UV-Vis	Ultraviolet-visible light spectroscopy
vCDJ	Variant Creutzfeldt-Jacob disease
XFEL	X-ray free electron lasers
χ	Magnetic susceptibility tensor

1. Introduction

1.1 Amyloid proteins

1.1.1The Amyloid State

The function of a protein is directly tied its structure. This paradigm is well established in molecular biology and is used to understand the role of protein structure in disease. The structure of a protein is largely determined by the side chains of its amino acid sequence.[1] A protein in an aqueous environment is subject to the hydrophobic effect. The amide backbone and non-polar side chains minimise their exposure to the solvent by folding within each other, while polar side chains will orient themselves to the surface of the protein.[2] Hydrogen bonding can occur between suitably functionalised side chains, and between side chains and the aqueous media. Other key interactions include salt bridges between charged residues (e.g. the protonated ε-amine of Lys and carboxylate of Asp or Glu), and disulphide bridges between cysteine resides.[2] The summation of these interactions determine the structure of a given protein, while perturbations to these interactions can result in proteins adopting abnormal structures, resulting in dysfunction. The amyloid state of proteins exemplifies such structure-related function. Characterised by large, insoluble, ordered aggregates, amyloids are commonly associated with neurodegenerative diseases.[3] While any protein is capable of forming amyloid aggregates, proteins that are particularly prone to the amyloid state are referred to as 'amyloids.'[4]

Amyloid aggregates are fibrillar, made up of protofilaments twisted around each other, and are generally a few nanometres in width, but can reach micrometres in length.[5] Each protofilament possesses a cross β-sheet structure in which the protein chains are oriented perpendicular to the axis of the fibril and form β-sheets with neighbouring strands above and below, creating an intermolecular β-sheet parallel to the axis of the fibril (**Figure**

1).[6, 7] This general structure is observed regardless of the size or amino acid sequence of the parent protein, and arises due to inter-backbone interactions.[8] This is quite different to the native structure of a globular protein, which is largely determined by side chain interactions within the same protein molecule, and between the protein and surrounding media.

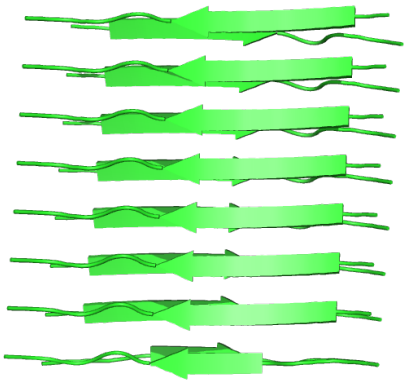

Figure 1.1: Amyloid fibril of transthyretin, demonstrating the cross-β sheet structure inherent to amyloid fibrils (PDB 2m5n).[6]

The proteins that form amyloids are varied in both sequence and size, but the amyloid state is generally only thermodynamically stable for protein fragments, and peptides, shorter than 150 residues in length.[9] While the sequence of an amyloid protein has a limited effect on the main fibril structure, it does affect its propensity to aggregate and the speed of aggregation.

1.1.2 Types of amyloids

First identified as deposits in human tissue, amyloids have long been associated with disease in humans, particularly neurodegenerative diseases.[3] Amyloid-β is perhaps the most studied amyloid, being the major component of senile plaques.[10] These extracellular deposits are found in the tissue of brains affected by Alzheimer's disease (AD), the most common form of dementia. Amyloid-β (Aβ) refers to a short peptide fragment, generally either 40 or 42 amino acids, derived from amyloid precursor protein (APP) which is ubiquitous in neuronal cell membranes.[11] While the connection between

senile plaques and AD was identified in 1906, the hypothesis that Aβ is the causative agent of AD was only posited in the early 1990s.[10-12] The 'amyloid hypothesis' of AD is widely held, but not without controversy. A competing hypothesis holds that AD arises due to amyloids formed from tau protein that has undergone hyperphosphorylation.[13, 14] Aggregated tau is found in a number of other neurodegenerative diseases, collectively labelled tauopathies, including frontotemporal dementia, chronic traumatic encephalopathy and encephalopathy from lead poisoning.[15]

Parkinson's disease is the second most common neurodegenerative disease behind AD, and affects the motor system.[16] The symptoms typically consist of shaking and difficulty in movement, in contrast to the memory loss associated with AD and other dementias.[17] These motor symptoms are collectively referred to as parkinsonism and are also observed in some forms of dementia. Amyloid deposits of α-synuclein are associated with disorders that cause parkinsonism, and these are found as structures called Lewy bodies within the neurons of those affected.

The other major neurodegenerative diseases with an associated amyloid are transmissible spongiform encephalopathies. Diseases of this class are characterised by amyloid fibrils formed by human prion protein, referred to as prions.[18] Transmissible spongiform encephalopathies are unique among amyloid diseases because some are contagious, believed to be spread by contact with prions.[19, 20] Most contagious prion diseases are found in other animals: scrapie in sheep and bovine spongiform encephalopathy (BSE) in cows. Prion diseases in humans are often sporadic or hereditary, but consumption of tissue infected with BSE is believed to cause variant Creutzfeldt-Jakob disease (vCJD) in humans.[19, 21] Kuru is another notable example of a human transmissible spongiform encephalopathy, and is believed to be spread by consumption of infected brain tissue in funeral cannibalism, as formerly practised by the Fore people of Papua New Guinea. [22]

While amyloids are closely associated with disease in humans, many other organisms have a variety of constructive uses for amyloid proteins.[23, 24] In this context, these proteins are termed 'functional amyloids' and are commonly found in bacteria, yeasts and filamentous fungi. The broadest class of functional amyloids are components of biofilms, the network of extracellular proteins, lipids and saccharides that attach microbial colonies to surfaces and shield them from the external environment. Curli proteins are one such component of the biofilms of proteobacteria, with the *Escherichia coli* curli protein the most studied. These fibrils are composed of major curlin subunit (CsgA), whose assembly is templated by several associated proteins, and forms a scaffold to which glycans and other proteins assemble to construct the biofilm.[25] This templated assembly avoids potential toxicity of CsgA to the bacterium.[26] There are also distinct amyloid components in biofilms generated by *Psuedomonas*, *Bacillus*, and *Staphylococcus* species.[27-29] In another example of functional amyloid, the pili of *Mycobacterium tuberculosis* are adhesive organelles composed of an amyloid core; these are different to the biofilms formed by other genera but also serve to attach the bacteria to a host surface.[30] In pathogenic strains of *M. tuberculosis*, these amyloids are crucial virulence factors: knockout strains which lack them have a significantly reduced ability to infect other organisms, and are often completely non-infectious.[29, 31]

Amyloids are also exploited by filamentous fungi and some bacteria to form hydrophobic structures that are key to their life cycle and survival. These amyloidogenic proteins are referred to as *hydrophobins* in filamentous fungi. Waterborne filamentous fungi, such as *Schizophyllum commune* secrete hydrophobins which then assemble into fibrils (called *rodlets* in this context) at the air-water interface.[32] Hydrophobin rodlets lower the surface tension and allows aerial hyphae to grow into the air and facilitate spore dispersal. The hydrophobins also form a water-proof coat around spores to prevent wetting, maximising their dispersal.[33] The spores of *Aspergillus fumigatus*, a human pathogen, are coated in hydrophobin rodlets that mask surface antigens and allow the spores to

evade immune recognition in hosts.[34] The bacterium *Streptomyces coelicolor* (best known for the diverse profile of natural products it can produce) also utilises amyloids called chaplins to coat hyphae and spores to facilitate spore dispersal.[35]

Some yeasts incorporate prions as functional amyloids, where they act as epigenetic elements and cause a change in yeast phenotype without an alterating of the genome. Two genes in *Saccharomyces cerevisiae* [PSI+] and [URE3] were identified in 1965 and 1971 respectively, before the existence of prions was established.[36, 37] Both displayed non-mendelian inheritance but the prion nature of the gene products was not recognised until the 1990s.[38] The [PSI+] gene encodes for Sup35p. In its unaggregated state, this protein acts as a translation release factor, while the aggregated form of Sup35p acts as a nonsense repressor and causes translation to continue past the stop codon, altering protein expression and unmasking silent genes in a non-specific manner.[39] One hypothesis posits that the role of the Sup35p prion is to increase adaptation in certain environments by inducing phenotypic plasticity, however the Sup35P prion has only been observed in laboratory conditions.[40, 41] The protein Ure2p is switched on in the presence of a preferred nitrogen source, such as ammonium salts, and supresses genes which induce the uptake and use of poor nitrogen sources like amino acids. When Ure2p aggregates to form the prion [URE3], uptake and catabolism of poor nitrogen sources occurs, even in the presence of a preferred source.[38] In a further example, the ascomycete fungus *Podospora anserina*, deploys the HET prion in controlling programmed cell death.[42]

1.1.3 Amyloid beta (Aβ)

As mentioned briefly in **Section 1.1.2**, Aβ has been subject to extensive study due to its close association with AD. The parent protein from which Aβ peptides arise is APP, a membrane protein found in high concentrations in the synapses of neurons.[43] No definitive biological role has yet been identified for APP, but there is growing evidence

that it has numerous functions, including in synapse formation, modulating synapse activity, regulating metal metabolism and regulating oxidative stress.[44-48] Aβ is produced by the cleavage of APP by two proteases: β-secretase and γ-secretase.[49] While the peptides produced from the action of both these enzymes are collectively called amyloid-β, the length of the resulting peptide varies depending on where cleavage by γ-secretase occurs.[49] The 40 residue peptide, denoted as $A\beta_{40}$, and the 42 residue peptide, $A\beta_{42}$, are the two most commonly studied. Although both are able to aggregate, $A\beta_{42}$ is more prone to aggregation and considered the most toxic Aβ peptide, while $A\beta_{40}$ is the more abundant.[50]

Theories about the nature of Aβ induced toxicity have evolved since the introduction of the amyloid cascade hypothesis in the 1990s. Monomeric Aβ itself is non-toxic, and it was initially thought that the fully formed Aβ fibrils, which make up senile plaques, were the toxic agent in Alzheimer's disease. However this idea fell out of favour due to the failure of antibody therapies targeting fibrils in clinical trials, and the lack of correlation between the number of senile plaques and progression of AD in patients.[51] Thus focus has shifted towards soluble intermediate oligomers of Aβ as the possible source of toxicity. Oligomers are considered to be in equilibrium with, and intermediate between, monomeric and fibrillar Aβ and comprise of a variety of different species that vary in their molecular weight and connectivity.[52] However, the toxicity of different sizes and types of isolated oligomers tends to be similar: they inhibit long-term potentiation of neurons and induce tau hyperphosphorylation in most cases.[53-56] Some oligomers cause a demonstrable cognitive impairment in mice, while others have been shown to be directly cytotoxic.[57, 58] Overall there is compelling evidence for the toxicity of Aβ oligomers and related intermediates, which compels investigation into the aggregation process itself.

The aggregation of Aβ was initially modelled as a nucleated polymerisation mechanism, like a crystal growing out of a saturated solution.[59] This mechanism, like other nucleated-growth mechanisms, consists of three phases: a lag phase, a growth phase and an end phase (**Figure 1.2**). In the lag phase, the solution contains mostly monomers which need to undergo a conversion into an aggregated nucleus. When enough nuclei are formed, the solution enters the growth phase, through which monomers attach to nuclei to grow fibrils. The end phase is reached when the monomer level is depleted to below the critical aggregation concentration.[60, 61] Like crystals, the formation of fibrils from monomers can be seeded by the addition of fully formed fibrils, and the rate limiting step to this reaction is the thermodynamically unfavourable conversion of disordered monomers into a high-energy, ordered nucleus. In this mechanism, nuclei and intermediate species are present in low concentrations throughout the course of the reaction, and either monomers (early) or fibrils (late) are the dominant species.[59]

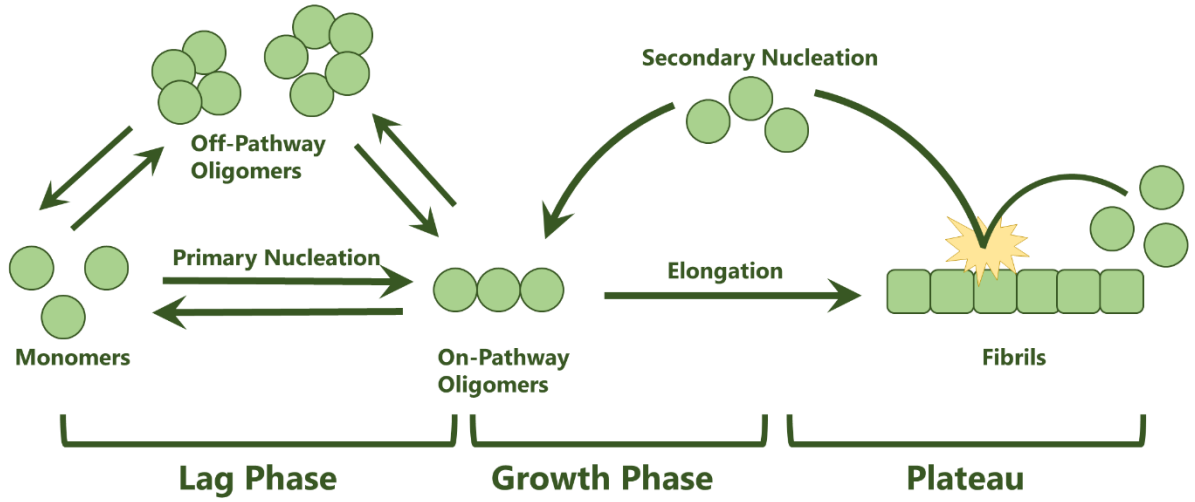

Figure 1.2: Schematic of the nucleated conformational conversion mechanism of Aβ aggregation.

However, this model does not account for metastable oligomers that have been observed and to which toxicity has been attributed. A modified model for Aβ aggregation has been developed to account for these species, via a nucleated conformational conversion mechanism (**Figure 1.2**).[62] This invokes a series of 'non-productive' oligomers that

cannot form fibrils, but do interconvert between monomers, nuclei and other oligomers. The lag phase thus consists of monomers and oligomers of several different flavours, and the rate limiting step is the conversion of non-productive oligomers into nuclei through fibril formation.[63, 64] Secondary nucleation, where a fibril catalyses the formation of new nuclei, and fibril breakage that allows for further elongation of existing fibrils, also impact upon the kinetics of aggregation.[63] This model of aggregation begets the study of not only the structure of Aβ fibrils but also the structure of the different oligomeric species, and consideration of the therapeutic potential of redirecting aggregation to non-amyloid structures.

1.1.4 The structures of Aβ fibrils

The structure of amyloid fibrils can be analysed with a variety of techniques. Electron microscopy (EM) and atomic force microscopy (AFM) are standard methods for analysing the overall structure of fibrils, whereas solid-state NMR, X-ray diffraction and cryo-EM can afford near-atomic resolution structures. Viewed under EM and AFM, aggregated Aβ is typically seen as long, unbranched fibres, although distinct polymorphs arise due to variations in both the monomer size and the aggregation conditions.[65] $A\beta_{40}$ can display a number of polymorphs depending on aggregation conditions, 3-fold symmetry is observed under static assembly conditions (**Fig 1.3A**), and fibres with 2-fold symmetry are observed after agitation during assembly (**Fig 1.3B**).[66] Other less common polymorphs of $A\beta_{40}$ have also been reported.[65] $A\beta_{42}$ is generally observed as fibrils 8 nm in width with two-fold symmetry (i.e. each composed of two interwound protofibrils) (**Figure 1.3C**).[67] EM and AFM have been used to demonstrate alternate aggregates, such as those induced by the polyphenol epigallocatechin gallate (EGCG) (**Fig 1.3D**).[68] The different morphologies of fibrils arises from differences in molecular packing, which requires high resolution techniques to examine further.

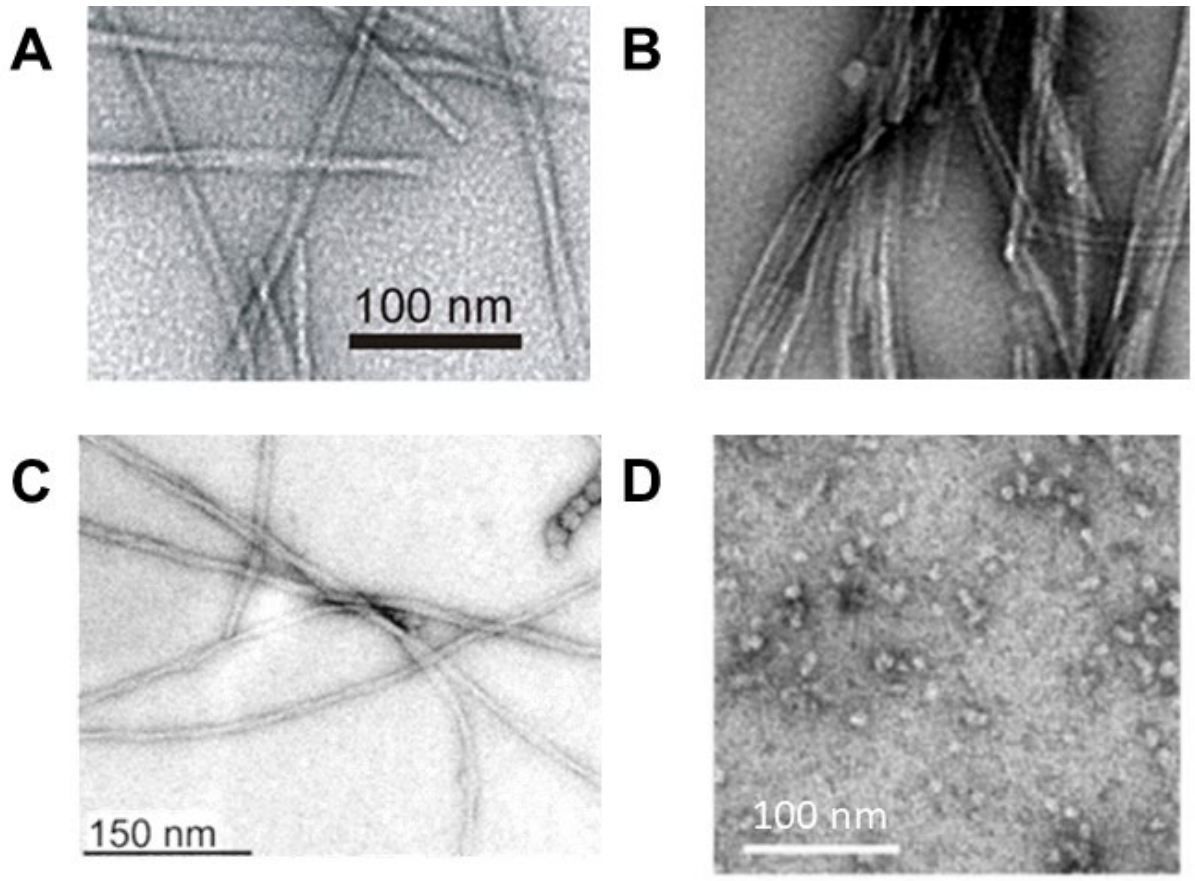

Figure 1.3: EM images of different Aβ morphologies: $A\beta_{40}$ trimer (**A**), $A\beta_{40}$ dimer (**B**),[69] $A\beta_{42}$ dimer (**C**),[67] $A\beta_{42}$ exposed to EGCG (**D**).[68] Figure reproduced from Paravastu *et al.*, Antzutkin *et al.*, and Ehrnhoefer *et al.*

Typically X-ray crystallography, and more recently cryo-EM, are used for such purposes. However, fibrils composed of full-length Aβ peptides tend to be heterogeneous to the extent that they do not crystallise, which also means they produce disordered, poorly resolved structures.[70] Solid-state NMR has been widely used to determine the structures at near-atomic resolution, and there has been some success in crystallising truncated peptides to examine certain regions of the fibril.[70] These methods have determined various common elements to Aβ fibril structure. The fibril monomers are arranged as in-register parallel β-sheets, with distances of 4.7-4.8 Å between sheets.[71] Side chains are packed tightly within the fibrils, water is excluded, and side chains do not form hydrogen bonds.[71] Rather, they are arranged so that their shapes complement each other, and Van

de Waals interactions are enabled, an arrangement called a 'steric zipper' as the side chain arrangement is reminiscent of a zip's teeth.[72]

Using NMR methods, 3D models for both polymorphs of $A\beta_{40}$ have been generated. They each show a similar 'U' shaped arrangement of monomers that expose polar residues to the solvent and bury hydrophobic residues (**Figure 1.4A**).[69] High resolution structures of $A\beta_{42}$ have been determined using both NMR and cryo-EM analyses of highly homogeneous fibrils assembled under different conditions. Colvin, *et al.* allowed $A\beta_{42}$ fibrils to assemble in 20 mM phosphate buffer, pH 8.0 and produced fibrils with an 'S' shaped or 'double horseshoe' monomer conformation (**Figure 1.4C**).[73] Gremer, *et al.* assembled fibrils in an aqueous HPLC buffer consisting of 30% acetonitrile and 0.1% trifluoroacetic acid, which caused monomers to adopt an alternate 'S-L' conformation (**Fig 1.4D**).[74] Both structures are consistent with fibril morphologies observed by EM, however the disparity raises more uncertainty about polymorphisms in $A\beta_{42}$-some of which may not be apparent using currently available tools- and their biological consequences.

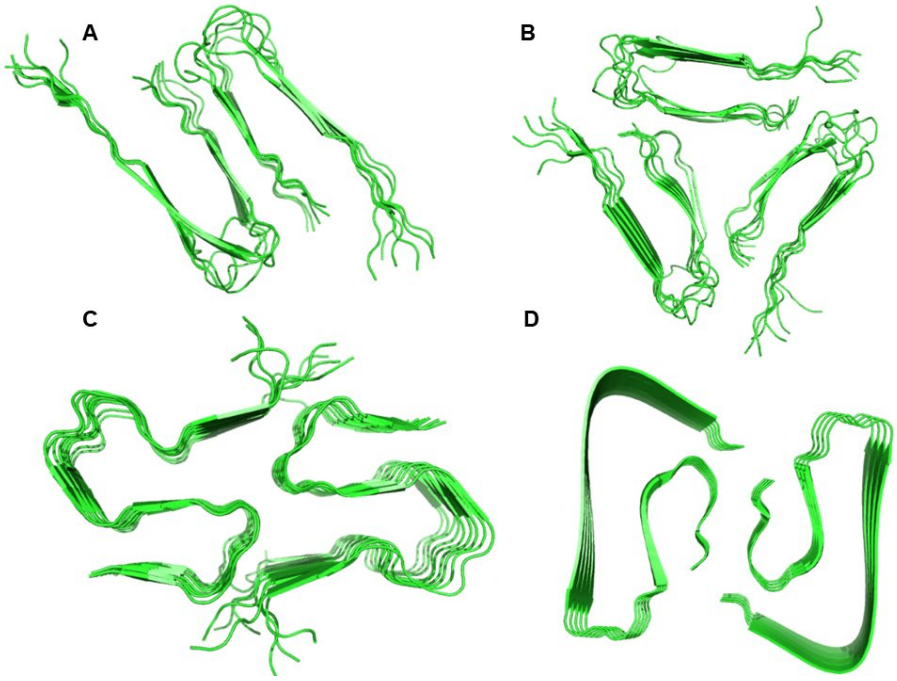

Figure 1.4: 3D structures of Aβ polymorphs: ssNMR structure of $A\beta_{40}$ dimer (PDB

2lmn, A),[69] ssNMR structure of $A\beta_{40}$ trimer (2lmp, B),[69] ssNMR structure of $A\beta_{42}$ dimer (PDB 5kk3, C),[73] cryo-EM structure of $A\beta_{42}$ dimer (PDB 5oqv, D).[74]

Therapies aimed at reducing the buildup of Aβ fibrils that have reached clinical trials fall into two main categories: secretase inhibitors that prevent the production of Aβ monomers, and monoclonal antibodies that target fibrils or soluble, fibrillar aggregates of Aβ and facilitate their removal. Three γ-secretase inhibitors have entered clinical trials for AD – semagacestat, avagacestat , and tarenflurbil – and all three failed. Semagacestat and avagacestat failed in phase 3 and 2 trials respectively as they increased cognitive decline and caused an increased risk of skin cancer.[75, 76] Tarenflurbil failed in phase 3 trials due to low efficacy as it had poor blood-brain barrier penetration.[77] Targeting γ-secretase is considered problematic as it acts on numerous other targets as well, including Notch 1 which is responsible for controlling cell differentiation.[78]

Multiple β-secretase inhibitors have also failed clinical trials: these compounds showed some efficacy in lowering Aβ levels, but patients showed no cognitive improvement and dangerous side effects were frequently observed.[79]

The monoclonal antibodies (mAbs) developed to target amyloid plaques and fibrils include solanezumab and bapineuzumab, both of which entered phase 3 trials for mild to moderate AD.[80, 81] However none of the antibodies developed to target plaques have passed clinical trials, as they did not appreciably slow cognitive decline. Two mAbs targeting soluble Aβ aggregates have been approved by the FDA: aducanumab and lecanemab. The approval of both therapies has been controversial, particularly for aducanumab, as while these drugs lower the level of aggregated Aβ in patients, they have demonstrated limited cognitive improvement in clinical trials.[82, 83]

1.1.4 Controlling the mechanism of Aβ aggregation

The failure of treatments targeting fibrillar Aβ have spurred investigation into the various oligomeric species that exist, and how the process of aggregation can be controlled to

prevent oligomer formation. The oligomers that are associated with toxicity *in vitro* are intermediates in the fibrillisation process: smaller, structured aggregates that eventually form fibrils.[84, 85] These "on-pathway" oligomers are predominantly formed through secondary nucleation, and their formation is accelerated once a critical concentration of fibrils is reached. [86] "Off-pathway" oligomers are amorphous and do not form fibrils, and can be generated when the aggregation process is perturbed by exogenous compounds.[68]

In order to reduce the production of toxic oligomers, the particular processes responsible for their formation need to be inhibited, rather than just blocking fibril formation outright. The inhibition of fibril elongation reduces the overall load of fibrils, but since fibrils catalyse the formation of oligomers through secondary nucleation, inhibiting fibril elongation is thus unlikely to reduce overall toxicity.[87] Similarly, inhibiting primary nucleation can slow the formation of fibrils but will not necessarily stop the formation of oligomers.[87] The development of compounds that inhibit secondary nucleation events, or that bind to monomeric Aβ and prevent the formation of "on-pathway" oligomers by directly binding to the monomer, dubbed "monomer sequestration," is a priority target.

Inhibition of secondary nucleation has been achieved using antibodies and chaperone proteins,[88, 89] as well as a class of small molecule retinoid receptor agonists that inhibit primary and secondary nucleation simultaneously.[90] Macromolecules are best suited to the inhibition of secondary nucleation, as their larger size allows them to more easily cover the surface area of the fibrils. While many small molecules have been reported to inhibit aggregation, there has only been one reported to date that has been confirmed to interact with monomeric Aβ directly, 10074-G5 **1** (**Figure 1.5**).[91] It has been proposed to bind to monomers and induce a conformation that stabilises it in solution, thus slowing the formation of oligomers and fibrils.[92] The compound has a reported binding constant of 40 μM, which is low for a typical small-molecule drug. One of the issues in identifying

molecules that bind to monomeric Aβ is that it is intrinsically disordered, so there are no binding pockets to which a small molecule can form a stable interaction.[93]

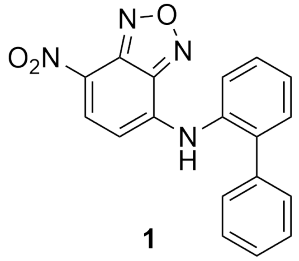

1

Figure 1.5: Structure of **1**, which inhibits Aβ aggregation by binding directly to monomeric Aβ.

While there are many assays to measure the effectiveness of Aβ aggregation inhibitors *in vitro*, there is a fundamental lack of effective animal models to demonstrate the efficacy of aggregation inhibitors at treating AD *in vivo*. There is a *Candida elegans* model remains which useful for determining whether anti-aggregation compounds maintain their activity *in vivo*, but this does not reveal any insight into reduction in of the toxicity induced by Aβ aggregation.[94] Rodent models have been developed and used to measure the effectiveness of amyloid-clearing therapies, however these are also limited, and compounds that were successful in these models did not translate to the clinic.[95] AD is a complex disease and there is no single animal model yet that can recapitulate all of the symptoms observed in human AD, however accurate animal models are required to understand the role of Aβ, and other factors, in the pathogenesis of AD.[96]

1.2 Determining the structure of a protein

1.2.1 X-Ray crystallography

The most commonly used, and arguably most powerful, method for the determination of protein structure is X-ray crystallography. When a beam of X-rays is directed at a crystal, the constituent atoms cause the X-rays to diffract at characteristic angles, generating a unique diffraction pattern that is used to assign the position of the atoms in a crystal lattice and thus determine the structure of the molecule. The technique relies

on the formation of a homogeneous crystalline sample of protein, which is achievable for many globular proteins. X-ray crystallography is a ubiquitous technique in structural biology and has been used to determine around 90% of protein structures deposited in the Protein Data Bank (PBD).[97]

The development of protein crystallography revolutionised drug discovery, leading to the advent of "structure-based" drug design, in which the structure of a small-molecule bound to a target protein is used to guide lead development[98] Initial attempts at using crystallography for lead discovery efforts were stymied by the expense and labour of crystallography compared to high-throughput screening methods, which are now favoured for the lead discovery phase.[99] Advances in computational techniques have resulted in the development of molecular docking programs that calculate the binding energies of small molecules on a pre-determined protein structure.[98] These advances have allowed crystallography to remain an important technique in the lead optimisation stage, where the structure of the lead molecule bound to the protein target is used as a guide for the development of compounds that bind more strongly.

While it remains a powerful technique for the study of protein structure, there are limitations to crystallography which make it difficult to apply to many biologically important proteins. Membrane proteins are a class of proteins which make up approximately 30% of known proteins, and many members this class are of great pharmacological interest.[100] Receptor proteins, such as G-coupled protein receptors, are membrane-bound and implicated in diseases and neurological processes such as pain, making them highly valued targets for drug development.[101, 102] It is often difficult to apply crystallography to their structure determination to membrane proteins due to inherent properties of the protein class itself: these are molecules are evolved to sit inside the lipid membrane of a cell or organelle, and thus have highly non-polar regions of their sequence, which makes crystallising them from aqueous buffer challenging.[103] These membrane-spanning portions of the protein are critical for the native structure of the

protein but make them difficult to solubilize so that diffraction-quality crystals can be grown. This can be overcome with the aid of surfactants in crystallisation solution, but they remain a difficult class of protein to study with this technique.[104]

Another limitation of crystallographic studies is that they capture structural information from the solid state.[105] This is a significant caveat as proteins are predominantly found in solution, and the solvation of a protein affects its overall structure.[106] The process of crystallisation can favour particular conformations over others, and the conformations that crystallise well may not be the most abundant conformations in the native state.[107] While models such as the "lock-and-key" for enzymes and substrates suggest that proteins are relatively rigid in their "on" and "off" states, it is widely accepted that proteins tend to be dynamic in the solution state.[4] The degree of dynamics that a protein will exhibit is different depending on the primary sequence and secondary structures it adopts.[4] A protein rich in secondary structural motifs will be more rigid, while regions that are composed of random coils will necessarily have more freedom to move in solution. These disordered regions of proteins often play important roles in biological sensing, molecular recognition and in the solubilisation of proteins, but they become invisible – or at least very difficult to visualise reliably – using crystallography.[108]

There is also a class of proteins which have a high proportion of disordered regions, which are dubbed intrinsically disordered proteins.[109] These proteins are increasingly recognised to have important biological functions, such as in phase condensation, and are also implicated in diseases like Parkinson's disease.[110] Since these proteins are highly dynamic, their structures cannot be represented by a single X-ray structure, and are instead better described using a series of structural ensembles that it inherits.

1.2.2 Emerging technologies in structural biology

Several emerging techniques have been developed in structural biology to overcome the challenges associated with conventional X-ray crystallography. These techniques do not

require large crystals to be grown, making the process of generating a structure much easier.

The invention of X-ray free electron lasers (XFEL) has expanded the capabilities of crystallographic studies. Compared to traditional light sources, XFEL produces a remarkably intense beam of photons and can do so in incredibly short pulses, and these advantages have led to the development of serial femtosecond crystallography (SFX).[111, 112] In a conventional crystallography experiment, the sample is placed in a beam of X-rays and continuously rotated to produce diffraction patterns at different angles, which are assembled to generate the three-dimensional diffraction pattern. The long exposure time causes radiation damage to the crystal, which is minimised by using large crystals and cooling the crystal during data collection.[113]

In contrast to conventional X-ray crystallography, SFX experiments are performed using a solution of microcrystals- which are far easier to produce than larger crystals- and the solution is passed through a pulsing XFEL beam.[114] The pulses are femtoseconds in length, which exposes the microcrystal to enough photons to generate a diffraction pattern before radiation damage completely destroys it. Since microcrystals are passed over the beam in a continuous stream, there is a random sampling at all angles which means a three-dimensional diffraction pattern can be assembled without rotating the sample.[115] The rapid pulsing also can be used for dynamic experiments, such as monitoring enzyme catalysis, as long as the movements can occur within the microcrystal lattice.[112]

Cryogenic electron microscopy (Cryo-EM) is another technique that has emerged in structural biology. As the name suggests, the technique uses electron microscopy rather than diffraction to generate a structure of the protein. An aqueous protein sample is applied to a grid and flash-frozen using a cryogenic liquid (typically liquid ethane), and then visualised under an electron microscope.[116] A slide prepared in this manner

contains many copies of the protein in random orientations to the lens, and these images are reconstructed to give a 3D structure of the protein.[116, 117] Cryo-EM has been particularly advantageous when used to solve structures of large biomolecular complexes, such as virus capsids and protein complexes.[118] Smaller structures are more difficult to solve using Cryo-EM, as they are trickier to visualize using microscopy, but advances in electron detector technology and software have allowed high resolution structures of smaller proteins to be developed.[119]

Microcrystal electron diffraction is a related technique which combines elements of Cryo-EM and X-ray diffraction: microcrystals of the protein of interest are cryogenically frozen and visualised with an electron microscope in diffraction mode, which produces an electron diffraction pattern that is analogous to X-ray diffraction patterns.[120] These diffraction patterns can then be processed using X-ray diffraction software to produce a 3D structure.[121, 122]

AlphaFold is an artificial intelligence program that emerged in 2020 as a structural biology tool. AlphaFold is a neural network that predicts the structure of a protein based on its sequence alone. Having been trained on a library of reported protein structures, the program is able to assess the most likely distance and dihedral angle between two amino acids in a sequence, and thus generate an overall structure.[123] The ability to accurately determine the structure of a protein based on sequence alone is undoubtedly a revolutionary step forward in structural biology, the benefits of which will be seen in the coming years.[124]

However, there are some limitations to the application of AlphaFold. The structures provided give no information on dynamics, and the application to structure-based drug design is limited to the sophistication of docking software.[125, 126] The sequence-structure paradigm which forms the basis of AlphaFold's predictions also struggle with intrinsically disordered regions.[127] The conformational heterogeneity of these regions naturally

makes the prediction of one specific structure difficult, and often their structure(s) are highly dependent on one or more binding partners.[126, 127] This being said, AlphaFold is still a powerful and complementary tool to be used in conjunction with other biophysical techniques.[125]

1.2.3 Protein NMR

Nuclear magnetic resonance spectroscopy (NMR) is a powerful tool for the structural characterisation of organic molecules. While originally applied to small molecules, the technique can also be used to study the structure of proteins. It has become widely used in structural biology, although not to the same extent as protein crystallography, and underpins about 9% of structures deposited in the PDB.[97] Both solution-state and solid-state NMR techniques have become useful for the structural determination of proteins that are difficult to crystallise, making protein NMR a complementary technique in a structural biologist's toolkit.

The principle behind protein NMR is that one can obtain a series of distance restraints for each nucleus in the protein, which can then be used to calculate a structure (or ensemble of structures) using a computational algorithm.[128] The first step in this process is to assign each NMR backbone resonance to an amino acid. In early protein NMR experiments, this was done using double quantum filtered correlation spectroscopy (COSY) or total correlations spectroscopy (TOCSY) experiments to identify spin systems, followed by sequential Nuclear Overhauser effect spectroscopy (NOESY) experiments to assign each to an amino acid along the peptide chain.[129] Developments in isotopic labelling methods of proteins has now given rise to triple resonance experiments. These require uniformly ^{15}N- and ^{13}C- labelled protein, and involve a ^{1}H-^{15}N heteronuclear single quantum coherence spectroscopy (HSQC) experiment, and a series of experiments to correlate each NH resonance to a ^{13}C resonance sequentially.[130]

Once these resonances have been assigned to the protein backbone sequence, distance restraints are then measured. NOE derived distance restraints are considered the most important source of structural information, since they arise from a direct through-space correlation between different nuclei, and have traditionally been the sole source of distance restraints in protein NMR.[131] ^{3}J couplings are used to derive the dihedral angle between amino acids, and are generally the second most important data set.[132] As more high-resolution protein structures have been reported along with their chemical shift data, it has become possible to predict a protein's structure directly from the chemical shifts derived from triple-resonance experiments.[133] Typically, this information is used to complement the data obtained from the previously described experiments.

While the distance restraints from NOEs, ^{3}J-couplings and chemical shifts provide useful information on protein structure, cumulative errors in the overall structure can occur because these are short-range effects.[134] The accuracy of the structural model can be improved by long-range information derived from small-angle X-ray scattering (SAXS), or from residual dipolar couplings (RDCs) obtained from NMR. SAXS is a solution-state technique where the scattering of X-rays by a monodispersed macromolecule in solution is measured and gives information on the size and shape of the molecule. The data obtained from SAXS is typically fit to a model derived from molecular dynamics simulations in order to determine the overall shape of the protein.[135]

RDCs arise in NMR spectra from a net anisotropic alignment of the molecule of interest in solution.[136] A common method to induce this alignment is to introduce a liquid crystalline substance into the NMR solution. These can be charged media which are often themselves biomolecules, such as cellulose[137] or phage viruses,[138] which align the protein based on electrostatic forces. Uncharged media, which are typically lipid bicelles[136] or polyethylene glycol polymers[139], align the media based on steric interactions. The alignment of the protein means that dipolar interactions between nuclei do not average to zero by molecular tumbling, and manifest as peak splitting in

the NMR spectrum.[140] The orientation of the protein, or domains within the protein, can then be determined by comparing the measured RDCs to calculated values.

1.2.4 Paramagnetic effects in protein NMR

Paramagnetic centres in proteins give rise to magnetic effects observable in ^{1}H-^{15}N HSQC experiments, which can be used for the determination of other structural information, including with other bound ligands, and to measure protein dynamics. The paramagnetic centre can be the native metal centre in a metalloprotein, or it can be introduced using an appropriate tag which can be used to measure different paramagnetic effects, depending on the metal introduced (**Figure 1.6, 2-7**).[141-146] Such tags include metal-binding peptides that are introduced to the C- or N- terminus of the protein as a fusion tag.[147] There are also a number of metal chelating tags that react with cysteine to form disulfide or thioether bonds. Another popular tag for paramagnetic relaxation enhancement measurements (*vide infra*) are stable nitroxide radical tags derived from TEMPO with similar cysteine-reactive motifs.(**Fig. 1.6, 8-9**).[148]

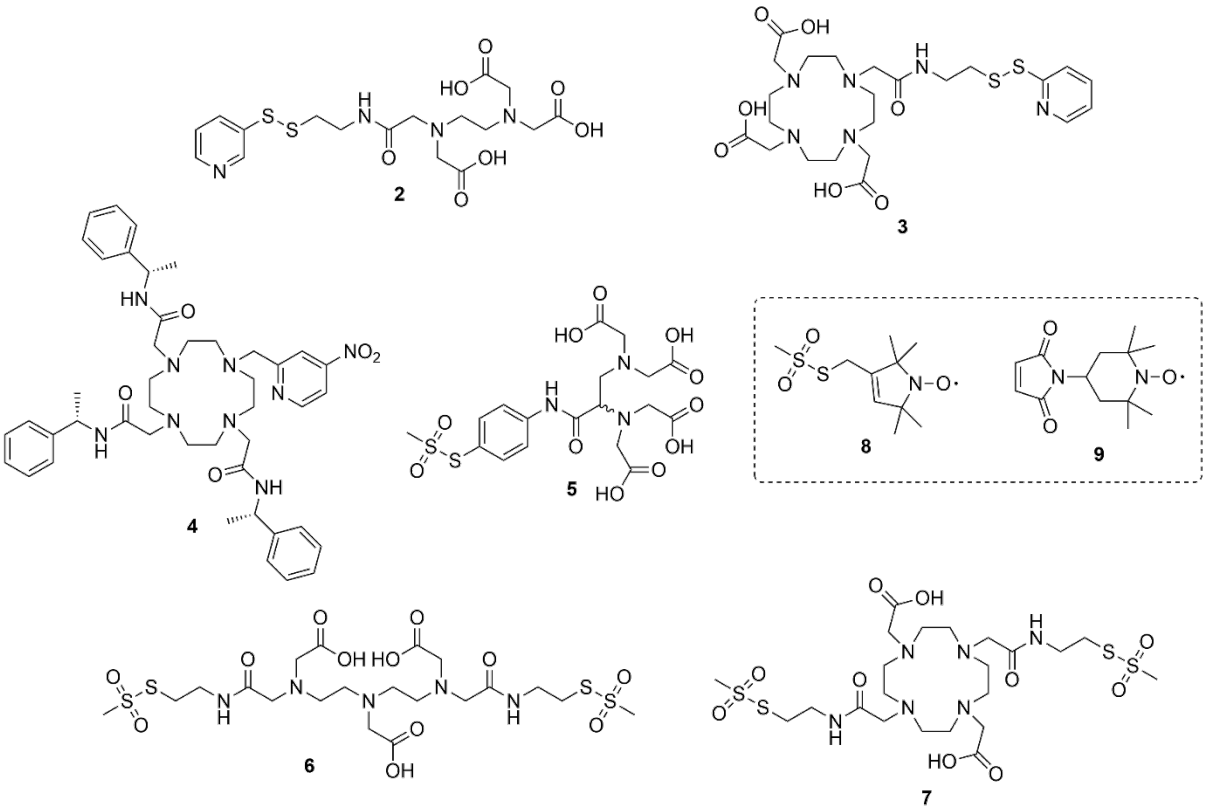

Figure 1.6: A selection of reported paramagnetic tags. **2-7** are metal chelators using either cyclen or EDTA derived scaffolds, **8-9** are stable nitroxylx radicals. In each case, the tag can form a covalent link to the protein of interest via reaction of the disulphide (**2**, **3**), 4-nitropyridine (**4**), thiosulphonate ester (**5-8**) or maleimide (**9**) moiety with a reactive amino acid side chain, typically a cysteine.

The paramagnetic effects that arise in an NMR spectrum depend on the nature of the paramagnetic species. If the magnetic moment of the paramagnetic centre changes with it taking up different orientations in a magnetic field, then the magnetic susceptibility tensor (χ) is said to be anisotropic; if it does not change then χ is isotropic. Nitroxide radicals, Gd^{3+} and Mn^{2+} ions have isotropic magnetic susceptibilities, whereas Cu^{2+}, Co^{2+}, and the other paramagnetic lanthanides have an anisotropic magnetic susceptibility.[141, 149, 150]

All paramagnetic centres cause an increase in the transverse nuclear relaxation rates of nuclei, which manifests as a reduction in signal intensity in the NMR spectrum (**Figure**

1.7). This effect is called paramagnetic relaxation enhancement (PRE) and it is the most commonly used paramagnetic effect in structural biology.

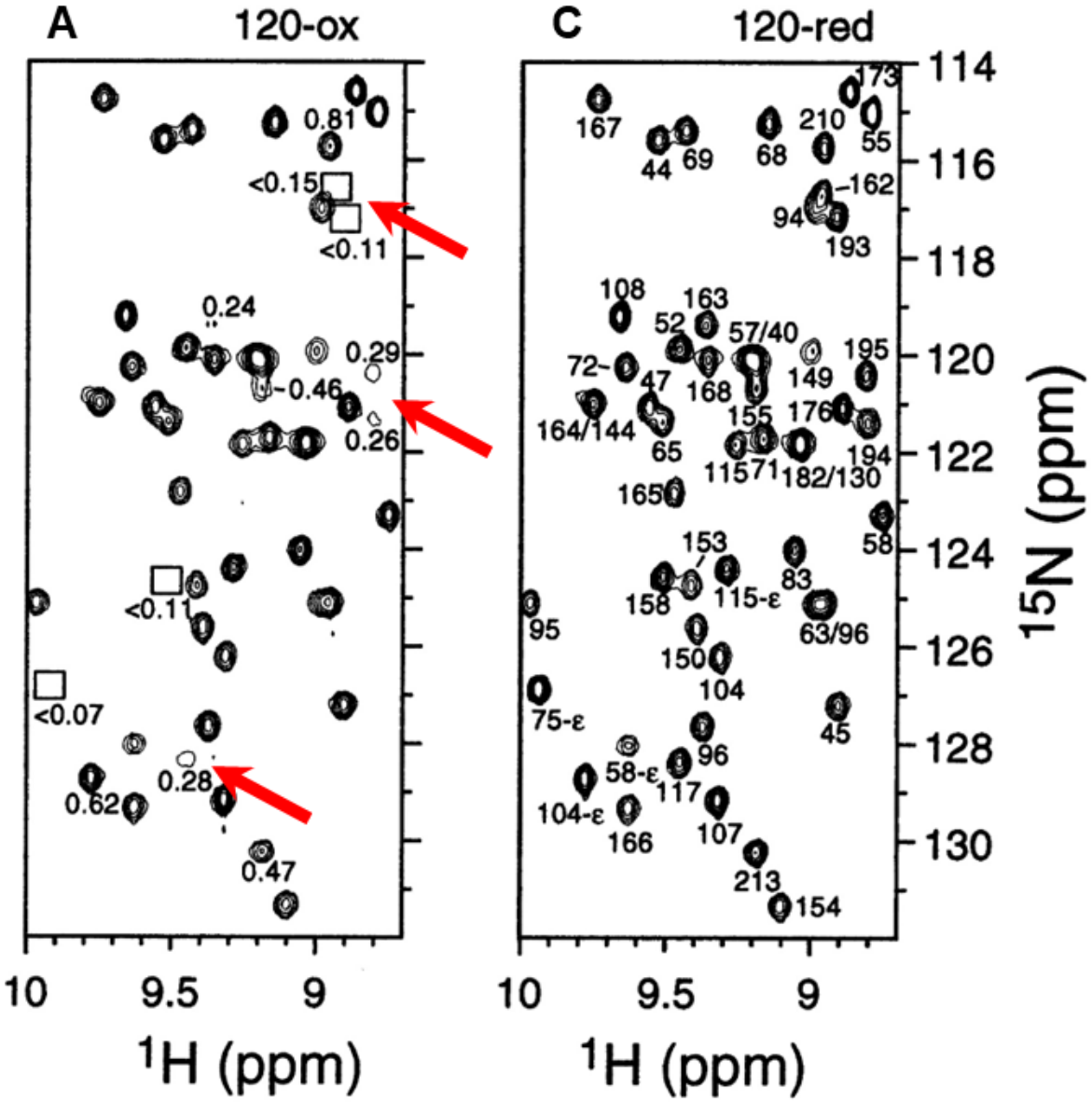

Figure 1.7: Example ^{1}H-^{15}N HSQC spectrum where PRE manifests as a reduction in signal intensity for peaks near the tag in the paramagnetic spectrum (A) versus the diamagnetic spectrum (B).[148] Peaks closest to the paramagnetic tag are broadened beyond detection, and the reduction in peak intensity decreases with increasing distance from the tag through space.

PRE influences both the longitudinal (T_1) and transverse (T_2) relaxation rates, but the T_1 relaxation rates are rarely used due to difficulties in obtaining the paramagnetic

contribution to the relaxation rate and cross-relaxation interference.[151] The relationship between the T_2 relaxation rate and the distance from the paramagnetic centre is described by **Equation 1**.

$$T_2^{para} = \frac{1}{15}\left(\frac{\mu_0}{4\pi}\right)^2 \frac{\gamma_I^2 g_e^2 \mu_B^2 S(S+1)}{r_{IM}^6}\left(4\tau_c \frac{3\tau_c}{1+\omega_I^2\tau_c^2}\right)$$

Equation 1: Where T_2^{para} is the paramagnetic contribution to the transverse relaxation rate, γ_I is the gyromagnetic ratio of nucleus I, g_e is the electronic g factor, μ_B is the Bohr magneton, S is the spin quantum number, r_{IM} is the distance between nucleus I and the paramagnetic centre, τ_c is the correlation time and ω_I is the Larmor frequency of nucleus I.[152]

The paramagnetic contribution to the transverse relaxation rate can be obtained by comparing the peak broadening compared to a diamagnetic reference, described in **Equation 2**.[148]

$$\frac{I^{para}}{I^{dia}} = \frac{T_2^{dia} exp\left(-T_{dia}^{para} t\right)}{T_2^{dia} + T_2^{para}}$$

Equation 2: Where I^{para} and I^{dia} are the peak heights for the paramagnetic and diamagnetic spectrum respectively, and t is equal to the INEPT time in the HSQC experiment.[148]

The key factor in this relationship is that the distance dependency of the relaxation enhancement is $1/r^6$. This steep distance dependency enables the measurement of the distance between affected nuclei and the paramagnetic centre. This can be used for the qualitative determination of residues that are nearby the paramagnetic centre, and if the magnetic susceptibility is isotropic, it is possible to obtain a quantitative measure of distance using PRE.[148] It is important to note that the measurement of all paramagnetic effects by NMR require a comparison to a diamagnetic reference spectrum. This is obtained by either labelling the protein with a tag chelating Zn^{2+}, or in the case of

lanthanide probes either La^{3+}, Y^{3+} or Lu^{3+}. Nitroxide radical tags can be conveniently reduced *in situ* to provide a diamagnetic reference.

PRE data can be used as a source of distance constraints for assigning the structure of a protein. This is particularly useful in cases where NOEs cannot be obtained in sufficient number, or are difficult to interpret.[148] This situation often arises in proteins with large α-helical content such as membrane proteins,[153] where the amide backbone mostly displays short-range NOEs, and proteins with many soluble loops.[154]

PRE is particularly useful for probing the dynamics of a protein, including its interactions with ligands or protein binding partners. By tagging either the protein, the ligand, or the protein binding partner with a paramagnetic centre, intermolecular PREs can be measured on the residues where the interactions occur. This is also apparent in fast-exchange regimes where there is only a weak binding between the partners, or in lowly-populated states. In these cases, NMR peaks are a population-weighted average of the discreet signals corresponding to the different states, and a PRE affecting one state will be observed as a reduction in the height of the averaged peak.[155]

This approach has been used in order to probe the conformation of the transcription factor HOXD9 as it searches for a binding site along paramagnetically labelled DNA.[156] Two short DNA duplexes, one containing the recognition sequence for HOXD9 and one without, were labelled separately at four sites with EDTA and complexed with Mn^{2+}. The PREs measured at high salt concentration, in which HOXD9 is in fast exchange with DNA, revealed that there were lowly populated states in which HOXD9 was bound weakly to DNA sites outside the recognition sequence. These experiments also showed that HOXD9 searches for the recognition sequence by hopping between different DNA strands, rather than sliding along the same strand.

Which residues of a protein that are solvent exposed can also be measured using freely soluble paramagnetic probes, which will only exert PRE on the solvent exposed

residues.[157] This can be used to map the topology of membrane proteins, and determine which portions reside outside the membrane. This methodology has been applied to the structure determination of the NS2B protein that is important for the replication of Dengue virus.[158] Solvent PRE has also been used as a label-free approach to probe the dynamics of multidomain proteins by examining the ensemble-averaged PRE and comparing this to calculated PRE for each state.[159] Solvent PREs can also be used to complement other techniques, when determining the structural ensembles of intrinsically disordered proteins.[160]

If the paramagnetic metal used has an anisotropic χ, then it can also induce changes in the chemical shift of nuclei, called paramagnetic shifts. There are two kinds of paramagnetic shifts: contact shifts, which arise from through-bond interactions and are generally only observed on the paramagnetic tag,[161] and pseudo-contact shifts (PCSs) which arise from through-space interactions. The change in chemical shift due to a PCS is described in **Equation 3**.[162]

$$\Delta\delta_{pc} = \frac{1}{12\pi r_{IM}^3}\left[\Delta\chi_{ax}(3cos^2\theta - 1) + \frac{3}{2}\Delta\chi_{rh}(sin^2\theta cos2\Omega\right]$$

Equation 3: Where $\Delta\delta_{pc}$ is the pseudo-contact shift, r_{IM} is the distance between nucleus I and the metal centre, $\Delta\chi_{ax}$ is the axial component of the magnetic susceptibility tensor, $\Delta\chi_{rh}$ is the rhomboid component of the magnetic susceptibility tensor.

PCSs have a distance dependency of $1/r^3$, which means that they can be observed in nuclei further away from the paramagnetic centre than PRE. Additionally, PCSs contain information on the angle of the nucleus compared to the magnetic centre, which makes them a powerful observable in NMR. However, due to the angular dependency, PCSs are more prone to conformational averaging than PREs are, and can average to zero if the paramagnetic tag is attached *via* a particularly flexible linker.[163] Because these metals

have an anisotropic χ tensor, chemical tags chelating either Co^{2+} or paramagnetic lanthanide ions (except for Gd^{3+}) are used to measure PCSs. One further issue with measuring PCSs is the appearance of multiple sets of shifted peaks, arising due to diastereomer formation between the (chiral) protein and the enantiomeric complexes that form from chiral metal complexation. This kind of diastereomer formation can be avoided by biasing the ligand to adopt a single geometry, either by introducing a stereocentre into the ligand (**Figure 1.6, 4-5**)[143, 144], or by tethering it to two sidechains in the protein (**Figure 1.6, 6-7**).[145, 146]

PCSs are a powerful complement to NOEs for the refinement of protein structure, as the effects are long-range and contain angular information. For example, the solution structure of Calbindin D_{9k} was refined using PCSs generated by substituting Ce^{3+}, Yb^{3+} and Dy^{3+} into its calcium binding site.[164] PCSs have also been used as the sole source of distance restraints for a protein structure, achieved using multiple tagging sites, and two different paramagnetic lanthanides to maximize coverage of the protein.[165]

PCSs can be used to determine the structure of protein-ligand complexes, and so have been exploited in drug screening experiments. They are particularly advantageous for studying weakly binding ligands, including ligand fragments for fragment-based drug design, which are usually difficult to study crystallographically. Structural information can be gained by measuring the PCSs induced in ligand or ligand fragment signals by a tagged protein and using an excess of ligand, or by tagging the ligand itself and measuring PCSs in the protein spectrum.

An early example of the first of these methods saw the determination of the binding mode of lactose to galectin-3 labelled with Dy^{3+} (**Figure 1.8**).[166] A ligand:protein ratio of 5:1 produced a sufficient signal:noise ratio allow measurement of PCSs on the natural abundance ^{1}H-^{13}C HSQC spectrum of the ligand. While one metal ion provided sufficient information for this experiment, in general using multiple lanthanides with different χ

tensors improves the accuracy of the calculated structure.[167] A strategy of paramagnetically labelling protein has been used for fragment-screening in drug discovery, for example, a fragment-screen against the HIV-1 protein gp41 conducted by labelling a peptide known to bind strongly to gp41 and observing PCSs induced in the ligand fragment spectra.[168]

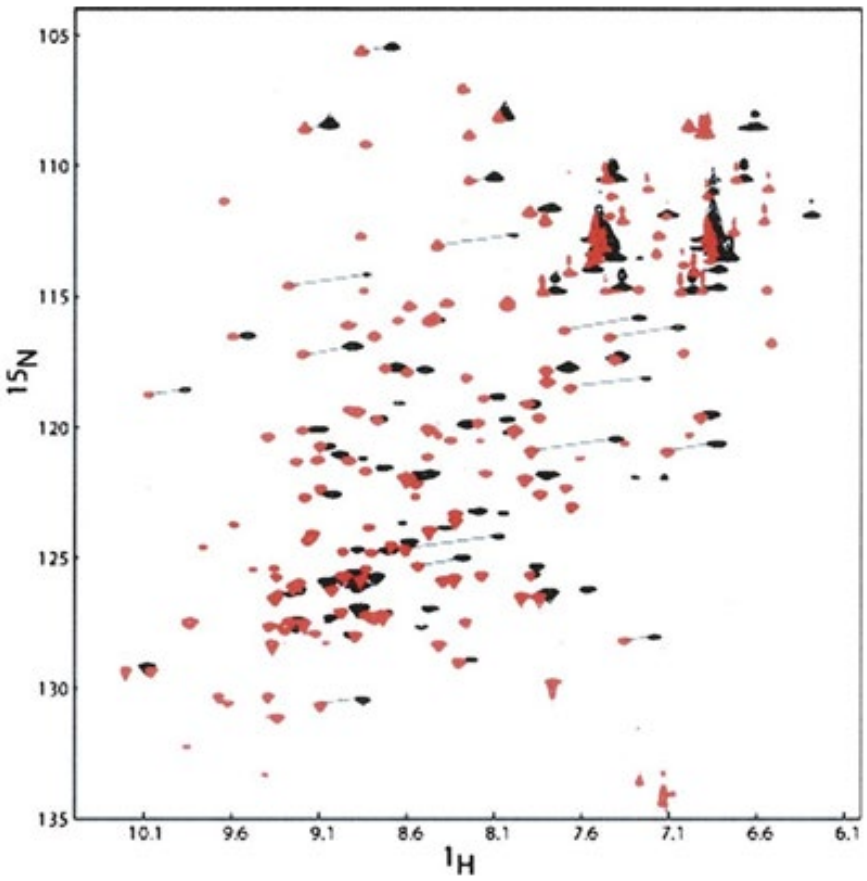

Figure 1.8: An example of PCSs manifesting in an ^{1}H-^{15}N HSQC spectrum, comparing the diamagnetic spectrum (red) and the paramagnetic spectrum (black) of galectin-3. Residues closest to the tag are broadened beyond detection due to PRE, residues close to the tag but beyond the distance for PRE experience a change in chemical shift dependent on the distance and angle of exposure to the tag.[166]

The strategy of labelling a ligand with a paramagnetic tag has been used to investigate the binding site of ligands to a protein using PCSs. There are some difficulties in using

this strategy, as incorporation of the lanthanide binding site needs to be sufficiently rigid that the χ tensor does not average to 0, while also not interfering with the normal binding of the small molecule. Nevertheless, the strategy has been used to identify the binding site of low-affinity small molecules to a target protein, for example the tagging of sevoflurane, an anaesthetic, with a Dy^{3+} label, used to identify the binding site on calmodulin.[169]

Labelling a protein with a paramagnetic centre also causes it to align weakly in the magnetic field used in obtaining an NMR spectrum. This can be used to measure RDCs without the need for external media, however the RDCs observed are often smaller than those induced using external media and are prone to conformational averaging like PCSs.[163]

1.3 Metal complexes and their application as probes

1.3.1 General aspects of lanthanide chemistry

Lanthanides have a broad range of applications in materials and biomedical sciences due to their unique magnetic and luminescent properties. The lanthanides range from lanthanum to lutetium, with yttrium also included – despite being a transition metal – due to its chemical similarity to the lanthanides. The defining characteristic of the lanthanides are the *4f* orbitals, which fills across the series. The most stable oxidation state for lanthanides is 3+, with electrons are first lost from the *5d* and *6s* orbitals as they are much higher in energy than the *4f* orbitals, leaving trivalent lanthanides with an electronic configuration of $[Xe]4f^n$.[170] The chemistry of aqueous lanthanides is dominated by 3+ oxidation state, although there are exceptions such as cerium, which is also found in the 4+ oxidation state, and samarium and europium, which can be found in the 2+ oxidation state. The valence *4f* orbitals are radially contracted and penetrate the [Xe] core, and as a result are shielded from the environment by the *5s* and *5p* orbitals.[171] This limits interactions with ligand orbitals and thus there is only a limited crystal field

splitting.[172] Lanthanides tend to have high coordination numbers (8 or 9) as their ionic radii are large compared to transition metals. As the *4f* orbitals are buried within the *5s* and *5p* orbitals, bonds have a primarily electrostatic character and ligand geometry is determined by the minimisation of steric interactions.

The trivalent lanthanides, with the exception of La^{3+}, Lu^{3+} and Y^{3+}, possess unpaired electrons and are paramagnetic. Because there are 7 *f* orbitals, it is possible to have up to 7 unpaired electrons, as with Gd^{3+}, which results in the lanthanides having a large magnetic moment. The magnetic properties of lanthanide ions are largely unaffected by their coordination environment, and at room temperature lanthanide complexes tend to have the same magnetic moment as expected for a free ion.[173] This is different to transition metals, where the coordination environment can have a profound effect on the spin state, and the magnetic moment of a complex.

Lanthanides are capable of fluorescence and phosphorescence, which are grouped under the term 'luminescence' properties. Lanthanide luminescence is governed by *f-f* transitions which are formally forbidden according to the Laporte selection rule.[174] The low probability of these transitions means that lanthanide luminescence is low intensity, and has a correspondingly low molar absorptivity.[175] However, there tends to be a high number of peaks associated with lanthanide absorption and emission spectra, when compared to *d* transition metals, due to the high number of microstates accessible within each electronic configuration.[176, 177] Sharp peaks are also observed in these spectra, as there is less vibronic coupling between the ion and ligand than compared to transition metals.[178] Long luminescent lifetimes are also observed, due to the low probability of *f-f* transitions.[179] As with magnetism, there is little difference between the electronic spectra of the free ions and those of their complexes. While direct excitation of the lanthanide is inefficient, luminescence can be achieved *via* the antenna affect: an antenna chromophore that is close in energy and has good orbital overlap with the lanthanide ion can be used to excite the metal and induce luminescence.[180]

1.3.2 General aspects of transition metal chemistry

Transition metals are the elements in the *d* block of the Periodic Table, the chemistry of which is defined by the valence *d* electrons. The focus on this section will be on the *3d* metals, which have more generalisable chemistry and are the ones used in this research.

In contrast to lanthanides, the valence electrons of *d* transition metals reside in *d* and *s* orbitals. Transition metals can have a range of oxidation states, depending on their group in the Periodic Table, as there is a smaller energy gap between the valence *s* and *d* orbitals, compared to the large gap between the *4f* orbitals and the valence *6s* and *5p* orbitals in lanthanides. The *d* orbitals often overlap with ligand orbitals, so transition metal complexes can experience large ligand-field splitting. The ligand geometries of these complexes are determined by the orientation of the *d* orbitals in the metal centre. The most common geometries are octahedral, tetrahedral and square planar for *3d* complexes. Due to the influence of ligand-field effects on energy levels, the coordination environment of a transition metal can have a profound influence on its magnetic and optical properties.

1.3.3 Important aspects of ligand design

The unique magnetic and luminescent properties of lanthanides, which are independent of the coordination environment, have spurred the development of functionalised lanthanide complexes for fluorescence sensing and magnetic resonance imaging (MRI) purposes. Stability of these complexes is critical, particularly for MRI contrast agents. Free lanthanide ions are toxic to humans, as their similar ionic radii means they bind in place of calcium in proteins. [181] The higher charge density of the lanthanides means they bind more strongly than calcium, and as a result they disrupt the many calcium dependent pathways in the body, causing nephrogenic systemic fibrosis.[182]

The requirements for a ligand to form a thermodynamically stable complex differ between the lanthanides and the *3d* metals, as can be inferred from the thermodynamic

stability constants listed in **Table 1.1**. The ligand requirements for lanthanides differ little across the series and they favour ligands with multiple electron donors, especially hard electron donors such as carboxylates. Lanthanides from further along the series (e.g. Yb^{3+}) form more stable complexes than those earlier in the series as they have smaller ionic radii, which reduces the steric strain on the ligands.[183] Lanthanides can have a coordination number of 8 or 9, depending on their place in the series.[184] 6-Coordinate ligands like EDTA **12** and NOTA **14** can form complexes with the lanthanides but these are not as stable as 8-coordinate ligands like DOTA **17** or DTPA **13**.[185] Typically, a water molecule will occupy the 9th coordination site, as the steric strain associated with occupying the 9th site is too great for most ligands.

Table 1.1: Thermodynamic stability constants (logK) of *3d* transition metal and lanthanide complexes with common linear and macrocyclic chelating ligands.

Ligand	Ni^{2+}	Cu^{2+}	Zn^{2+}	Nd^{3+}	Eu^{3+}	Yb^{3+}
Cyclen **10**	16.4[186]	22.7[187]	16.2[187]	-	-	-
Cyclam **11**	22.2[186]	27.2[188]	15.0[188]	-	-	-
EDTA **12**	18.52[189]	18.70[189]	16.44[189]	16.6[190]	17.3[190]	19.6[190]
DTPA **13**	20.17[191]	21.38[191]	18.29[191]	21.7[190]	22.5[190]	22.7[192]
NOTA **14**	28.3[193]	19.5[193]	22.5[193]	13.13[194]	13.86[194]	15.35[194]
TETA **15**	19.82[195]	21.60[195]	16.27[195]	14.51[196]	15.46[196]	16.55[196]
DO3A **16**	-	-	-	-	20.1[197]	-
DOTA **17**	20.03[195]	22.21[195]	21.05[195]	22.99[194]	23.45[194]	25.00[194]

In contrast to the lanthanides, *3d* metals tend to have a coordination number of 6, and the stability of the complexes is dependent on the ability of the ligand to conform to the coordination geometry. The *3d* transition metals can form relatively stable complexes with 4-coordinate ligands like cyclen **10** or cyclam **11**, as the metal can sit within the cavity

of the ligand.[198] In particular, Cu(II) complexes are quite stable with these ligands, as 4 electron donors are enough to satisfy the tetragonally distorted ligand field of Cu(II). In this case, cyclen forms less stable complexes than cyclam as the macrocycle has to distort itself more to accommodate the metal ion.[189, 199] Increasing the denticity of the ligand can improve the stability of complexes for some metals, like Zn(II). However, increasing denticity to 8 does not result in as large an increase in stability as with lanthanides, as the transition metals are coordinatively saturated at 6 electron donors.[200]

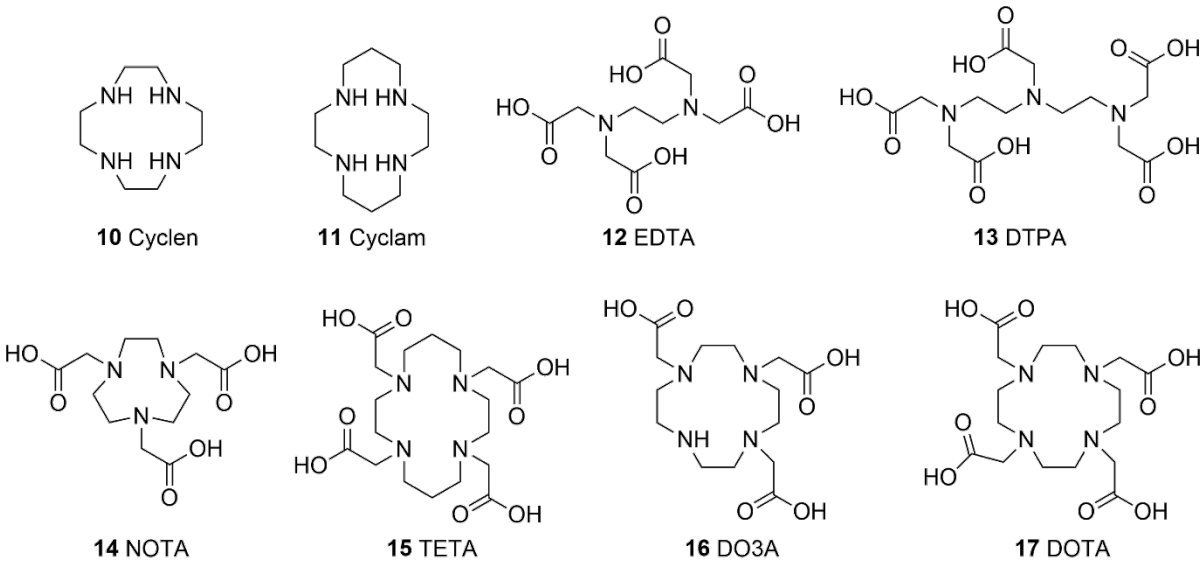

Figure 1.9: Structures of the ligands described in **Table 1.1**.

The macrocyclic effect is important for the stability of complexes with both types of metal and is pronounced in the difference in the stability of lanthanide complexes with DTPA *vs* DOTA. This is because the rigidity of the cyclen macrocycle pre-organises the ligand to wrap around the lanthanide, reducing the entropic penalty of coordination.[193] There are other factors that can diminish the macrocyclic effect, however. When comparing NOTA to EDTA, which are both 6 donor ligands, NOTA complexes are much less stable than EDTA complexes for the lanthanides.[194] This is due to two factors. The first is that EDTA has four carboxylates, which coordinate more strongly to the hard lanthanide ions, compared to NOTA which has 3. The flexibility of EDTA also allows it to wrap more effectively around the large ionic radius of the lanthanide, whereas NOTA is simply too small.[194] The complexes with TETA **15** are also not as stable as DOTA complexes , as the

carboxylates are oriented on opposite planes of the macrocycle to each other, reducing the pre-organisation of the ligand.[201]

These requirements for formation of a stable complex need to be taken into account when designing ligands, particularly those that are destined for biomedical purposes. The polyaza macrocycles have become attractive scaffolds for the design of functionalised metal complexes. The introduction of a pendant group to one or more of the amines is synthetically straightforward, and typically only has a minor impact on metal complexation and subsequently stability.

1.3.4 Metal complexes as responsive fluorescent probes

Macrocyclic polyamines have become attractive scaffolds for the design of fluorescent sensors. It is generally straightforward to attach a functional pendant group to one of the nitrogens while maintaining the ability of the ligand to stably coordinate a metal.

There have been reported "switch-on" sensors for transition metals that are derived from an unmetallated macrocycle appended with a pendant fluorophore (**Figure 1.10**).[202-206] The rationale behind this design is that fluorescence of the pendant group is quenched in the unmetallated ligand by photoinduced electron transfer (PET) from the amines to the excited fluorophore. When a suitable metal is introduced, coordination of the metal to the amines prevents PET from occurring and an increase in the fluorescence response is observed.[202] This effect occurs most commonly with zinc, and a variety of Zn^{2+} sensors have been developed using a different fluorophores and macrocyclic scaffolds, including cyclen and cyclam. These sensors give a selective response for Zn^{2+} ions over other metals, except for Cu^{2+}, and Hg^{2+} ions, due to the competitive

formation of complexes with these metals, which typically results in fluorescence quenching.[204]

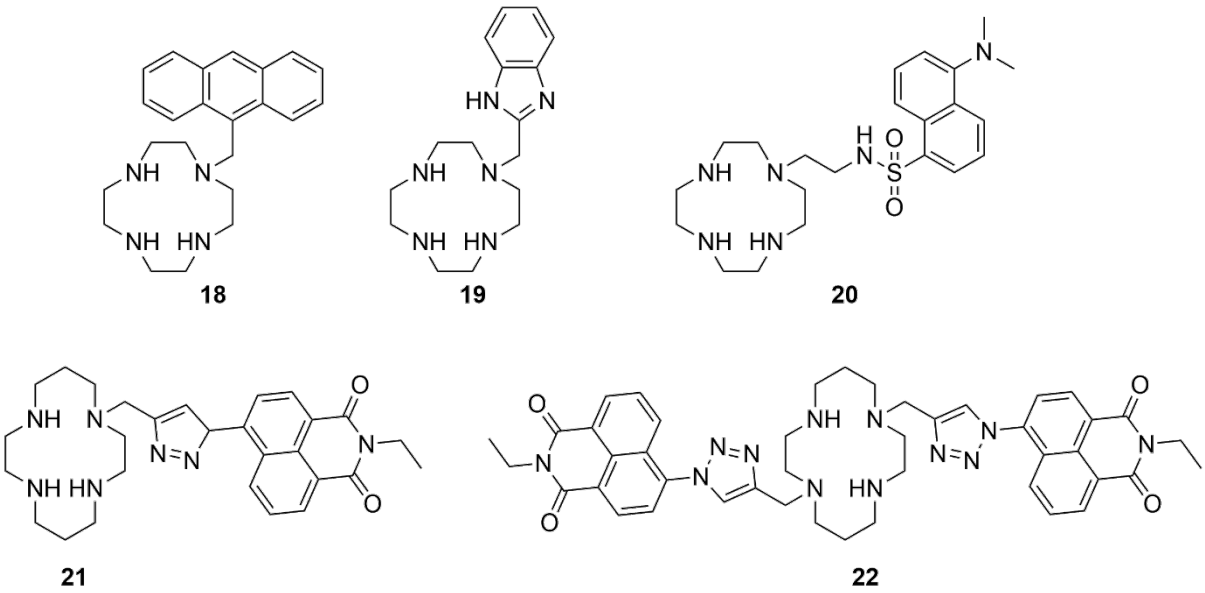

Figure 1.10: Fluorescent Zn^{2+} sensors derived from cyclen (top) and cyclam (bottom) scaffolds.[202-206]

Fluorescent "switch-on" zinc probes that utilize lanthanide luminescence have also been developed (**Figure 1.11**). One example of these sensors (**23**) uses a di(2-picolyl)amine (DPA) moiety both to bind Zn^{2+} ions and act as an antenna for Eu^{3+} or Tb^{3+} luminescence.[207] Operating on a similar principle as the previously mentioned sensors, coordination of a Zn^{2+} ion inhibits PET quenching of the DPA moiety, which then induces luminescence in the lanthanide ion *via* the antenna effect. A similar probe (**24**) used Gd^{3+} as the lanthanide and a tripicolyl-1,4,7-triazacyclononane (TACN) moiety for Zn^{2+} binding.[208]

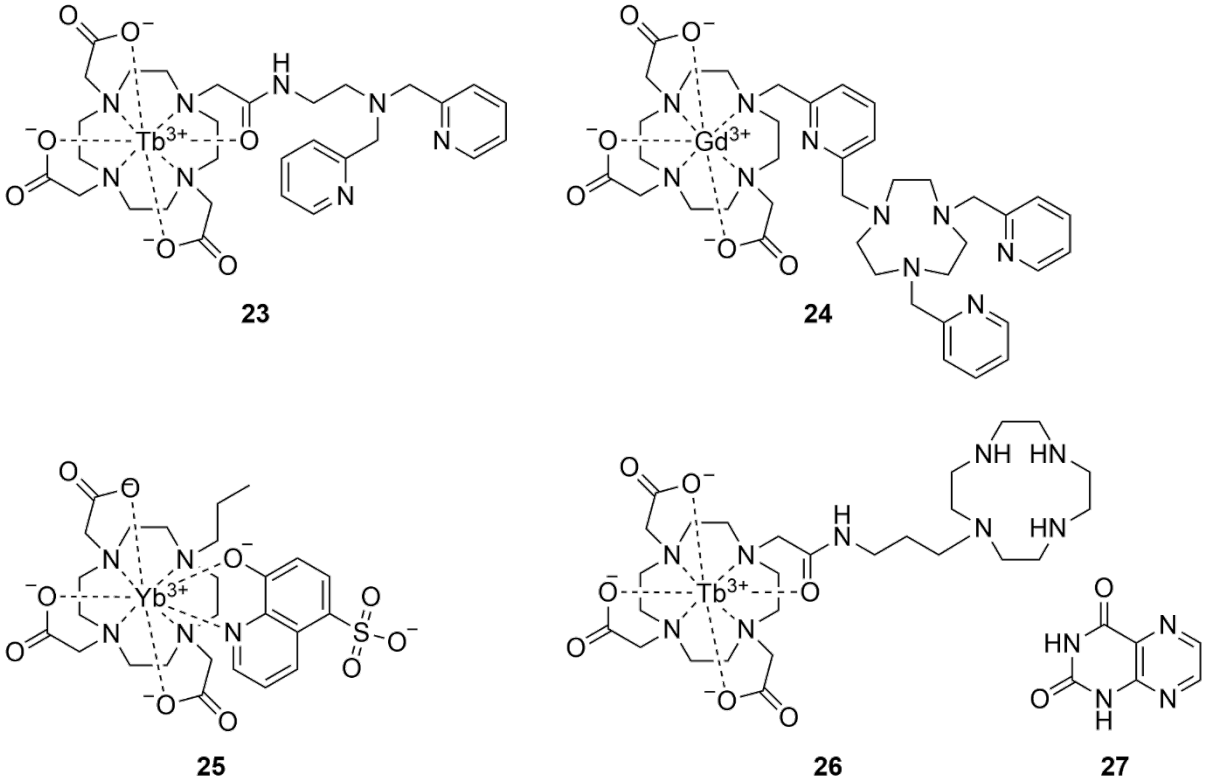

Figure 1.11: Luminescent Zn^{2+} sensors that exploit lanthanide luminescence. [207-210]

Another strategy for Zn^{2+} sensing has been the displacement or formation of a fluorescent ternary complex between Zn^{2+}, a luminescent lanthanide complex and an antenna chromophore (**Figure 1.11**). Comby *et al.* reported a sensor composed of a non-emissive ytterbium complex (**25**) and an 8-hydroxyquinoline antenna chromophore.[209] The ternary complex is decomposed (and luminescence switched off) by the addition of Zn^{2+} ions, which coordinate to the 8-hydroxyquinoline and form a separate luminescent complex. One advantage to ternary complexes is that they can be used to make "dark" sensors, which exhibit no fluorescence when the analyte is not bound. The Tb^{3+} based sensor (**26**) reported by Winnett, *et. al.* uses a cyclen macrocycle to bind a Zn^{2+} ion, which then forms a ternary complex with lumazine (**27**) which acts as the antenna chromophore. [210]

Macrocyclic metal complexes have also been used for anion sensing (**Figure 1.12**). A common strategy for HS^- detection involves the use of a fluorescent copper complex.

Coordination of copper to the ligand quenches the fluorescence of the pendant fluorophore. When HS^- ions are introduced to the sensor they induce demetallation of the complex by forming CuS, unmasking the fluorescence of the pendant fluorophore. This has been applied to a cyclam-based sensor (**28**), which uses anthracene fluorescence as the reporter,[211] and for a terbium complex (**29**) in which the DPA moiety is used to induce terbium luminescence.[212] A cyclam-copper complex (**30**) has also been used to sense HNO production in cells.[213] The mechanism of detection is based on reduction of Cu(II) to Cu(I), which restores the fluorescence of the complex by making it diamagnetic.

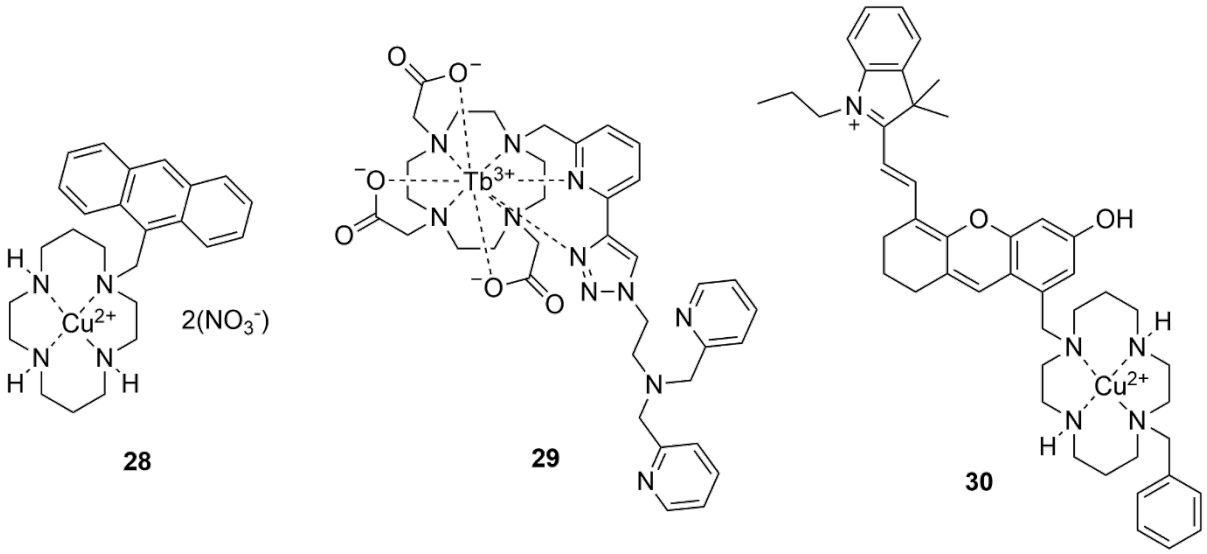

Figure 1.12: Fluorescent anion sensors that utilize a responsive pendant group.[211-213]

Lanthanide complexes have also been used to sense a variety of other anions (**Figure 1.13**). The principle behind this approach to sensing is that by employing a coordinatively unsaturated luminescent complex, reversible displacement of bound water by the anion will alter the luminescence. Anions bearing a single negative charge, such as fluoride can be sensed using an 8-coordinate complex which has one free coordination site, as demonstrated by **31**.[214] Dianions can be sensed using 7-coordinate complexes, which leave two water molecules to be displaced.[215] Selectivity for different anions can be tuned

by altering the overall charge of the complex, the charge of specific sidechains, or by altering the steric crowding at the metal centre. This tuneability can be seen in the differences in sidechain size and charge between complexes **32** and **33**, which are selective for bicarbonate and citrate, respectively.[215, 216]

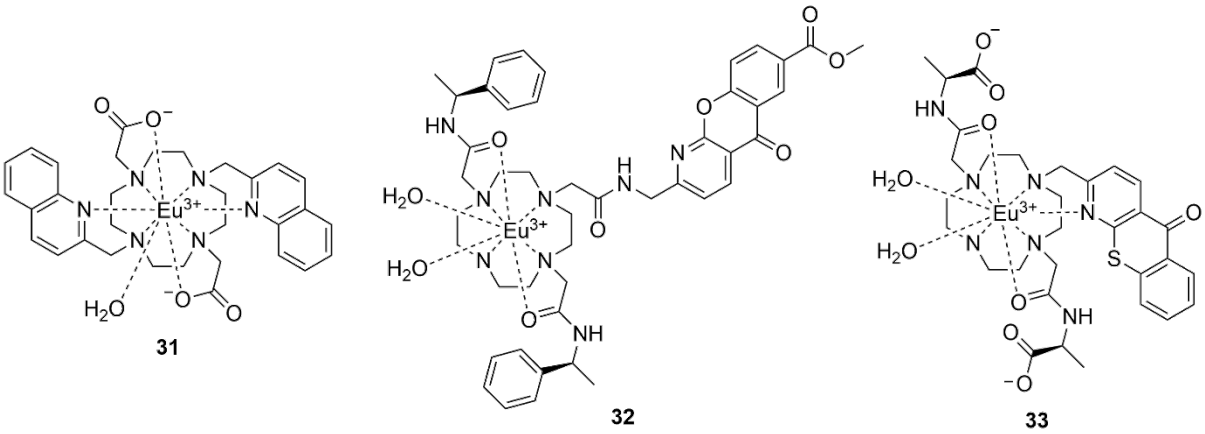

Figure 1.13: Anion sensing lanthanide complexes that exploit a change in luminescence by direct coordination to the lanthanide.[214-216]

1.3.5 Lanthanide complexes as magnetic resonance imaging probes

The magnetic properties of lanthanide complexes and some transition metal complexes have made them attractive MRI contrast agents. Two common mechanisms for contrast generation are through modulating T_1 relaxation of water and through paramagnetic chemical exchange saturation transfer (PARACEST).[217, 218] T_1 relaxation agents are paramagnetic complexes which increase the T_1 relaxation time of protons in bulk water molecules, providing contrast on an MRI image. The two contributions these agents make to the relaxivity are classified as either outer sphere or inner sphere. Outer sphere relaxivity is dependent on the diffusion rate of water molecules in the local environment. On the other hand, inner sphere relaxivity is dependent on the hydration number of the complex, and the rate of exchange between metal-coordinated and bulk water molecules.[217] Together these factors mean that inner sphere relaxivity can be tuned by ligand design.

T_1 agents tend to be Gd^{3+} complexes (**Figure 1.14**), as the 7 unpaired *f* electrons result in a large magnetic moment and thus such complexes have the greatest effect on T_1 relaxation.[219] Due to toxicity concerns about free Gd^{3+} ions, efforts have also been made to develop Mn^{2+} contrast agents, as there are 5 unpaired *d* electrons in Mn^{2+} which contribute a strong magnetic moment, albeit weaker than Gd^{3+}. Free Mn^{2+} ions are also permeable to the blood-brain barrier and can be used for functional brain imaging, whereas Gd^{3+} chelates tend to be too bulky. The only approved Mn^{2+} contrast agent, mangafodipir, was withdrawn from the US and European markets due to poor sales, leaving no commercially available Mn^{2+} contrast agents.[220]

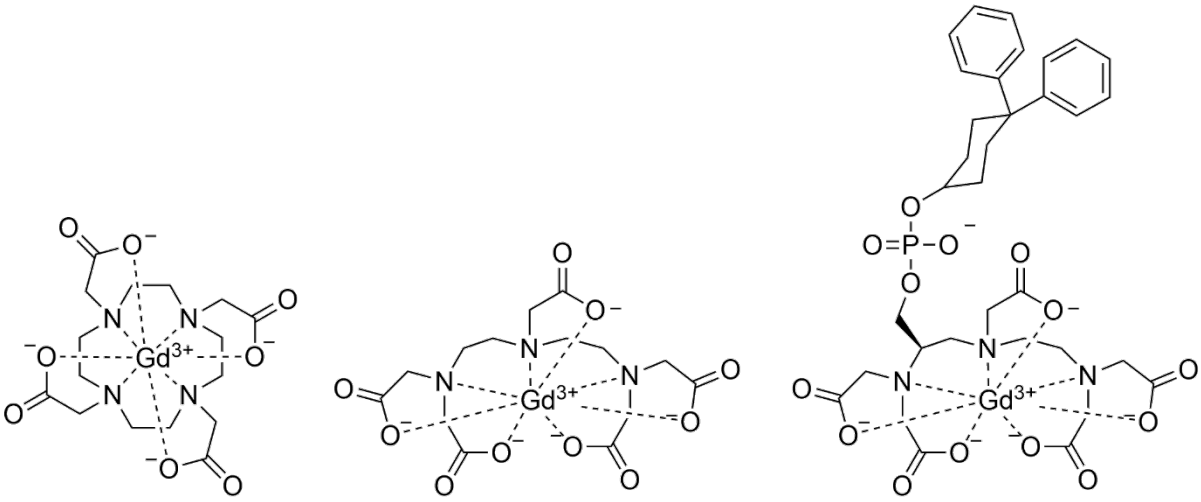

Figure 1.14: Commercially available Gd^{3+} contrast agents.[221]

The dependency of T_1 relaxation on the hydration number of the complex has enabled the development of several responsive MRI contrast agents (**Figure 1.15**). Incorporating metal-chelating motifs allows for the contrast agent to be responsive to the local concentration of particular metal ions: the dinuclear probe **37** for example is specific for Ca^{2+} ions,[222] while probe **38** is specific for Zn^{2+} ions.[223] When the analyte metal is not bound, the carboxylates in the chelating motif are coordinated to the Gd^{3+} centre(s), and when the analyte binds, these carboxylates are displaced from the Gd^{3+} ion allowing a second water molecule to coordinate in its place. A redox-active probe incorporating a spironaphthoxazine dye **39** is able to switch between an 8-coordinate mode in oxidising

environments and a 7-coordinate mode in reducing environments through the spironaphthoxazine isomerism.[224]

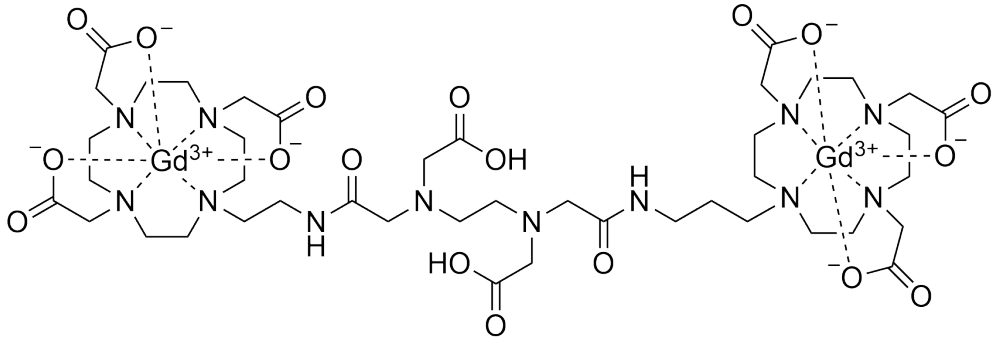

37

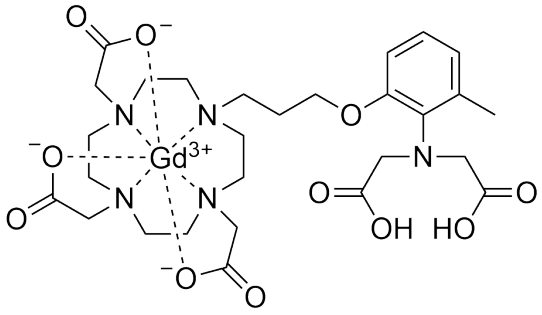

38

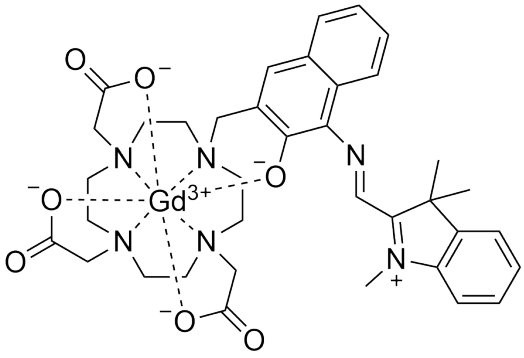

39

Figure 1.15: T_1 relaxation contrast agents that are responsive to the local environment.[222-224]

Chemical exchange saturation transfer (CEST) is an MRI technique that takes advantage of magnetisation transfer from the exchangeable protons on a particular small molecule to bulk water molecules.[225] The slow-exchanging protons of the CEST probe are selectively saturated by radiofrequency pulses, which causes a decrease in the signal. The signal of bulk water molecules in exchange with the CEST probe is also decreased *via* saturation transfer. The technique requires the exchangeable protons to have a large difference in chemical shift compared to the bulk water molecules. Paramagnetic molecules with anisotropic χ tensors are advantageous for CEST experiments since they induce a large difference in chemical shift compared to bulk water.[218]

As with T_1 contrast agents, responsive PARACEST complexes have been developed through modification of the ligand scaffold. In addition to probes that respond to

changes in metal ion concentration, probes have been developed which respond to anion concentration, pH, glucose levels and to enzymatic activity (**Figure 1.16**).[226-229] The Eu^{3+} complex **40** is responsive to carbonate, lactate, acetate and citrate; which coordinate to both the outer-sphere and inner-sphere of the probe.[227] Complex **41** is responsive to glucose concentration and which is proposed to bind to the boronic acid moieties outside the coordination sphere of the Eu^{3+} ion.[228] Complex **42** gives a pH-responsive CEST spectrum due to the phenol moiety, which is able to conjugate to the carbonyl at high pH and alter the coordination of the carbonyl to the Eu^{3+} centre, and the complex can be used to directly measure the pH in a concentration independent manner.[229]

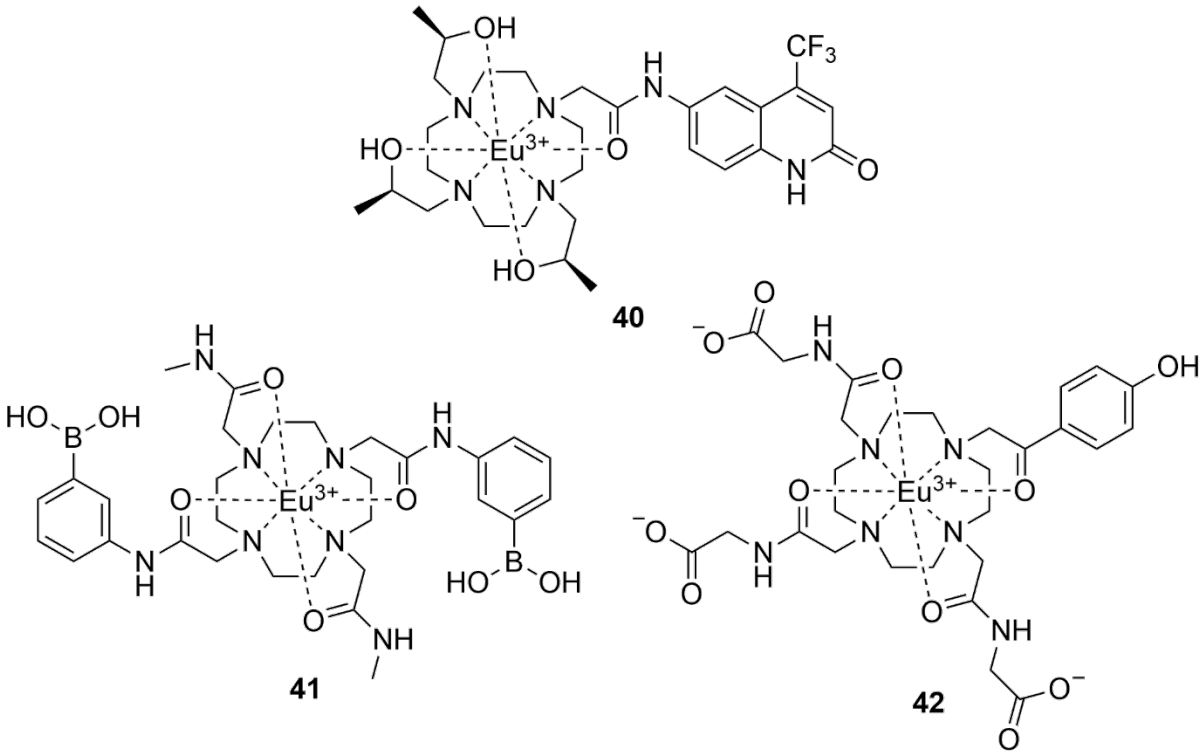

Figure 1.16: PARACEST contrast agents that are responsive to the local environment.[227-229]

1.4 Project aims

The Rutledge group has a long-standing interest in developing chemical probes derived from a cyclam scaffold. A number of fluorescent probes for the sensing of metal ions have been reported, including a coumarin-appended cyclam probe that can distinguish

between Cu^{2+} and Hg^{2+} ions in solution *via* $S_2O_3^{-}$ -induced demetallation.[230-233] Work in this area lead to serendipitous discovery that the fluorescent Zn^{2+} sensor **22** was selectively active against *Mycobacterium tuberculosis*, including against antibiotic-resistant strains.[234, 235]

Efforts to target Aβ began with investigation into a peptide-cyclen conjugate which had been reported to cleave formed Aβ fibrils.[236, 237] The molecule consisted of a KLVFF peptide fragment conjugated to unmetallated cyclen. It was proposed to bind to $A\beta_{42}$ fibrils *via* the KLVFF motif and chelate fibril associated Cu^{2+} ions, thus becoming proteolytically active and cleaving the $A\beta_{42}$ fibrils. The proteolytic activity could not be reproduced but some of the conjugates were able to disrupt $A\beta_{42}$ fibrilization and prevent fibril-induced toxicity to neuronal cells. This spurred the development of a number of derivatives in which a cyclam is conjugated with small molecules known to bind to $A\beta_{42}$ and prevent its aggregation, as well as their Cu^{2+} and Zn^{2+} complexes (**Figure 1.16**). One conjugate in particular stood out as having excellent anti-aggregation properties and low cytotoxicity: the bis-perphenazine conjugate **58** and its complexes with Cu^{2+} **59** and Zn^{2+} **60**. While it is a promising candidate, at the outset of this study, little was known about whether it could reduce $A\beta_{42}$ -induced toxicity, what stage of the aggregation it inhibits and how it binds to $A\beta_{42}$.

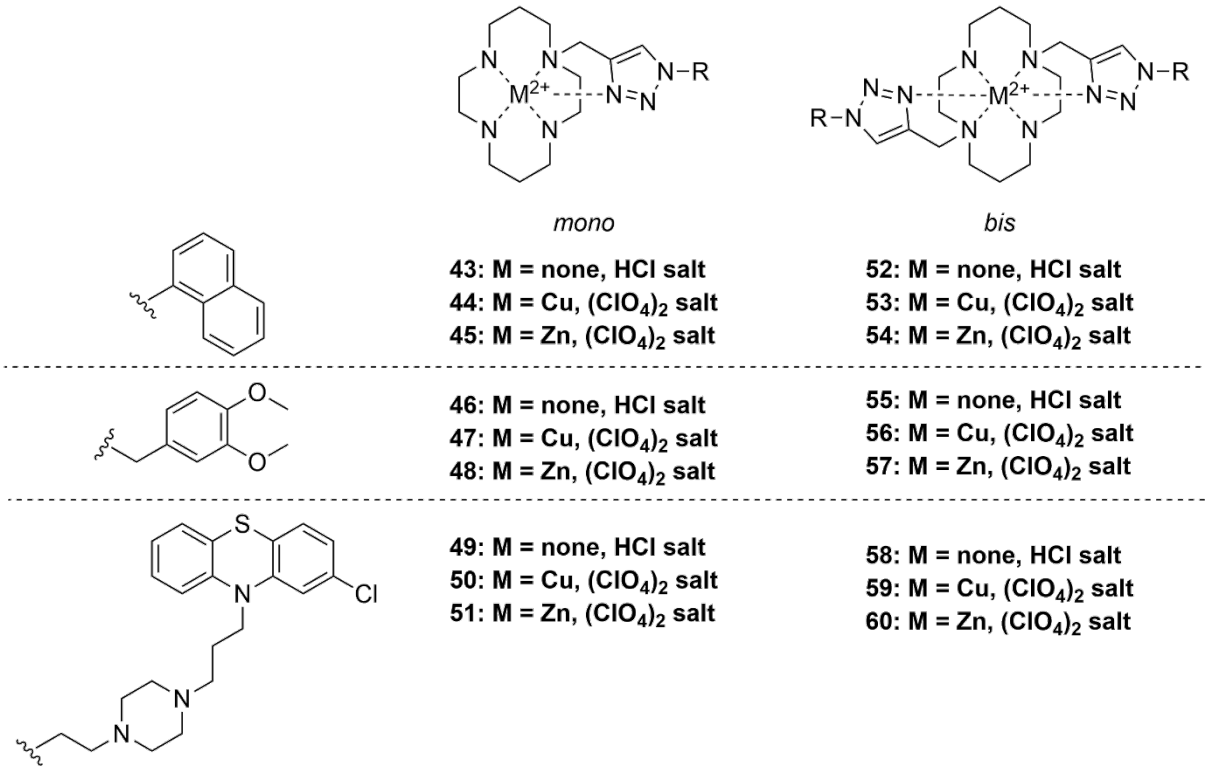

Figure 1.16: Structures of the cyclam conjugates developed to inhibit Aβ aggregation.

The aims of this project were to further investigate how **58** and its complexes interact with $A\beta_{42}$ to inhibit aggregation, and whether there is a therapeutic potential to treat AD with this class of compounds. The first goal of this investigation is to develop a scalable synthesis of the conjugate so that neuronal cell rescue assays could be performed, and kinetic studies could be undertaken to determine which stage of Aβ aggregation is inhibited by **58**. The second goal is to develop a modified probe compound based on this lead, capable of forming paramagnetic complexes with either Mn^{2+} or Ln^{3+} ions. These complexes could exert PRE, which could be observed in the HSQC NMR spectrum of $A\beta_{42}$, and thus be used to investigate how these complexes bind to $A\beta_{42}$ to inhibit its aggregation.

2. Synthesis and Activity of Bis-Perphenazine Cyclam Complexes

2.1 Overview

The first goal of the project was to gain a deeper understanding of how the bis-perphenazine derivative **58** and its metal complexes interact with $A\beta_{42}$, particularly to determine whether the anti-aggregation effects translate to a reduction in Aβ induced toxicity, and which stage of the aggregation process it inhibited. These results, if promising, would then become the basis for further chemical development of the lead compounds to improve potency and pharmacokinetics. This required the resynthesis of **47** and its copper (**51**) and zinc (**52**) complexes, in larger quantities than had previously been achieved.

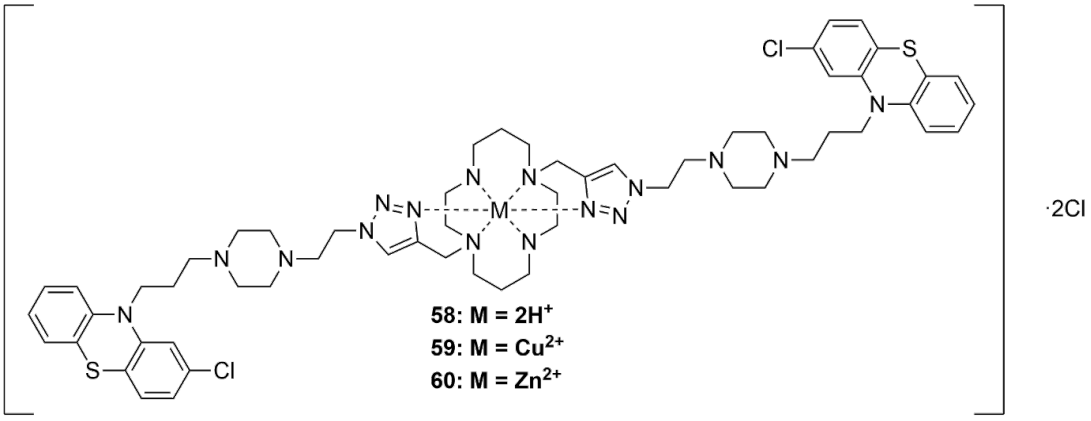

Figure 2.1: Structure of lead compound **58**, and copper and zinc complexes.

A synthetic route to these compounds had been previously established within the group. The retrosynthetic scheme is shown in **Scheme 2.1**, whereby the scaffold **58** can be convergently synthesised from bis-alkyne **61** and azide **62** *via* the Cu(I)-catalysed azide-alkyne cycloaddition (CuAAC) reaction. Alkyne **61** is synthesized across 4 steps from cyclam **11**, which is also commercially available. Azide **62** can be synthesized from the commercially available compound perphenazine **63** in one step. Some alterations to the synthetic scheme were required to render it more amenable to scale-up, discussed further

below; in particular, protocols which avoided the need for chromatography were developed in preference to the original procedures.

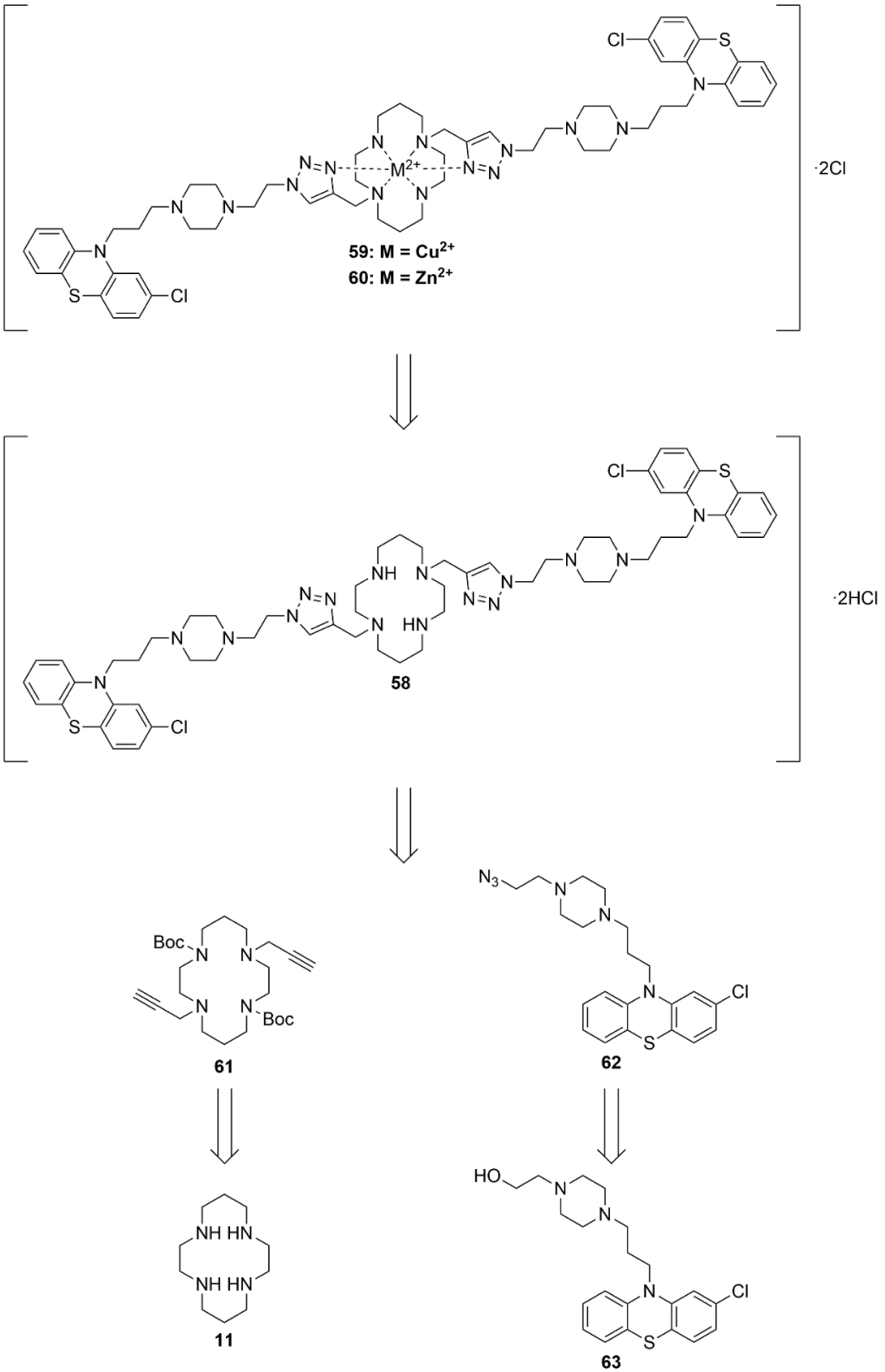

Scheme 2.1: Retrosynthetic scheme for the synthesis of **58**, **59** and **60**.

Once the compounds **58**, **59** and **60** were in hand, their effects on $A\beta_{42}$ aggregation could be investigated in-depth. Thioflavin-T (ThT) assays were used to investigate their effect on the kinetics of assembly of $A\beta_{42}$ into fibrils. Transmission electron microscopy (TEM) was used to confirm the structure of the end-stage aggregates formed in the presence of these compounds. Finally, the ability of these compounds to prevent Aβ associated toxicity on cultured neuronal cells was assessed.

2.2 Synthesis of the bis-propargyl cyclam building block

An efficient route towards 1,8-disubstituted cyclam compounds is through a Boc-protected bis-propargyl intermediate *via* the Guilard procedure.[238] The synthesis of bis-propargyl cyclam **61** had been developed previously and is a well-established route to the click coupling partner (**Scheme 2.2**).[235]

The first step was the alkylation of cyclam **11** using aqueous formaldehyde, which formed methylene bridges between each pair of nitrogens. The product **64** formed as a white precipitate which is conveniently isolated *via* vacuum filtration to give the product in 83% yield and requiring no further purification. Contrary to other reports,[230, 232, 235] it was found that increasing the reaction time beyond 1 hour resulted in a drop in yield, with a yield of 64% obtained after 3 hours. Presumably this was due to the reversibility of aminal formation in water; while precipitation of the product provides the driving force for the forward reaction it is apparent that the reverse can still occur, and over time substantially reduces the yield.

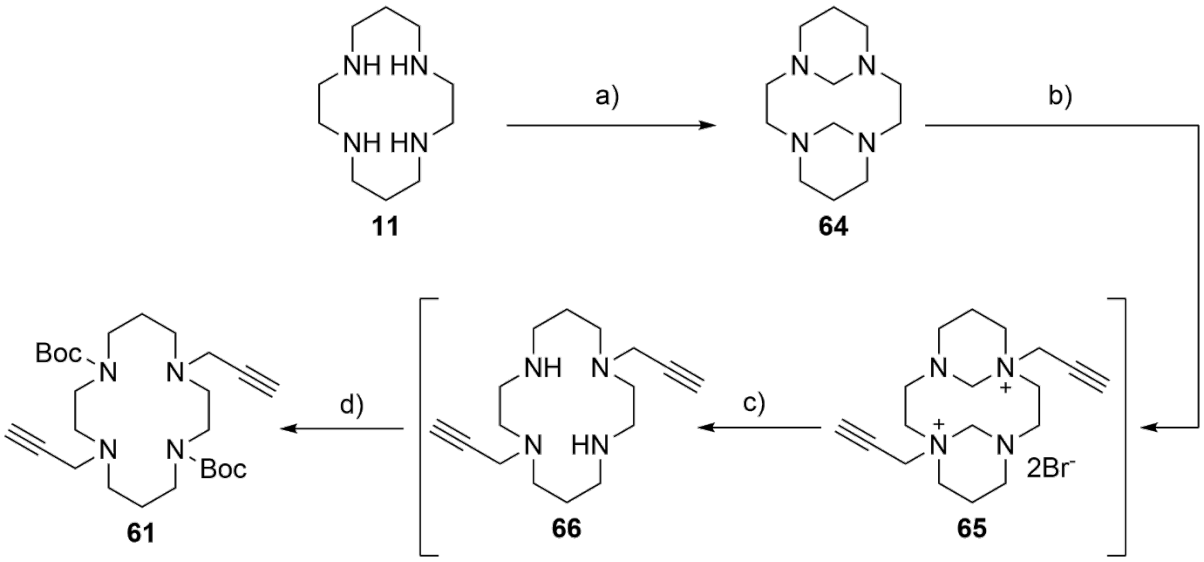

Scheme 2.2: Synthesis of Boc-protected bis-propargyl cyclam **61**. Conditions: a) formaldehyde, H_2O, 0° C 1h, 83%; b) propargyl bromide, MeCN, rt, 16 h, not isolated; c) 2.5 M NaOH, MeOH/H_2O, rt, 1 h, not isolated; d) Boc anhydride, MeOH/H_2O, rt, overnight 88% over 3 steps.

The bridged cyclam was then alkylated with propargyl bromide, affording the 1,8- bis substituted product **65** as a white precipitate which was isolated *via* vacuum filtration. The alkylation forms quaternary ammonium salts, and preferentially reacts at diagonally opposite nitrogens to minimise the inter-charge repulsion.[238] Over-alkylation was not observed as the size of the macrocycle can only accommodate two positive charges. The aminal bridges were then hydrolysed using sodium hydroxide in a mixture of water and methanol to maintain solubility of the freebase **66**.

Boc-anhydride was then added directly to the mixture and allowed to react overnight, which resulted in the Boc-protected product **61** precipitating from the reaction mixture. The product was isolated *via* vacuum filtration, after removing the methanol under reduced pressure, to give **61** in 88% yield over three steps. The purity was generally sufficient for use in the next step, but the product could be recrystallized from boiling acetonitrile when greater purity was necessary.

2.3 Development of a scalable perphenazine-azide synthesis

With the alkyne click-coupling partner in hand, the next step is the synthesis of the azide **62** from commercially available perphenazine **63**. The method originally developed in the Rutledge group used diphenylposphoryl azide (DPPA) and 1,8-diazabicyclo(5.4.0)undec-7-ene (DBU) in DMF to directly convert the alcohol into the azide. The main drawback to the method was that the displacement of the intermediate phosphate ester **67** by the azide anion was sluggish, requiring an elevated temperature of 70° C and an excess of DPPA, DBU and sodium azide to drive the reaction to completion. The procedure also used dichloromethane as the solvent in the aqueous workup, which presented an explosion hazard due to the presence of sodium azide in the mixture.[239]

By experimenting with the solvent, it was found that the rate of phosphate displacement was greatly accelerated using THF, which allowed the use of a slightly lower temperature of 50 °C, only a small excess of DPPA (0.5 equivalents superstoichiometric) and DBU (0.5 equivalents superstoichiometric) and no additional sodium azide to drive the reaction to completion. The product **62** could be isolated in a reasonable yield of 68% (**Scheme 2.3**).

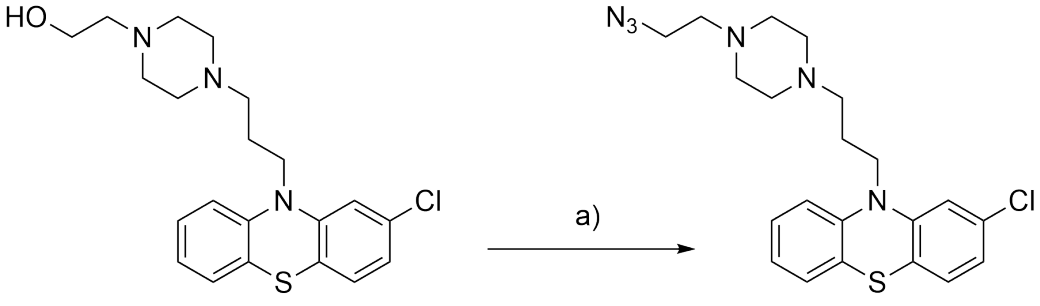

63 **62**

Scheme 2.3: Direct conversion of **56** to the corresponding azide **57** using DPPA/DBU. Conditions: DPPA, DBU, THF, 50° C, overnight, 68%.

While the improved DPPA method was sufficient for preparing smaller quantities of the azide (< 0.5 g), the method was not ideal at scale due to the presence of significant

quantities of diphenylphosphate **68** (**Scheme 2.4**). This by-product proved difficult to separate from **62** during the aqueous workup, as it has a limited solubility in water, even at elevated pH. Presumably this is in part due to the use of THF as the solvent, which like DMF, is able to act as a phase-transfer agent in aqueous workup.[240] Both perphenazine **63** and its azide **62** were unstable on silica, and attempts at separation on alumina gave irreproducible results and poor separation.

Separation could be achieved using reversed-phase column chromatography, however this was difficult due to the low solubility of **62** in aqueous mixtures, necessitating small sample loading, and usually still left a significant amount of diphenylphosphate **58** in the product (up to 10%). The presence of diphenylphosphate complicated the subsequent click-coupling and accelerated the decomposition of **62** in storage, requiring an alternative procedure that produced minimal by-products be found.

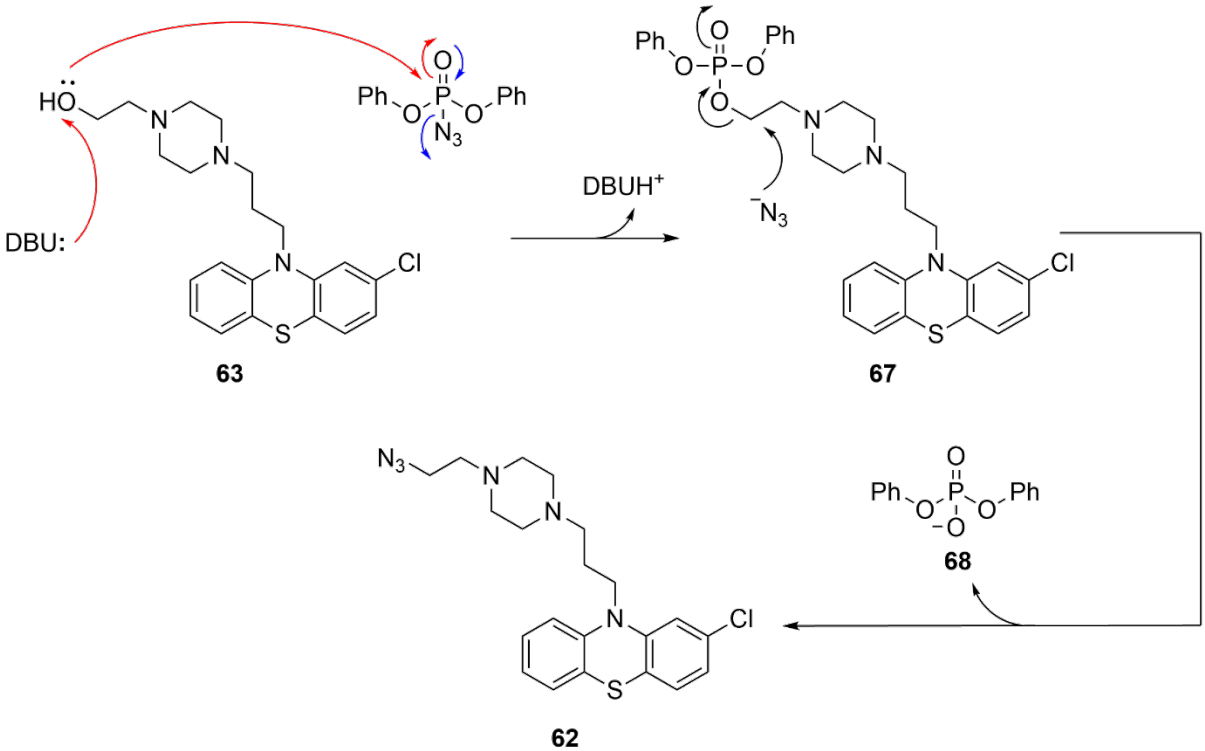

Scheme 2.4: Mechanism of the azidation of perphenazine by DPPA and DBU. Initial formation of the phosphoester is rapid, nucleophilic attack by the azide anion is relatively slow.

Direct azidation of the alcohol **63** using the Mitsunobu reaction was ruled out as it would generate triphenylphosphine oxide as a by-product,[241] which was anticipated to be similarly difficult to remove from the product. Previous efforts in the group to synthesise the corresponding alkyl chloride from **63** had also been unsuccessful, which ruled out the synthesis of **62** *via* the chloride.[242]

The mesylate was chosen instead as a suitable intermediate for large scale synthesis of **62**, as the mesylate anion is a good leaving group with excellent solubility in water, which should afford the pure product without the need for chromatography. Standard conditions were employed to make the mesylate[243]; perphenazine **63** was treated with mesyl chloride and a slight excess of triethylamine in THF at 0° C for 1 hour. The reaction resulted in the formation of two products: the desired mesylate **69** and the alkyl chloride **70**, which was formed by displacement of the mesylate by the chloride anion produced from mesyl chloride as the mesylate forms. While chlorination like this is often an unwanted side-reaction as it can cause scrambling of stereocentres, in this case the formation of the chloride was not seen as a problem. At first it was thought surprising to see such a high conversion (up to 50%) to the chloride with a short reaction time at 0° C. However, this is presumably due to an intramolecular reaction of the mesylate with the piperazine to give an aziridinium intermediate **71**, which could then form the chloride. Indeed, the aziridinium species was subsequently observable on LRMS (**Scheme 2.5**).

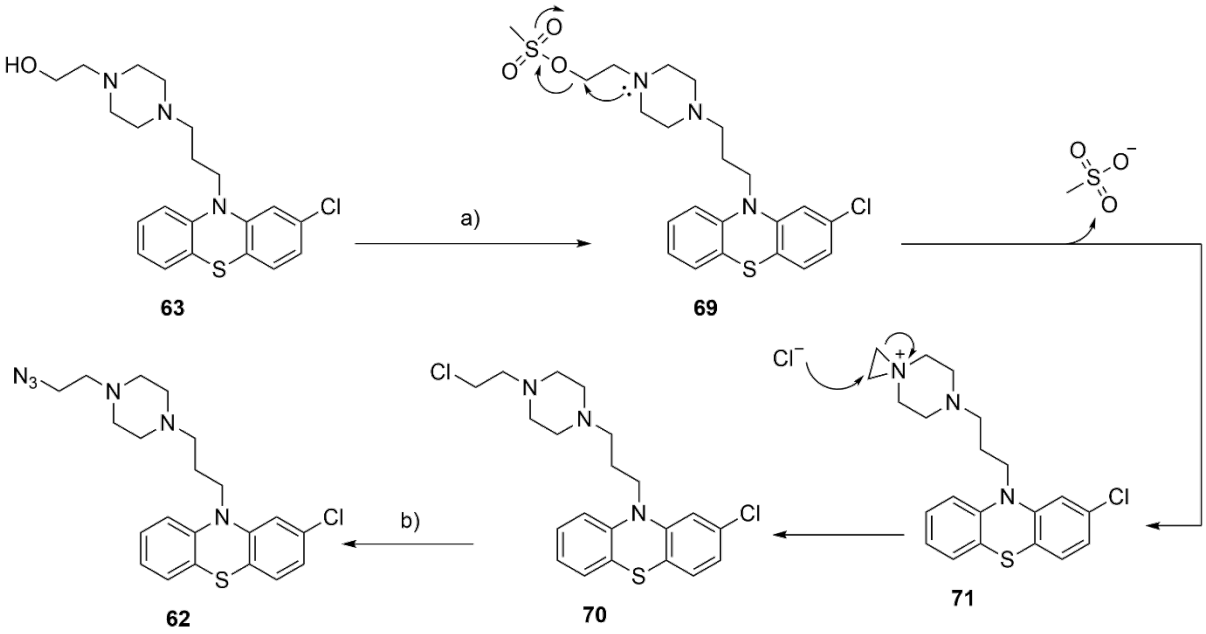

Scheme 2.5: Azidation of **62** *via* an intermediate mesylate and alkyl chloride. Conditions: a) mesyl chloride, Et_3N, THF, 0° C, 1 h, not isolated; b) NaN_3, DMF, 50° C, 16 h, 78%.

The mesylate/chloride mixture was not isolated, due to the inferred instability of the mesylate, and instead telescoped into the azidation step. In order to avoid DMF, which complicated the workup, the azidation was attempted first using sodium azide in acetonitrile. Unfortunately, these conditions were not satisfactory, and gave **62** in an isolated yield of only 27 %, likely due to the insolubility of sodium azide in acetonitrile.

Alternatively, more soluble azide sources were investigated, both trimethylsilylazide and tetramethylguanidinium azide but both resulted in disappointing yields of 42% and 49% respectively. The yield was substantially improved with all azide sources using DMF, with the best yields being obtained using sodium azide in DMF at 50° C overnight.

The aqueous workup of this reaction was complicated by the presence of DMF, as the product **62** was proved reasonably insoluble in both the neat solvent and in mixtures with ethyl acetate, toluene and ether. Isolation *via* filtration was not possible as the azide is an oil, and due to safety concerns DCM could not be used as an extraction solvent even though **62** is highly soluble in it. Despite these difficulties, the azide **54** could be isolated

in 78% yield, with complete conversion confirmed by NMR, and this material was sufficiently pure to be used in the next step.

2.4 Coupling the two fragments *via* a click reaction

The two fragments – bis-alkyne **61** and azide **62** – were coupled using the CuAAC reaction, commonly referred to as simply the 'click reaction.' The CuAAC is by far the most common method used to synthesise triazoles. The reaction is a popular method to conjugate two molecules as it has a fast reaction rate and uses simple reagents, while the introduction of azides and alkynes to molecules is generally straightforward.[244] The importance of this reaction to modern chemistry is illustrated by the awarding of the 2022 Nobel Prize for Chemistry to K. Barry Sharpless, Morten Meldal, and Caroline Bertozzi for their contributions to its development.[245]

Standard conditions for the CuAAC reaction, first described by Rostdovtsev, *et al*, were used for the synthesis of **72**. The bis-alkynyl cyclam **61** and a slight excess of the perphenazine azide **62** were dissolved in a degassed mixture of THF and water, then 20 mol% copper sulphate and 50 mol% sodium ascorbate were added, and the mixture was stirred overnight under N_2. Using Boc-protected cyclam prevents the poisoning of the Cu(I) catalyst *via* chelation of Cu^{2+} ions before they can be reduced *in situ*. Using this procedure, the product was obtained in a reasonable yield of 60%.

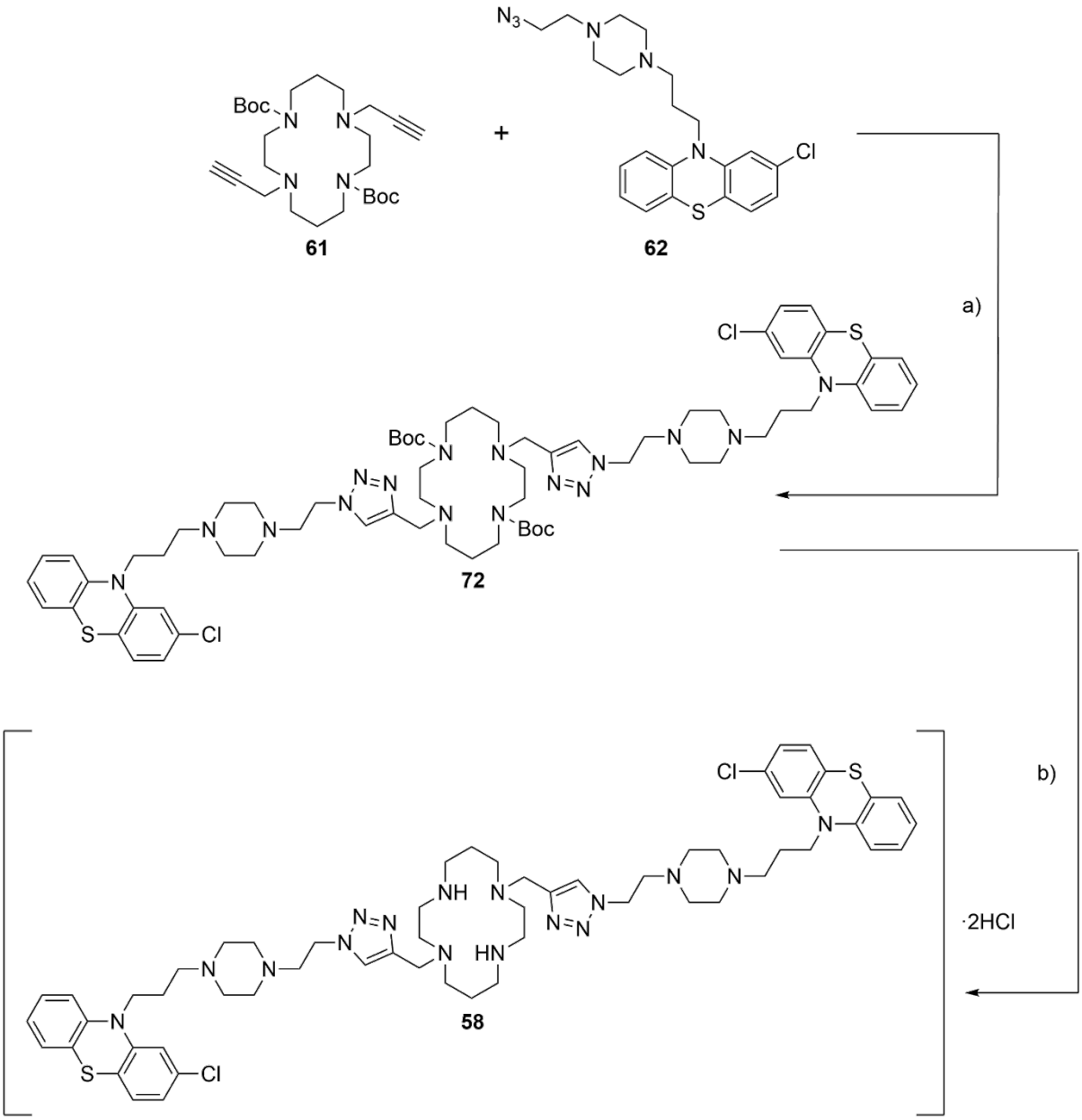

Scheme 2.6: Click coupling between **53** and **54** to yield **64**. Conditions: a) **53**, **54**, $CuSO_4$, sodium ascorbate, THF/H_2O, rt, 16 h, 60%; b) HCl (4 M in dioxane), 0° C to rt, 30 min, 83%.

The Boc-deprotection was carried out using previously established conditions using HCl in dioxane[246] The protected conjugate **72** was dissolved in a small amount of dioxane and treated with a solution of 4 M HCl in dioxane at 0° C. The reaction is rapid, typically reaching completion after 30 minutes, and the deprotected amine precipitated as the HCl salt **58** in 83% yield. The number of HCl molecules that combined with amines in the salt with **58** was determined using quantitative NMR. Phenothiazine moieties are

prone to oxidation at low pH,[247] but fortunately the short reaction time resulted in minimal side-reactions, and any decomposition products were easily separated using reversed-phase column chromatography.

2.5 Synthesis of the Cu^{2+} and Zn^{2+} complexes

The HCl salt of **58** was converted to the freebase before metal complexation through the use of Ambersep 900 OH form resin, a conversion which could be performed either in batch mode or by passage through a column of the resin. The ligand was then mixed with a methanolic solution of the appropriate metal salt and stirred at ambient temperature for 4 hours to give the metal complex in yields of 86%. Initially perchlorate salts of Cu(II) and Zn(II) were used to synthesise the metal complexes, as the resulting complexes precipitated easily from methanol and could be isolated *via* filtration. However, it was found that the solubility of the complexes in water was greatly improved by switching to the chloride salts, which were isolated *via* precipitation from a mixture of methanol and diethyl ether, with no change in the overall yield.

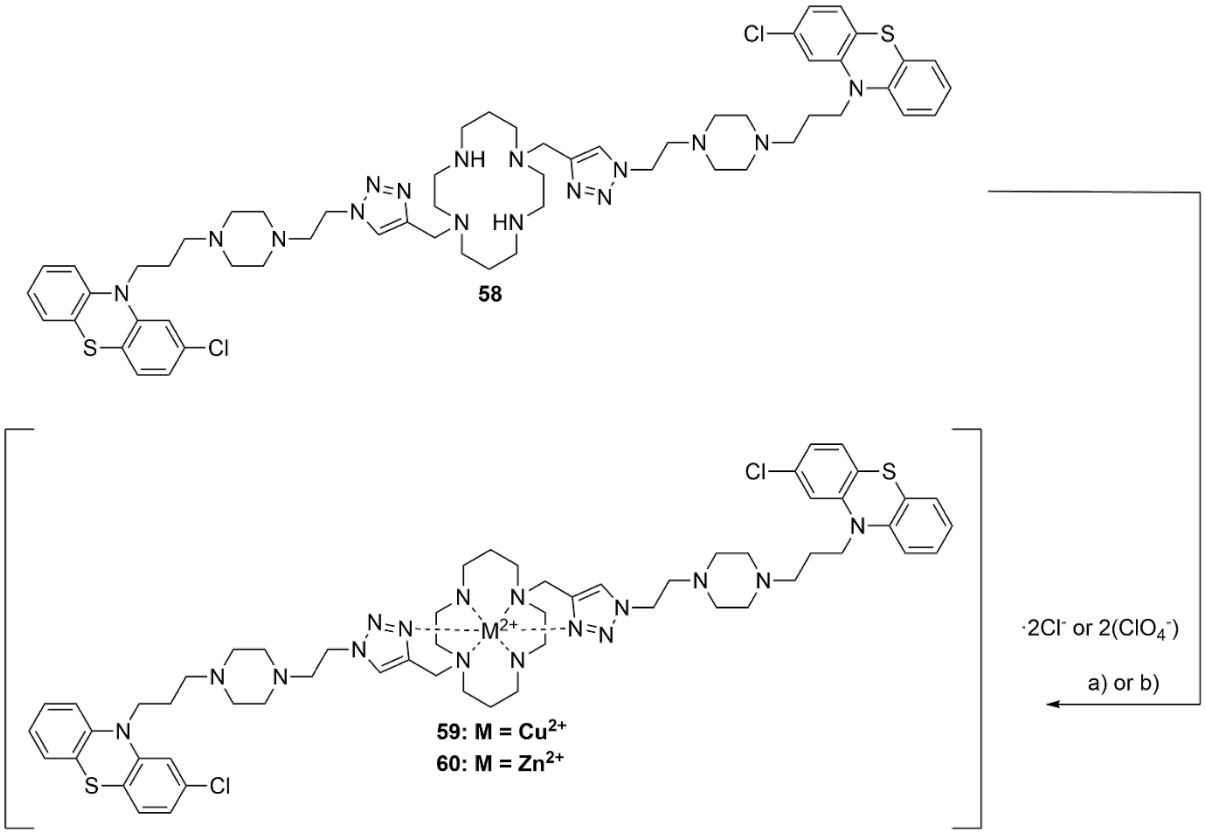

Scheme 2.7: Metal complexation of **58**. Conditions: a) $CuCl_2 \cdot 2H_2O$ or $Cu(ClO_4)_2 \cdot 6H_2O$, MeOH, rt, 4 h, 86%; b) $ZnCl_2 \cdot 4H_2O$ or $Zn(ClO_4)_2 \cdot 6H_2O$, MeOH, rt, 4 h, 87%.

2.7 The thioflavin-T assay

The first set of experiments performed with compounds **54**, **59** and **60** were thioflavin-T (ThT) fluorescence assays to measure the concentration dependence of their anti-aggregation activity. The ThT fluorescence method is a standard assay to measure the aggregation of amyloidogenic proteins, and to monitor the effect of a compound on amyloid assembly.[248] ThT **73** is a benzothiazole dye which exhibits a dramatic increase in fluorescence intensity (several orders of magnitude) when bound to amyloid fibrils.[249] The excitation maximum is also red-shifted from 385 nm to 450 nm, as is the corresponding emission maximum, from 445 nm to 482 nm.

The fluorescence of the unbound dye is proposed to be quenched as a result of rotation around the carbon-carbon bond bridging the benzothiazole and aniline fragments

(**Figure 2.2**).[250] When ThT binds to a groove in the cross-β sheet of an amyloid fibril, this rotation is hindered and the fluorescence cannot be quenched, leading to an increase in emission intensity. ThT is not specific to any one amyloid type and tends to bind to all amyloids with low micromolar affinity.[251] The fluorescence response of ThT is not necessarily specific to amyloids, and this compound can exhibit the characteristic increase in fluorescence when bound to hydrophobic pockets in other proteins, such as acetylcholinesterase[252] and human serum albumin.[253] Nevertheless, it still provides valuable information for the characterisation of the interaction of small molecules with amyloidogenic proteins.

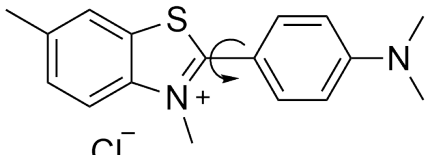

73

Figure 2.2: Structure of ThT, demonstrating the bond rotation that quenches fluorescence in the unbound dye.

The ThT fluorescence assay is performed by incubating monomeric $A\beta_{42}$ with the given small molecule and an excess of ThT. As normal amyloid assembly occurs, the fluorescence intensity over time produces a sigmoidal curve, representative of a nucleated growth mechanism (**Figure 2.3**). The curve can be split into three phases which correspond to different microscopic stages in the aggregation pathway: the lag phase, the growth phase and the end phase (or plateau).

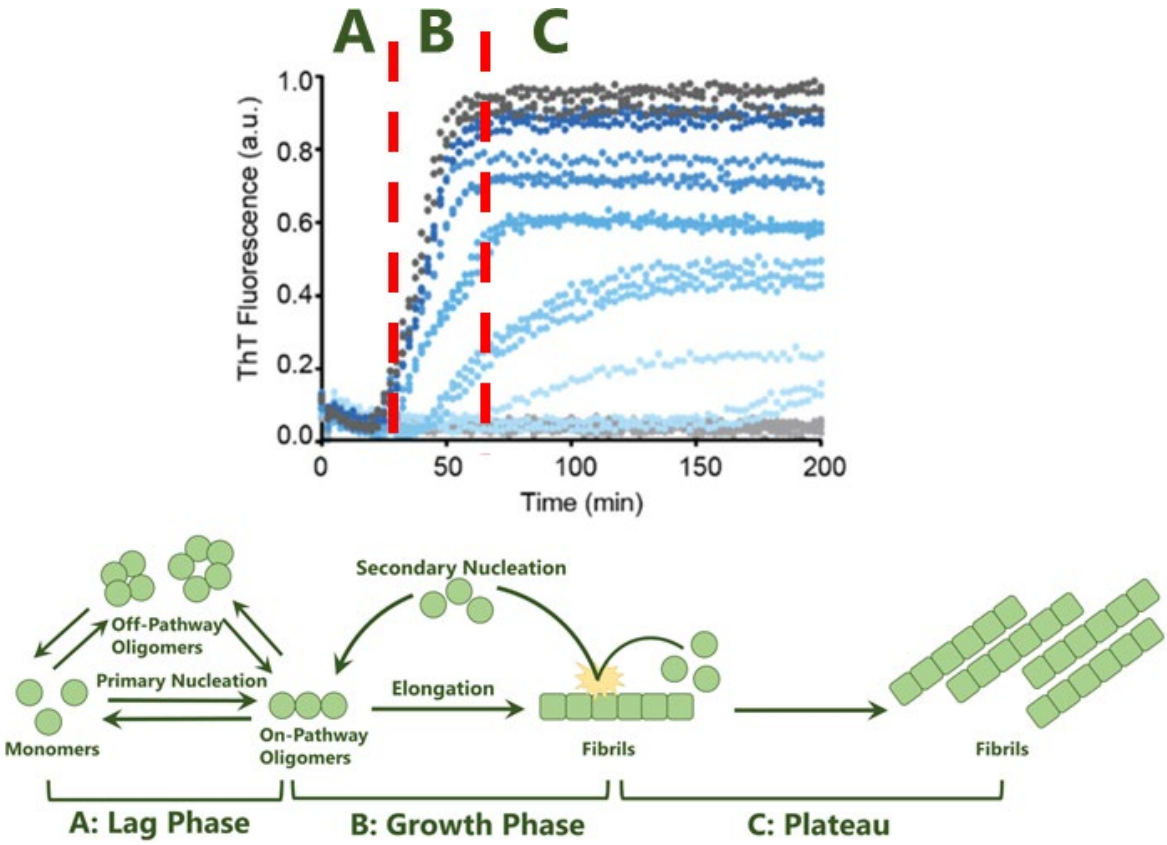

Figure 2.3: Representative graph of a ThT assay, with fluorescence intensity over time showing a sigmoidal curve. Section **A** is the lag phase, section **B** is the growth phase and section **C** is the end phase.

The lag phase (**Figure 2.3A**) is at the beginning of the aggregation process, ThT fluorescence is at a minimum as the solution mostly consists of monomeric and oligomeric Aβ, which is non-fibrillar. Monomers are assembling into seeds at this stage, so primary nucleation is the dominant process.[50] The growth phase (**Figure 2.3B**) occurs once enough seeds have elongated into fibrils; fluorescence begins to increase as fibrillar Aβ has formed. These fibrils allow secondary nucleation events to occur, catalysing the formation of oligomeric species which grow also into fibrils and the result is a rapid increase in the rate of fluorescence.[254] The plateau is reached (**Figure 2.3C**) once all monomeric and oligomeric Aβ has been converted into fibrils, ThT fluorescence stops increasing and the system is at equilibrium.[63] The growth phase is thought to generate the highest concentration of toxic oligomers, as these species have been shown to primarily arise form secondary nucleation processes.[86]

While these phases are indicative of the underlying processes involved in the assembly of an amyloid into fibrils, little information can be gleaned from a ThT assay at a single concentration of monomer or inhibitor. Multiple ThT assays performed at a variety of protein and inhibitor concentrations are required for the analysis of the kinetics of the aggregation process.[87]

2.8 Anti-aggregation activity of the conjugates

The assays described in this section were performed by Sarah Ball. The aggregation inhibition of **58**, **59** and **60** was first characterised using 10 μM $A\beta_{42}$, with each compound displaying a concentration-dependent inhibition of aggregation that reached a maximum at a ratio of 5:1 inhibtor:Aβ (**Figure 2.4A-C**). The activity at lower concentrations of compound was characterised using 2.5 μM $A\beta_{42}$, and at low concentrations of conjugate an increase in the lag phase of the aggregation was observed (**Figure 2.4E-F**). Interestingly, **59** and **60** still exhibited significant inhibition at lower concentrations than the unmetallated **58**.

It is has been reported that high concentrations of free Cu^{2+} and Zn^{2+} ions are able to alter the aggregation of Aβ.[255-257] Thus it was thought possible that the anti-aggregation effects of **59** and **60** could be due to free metal ions arising from demetallation of the complexes *in situ*. In order to rule this scenario out, the aggregation of $A\beta_{42}$ in the presence of the complexes and an excess of EDTA was compared to the aggregation in the presence of $CuSO_4$ and $ZnSO_4$, and these metal ions plus excess EDTA (**Figure 2.5**).

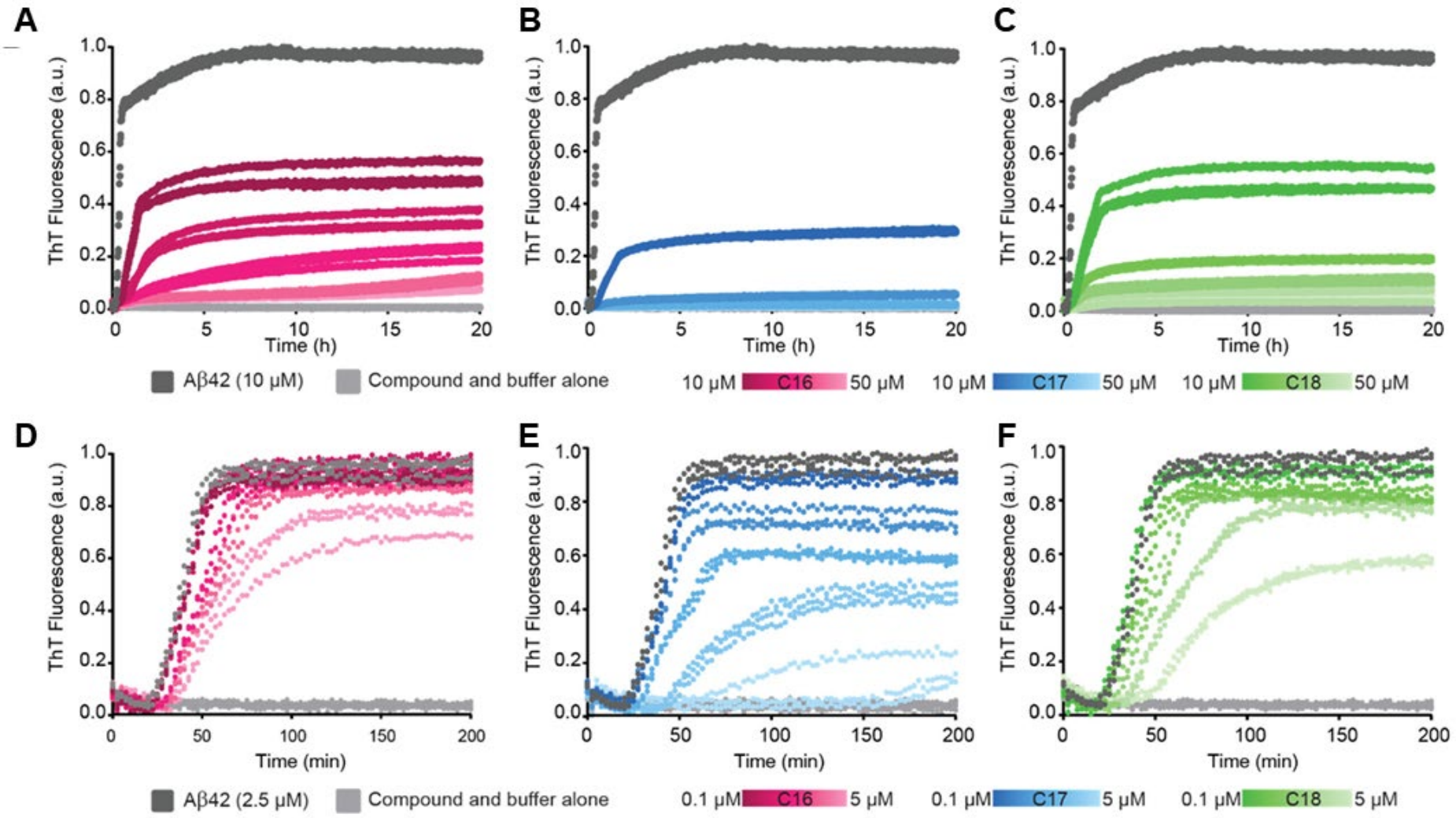

Figure 2.4: Concentration dependent inhibition of $A\beta_{42}$ aggregation demonstrated by ThT fluorescence. Top row: 10 μM $A\beta_{42}$ with 1% DMSO against **58** (**A**), **59** (**B**) and **60** (**C**), with concentration increasing from 10 μM (darkest curve) to 50 μM (lightest curve). Bottom row: 2.5 μM $A\beta_{42}$ with 1% DMSO against **58** (**D**), **59** (**E**) and **60** (**F**), with concentration increasing from 0.1 μM (darkest curve) to 5 μM (lightest curve). *N*=3. *Assays conducted and figure constructed by Sarah Ball.*

The free metal salts $CuSO_4$ and $ZnSO_4$ both demonstrated a concentration-dependent inhibition of Aβ assembly (**Figure 2.5A-B**) which was diminished by the presence of EDTA (**Figure 2.5D-E**). Happily, both complexes **59** (**Figure 2.5C**) and **60** (**Figure 2.5F**) maintained their aggregation inhibition even in the presence of EDTA, indicating that the observed inhibition of aggregation by these compounds was not due to free metal ions arising from demetallation of the complexes.

2.9 Kinetic modelling of the anti-aggregation effects

In order to understand which part of the aggregation process was inhibited by these compounds, the data in **Fig. 2.4** were analysed using AmyloFit.[258] AmyloFit is an online software package that allows users to perform global fits of concentration-dependent aggregation data to kinetic models of aggregation, and thus determine which part of the process is being inhibited by a compound. Kinetic modelling experiments were performed by Sarah Ball and Manuela Zimmerman.

The aggregation of $A\beta_{42}$ in the absence of the compounds and any seeds can be described by the integrated rate law (**Equation 2.1**)[86]

$$\frac{M(t)}{M\,(\infty)} = 1 - \left(\frac{B_+ + C_+}{B_+ + C_+ e^{\kappa t}}\,\frac{B_- + C_+ e^{\kappa t}}{B_- + C_+}\right)^{\frac{k_\infty^2}{\kappa \tilde{k}_\infty}} e^{-k_\infty t}$$

Equation 2.1: Integrated rate law for assembly of $A\beta_{42}$ into fibrils, where M is the total fibril mass, $B_\pm = \left(k_\infty \pm \tilde{k}_\infty\right)/(2\kappa)$, $C_\pm = \pm\lambda^2/(2\kappa^2)$, $k_\infty = \sqrt{\frac{2\kappa^2}{[n_2(n_2+1)]} + 2\lambda^2/n_c}$, $\tilde{k}_\infty = \sqrt{k_\infty^2 - 4C_+C_-\kappa^2}$, where the rate of aggregate formation through primary pathways is $\lambda = \sqrt{2k_+k_n m(0)^{n_c}}$, the rate of aggregate formation through secondary pathways is $\kappa = \sqrt{2k_+k_2 m(0)^{n_2+1}}$, k_n is the rate constant for primary nucleation, k_+ is the rate constant for elongation, k_2 is the rate constant for secondary nucleation, $m(0)$ is the initial concentration of soluble monomers, n_c is the reaction order for primary nucleation pathways and n_2 is the reaction order for secondary nucleation pathways.

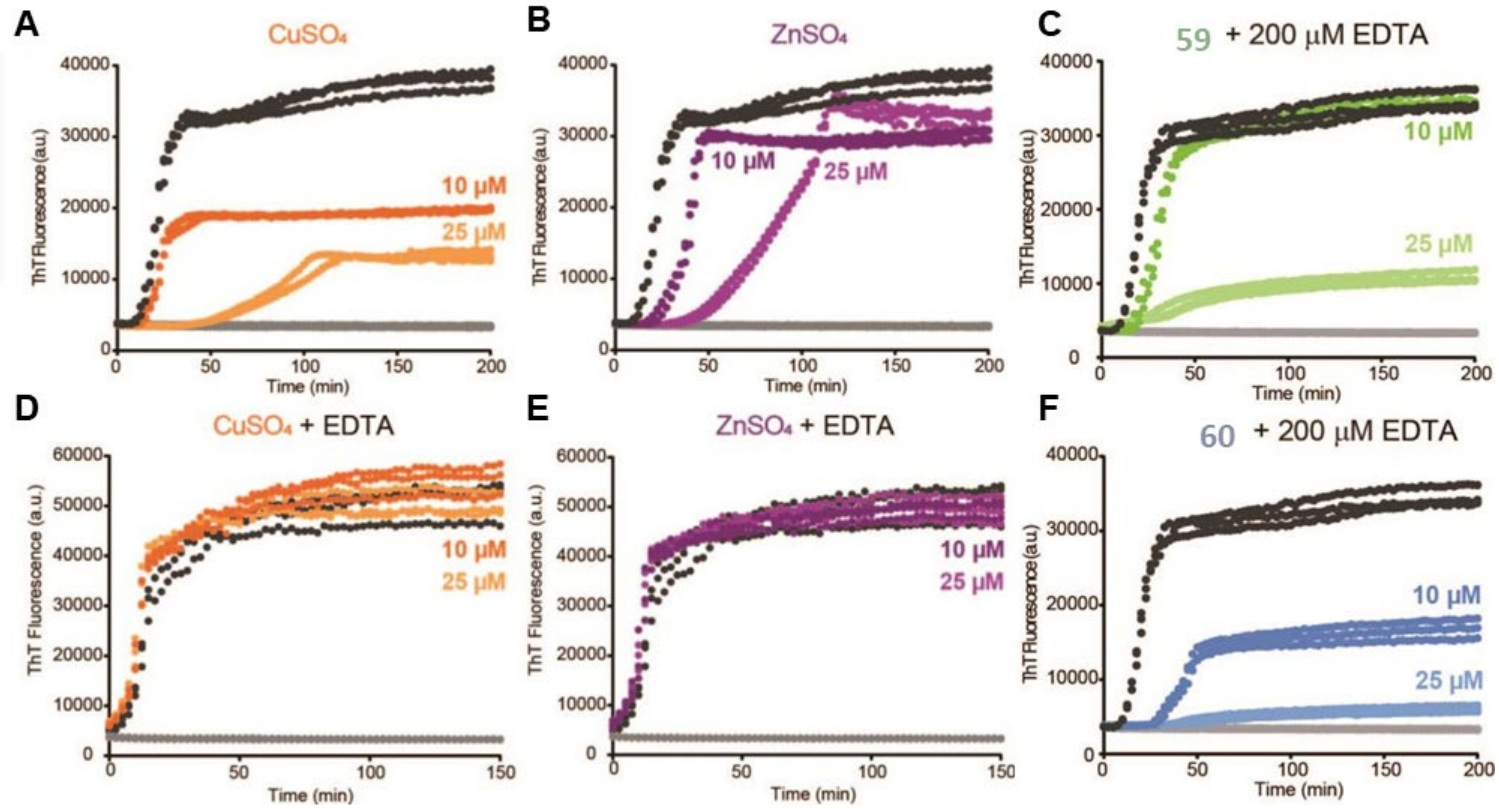

Figure 2.5: Effect of EDTA on the aggregation inhibition of free Cu^{2+} and Zn^{2+} ions, and compounds **59** and **60**. **A**: 10 μM$A\beta_{42}$ with 1% DMSO, 10 and 25 μM $CuSO_4$; **B**: 10 μM $A\beta_{42}$ with 1% DMSO, 10 and 25 μM $ZnSO_4$; **C**: 10 μM $A\beta_{42}$ with 1% DMSO, 10 and 25 μM **59**, and 200 μM EDTA; **D**: 10 μM $A\beta_{42}$ with 1% DMSO, 10 and 25 μM $CuSO_4$, and 200 μM EDTA; **E**: 10 μM $A\beta_{42}$ with 1% DMSO, 10 and 25 μM $ZnSO_4$, and 200 μM EDTA; **F**: 10 μM $A\beta_{42}$ with 1% DMSO, 10 and 25 μM **60** and 200 μM EDTA. *N*=3. *Assays conducted and figure constructed by Sarah Ball.*

The mechanism of inhibition was then probed by modelling the aggregation and systematically varying one rate constant in the rate law or by varying the concentration of available monomer. The data shown in **Figure 2.3** was then fitted to these models to determine the likely mechanism of inhibition.

This kinetic analysis of aggregation in the presence of each compound made it possible to rule out the inhibition of primary nucleation as the major contribution to the observed inhibitory activity, due to the poor fit of experimental data to the model where inhibition of primary nucleation dominates. The data agreed best with models demonstrating the inhibition of secondary nucleation, elongation and of monomer sequestration (**Figure 2.6**), but no single model was a significantly better fit than the other. This can often be the case with aggregation inhibitors, as due to the complexity of the aggregation process, multiple microscopic stages can be inhibited by the one compound.[258] In these cases, follow-up experiments are crucial to determining the mechanism of action of the aggregation inhibitor.

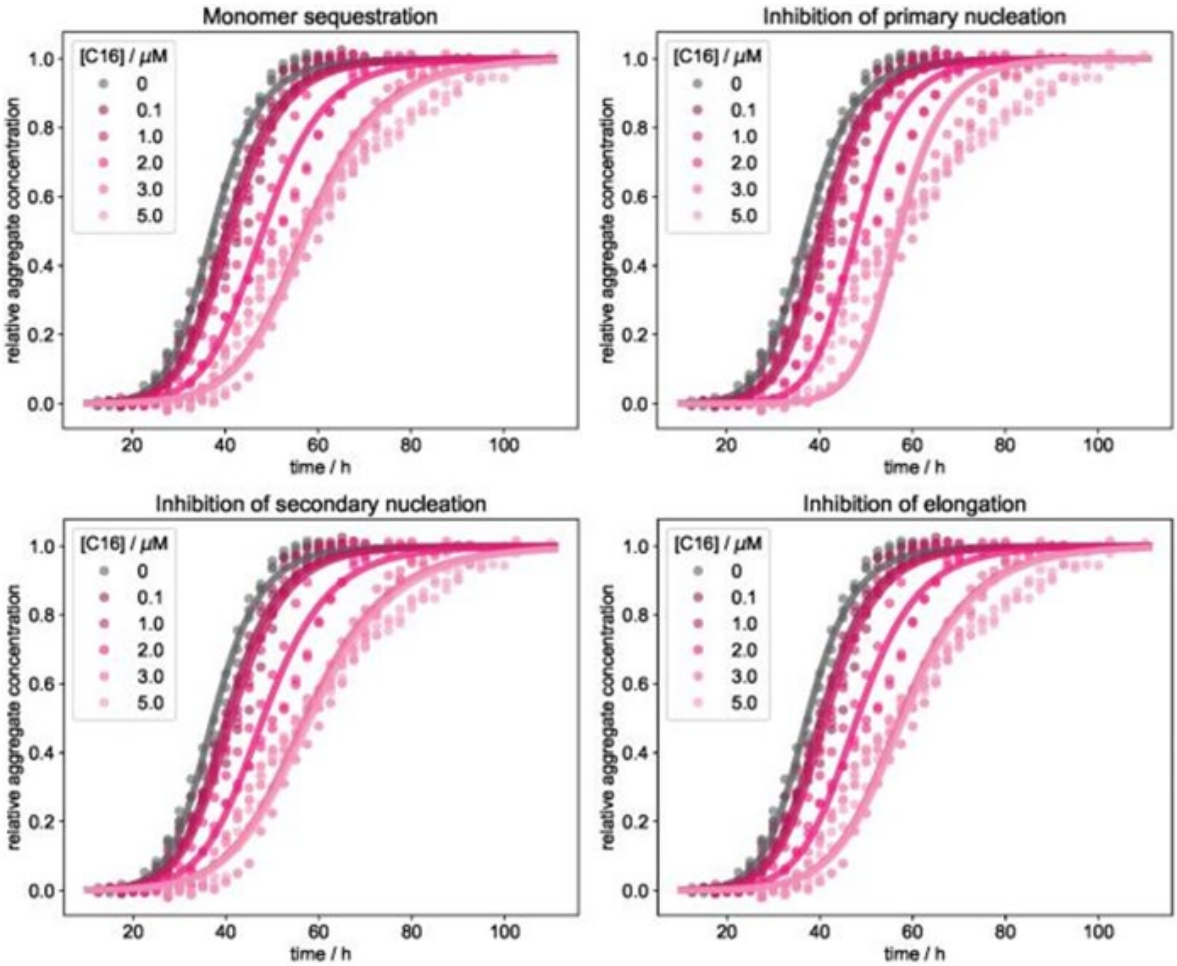

Figure 2.6: Example of global fitting of ThT fluorescence data to models of aggregation inhibition by **58**. Primary nucleation can be ruled out as a major contributor to the aggregation inhibition. *Modelling and figure constructed by Manuela Zimmerman*

Further evidence that the inhibition of primary nucleation is not the cause of the aggregation inhibition is apparent in the ability of **58**, **59** and **60** to inhibit $A\beta_{42}$ aggregation in the presence of seed fibrils (**Figure 2.7**). The presence of seed fibrils overrides primary nucleation in the assembly of amyloid fibrils, and instead secondary nucleation and elongation are the main contributors to fibril growth. Therefore inhibition of aggregation in the presence of seeds indicates that these three compounds inhibit both secondary nucleation and elongation, either by interacting with the fibrils or by sequestering monomeric Aβ.

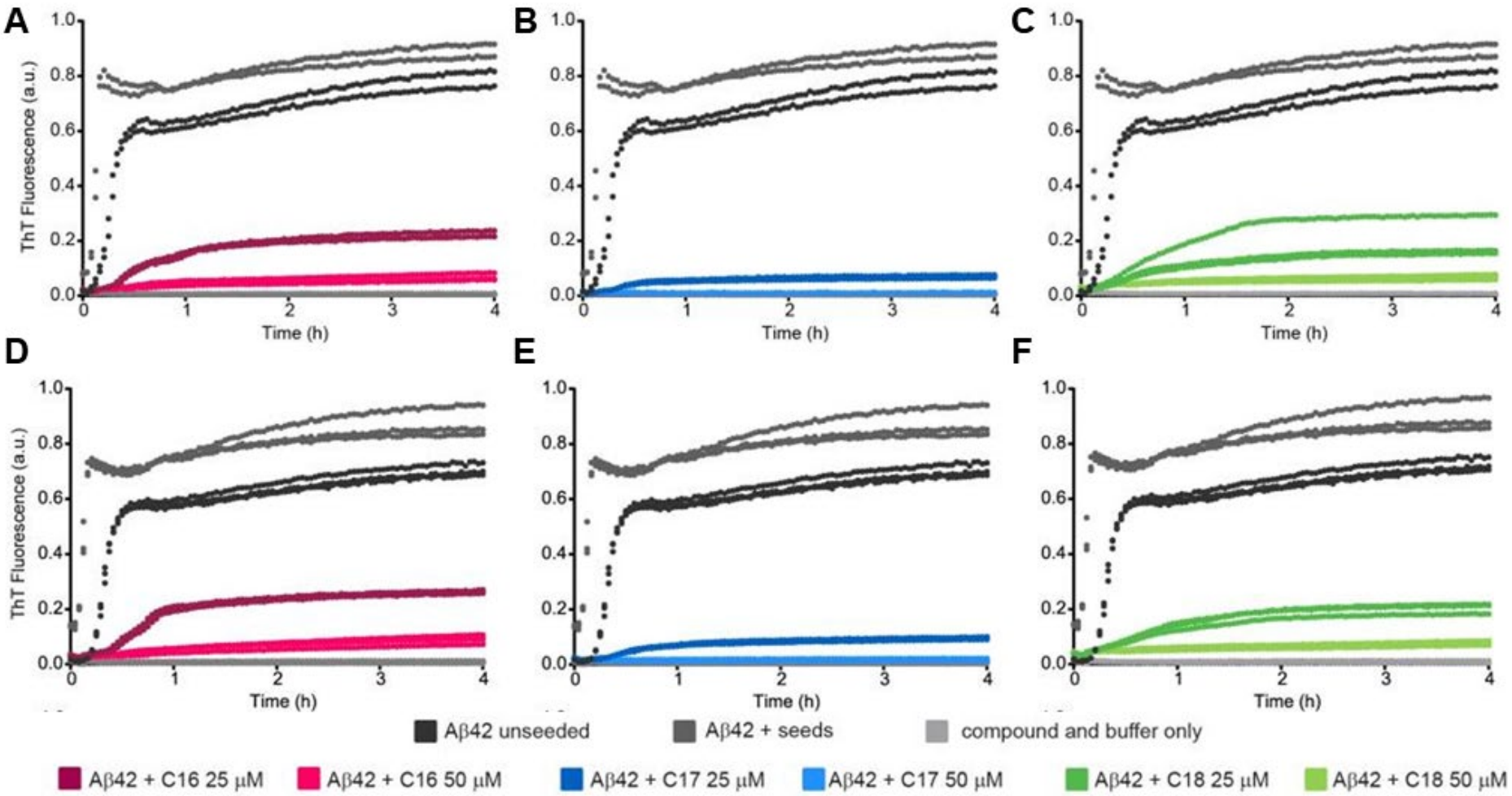

Figure 2.7: Effect of seed fibrils on the aggregation inhibition of **58**, **59** and **60**. Top row**:** 10 μM $A\beta_{42}$ with 1% DMSO and 1% seeds, 25 and 50 μM **58** (**A**), **59** (**B**) and **60** (**C**). Bottom row: 10 μM $A\beta_{42}$ with 1% DMSO and 5% seeds, 25 and 50 μM **58** (**D**), **59** (**E**) and **60** (**F**). *N*=3. *Assays conducted and figure constructed by Sarah Ball.*

2.10 Morphology of end-stage aggregates

Having established the possibility that these compounds may be inhibiting $A\beta_{42}$ fibrillisation by monomer sequestration, the morphology of the end-stage aggregates that $A\beta_{42}$ formed in the presence of these compounds was studied. Very little $A\beta_{42}$ remained in solution once the plateau of ThT fluorescence was reached, when the peptide was incubated with **58**, **59** and **60** (**Figure 2.8B-D**). The insoluble aggregates were isolated *via* centrifugation and the morphology was observed using transmission electron microscopy (TEM). TEM experiments were conducted by Victor Lo.

The aggregates were amorphous with a beads-on-string appearance, approximately 20 nm wide and over 1μM in length. Only a small amount of fibrillar $A\beta_{42}$ was observed in some of the samples. The lack of fibrillar $A\beta_{42}$ is congruent with a monomer sequestration mechanism. If these compounds were only inhibiting secondary nucleation, a reasonable amount of fibrillar Aβ would be expected, on the basis that primary nucleation and elongation would still occur.[90] By interacting directly with the monomer, the compounds can inhibit each of the different contributions to fibril growth, and avoid the formation of toxic oligomers that accompany it.

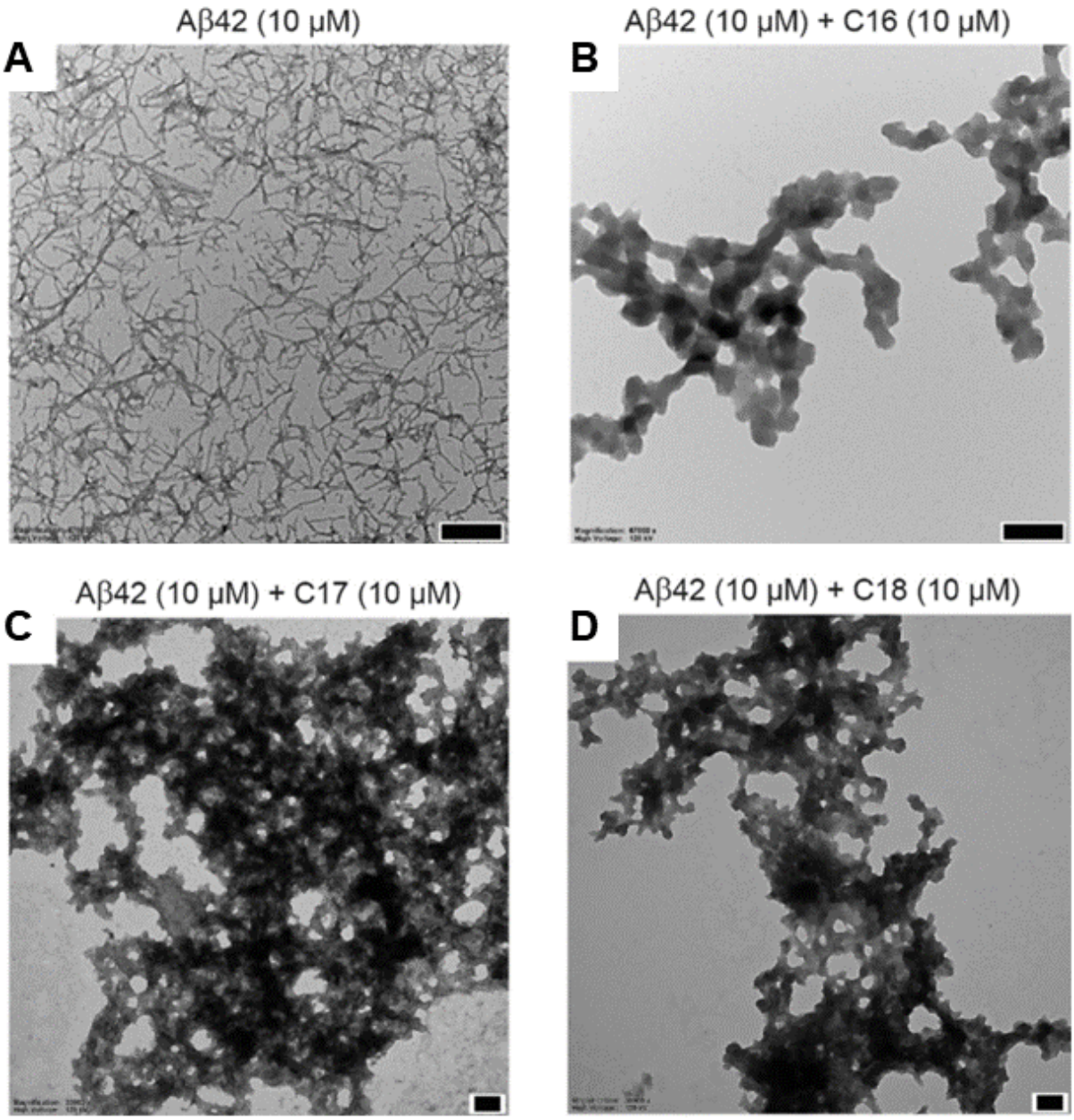

Figure 2.8: Representative examples of the morphology of the aggregates formed by $A\beta_{42}$ observed by TEM. **A:** 10 μM $A\beta_{42}$ alone; **B:** 10 μM $A\beta_{42}$ in the presence of 10 μM **47** after 24 h; **C:** 10 μM $A\beta_{42}$ in the presence of 10 μM **51** after 24 h; **D:** 10 μM $A\beta_{42}$ in the presence of 10 μM **52** after 24 h. Scale bar represents 200 nm. *TEM experiments conducted and figure constructed by Victor Lo.*

2.11 Effect of the conjugates on Aβ-induced neurotoxicity

Having established the effects of **58**, **59** and **60** on the physical process of $A\beta_{42}$ aggregation, the ability of these compounds to prevent $A\beta_{42}$-induced toxicity was

investigated. The compounds were co-administered with monomeric $A\beta_{42}$ to SH-SY5Y cells that had been induced to differentiate to an AD-appropriate phenotype by the administration of retinoic acid and brain-derived neurotrophic factors.[259] The compounds themselves demonstrated no toxicity toward neuronal cells, and they were able to prevent the toxicity induced by $A\beta_{42}$ oligomers produced by aggregation (**Figure 2.9A-B**). A concentration-response curve was generated for **58**, showing an IC_{50} of 2.3 μM. Interestingly, perphenazine itself was also able to prevent toxicity to a similar degree, despite it being unable to inhibit $A\beta_{42}$ aggregation at the same concentration (**Figure 2.9D**). Neuronal cell assays were performed by Michael Sullivan, André McKenzie and Eryn Werry.

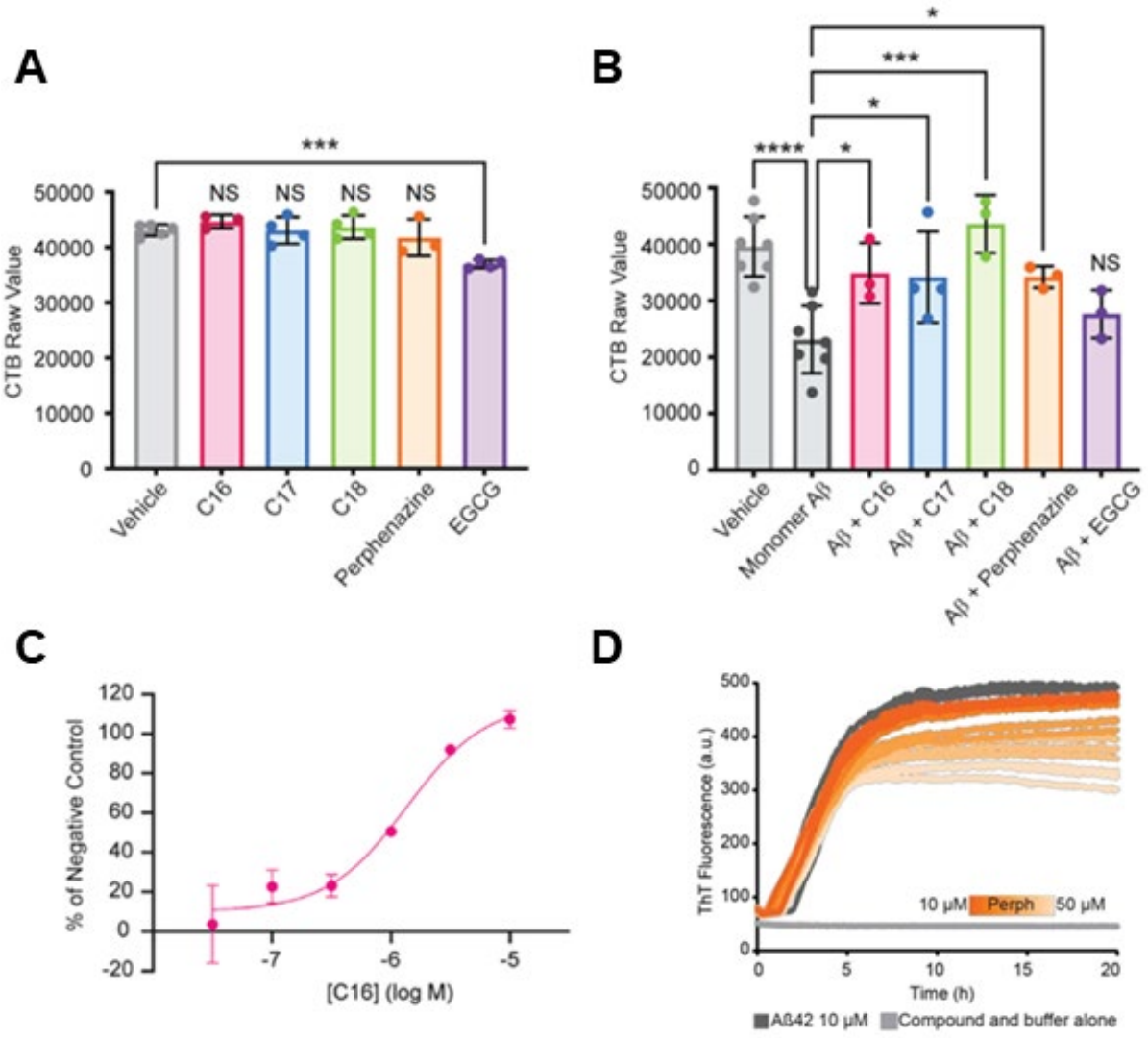

Figure 2.9 Reduction of $A\beta_{42}$ -induced toxicity by **58**, **59** and **60**. Cell viability measured using the CellTiter Blue Assay after 24 h incubation with vehicle, 10 μM compound, with or without 20 μM $A\beta_{42}$**. A**: Compounds **58** (pink), **59** (blue), **60** (green), perphenazine **63** (orange) or EGCG (purple) alone; **B:** Compounds with monomeric $A\beta_{42}$. Data are the mean ± SD of $N \geq 3$ independent experiments. One-way ANOVA followed by Bonferroni's multiple comparisons test at the 0.05 level was used to determine the difference between vehicle and compounds (**** $p<0.0001$, *** $p<0.001$, * $p<0.05$, NS = nonsignificant). **C:** Concentration-response curve for **58** incubated with $A\beta_{42}$ showing mean ± SD, IC_{50} = 2.3 μM. **D:** ThT fluorescence assay showing the aggregation of 10 μM $A\beta_{42}$ with 1% DMSO in the presence of 10-50 μM of perphenazine. *Neuronal cell assays were conducted and figures constructed by Michael Sullivan, André McKenzie and Ery Werry. ThT fluorescence assays were conducted and figure constructed by Sarah Ball.*

2.11 Characterising the interaction with monomeric Aβ using NMR

Having demonstrated that these compounds likely inhibit aggregation through monomer sequestration, and that they are able to prevent $A\beta_{42}$ induced toxicity, the interaction between the compounds and monomeric $A\beta_{42}$ were investigated further. NMR was utilized to determine a binding constant for the compounds against monomeric $A\beta_{42}$. Titration of 0.1-5 equivalents of **58**, **59** and **60** each resulted in a decay in signal intensity in the 1D NMR, consistent with the compounds binding to $A\beta_{42}$ and causing it to aggregate out of solution. The signal decay curves from these titrations (**Figure 2.10**) were fitted to a quadratic equation to calculate an apparent K_D of each compound, giving a value of 4.6 μM (95% CI, 3.1-6.5) for **58**, 3.4 μM (95% CI, 2.2-4.9) for **59** and 3.7 μM (95% CI, 2.4-5.3) for **60**.

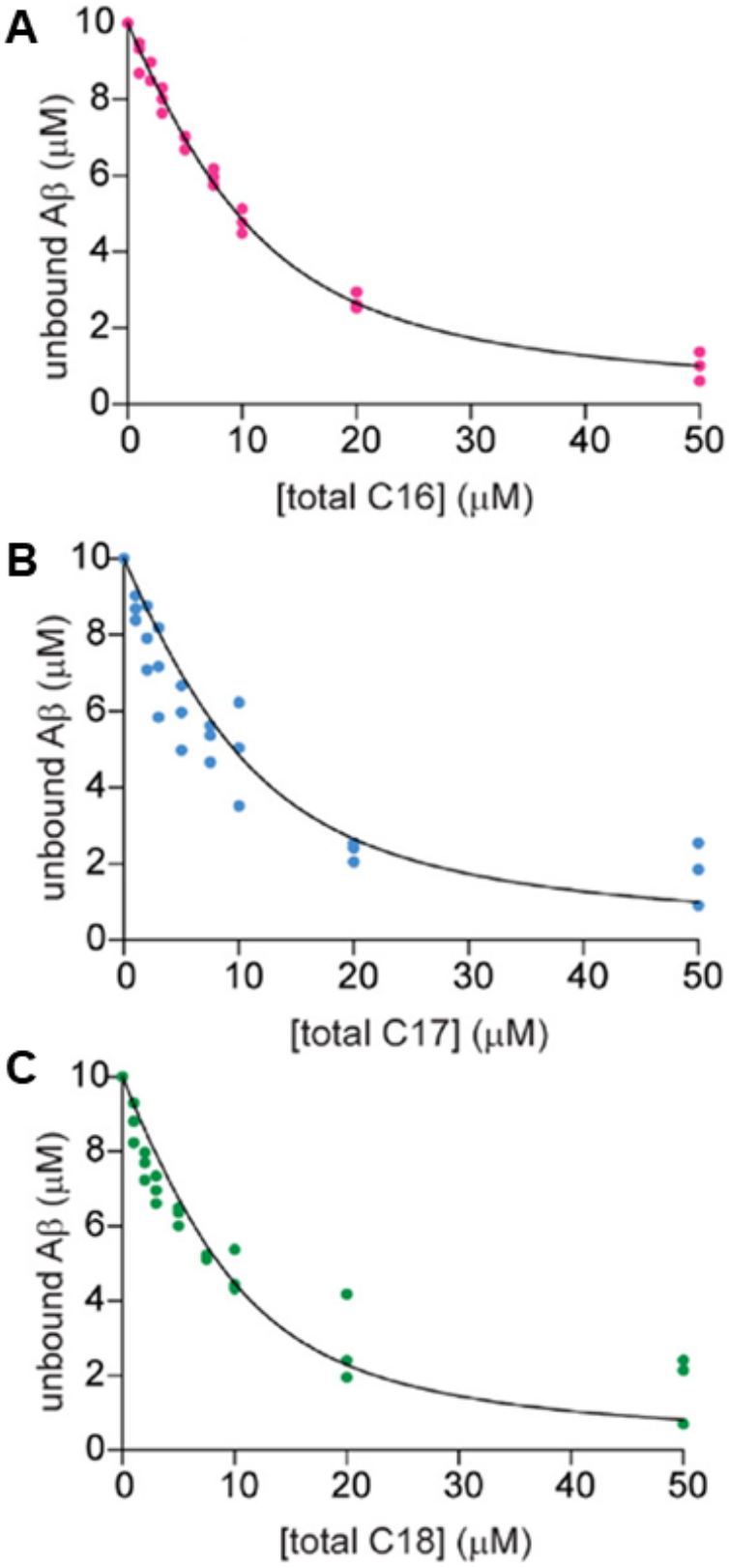

Figure 2.10: Binding curves constructed from signal decay curves used to calculate the apparent K_D of each compound to $A\beta_{42}$. **A: 58**; **B: 59**; **C: 60**. *NMR titrations were conducted and figure constructed by Sarah Ball and A/Prof. Ann Kwan.*

As an intrinsically disordered peptide, the NMR signals observed for $A\beta_{42}$ are a weighted average corresponding to a number of conformations (or ensembles). A sufficiently strongly binding compound could potentially induce the peptide, or a particular region of the peptide, to adopt one conformation and induce a change in the overall averaged chemical shift.

In order to probe which regions of $A\beta_{42}$ interact with these compounds, a ^{1}H-^{15}N HSQC spectrum was measured with ^{15}N-labelled $A\beta_{42}$ in the absence and presence of **58** (**Fig 2.11**). HSQC NMR data was collected and analysed by Sarah Ball and Ann Kwan. Unfortunately, no specific changes in chemical shift were observed, instead the peaks began decreasing in intensity uniformly, indicating the aggregation and subsequent precipitation of $A\beta_{42}$.

This could be the result of several different phenomena; the first is that **58** binds relatively weakly to the monomeric peptide in a non-specific manner, and thus is not able to induce a specific conformational change in the peptide. Compound **58** could be binding in a specific, but weak, manner which contributes to only a small population of the conformational ensembles that then induces rapid aggregation. Alternatively, the compound could be binding to Aβ in a manner that maintains its intrinsic disorder, which would not sufficiently perturb the structural ensembles adopted to shift the NMR spectrum, but does result in an increase in aggregation rate.

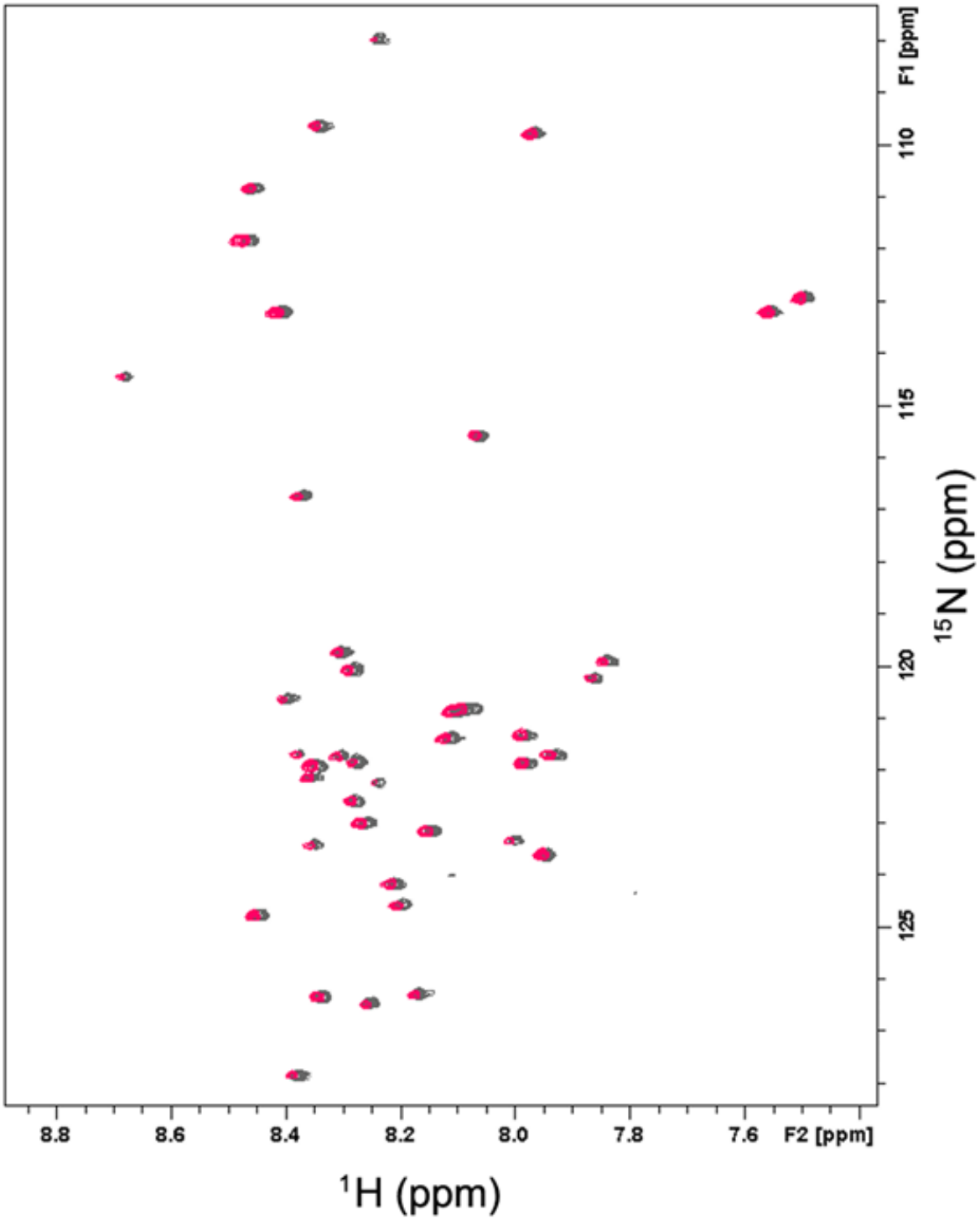

Figure 2.11: Overlay of the ^{1}H-^{15}N HSQC spectra of Aβ_{42} alone (grey) and 1:1 Aβ_{42} and **58** (pink). Spectra were recorded at 800 MHz at 4° C. *Spectra recorded by Sarah Ball and Ann Kwan*.

2.12 Conclusions

A convergent, scalable synthetic route to **58**, **59** and **60** was developed to afford **58** in an overall yield of 28% and **59** and **60** in an overall yield of 25%. The procedure was amenable to scale up and was used to synthesize enough material to characterize the interaction between **58**, **59**, and **60** with $A\beta_{42}$, using a range of biophysical methods.

All three compounds were shown to strongly inhibit $A\beta_{42}$ fibrilization, most likely through a mechanism of monomer sequestration, and to trigger the formation of amorphous aggregates of Aβ. There are very few reports of aggregation inhibitors operating *via* such a mechanism. These compounds also mitigate some of the toxicity caused by $A\beta_{42}$ oligomers produced during the fibrillization process. Apparent binding constants of **58**, **59** and **60** to monomeric Aβ were determined, but these compounds did not bind sufficiently strongly to induce chemical shift changes observable in a standard ^{1}H-^{15}N HSQC experiment.

3. Synthesis of Bis-Perphenazine Lanthanide Complexes

3.1 Rationale for the chapter

Efforts to identify how the compounds **58**, **59** and **60** were binding to Aβ by measuring chemical shift changes in the HSQC were unsuccessful. As discussed in Chapter 2, there was no change in chemical shift observed when the compounds were titrated in, indicating that either their binding to Aβ was weak, or a lowly-populated state was involved. Paramagnetic NMR effects are known to be highly sensitive and are excellent at uncovering binding information for weakly binding-compounds that are in fast exchange with the unbound state. Thus, it was decided to develop a paramagnetic probe compound derived from **58** in order to identify how **58** binds to Aβ.

While **59** is a Cu(II) complex and thus paramagnetic, Cu^{2+} ions are not ideal for PRE experiments for several reasons. This is due largely to their anisotropic χ-tensor in such ions, which induces contact shifts and PCSs in the NMR spectrum. While PCSs can themselves be used as a source of distance restraints, they complicate the NMR spectrum, as do contact shifts.[260] The PRE that is exerted is also anisotropic,[261] and sensitive to cross-correlation effects as the electrons in Cu(II) relax *via* the Curie mechanism.[262-264] These three factors make it difficult to extract quantitative measurements of PRE effects exerted by Cu(II) ions.

Attempts to synthesise the Mn(II) complex of **58** were initially successful, but this complex proved highly susceptible to oxidation which precluded its use in further experiments. This susceptibility to oxidation was likely due to the coordination of the triazoles being weak enough to allow O_2 to displace them and oxidise the Mn(II) centre.

With these considerations, it was decided that a new ligand scaffold capable of coordinating Ln^{3+} ions would need to be synthesised. The initial strategy was to simply

incorporate two acetate arms into the structure of **58**, adding two extra points of coordination, which should be enough to satisfy the coordination preferences of a lanthanide ion. This would make the resulting molecules analogous to TETA, which is well known to form complexes with Ln^{3+} ions (**14**). While TETA complexes are relatively unstable compared to other ligands, this was considered a good starting point given that it required minimal alteration to the lead compound structure and, it was surmised, its capacity to interact with Aβ.

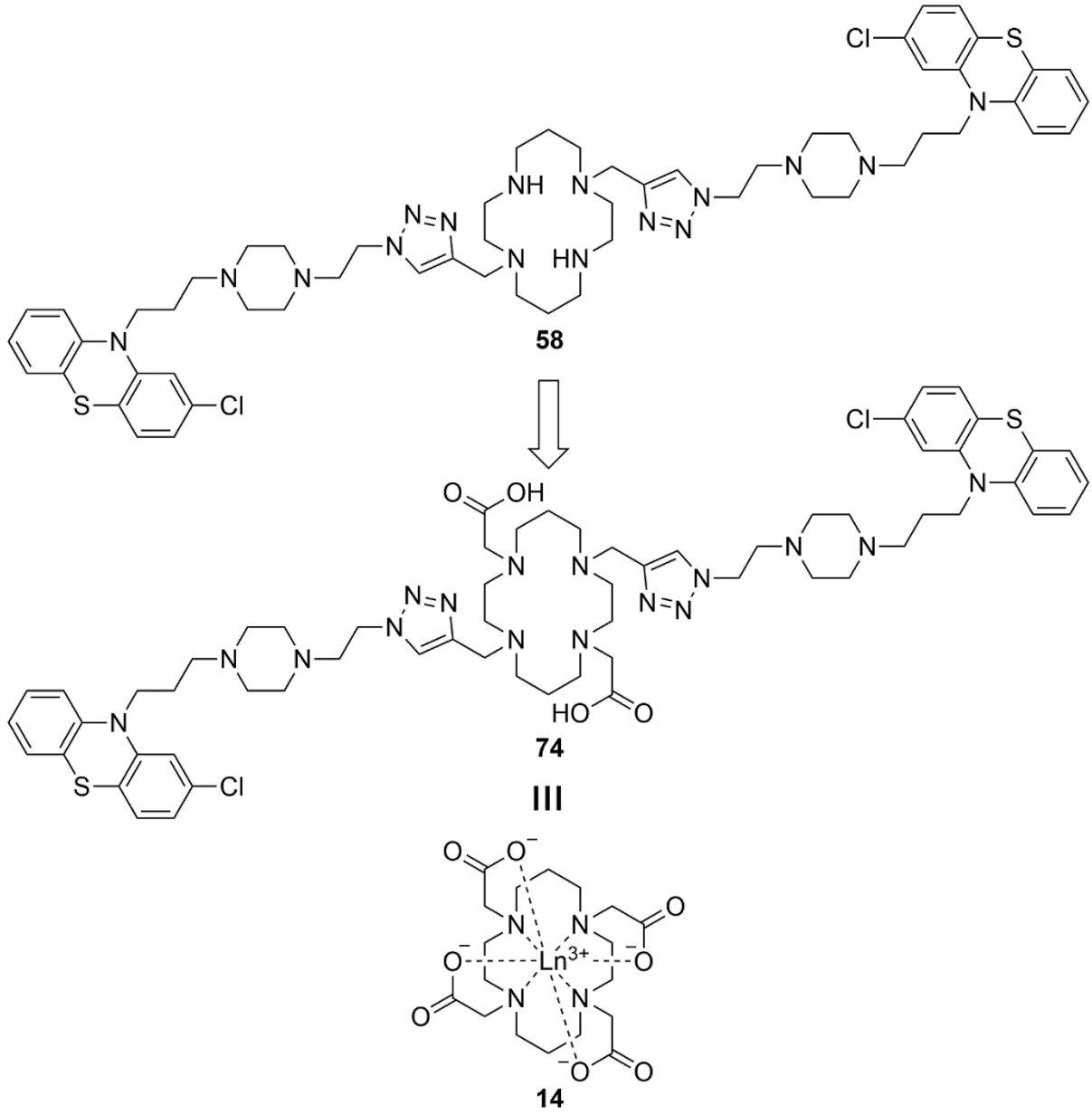

Figure 3.1: The translation of **58** into a lanthanide-coordinating ligand **74**, to form complexes with lanthanides as TETA (**14**) does.

The new target **74** could be synthesised with only minor alterations to the synthetic scheme for **58**, by alkylating the intermediate bis-propargyl cyclam with *tert*-butyl bromoacetate rather than Boc anhydride. The product of this reaction could then be coupled to the same perphenazine azide **62** using the CuAAC reaction.

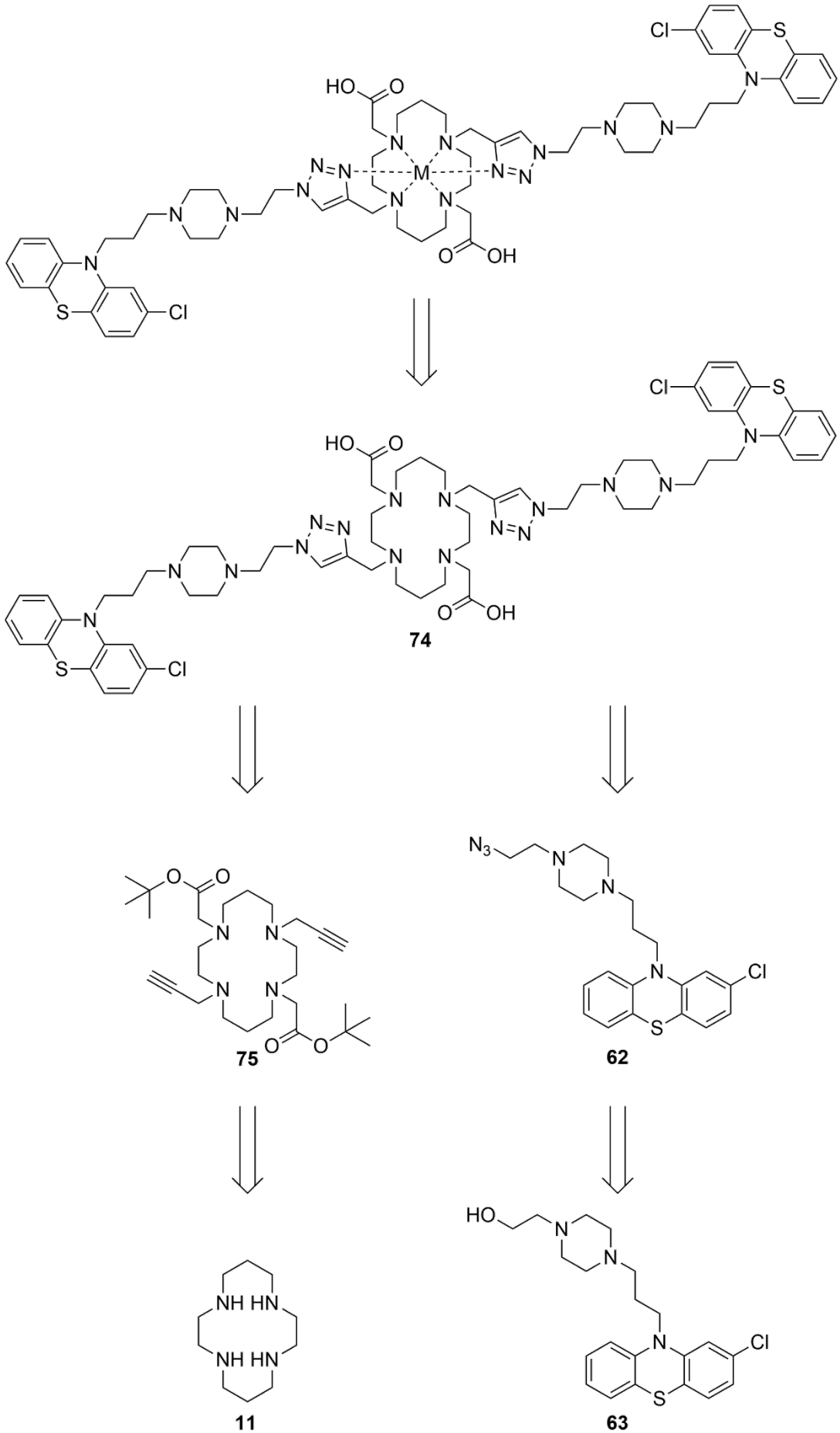

Scheme 3.2: Retrosynthetic scheme for **65** and its metal complexes.

3.2 Synthesis of the *t*-butyl protected bis-propargyl cyclam diacetate

The synthesis of *tert*-butylacetate cyclam **75** is identical to the synthesis of Boc-protected bis-propargyl cyclam **61** until the unprotected bis-propargyl intermediate **66** is reached. Compound **66** was isolated from the reaction mixture by removing the methanol under reduced pressure and extracting into DCM, which allowed isolation of crude **66**. No purification was performed as minimal side-products are carried through the synthesis to **66**, and it was envisaged that **75** could be prepared following a telescoped procedure as had worked with **61**.

Thus, alkylation was initially performed by adding a slight excess of *t*-butyl bromoacetate to a solution of **66** in acetonitrile with sodium carbonate as the base. Residual solid sodium carbonate was removed *via* vacuum filtration and the resulting residue was purified *via* column chromatography to give the product **75** in a disappointing yield of only 13%.

The reaction clearly needed optimisation, and the first round of reaction improvement focused on the number of equivalents of *t*-butyl acetate, the base and the solvent. Initially, careful control of stoichiometry was thought necessary to avoid over-alkylation of the cyclam, and the reaction was kept at room temperature for the same reason. However, the presence of residual cyclam in the TLC of the first reaction indicated that more of the alkylating agent may be needed. While a solid base like sodium carbonate was easy to remove, the use of triethylamine was explored as it is a common amine base for alkylations. Finally, DMF was used as an alternative solvent, since some cyclam compounds and intermediates are poorly soluble in acetonitrile. The results of these optimisation experiments are summarised in **Table 3.1**

Table 3.1 Reaction optimisation for the synthesis of **75** (**Scheme 3.2**). All reactions were performed at room temperature. Yields are isolated yields. *Yield obtained

on repeat. † Over-alkylated product **76** observed on TLC but not quantified. ‡ *t*-butyl bromoacetate was added dropwise over 30 min § NMR and TLC showed complete conversion to a mixture of over-alkylated product **76**

Equivalents of alkylating agent	**Base**	**Solvent**	**Reaction time (h)**	**Yield**
2.2	Na_2CO_3	MeCN	16	13% (28%*)†
2.2	Na_2CO_3	MeCN	4‡	34%
3	Na_2CO_3	MeCN	16	37%†
3	Na_2CO_3	MeCN	4‡	37%
3.5	Na_2CO_3	MeCN	16	-§
2.2	Et_3N	MeCN	16	22%†
3	Et_3N	MeCN	16	26%†
3.5	Et_3N	MeCN	16	8%†
2.2	Na_2CO_3	DMF	16	38%†
2.2	Na_2CO_3	DMF	4‡	46%
3	Na_2CO_3	DMF	16	52%†
3	Na_2CO_3	DMF	4‡	56%
3.5	Na_2CO_3	DMF	16	57%†
3.5	Na_2CO_3	DMF	4‡	64%

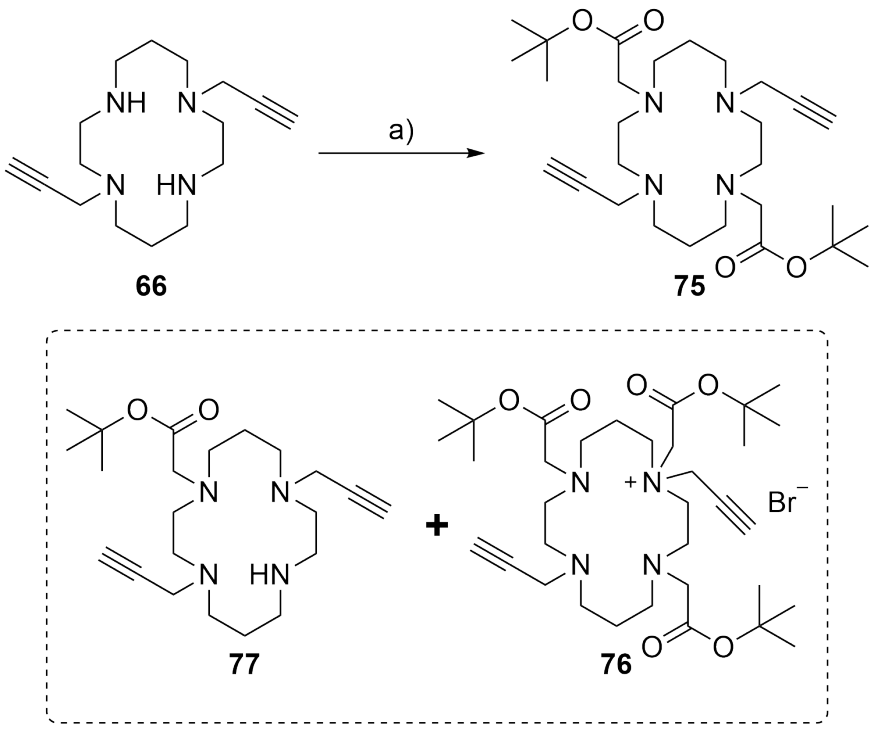

Scheme 3.2: Synthesis of **66**, with under- and over-alkylated side products **77** and **76** shown in the box. Conditions: **62**, *t*-butylbromoacetate, Na_2CO_3, DMF, rt, 4 h, 64%.

All of the reactions run in acetonitrile returned poor yields regardless of the base chosen or equivalents of alkylating agent used. This was determined to be due to the poor solubility of the intermediates in acetonitrile, as analysis of the filtrand from workup found partially-alkylated cyclam precipitated amongst the Na_2CO_3. Using DMF delivered higher yields in all the experiments, due to the higher solubility of the intermediates in this solvent. When the *t*-butyl bromoacetate was added all at once and the reaction left for 16 h, it was found that significant amounts of over-alkylated product was formed. Slow addition of *t*-butyl bromoacetate over 30 minutes and shortening the reaction time to 4 hours prevented the formation of the over-alkylated product **76** and increased the yield of the desired product **75**.

While the yield achieved using the optimised procedure was acceptable, one disadvantage was the need for column chromatography to separate out the partially-alkylated intermediate **77**. One of the advantages of the synthetic approach to Boc-

protected bis-propargyl cyclam **61** was the ease of isolating the solid product from the reaction mixture. Using solid Na_2CO_3, and DMF as the solvent, precluded the isolations of the product *via* filtration, and it was decided that recrystallisation would improve the overall effectiveness of the new procedure. A screen of single and mixed solvent systems found that, fortuitously, the product crystallises from a mixture of DMF and water. The purification step then became to add water to the filtered reaction mixture and allow it to stand overnight, affording the pure product as white needles.

3.3 Click coupling to *t*-butyl protected bis-propargyl cyclam diacetate

The first attempt at click coupling the *tert*-butyl acetate cyclam derivative **75** and perphenazine azide **62** used the standard conditions that had been applied to synthesise of **72**. Upon adding **75** to the solution of $CuSO_4$ and sodium ascorbate, a bright blue solution was formed indicating that **75** had formed a complex with the Cu^{2+}.

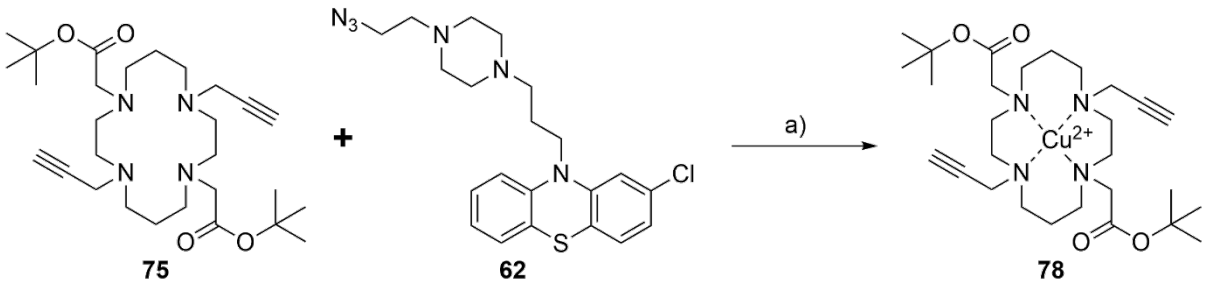

Scheme 3.3: Attempted click coupling of **75** and **62** using $CuSO_4$ and sodium ascorbate. Conditions: a) **75**, **62**, $CuSO_4$, sodium ascorbate, THF/H_2O, rt, 16 h.

The addition of more sodium ascorbate in an effort to reduce the Cu(II) down to Cu(I) was unsuccessful; the most likely reason for this is that the reduction potential of Cu(II) is lowered significantly when it becomes chelated by macrocyclic ligands, rendering the Cu(II) centre resistant to reduction.[265-269] It was clear that Cu(II) needed to be avoided outright in this reaction mixture, as the resulting complex with **75** was too stable for the reaction to be rescued once complexation had occurred.

Thus, it was decided to use Cu(I) salt as the copper source, along with a suitable ligand to stabilize Cu(I) as a complex. Many ligands from varying structural classes have been reported,[270-273] and from these tris-(benzyltriazolylmethyl)amine (TBTA, **79**) was chosen as a starting point. TBTA has been shown to stabilise the Cu(I) oxidation state under aerobic conditions, preventing disproportionation of Cu(I) and accelerating the rate of CuAAC reactions.[270] It was thought that **75** would not effectively compete for Cu(I), since many tetraazamacrocylic ligands have been shown to be less effective at chelating Cu(I) than Cu(II) due to the differences in coordination geometry between these two ions.[274-276]

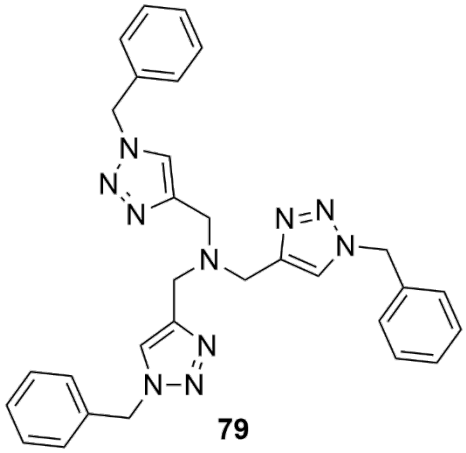

79

Figure 3.4: Structure of TBTA **79**, a ligand that stabilizes Cu(I) and accelerates the click reaction.

Click coupling using TBTA was attempted by first stirring a mixture of TBTA, CuI and sacrificial sodium ascorbate in a mixture of water and THF under nitrogen to form the $[Cu(TBTA)]^+$ complex. Solutions of **75** and **62** were then added to the mixture which was stirred at room temperature. Pleasingly, the appearance of product was observed on TLC in less than 30 minutes, however complete conversion was not observed, even after stirring overnight. Over this time, the reaction did not reach completion and the mixture had turned a blue colour, indicating that despite the anaerobic conditions, Cu(I) was eventually oxidised and form a complex with **75** or coupled product **80**.

The slow reaction rate which saw this reaction failing to reach completion was considered to be due to the steric bulk around the cyclam centre; to overcome this the reaction was repeated at a higher dilution (33 mM) and at reflux, modifications to the procedure which allowed the reaction to proceed to completion.

Reaction workup was complicated by the ability of the product **80** to coordinate Cu(II) once the reaction is opened to air, which led to a drop in yield of 20%. To overcome this, EDTA in ammonium chloride buffer was used in the aqueous workup to chelate Cu(II) once it formed; due to the faster complexation kinetics of EDTA compared to cyclam, there was no detected formation of the Cu(II) complex of **80**, and the uncomplexed product could be isolated in 79% yield.

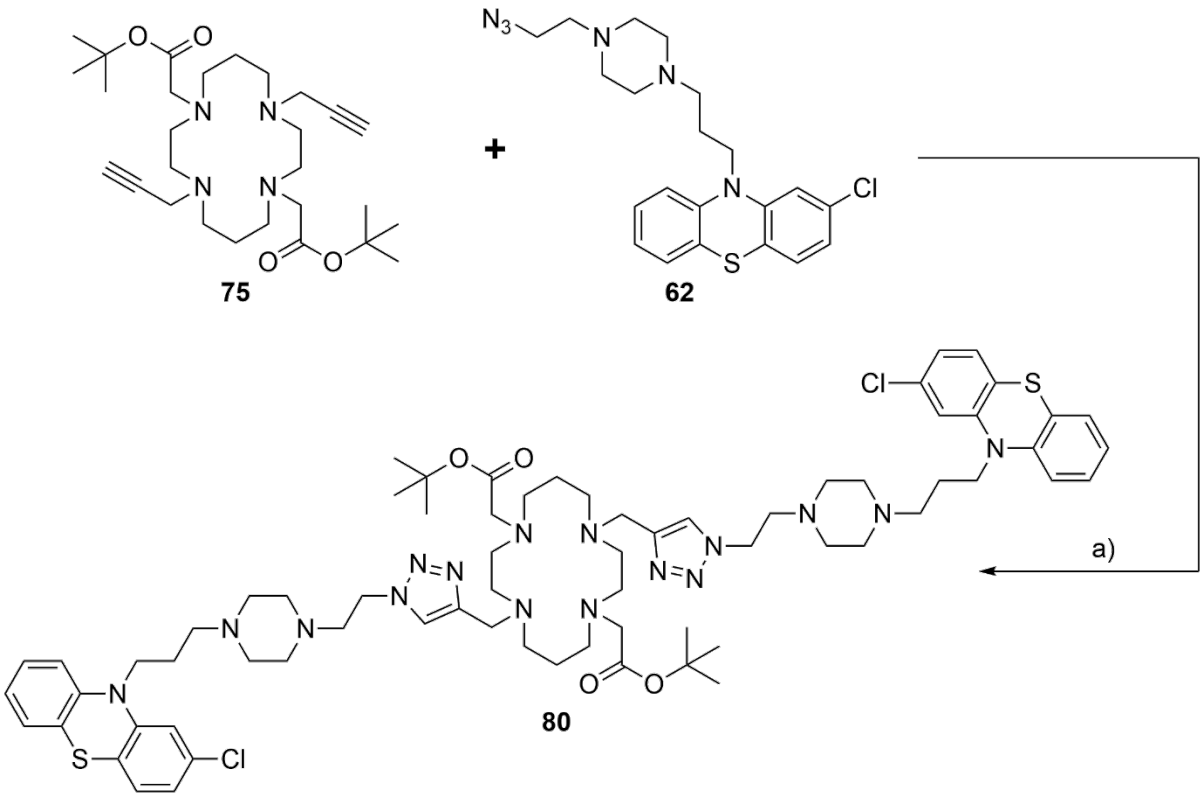

Scheme 3.5: Successful click coupling of **75** and **62** using CuI and TBTA. Conditions: a) **75**, **62**, CuI, TBTA, sodium ascorbate, THF/H_2O, 75° C, 3-4 h, 79%.

3.4 Removing the *t*-butyl esters

Acidic conditions are favoured for the deprotection of *tert*-butyl esters, with protocols typically using a mixture of trifluoracetic acid (TFA) and DCM, which affords the deprotected product after 16-48 hours.[277] Whilst it was known that the perphenazine moieties in **80** are sensitive to acid, deprotection was nonetheless initially attempted using these conditions.[278] However, acidic conditions unsurprisingly resulted in the decomposition of **80**. Since the decomposition of phenothiazines in acid also involves molecular oxygen,[247] the reaction was attempted again under anaerobic conditions, but a sluggish reaction rate meant that oxygen was able to seep into the reaction mixture and trigger decomposition of **80** before significant conversion to the product **74** could be achieved.

Lewis acids have also been reported to deprotect *t*-butyl esters.[279, 280] The deprotection was thus attempted with $ZnBr_2$, which unfortunately also induced oxidative decomposition of **80**, albeit as the minor product alongside the zinc complex of **80**, which was isolated as the major product. With these results, it was evident that acidic deprotection conditions needed to be avoided, since *t*-butyl ester cleavage could not be achieved as rapidly as the successful Boc-deprotection of **72** discussed earlier.

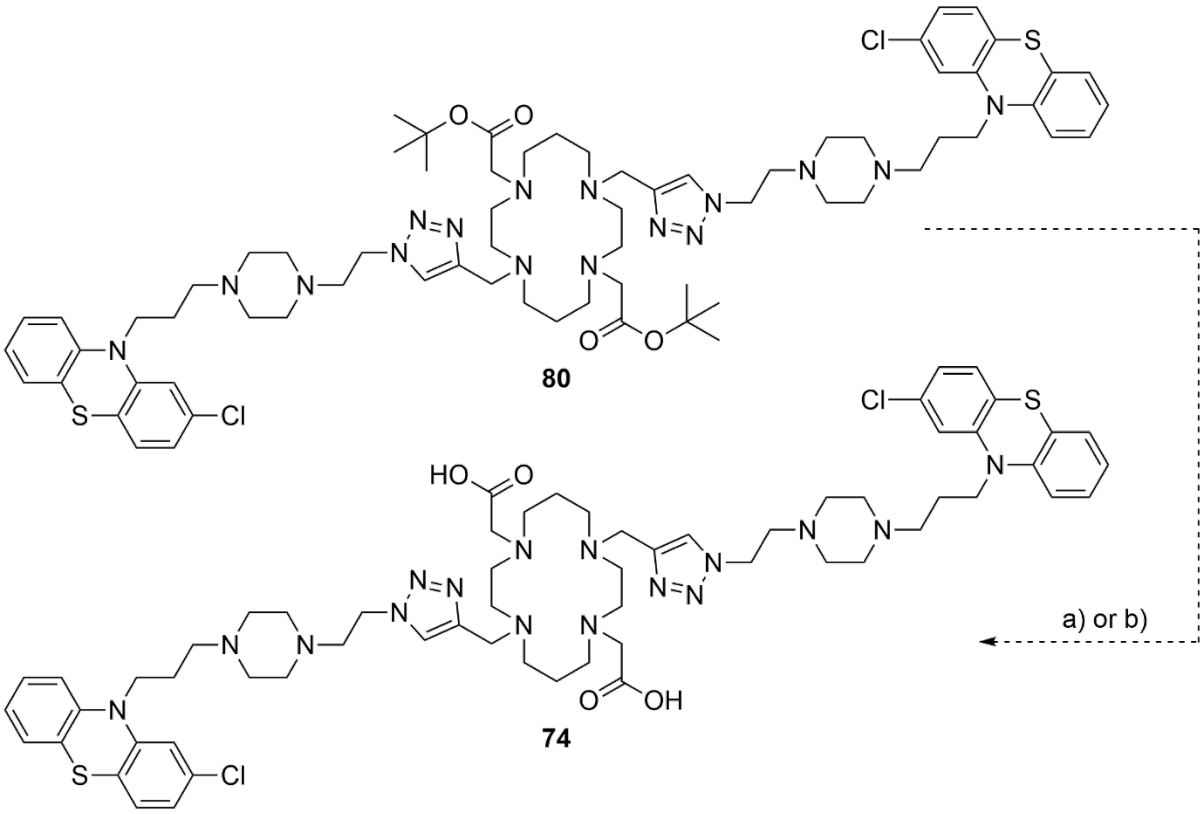

Scheme 3.6: Failed attempts at the deprotection of **80** under acidic conditions. Conditions: a) **80**, TFA/DCM, rt, 16 h; b) **80**, $ZnBr_2$, DCM, rt, 16 h.

The cleavage of *t*-butyl esters under basic conditions has been reported using NaH in DMF[281] or powdered KOH in THF.[282] Whilst the NaH/DMF mediated deprotection was initially posited as following a reductive mechanism,[281] later work demonstrated that deprotection was actually due to the formation of NaOH *in situ* which hydrolyses the ester.[282] Considering this, the basic deprotection was first attempted using powdered KOH in THF and **80** was stirred in a suspension of KOH in THF at room temperature. Unfortunately, no conversion to the product was observed under the literature conditions.

The reaction was attempted at reflux, considering that the steric bulk of **80** was likely contributing to the slow reaction rate. The higher temperature served to partially convert **80** to the deprotected product, however the stoichiometry of the original conditions was not sufficient for the full conversion of **80**. Sequential introduction of additional KOH to the reaction mixture resulted in the complete conversion to **74** after the addition of 25

equivalents of KOH. The large excess of KOH complicated workup, although the product could be isolated by careful neutralisation of the reaction mixture then desalting the mixture with a reversed-phase column.

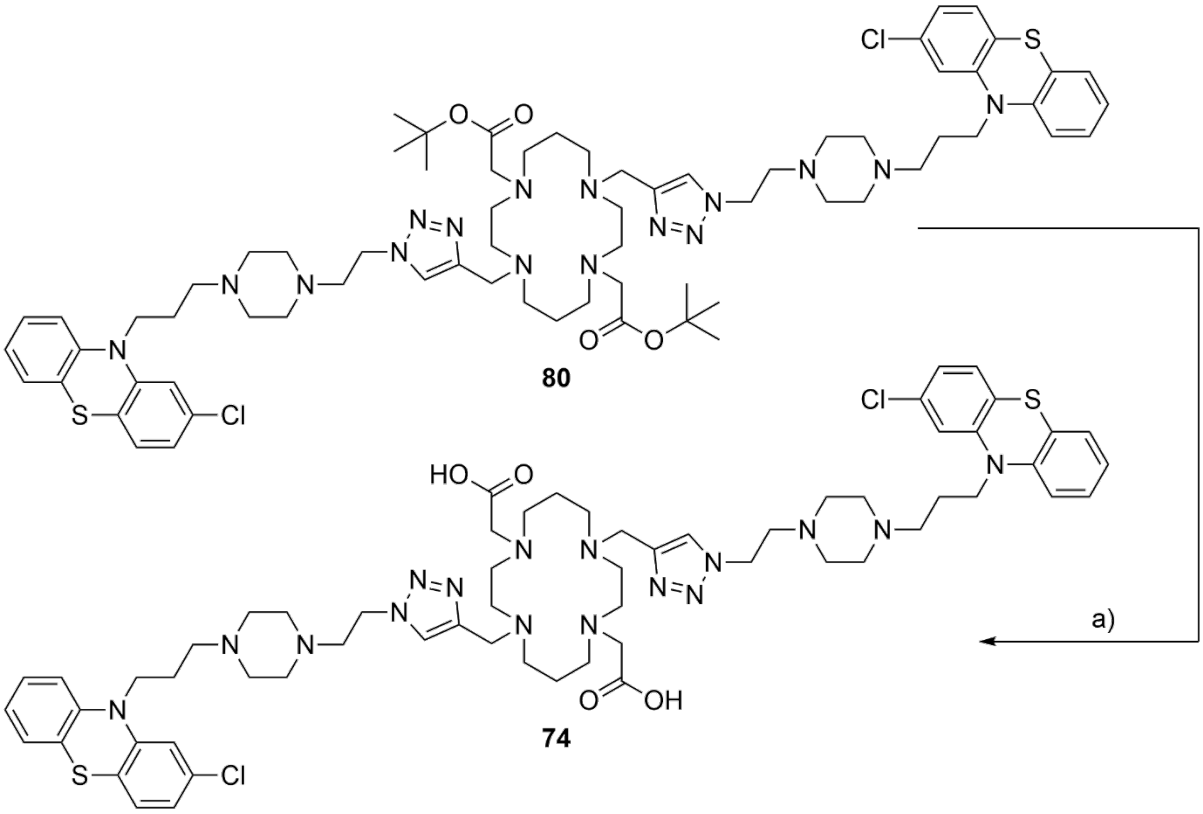

Scheme 3.7: Successful basic deprotection of **80**. Conditions: a) **80**, KOH, THF, reflux, 4 h, then neutralisation with 1M HC and reversed-phase chromatography 76%.

3.5 Synthesis of the metal complexes

Having developed an efficient route to the ligand **74**, the next step was metal complexation. The first metal complexes synthesized were the corresponding Cu^{2+} **81** and Zn^{2+} **82** (mirroring the complexes synthesised in Chapter 2) complexes and the Mn^{2+} complex **83**. These different complexes required slightly different conditions to achieve the best yields. Copper(II) complex **72** was synthesised by refluxing a solution of **74** and $CuCl_2{\cdot}2H_2O$ in methanol overnight; the complex precipitated from solution upon cooling which facilitated isolation by centrifugation. Zinc(II) complex **82** by contrast was

more soluble in methanol which hindered its isolation, and was instead synthesised by stirring a solution of **74** and $ZnCl_2$ in ethanol overnight at room temperature, with the resulting complex also being isolated by centrifugation. To make the manganese(II) complex **83** was synthesized by stirring a solution of **74** and $MnCl_2{\cdot}4H_2O$ in methanol overnight, and the complex was precipitated by concentrating the reaction mixture to half its volume and adding ether, to give the complex in 57% yield.

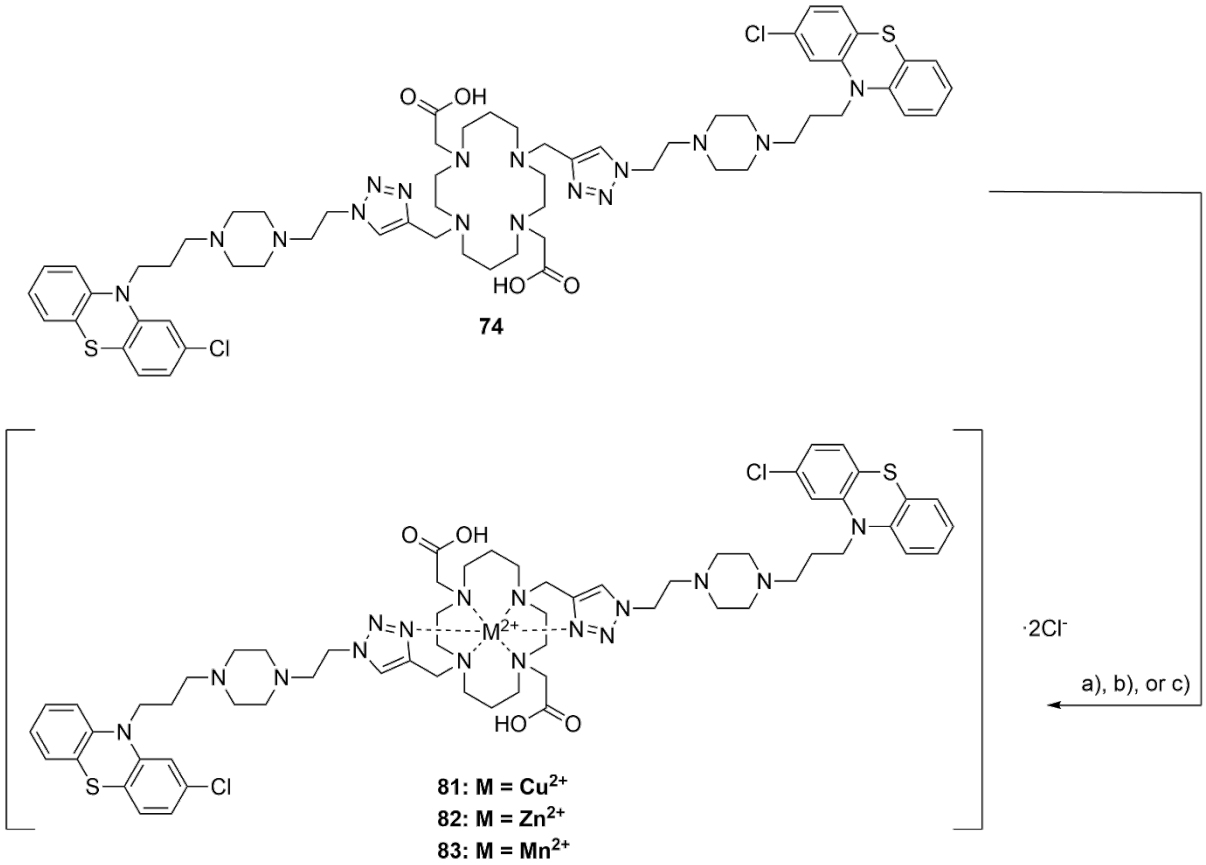

Scheme 3.8: Synthesis of Cu^{2+}, Zn^{2+} and Mn^{2+} complexes of **74**. Conditions: a) $CuCl_2{\cdot}2H_2O$, MeOH, reflux, 16 h, 59%; b) $ZnCl_2{\cdot}4H_2O$, EtOH, rt, 16 h, 49%; c) $MnCl_2{\cdot}4H_2O$, MeOH, rt, 16 h, 57%.

Following the successful synthesis of the Cu^{2+} and Zn^{2+} complexes, focus turned to lanthanide complexes. The formation kinetics of lanthanide complexes with macrocyclic polyamino/ carboxylate ligands is typically slow, due to the rigidity of the ligand and the number of bonds that need to form.[185]

Typical conditions[283-285] were applied to the attempted formation of lanthanide complexes with **74**, with a solution of the metal chloride (M = Y^{3+}, Gd^{3+} or Eu^{3+}) and **74** stirred at 50° C for two days. By this point a precipitate had formed in the reaction mixture, indicating possible complex formation; but LRMS indicated that only partial formation of a complex had occurred in all cases. Attempts to push the reaction to completion by extending reaction times, increasing the temperature, or adding extra equivalents of lanthanide salts, were unsuccessful. The reaction was repeated using lanthanide triflates, another common source of lanthanide ions, but similar results were obtained.

Given the high number of potentially coordinating groups in the structure of **74**, and the precipitation observed during the reaction which did not correspond to one single species according to LRMS analyses, it was rationalised that **74** instead forms alternative complexes, rather than the desired 1:1 in-cage complex between **74** and the lanthanide. The resulting species were insoluble, and the precipitation of this mixture of alternative complexes prevented the eventual formation of the target 1:1 complex.

3.6 Synthesis of the *t*-butyl protected bis-propargyl cyclen

The lack of success in synthesizing lanthanide complexes using **74** led to a shift in focus to synthesize ligands based on a cyclen scaffold. The synthetic scheme to the cyclen analogue **84** (**Scheme 3.6.1**) would be quite similar to the route to **74**, and the analogous bis-propargyl intermediate **85** is prepared from cyclen **10** in 4 steps.

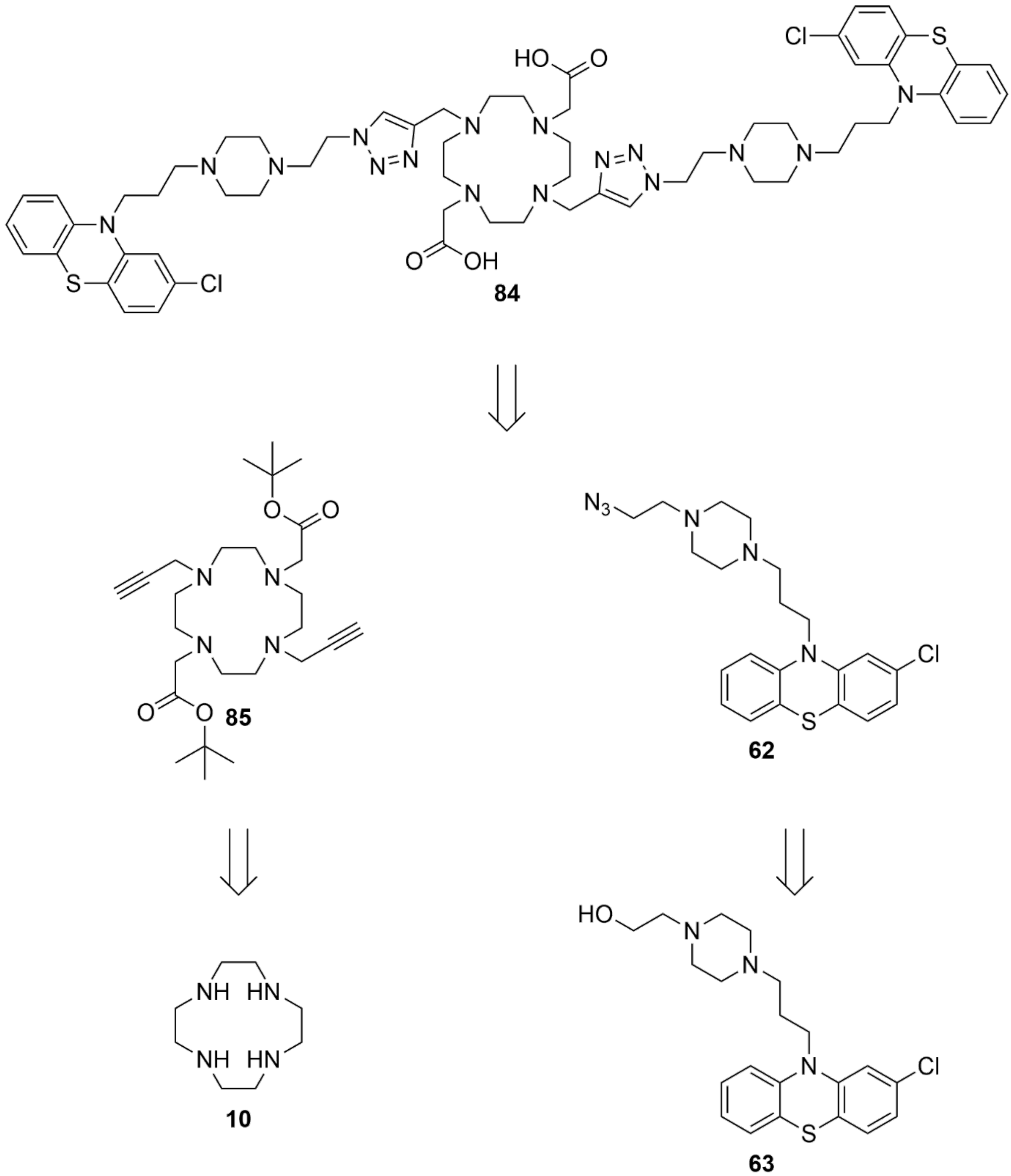

Scheme 3.9: Retrosynthetic scheme for the cyclen analogue **84**.

The synthesis of **85** began with Cbz protection of cyclen, using a procedure from Kovacs and coworkers.[286] Cyclen was dissolved in a mixture of water and dioxane and the mixture acidified to pH 3, after which a solution of benzyl chloroformate in dioxane was added dropwise over 24-48 hours, which results in the chemoselective 1,-7 protection of cyclen. The protonation constants of the nitrogen atoms cyclen are 10.5, 9.5, 1.6 and 0.8,

so at pH 3 two nitrogens are protonated and will not react with the benzyl chloroformate. This protonation occurs at diagonally opposite nitrogens to maximise charge separation, so the two remaining nitrogens react to deliver the observed 1,7- selectivity. The HCl byproduct formed during the reaction is enough to lower the pH below 2, at which point the reaction rate at any of the Ns becomes negligible, so regular pH adjustments are required using aqueous sodium hydroxide. Raising the pH above 3, or adding benzyl chloroformate too quickly, results in a loss of chemoselectivity, but care is taken to avoid these potential traps and this procedure afforded the protected cyclen **86** in 85% yield.

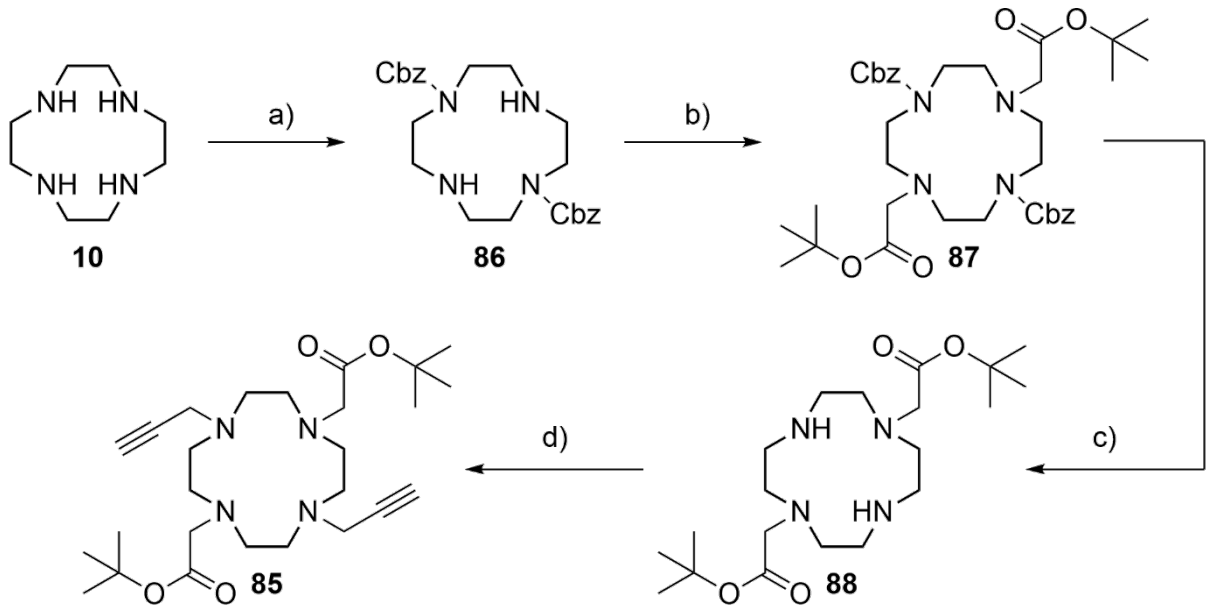

Scheme 3.10: Synthesis of **85** from cyclen. Conditions: a) benzyl chloroformate, H_2O/dioxane, pH 3, rt, 24-48 h, 85%;[286] b) *t*-butyl bromoacetate, K_2CO_3, MeCN, 50° C, 16 h, 74%;[287] c) H_2, Pd/C, MeOH, rt, 3 h, 91%;[286] d) propargyl bromide, Na_2CO_3, MeCN, 50° C, 48 h, 70%.[288]

The subsequent alkylation was achieved using modified conditions from Yamamoto, *et al.*[287] A slight excess of *t*-butyl bromoacetate was heated with **86** and potassium carbonate in acetonitrile overnight, affording **87** in 74% yield. The original protocol heated the reaction to reflux, but this proved was unnecessary and resulted in a slightly lower yield.

The Cbz protecting groups were then cleaved using standard hydrogenation conditions.[286] **87** was added to a suspension of Pd/C catalyst in methanol and stirred under H_2 for 3 h, which afforded **88** in 91% yield. Subsequent alkylation using propargyl bromide and sodium carbonate in acetonitrile at 50° C for 48 h afforded the bis-propargyl product **85** in 70% yield.[288]

3.7 Attempted click-coupling with the bis-propargyl cyclen

The click coupling of cyclen derived compounds has only been reported for macrocycles that were either coordinated to a metal prior, or had their amines protected. The failure of click coupling reactions with unprotected cyclen has been vaguely attributed to complexation of copper by the macrocycle.[288] Nonetheless, the click coupling of **85** with **62** was attempted given prior success coupling **62** to **75**, which also has unprotected nitrogens. The protocol for the synthesis of **80** was applied, whereby CuI and TBTA were combined under anaerobic conditions to pre-form the catalytic complex, followed by the addition of **62** and **85**. Unfortunately the reaction did not proceed under these conditions; and after stirring overnight the Cu(II) complex of **85** had formed, displaying a telltale blue colour.

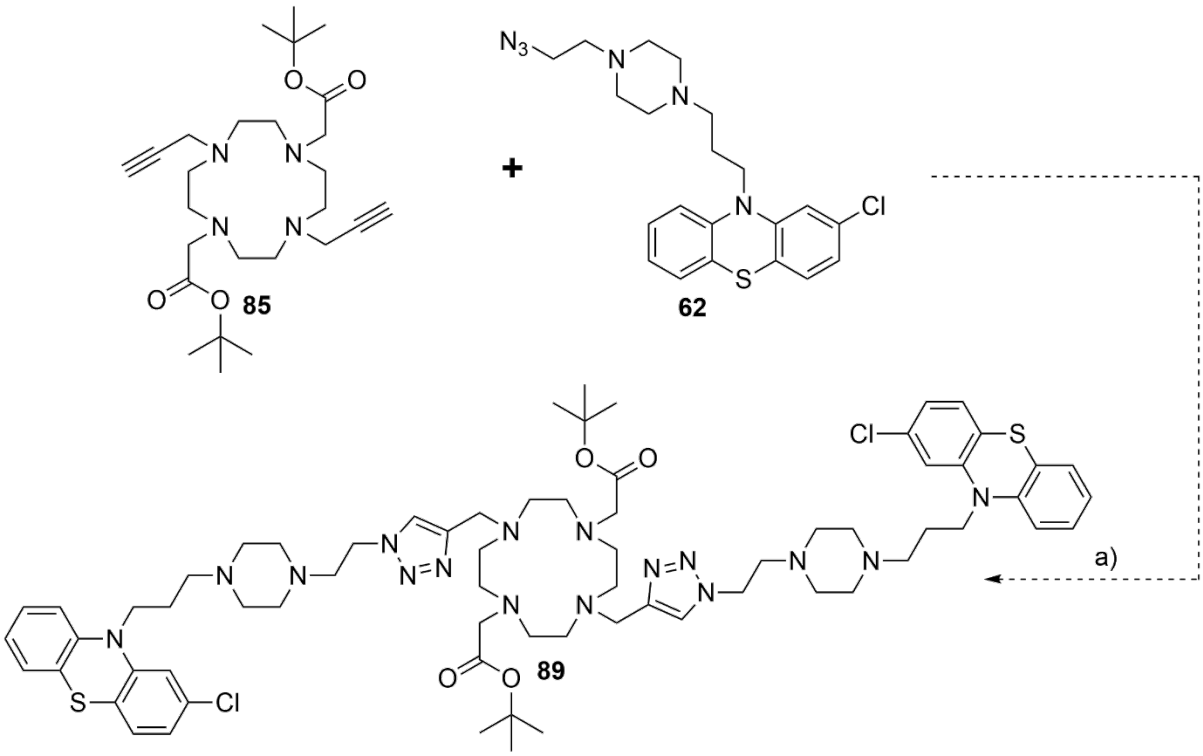

Scheme 3.11: Failed attempted click coupling of **85** and **62**. Conditions: a) CuI, TBTA, THF/H_2O, 75° C, overnight.

The reaction was repeated and monitored *via* LRMS during the first few hours, in order to determine whether a Cu(II) complex was forming under the initial reaction conditions. No species that could be attributed to a Cu(II) complex derived from **85** were directly observed.

It is possible that **85** coordinates Cu(I) and prevents the reaction from occurring in that way, with oxidation to the blue Cu(II) complex occurring subsequently. However, cyclic voltammetry studies on Cu(II) complexes of cyclen, DOTA and cross-bridged DO2A have demonstrated that these ligands cannot accommodate the coordination geometry of Cu(I), based on their irreversible cyclic voltammograms.[267, 268, 275, 289] Thus, it seems unlikely that **85** is able to accommodate the coordination geometry of Cu(I) and poison the catalyst by direct coordination.

The click coupling reaction of **85** was attempted with a different ligand, tri-benzimidazole **90**, which has been reported to induce faster reaction rates for the

CuAAC.[271] However, the reaction of **85** and **62** still did not proceed, even with this new ligand, indicating that the ligand was not a critical factor in the slow rate of reaction.

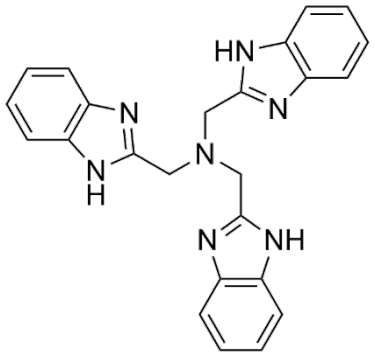

90

Figure 3.12: Structure of ligand **90**.

One possibility is that the reaction does not progress due to the rigidity of the cyclen core **85** when compared to the more flexible cyclam core of **75**. Both DOTA and TETA, which are analogous to **85** and **75**, tend to adopt a conformation in which the pendant acetate arms lie on one face of the macrocyclic ring, which pre-organises the ligands to form a cavity which can fully coordinate a lanthanide ion.[196, 290] It is envisioned that the pendant groups of **85** and **75** can both adopt similar conformations in solution, but that this sterically congested conformation is not conducive to a fast reaction rate.

The added flexibility of **75** compared to **85** would enable the macrocycle to convert between this conformation and one in which the alkynes are more accessible, resulting in the partial conversion of **75** to the click coupled product **80**, and complete conversion when the reaction is sufficiently heated. It is possible that the rigidity of **85** makes it unable to convert into a reactive conformation at a rate sufficient to allow the reaction to take place at a reasonable rate, and generate an acceptable amount of product before Cu(I) is oxidised to Cu(II) and chelated by **85**. This hypothesis is supported by the reaction rates of the click reaction on cyclen ligands, which are either protected or pre-complexed with the desired lanthanide, which typically take multiple days.[283, 284, 291]

Upon further consideration of the generally accepted mechanism of the CuAAC reaction (**Scheme 3.13**)[292], it was noted that the alkyne forms a complex with two Cu(I) nuclei,

placing further burden on the already sterically strained macrocycle. Thus, it was postulated that the reaction may be able to progress if the alkynes were incorporated into the side chain instead, relieving some of the steric strain on the macrocycle as the reaction proceeds.

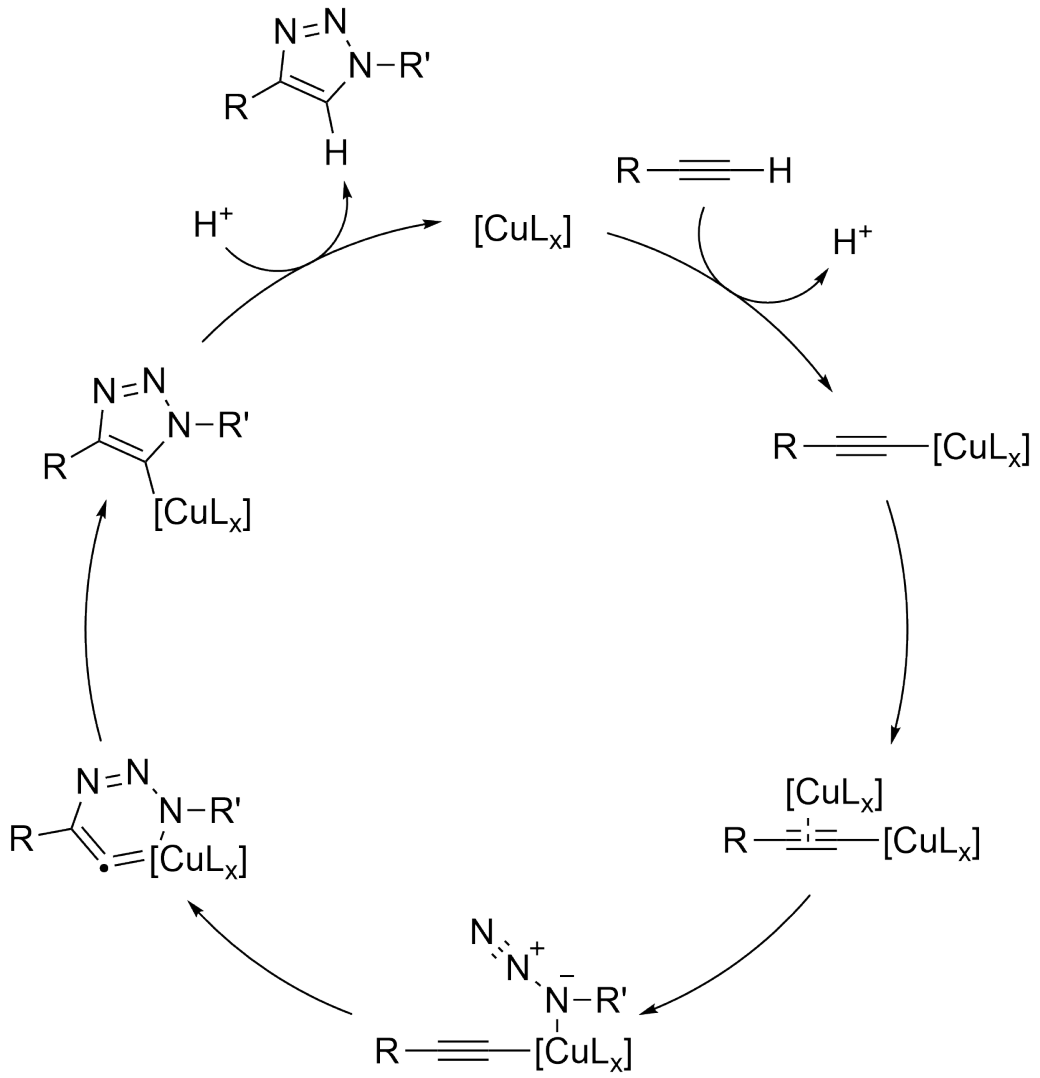

Scheme 3.13: Proposed catalytic cycle for the CuAAC reaction, adapted from Hein and Fokin[292]. An alternative mechanism has also been proposed which involves a dinuclear Cu complex that coordinates to the alkyne.[293]

In order to test this hypothesis, a model reaction was investigated involving an azide-substited cyclen **91** and phenylacetylene. The azide-substituted cyclen **91** was synthesized from cyclen in two steps (**Scheme 3.14**).

First, three of the nitrogens were alkylated with *t*-butyl bromoacetate using a procedure from Junker, *et al*[284]; three equivalents of *t*-butyl bromoacetate were added dropwise to a suspension of cyclen and sodium hydrogen carbonate in acetonitrile over 30 minutes at 0° C, and the mixture was then stirred at room temperature for two days. The solids were removed *via* filtration and the filtrate concentrated and then triturated with cold toluene to give the pure product **92** as a white powder in 52% yield. Tri-ester **92** was then reacted with 2-azidoethyl methanesulfonate (**93**,*vide infra*) and potassium carbonate in acetonitrile at 50° C overnight which gave the product **91** as a brown oil in 46% yield.

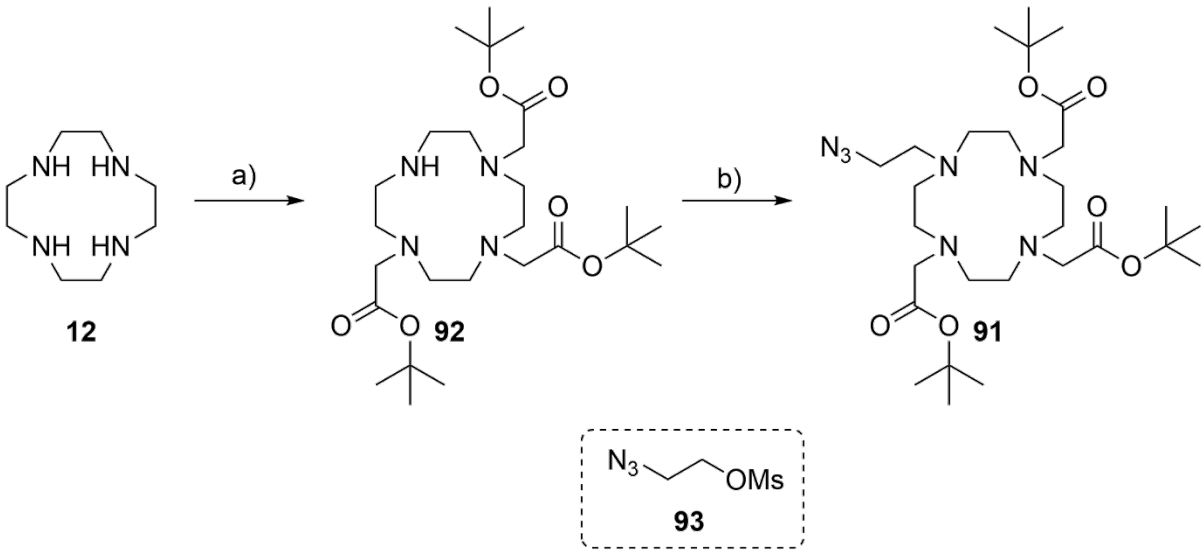

Scheme 3.14 Synthesis of **92**, where the azide is located on cyclen. Conditions: a) *t*-butyl bromoacetate, $NaHCO_3$, MeCN, rt, 48 h, 52%; b) **93**, K_2CO_3, MeCN, 50° C, 16 h, 47%.

2-Azidoethyl methanesulfonate was synthesised from 2-bromoethanol **94** in two steps (**Scheme 3.7.4**), using a procedure adapted from Hawker, *et al*.[294] A mixture of 2-bromoethanol and sodium azide in DMF was stirred at 50° C overnight to afford 2-azidoethanol **95**, which was not isolated for safety reasons. The original literature procedure used 2-chloroethanol and was reacted at ambient temperature, but it was found that using 2-bromoethanol required a higher reaction temperature. The solution was diluted with THF which precipitated the residual sodium azide from the mixture,

the filtrate was combined with mesyl chloride and triethylamine and the mixture was stirred at ambient temperature overnight to afford **93** in 67% yield over two steps.

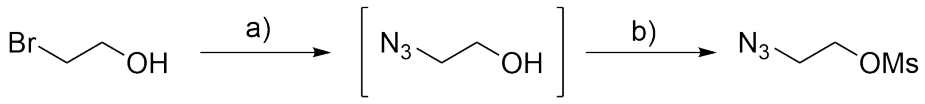

94 **95** **93**

Scheme 3.15: Synthesis of 2-azidoethyl methanesulfonate **85**. Conditions: a) NaN_3, DMF, 50° C, 16 h; b) mesyl chloride, triethylamine, THF/DMF, rt, 16 h, 67%.

The click coupling reaction between **91** and phenylacetylene **96** was attempted using three different conditions: CuI and TBTA in THF/H_2O; CuI and **90** in THF/H_2O; and CuI and diisopropylethylamine (DIPEA) in MeCN (**Scheme 3.7.5**). None of these conditions afforded the desired product **97**, making it was apparent that inverting the connectivity of the reaction was not going to overcome the barriers preventing the click coupling of these cyclen derivatives from proceeding.

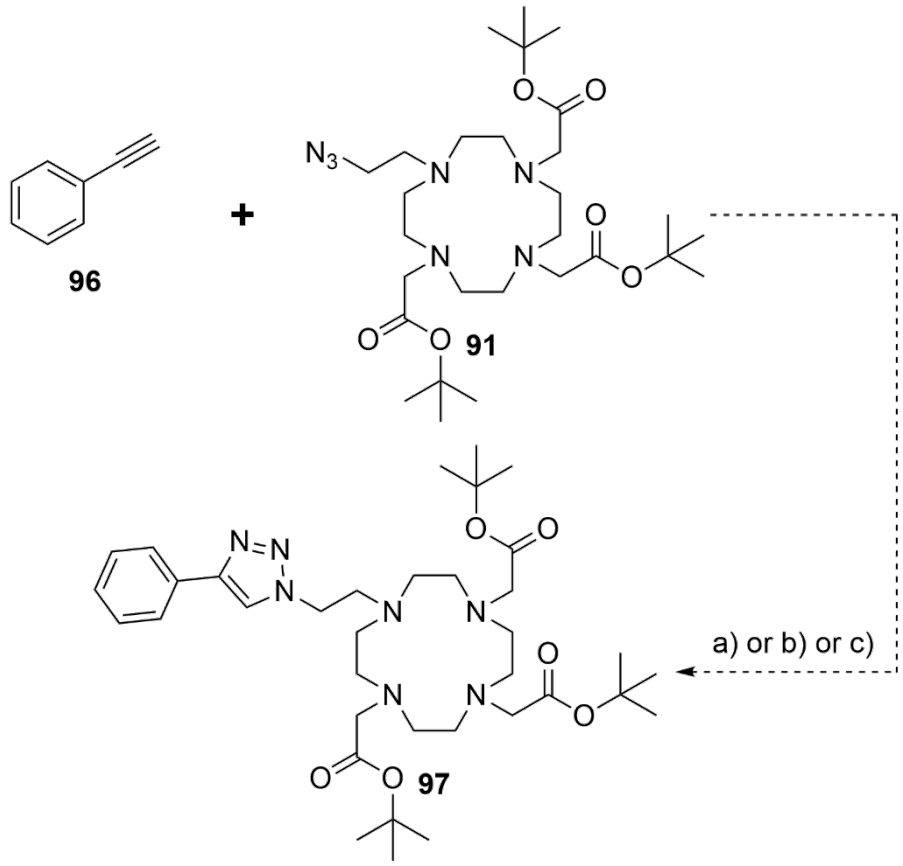

Scheme 3.16: Failed model click coupling of **91** and **96**. Conditions: a) CuI, TBTA, H_2O/THF, 75° C, 16 h; b) CuI, **90**, H_2O/THF, 75° C, 16 h; c) CuI, DIPEA, 80° C, 16 h

All of the attempted click coupling reactions with unprotected cyclen were performed at temperatures that had proved suitable for unprotected cyclam, and it is likely that even higher temperatures would be needed to increase the rate of reaction of cyclen and allow it to take place. This trend is mirrored in the alkylation reactions of cyclam, which proceed at room temperature, whereas the analagous reactions on cyclen require elevated temperatures and longer reaction times to achieve similar results. Click reactions performed on cyclen complexes typically require reaction times on the scale of days at room temperature, whereas on protected cyclam they are usually complete over one night. One previous report has used microwave conditions to perform the click reaction on cyclen complexes at 100° C in MeCN which proceed in reaction times between 15 and 60 min.[288] It is possible that these conditions could be extended to

unprotected cyclen analogues used in this study, however further investigations were not performed, as attention turned to other ways to resolve this issue.

3.8 Attempted click coupling of 6-coordinate lanthanide complexes

It was apparent that performing the CuAAC reaction on unprotected and unmetallated cyclen was not going to deliver a productive path to **89**, so attention turned to reports of single-armed cyclen complexes synthesised *via* click reactions performed on the pre-formed lanthanide complex of cyclen-alkynes.[283-285] This approach had initially been discounted since multiple lanthanide complexes were required for this project, and a divergent route from the unmetallated complex represents the simplest workflow. There is one prior report of the click reaction being performed on complexes of the bis-alkyne ligand **98**[288]; so attempts were made to synthesise lanthanide complexes of **98** via this method. Syntheses of lanthanide complexes of the cyclam analgoue **75** were also attempted using this strategy.

Thus the bis-carboxylate ligand **98** was obtained by sitrring a solution of **85** in a mixture of TFA and DCM at room temperature for 36 hours. Removing the solvent and trituration from a mixture of methanol and diethyl ether gave the bis-trifluoracetate salt of **98** in 90% yield, confirmed using quantitative NMR. The same method was applied to **75** to give the deprotected cyclam ligand **99** as the bis-trifluoroacetate salt in 88% yield.

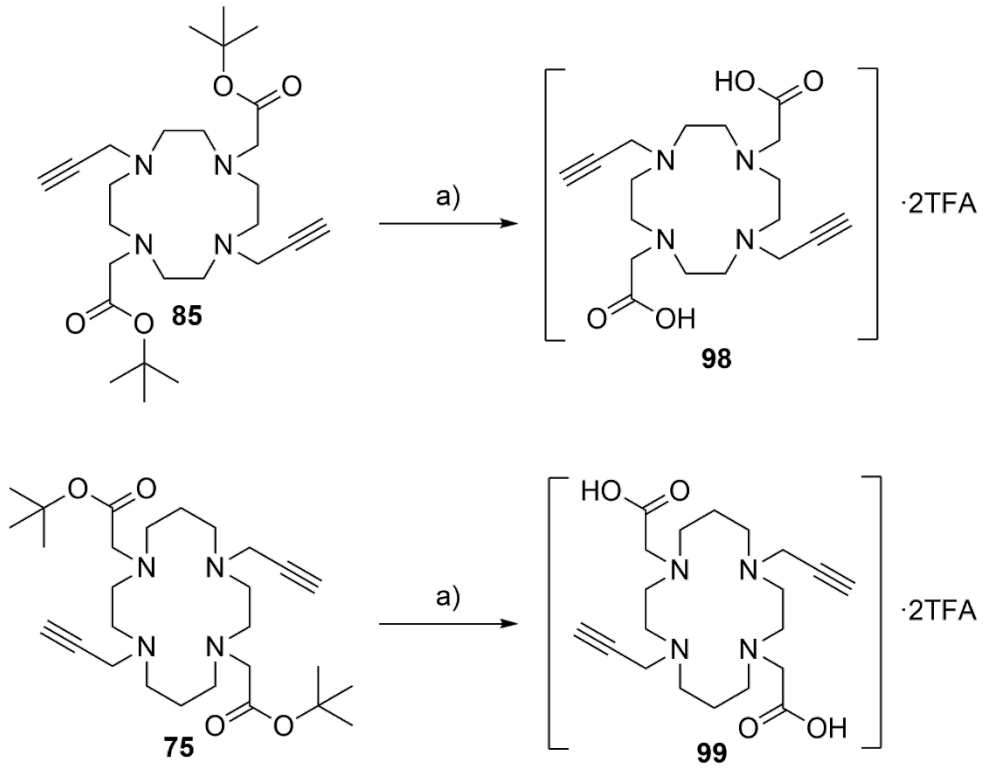

Scheme 3.17: Deprotection of bis-alkyne ligands **85** and **75** using TFA. Conditions: a) TFA/DCM, rt, 36 h, 88-91%.

The synthesis of metal complexes from these ligands was attempted using the conditions reported by Szíjjártó and coworkers.[288] Thus the desired lanthanide chloride was added to a solution of the ligand in methanol and stirred for 30 minutes, after which the pH was adjusted to 5 by the addition of either 1 molar aqueous HCl or 1 molar aqueous NaOH and the reaction was heated to 50° C for 24 hours (**Scheme 3.18**). However, this did not deliver the complete conversion to the product according to LRMS and NMR spectroscopy for either ligand. Switching to the triflate salts, and extending the reaction time did not improve results in a reproducible manner. Extended reaction times in particular resulted in formation of 2:1 ligand:metal complexes. In experiments where the 1:1 complex did form as a major product, the mixture was carried through to the click reaction in the hope that the final complex could be isolated from the mixture after the coupling reaction, however this approach also proved unsuccessful.

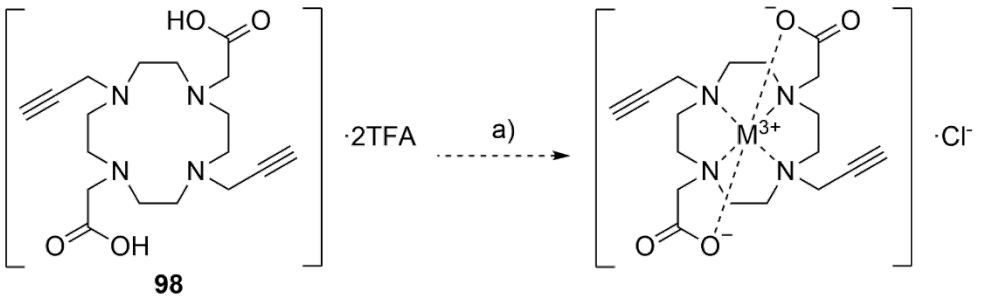

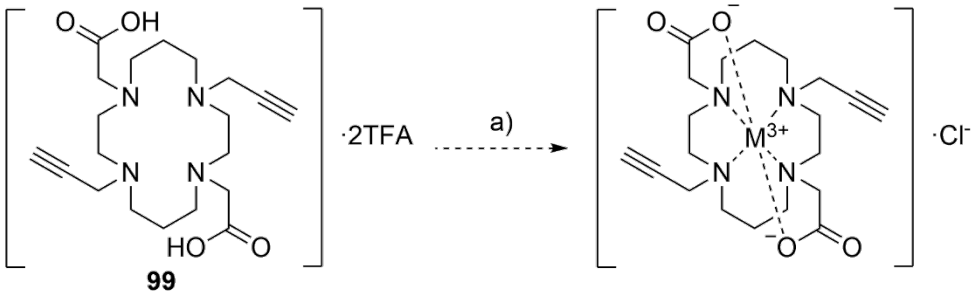

Scheme 3.18: Attempted synthesis of the lanthanide complexes of **98** and **99**. Conditions: a) $LnCl_3$, MeOH, pH 5, 50° C, 24 h where Ln= Y^{3+}, La^{3+}, Eu^{3+} or Gd^{3+}.

3.9 Synthesis of bis-perphenazine cyclen *via* alkylation

As synthesis of **89** *via* a CuAAC reaction of the alkyne-macrocycle conjugate had been ruled out, one alternative synthetic strategy would be to click the perphenazine azide **62** with propargyl alcohol to form **100**, which could then be functionalized and used to alkylate the cyclen intermediate **88**.

The synthesis of **100** was achieved using a slight modification to a procedure previously been developed in the group.[242] Propargyl alcohol and a solution of **62** were added to a solution of copper iodide, sodium ascorbate and DIPEA in acetonitrile and the mixture was stirred under nitrogen for 1 hour. The original procedure calls for an excess of DIPEA and an overnight reaction time, but it was found that the reaction was complete inside 1 hour and that reducing the DIPEA to 1 equivalent still allowed the reaction to take place and simplified purificiation. The crude product was conveniently purified by dissolving in hot acetonitrile and sonicating to induce precipitation, which allowed

isolation of **100** *via* vacuum filtration in 81% yield. This procedure could also be scaled up to a 5 gram scale with no change in percentage yield.

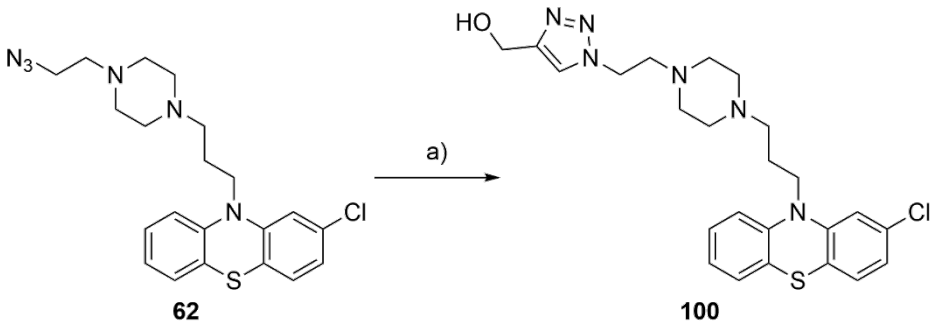

62 100

Scheme 3.19: Click coupling of **62** and propargyl alcohol. Conditions: a) propargyl alcohol, CuI, sodium ascorbate, DIPEA, MeCN, rt, 1 h, 81%.

The next step was to convert **100** to the corresponding alkyl bromide. This was first attempted using phosphorous tribromide, a standard reagent for converting alcohols to alkyl bromides.[295] Phosphorous tribromide was added to a solution of **100** in DCM at 0° C and the solution stirred at ambient temperature, which resulted in the complete decompostion of **100** within 1 hour. It was hypothesised that the hydrobromic acid produced by the reaction could be inducing decomposition of **100**, so the reaction was repeated with the incorporation of triethylamine, however the result was unchanged.

The next attempt to synthesize the alkyl bromide used the Appel reaction, a milder method of brominating an alcohol.[296] Triphenylphosphine, tetrabromomethane and **100** were stirred in DCM overnight, which also resulted in the complete decomposition of **100**. The final method attempted used the Finkelstein reaction on the mesylate derivative of **100** to form the alkyl bromide.[297] A solution of **100** in DCM was cooled to 0° C, treated with mesyl chloride and triethylamine and stirred for 1 hour. As had been seen with the synthesis of **62** *via* a mesylate, there was concomitant conversion of the mesylate to the corresponding alkyl chloride, which was carried through to the bromination step. When the mixture of mesylate and alkyl chloride was treated with

lithium bromide in refluxing acetone, only the alkyl chloride was recovered from the reaction mixture.

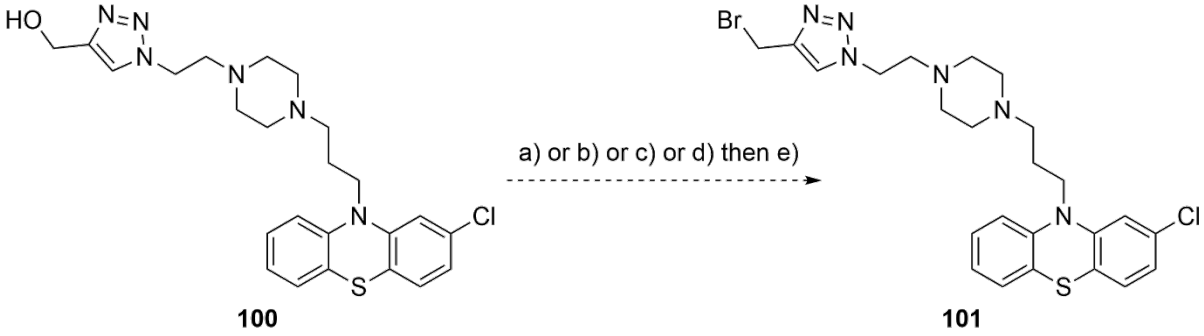

100 101

Scheme 3.20: Attempted synthesis of the alkyl bromide **101**. Conditions: a) PBr_3, DCM, 0° C to rt, 1 h; b) PBr_3, Et_3N, DCM, 0° C to rt, 1 h; c) PPh_3, CBr_4, DCM, rt, 16 h; d) Mesyl chloride, Et_3N, DCM, 0° C to rt, 1 h; e) LiBr, acetone, reflux, 16 h.

It became clear that the issue was likely due not to the reaction conditions, but due to the alkyl bromide being too unstable to isolate. Efforts were then directed towards synthesising and using the mesylate directly. Attempts to alkylate **88** with the mixture of mesylate and alkyl chloride of **92** yielded inconsistent results, returning either a mixture of small amounts of the desired product **89** with the mono-alkylated product, or a mixture of **89** and over-alkylated products. It was apparent that only one of the electrophilic species present (the mesylate and the chloride) could react productively with **88**, and that the conditions used were producing an inconsistent ratio of the two, but it was not clear which of these compounds was enabling the desired reaction.

Synthesis and deployment of the pure mesylate was explored first. Conditions from Tanabe and coworkers were used,[298] which apply tetramethyletheylenediamine (TMEDA) as the base, toluene as solvent and a reaction mixture kept at 0° C throughout. The hydrochloride salt of TMEDA generated in these conditions is insoluble in toluene at low temperatures, minimising attack on the mesylate by chloride anions. However, these conditions still resulted in a small amount of the chloride being generated, but it was considered low enough to assess the efficacy of the mesylate at alkylating **88**.

Unfortunately, no alkylation of **88** was achieved, and compounds arising from the decomposition of the mesylate **103** were observed on LRMS.

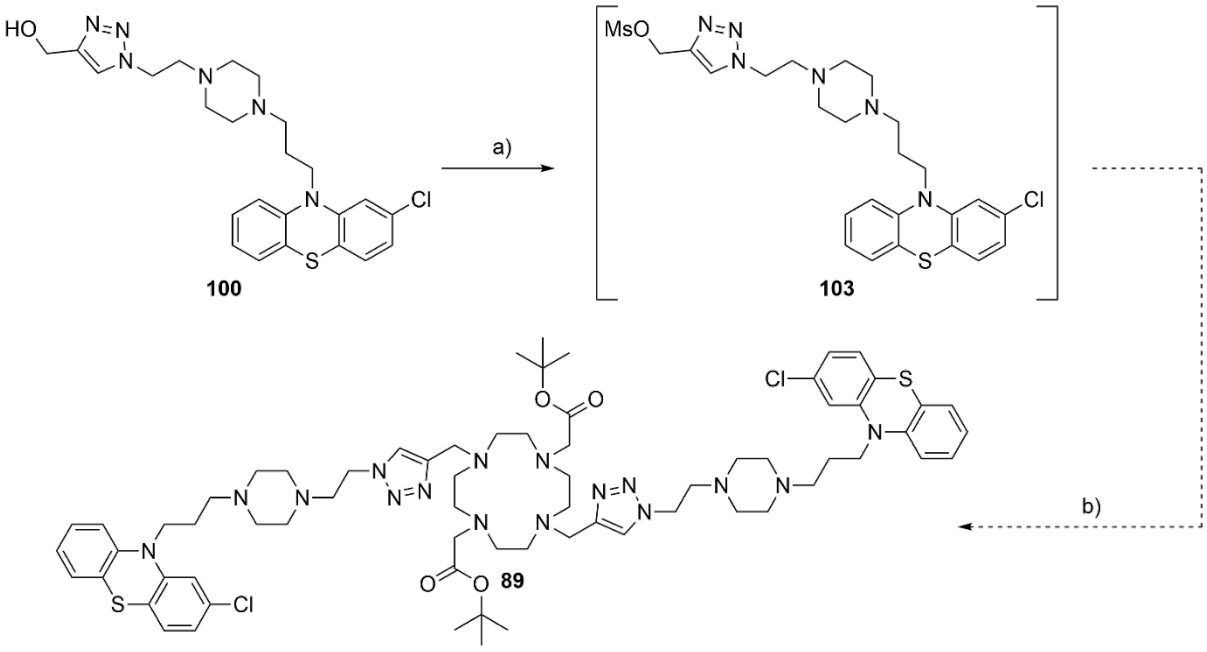

Scheme 3.21: Attempted synthesis of **89** *via* alkylation using **100**. Conditions: a) Mesyl chloride, TMEDA, toluene, 0° C, 1 h; b) **88**, K_2CO_3, MeCN, 50° C, 16 h.

Synthesis of the alkyl chloride was more straightforward: the alcohol **100** was reacted with mesyl chloride and triethylamine in DCM at room temperature overnight, which resulted in complete conversion to the corresponding chloride **104**. The chloride could be isolated, but decomposed within a few hours, so it was instead telescoped into the alkylation step with **88**. The alkylation step was performed in acetonitrile at 50° C using potassium carbonate as base, and converted some of **88** into the desired product **89**. Unfortunately, complete conversion did not occur, and instead a partially alkylated species was formed as the major product, and could not be separated from **89**. Swapping the base for either caesium carbonate or triethylamine, or using DMF as the solvent, slightly improved conversion to **89** but neither of these alternative conditions generated it as the major product. Using an excess of **104** resulted in a complex, intractable mixture, presumed to include several over-alkylated products that were inseperable.

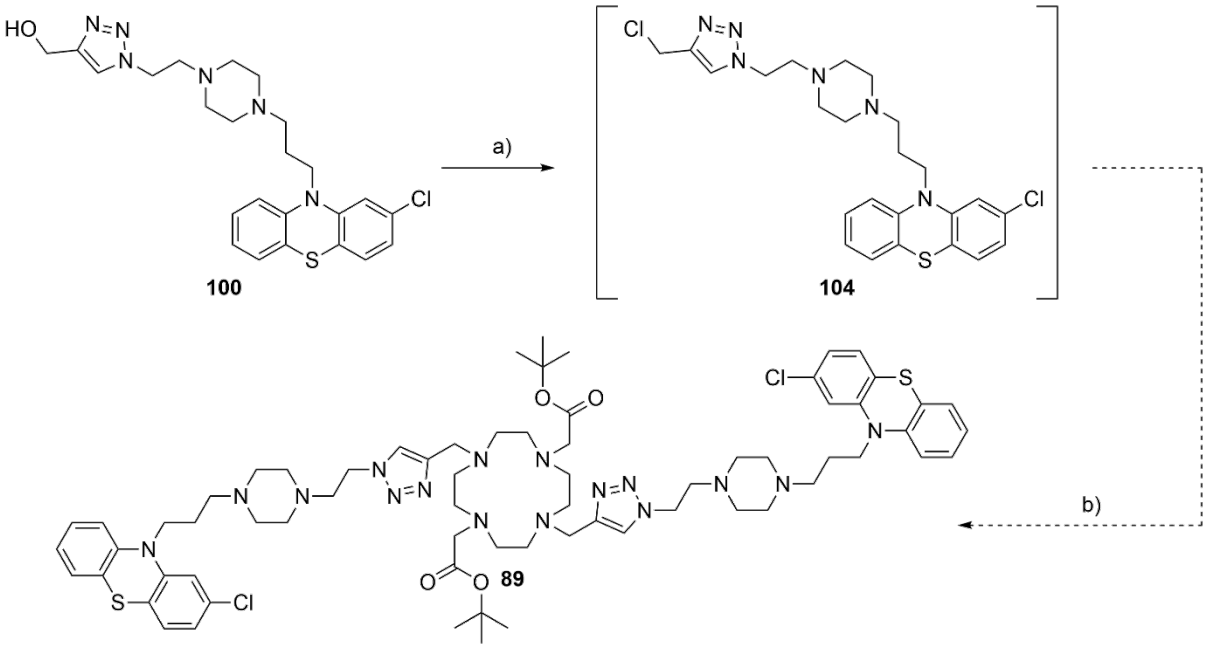

Scheme 3.22: Synthesis of **89** *via* alkylation using **100**. Conditions: a) Mesyl chloride, Et_3N, DCM, rt, 16 h; b) **88**, K_2CO_3, MeCN, 50° C, 16 h.

3.10 Conclusions

A convergent synthetic route to the ligand **74**, and its transition metal complexes **81**, **82** and **83** was developed, affording **74** in an overall yield of 32% and the metal complexes in overall yields of 16 – 19%. The synthesis was made possible by the development of a click-coupling procedure that is effective on unprotected cyclam, which to date has not been reported in literature. While the resulting bis-acetate cyclam scaffold was capable of forming stable complexes with transition metals, the ligand **74** was unable to form stable complexes with lanthanides. Presumably this is due to the flexibility of the cyclam macrocycle, which reduces the pre-organisation required to form a stable lanthanide complex. Unfortunately, the click reaction developed was unable to be extended to a cyclen scaffold, and alternative routes to the synthesis of a cyclen analogue of **74** were unsuccessful. An alternative scaffold is required to synthesise stable lanthanide complexes which can be used to as NMR probes to assess their binding to Aβ.

4. Synthesis and Activity of Single-Armed Perphenazine Complexes

4.1 Rationale

All attempts at synthesising lanthanide complexes with two perphenazine pendant groups had proven unsuccessful. Efforts were instead directed towards the synthesis of a single-armed cyclen complex related to D03A, as there is a wealth of literature demonstrating that such compounds are readily synthesized and can stably coordinate lanthanide ions. The corresponding single-armed cyclam complex **44** had shown similar anti-aggregation activity to the two-armed complex during the initial screening of compounds[299], and was thought to bind $A\beta_{42}$ in a similar manner and thus serve as a useful probe. Hence, single-armed compounds related to **49** such as the cyclen tricarboxylate **105** could thus serve as useful probes of Aβ aggregation in a similar way to the two-armed compounds discussed in previous chapters.

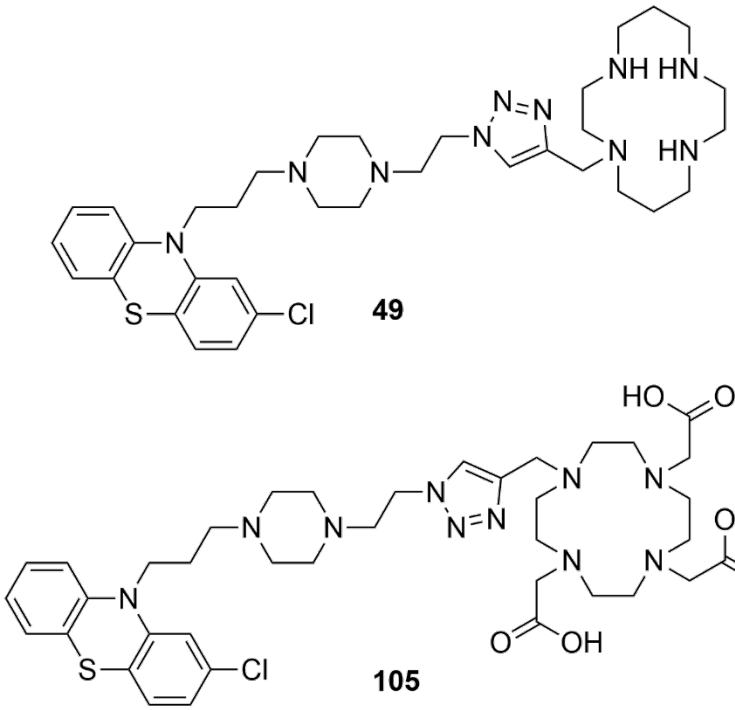

Scheme 4.1: Single-armed cyclen compound **49** previously evaluated as an inhibitor of $A\beta_{42}$ aggregation[299] and its cyclen analogue **105**.

Target ligand **95** could be synthesized from the same perphenazine azide **54** and a mono-propargyl cyclen building block **96**, which can itself be made from cyclen in three steps.

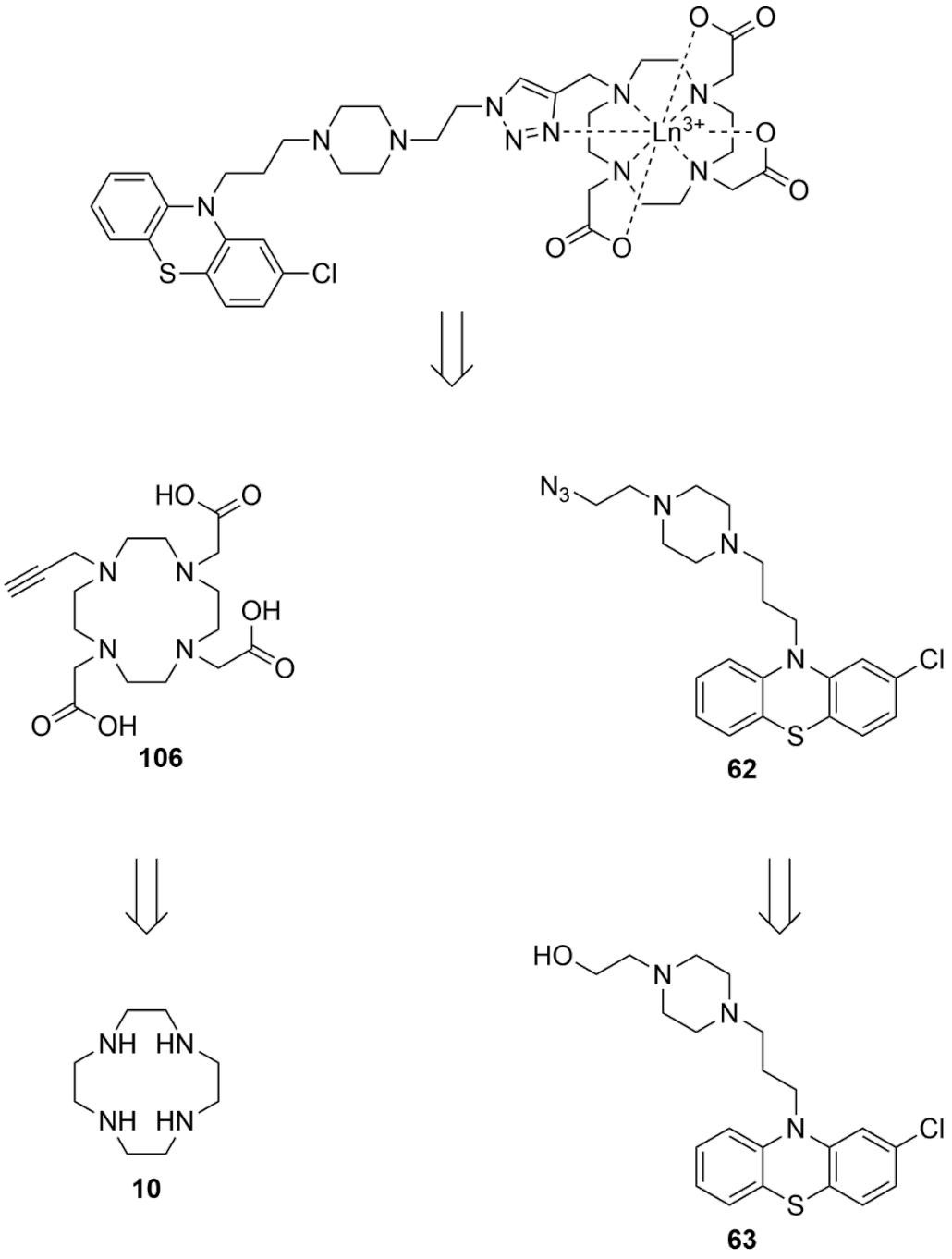

Scheme 4.2: Retrosynthetic scheme for the lanthanide complexes of **105**, derived from **62** and **106**.

4.2 Synthesis of propargyl-cyclen complexes

The synthesis of the alkyne-cyclen pro-ligand **106** began with tri-alkylation of cyclen **10** with *t*-butyl bromoacetate, as described in the previous chapter, which gave the tri-ester **92** in 52% yield. The tri-ester was then alkylated with propargyl bromide using conditions adapted from Junker and coworkers.[284] A suspension of the tri-ester **107** and potassium carbonate in MeCN was treated with a slight excess of propargyl bromide at 0° C and stirred at room temperature overnight. The solids were removed by filtration and the crude product was purified using silica column chromatography to give the alkylated product **107** as a white foam in 72% yield. Deprotection was performed by stirring a solution of pro-ligand **107** in TFA and DCM for 36 hours to afford the TFA salt **108** of ligand **106** in 85% yield.

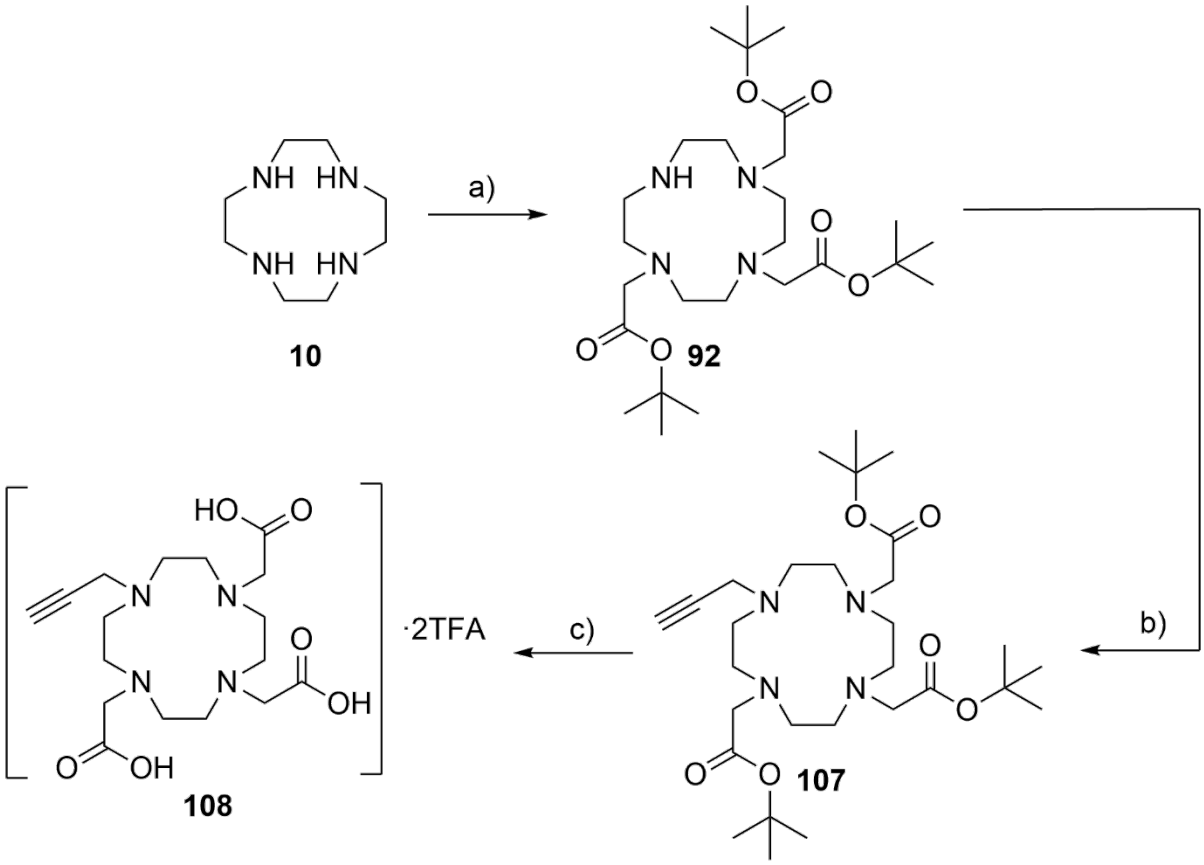

Scheme 4.3: Synthesis of **108** over three steps from cyclen **10**. Conditions: a) *t*-butyl bromoacetate, $NaHCO_3$, MeCN, 0° C to rt, 48 h, 52%; b) propargyl bromide, K_2CO_3, MeCN, rt, 16 h, 72%; c) TFA/DCM, rt, 36 h, 85%.

The next step was to synthesise lanthanide complexes from the deprotected ligand **108**. The metals selected for this were: gadolinium to be used as a purely PRE probe; europium as a probe which could induce PCSs; and yttrium as a diamagnetic reference. The synthesis of the complexes was attempted using standard conditions:[285] a slight excess of the metal triflate was added to a solution of ligand **108** in methanol and stirred for 30 minutes, the pH was then adjusted to 5 with the addition of either 1 molar aqueous HCl or 1 molar aqueous NaOH, and the mixture was then heated to 50° C and stirred for 48 hours. The complexes were then isolated by adjusting the pH to 10 with 1 molar aquoues NaOH, which caused the excess, uncomplexed lanthanide to precipitate from the reaction mixture. The solids were removed by centrifugation and the supernatant was passed through a syringe filter and lyophilised to give the crude products as a white powder, in a yield of 72% for the Y^{3+} complex **109**, 66% for the Eu^{3+} complex **110** and 70% for the Gd^{3+} complex **111**.

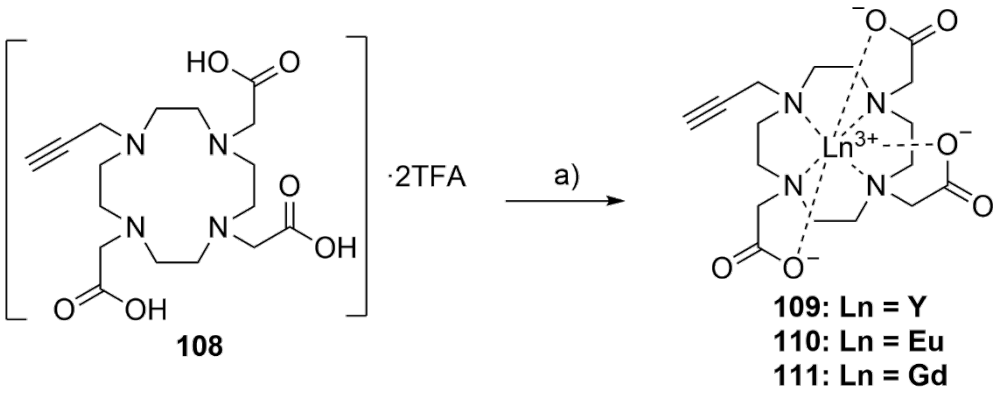

108

109: Ln = Y
110: Ln = Eu
111: Ln = Gd

Scheme 4.4: Metal complexation of **108** using lanthanide triflates. Conditions: a) $Ln(OTf)_3$, MeOH, pH 5, 50° C, 48 h, **109:** 72%, **110**: 66%, **111:** 70%.

The click coupling reaction was then attempted using the Y^{3+} complex **109**, as Y^{3+} is diamagnetic and would not interfere with monitoring the reaction, and characterising the final product, using NMR. A mixture of CuI, TBTA and sodium ascorbate in THF and water was stirred under nitrogen for 30 minutes, followed by the addition of a solution of the alkyne **109** and 1.5 equivalents of the azide **62** in THF and water, and the mixture then was stirred at 50° C overnight. This resulted in the complete conversion of the

alkyne **109** to the click-coupled product **112**, as observed on ESI LRMS. Most of the residual azide **62** could be removed by triturating the product with DCM, but a significant amount of the azide **62** still remained in the crude product. Unfortunately, all efforts to purify the click-coupled complex **112** were unsuccessful, and the product proved too hydrophilic to purify by RP-HPLC. No attempts to synthesize the other click-coupled complexes by this method were made due to the success of synthesising the mono-perphenazine ligand *via* an alternative alkylation (*vide infra*).

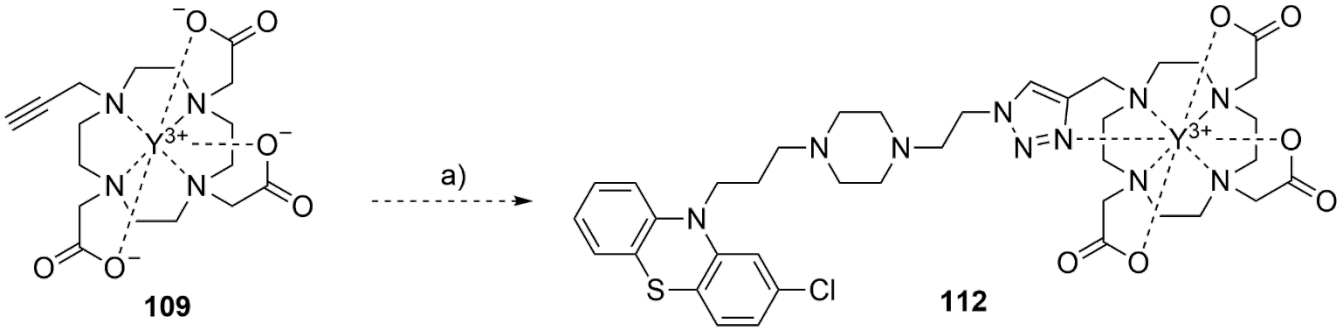

Scheme 4.5: Click coupling of **109** and **62**. Conditions: a) **62**, CuI, TBTA, sodium ascorbate, THF/H_2O, 50° C, overnight.

4.3 Synthesis of mono-perphenazine cyclen *via* alkylation

An alternative strategy was pursued to synthesize the non-metallated ligand **105** as a control compound for ThT assays, since the approach outlined in **Scheme 4.2** does not produce the unmetallated ligand **95** as an intermediate. The alternative route was adapted from the alkylation-based strategy outlined in **Chapter 3**, and uses the alkyl chloride **104** to alkylate the cyclen tri-ester **92** to give pro-ligand **113**.

Alkyl chloride **104** was generated as described in the previous chapter using mesyl chloride and triethylamine in DCM (**Section 3.9**). The alkylating agent **94** was then dissolved in DMF and one equivalent of cyclen tri-ester **92** and an excess caesium carbonate were added, before the mixture was stirred at 50° C overnight. It was found through a solvent and base screen, that only the combination of DMF and caesium carbonate precludes the formation of over-alkylated products in the reaction mixture,

simplifying purification greatly. The product could be conveniently purified by passing through a plug of activated alumina (Brockman grade II) to remove the residual alkyl chloride, giving pure product **113** in a yield of 65%.

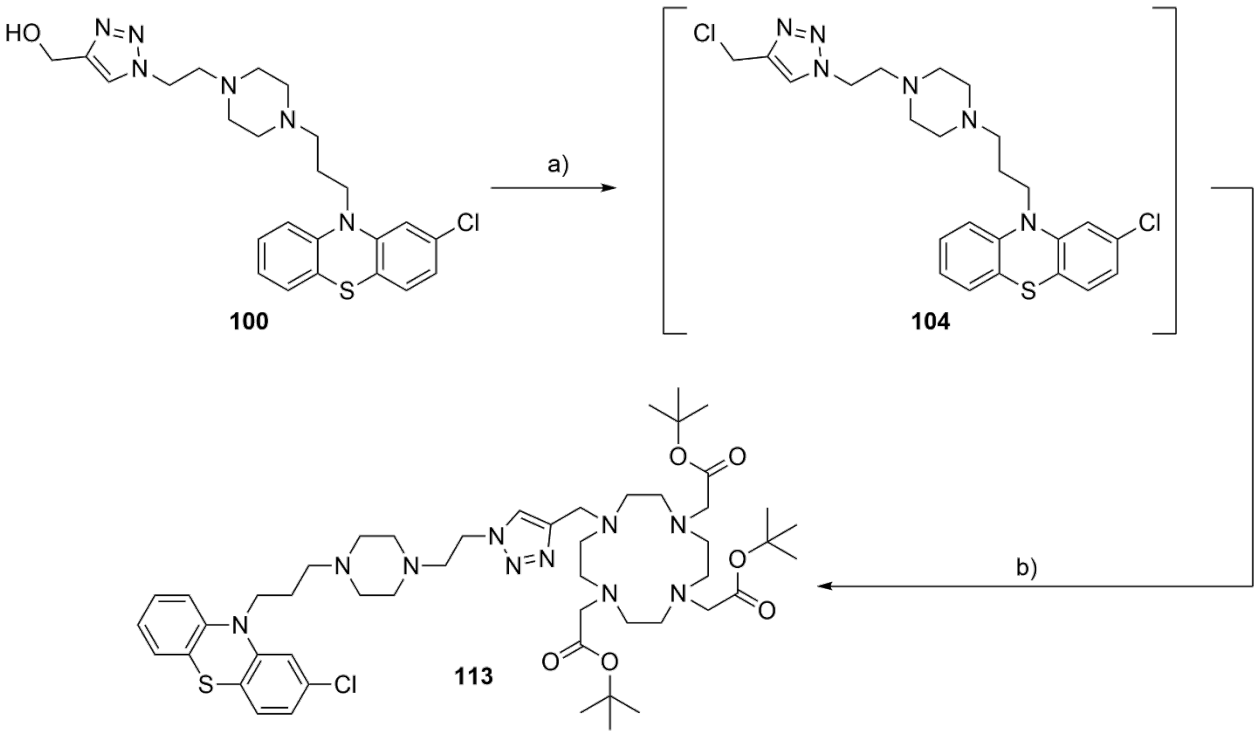

Scheme 4.6: Synthesis of **113** *via* the alkyl chloride **104**. Conditions: a) mesyl chloride, triethylamine, DCM, rt, 16 h; b) **92**, Cs_2CO_3, DMF, 50° C, overnight, 65%.

The deprotection of pro-ligand **113** was carried out using basic conditions: a suspension of tri-ester **113** and a large excess of powdered KOH in THF was refluxed for 4 hours which gave the product **105** in 64% yield. This alkylation-based route to **105** was able to produce enough material to synthesize all desired metal complexes.

The lanthanide complexes were prepared as described as described in Section 4.2 above by heating a solution of the ligand **105** and the appropriate triflate salt for two days, and then isolated *via* precipitation as described above. The perphenazine side arm makes the complexes lipophilic which enabled desalting using reversed-phase chromatography, and the complexes were obtained in yields of 86-99%. Transition metal complexes were also synthesized as alternative Aβ probes by stirring a methanolic solution of ligand **105** with the appropriate metal chloride at 50° C overnight. The complexes were isolated by

concentrating the reaction mixture, redissolving the solids in a small amount of methanol and water, and diluting with diethyl ether to induce precipitation of the complex, which was then isolated *via* centrifugation to give metal complexes **116**-**118** in yields of 64-75%.

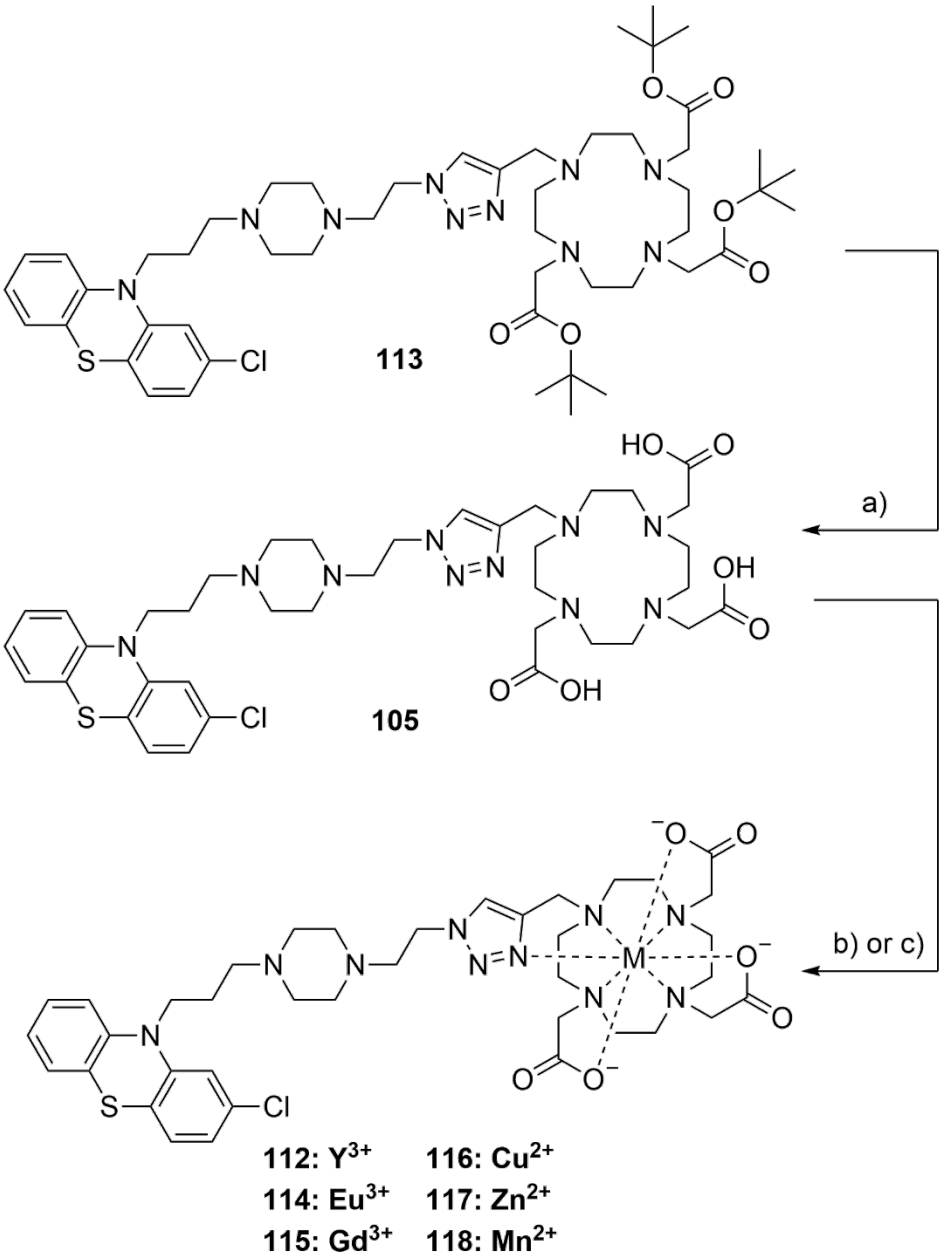

Scheme 4.7: Basic deprotection of **113** to give **105**, followed by the metal complexation with lanthanide and transition metals. Conditions: a) KOH, THF, reflux, 4 h, 64%; b) $Ln(OTf)_3$, MeOH, pH 5, 50° C, 48 h, **112**: 99%, **114**: 87%, **115:** 86%; c) $MCl_2 \cdot xHCl$, MeOH, 50° C, overnight, **116:** 75%, **117:** 74%, **118:** 68%.

4.4 Synthesis of single-armed perphenazine-cyclam compounds

A series of control compounds were synthesised to bridge the structural gap between the double-armed cyclam lead compound **58,** and the single-armed cyclen complexes derived from **105**. The single-armed cyclam ligand **49** and its Cu(II) and Zn(II) complexes were chosen as these would be used to confirm the anti-aggregation activity first measured in the initial screen of compounds prior to this current work[300], and so ensure that similar activity is maintained when only a single perphenazine pendant is present on the ligand scaffold.

A tri-acetate/mono-perphenazine substituted cyclam ligand **119** was also synthesized, so the influence of acetate arms could be compared directly to the parent compound **58**. Metal complexes of the tri-acetate cyclam **119** were not synthesized, on the expectation that, as with **58**, the unmetallated ligand and its metal complexes would have similar activity to each other, so any change in activity wrought by the introduction of pendant acetates would be apparent from comparing the ligand **119** with the parent compound **58**.

The first set of compounds synthesized were single-armed cyclam **49**, and its Cu(II) **50** and Zn(II) **51** complexes. This synthesis began with the Boc-protection of cyclam using three equivalents of Boc-anhydride in DCM, which gave **120** in 65% yield. The tri-protected macrocycle was then alkylated with propargyl bromide in acetonitrile to give **121** as a white solid in 69% yield. Click coupling was performed as described in previous chapters using CuI and TBTA in refluxing THF and water to give **122** in 55% yield.

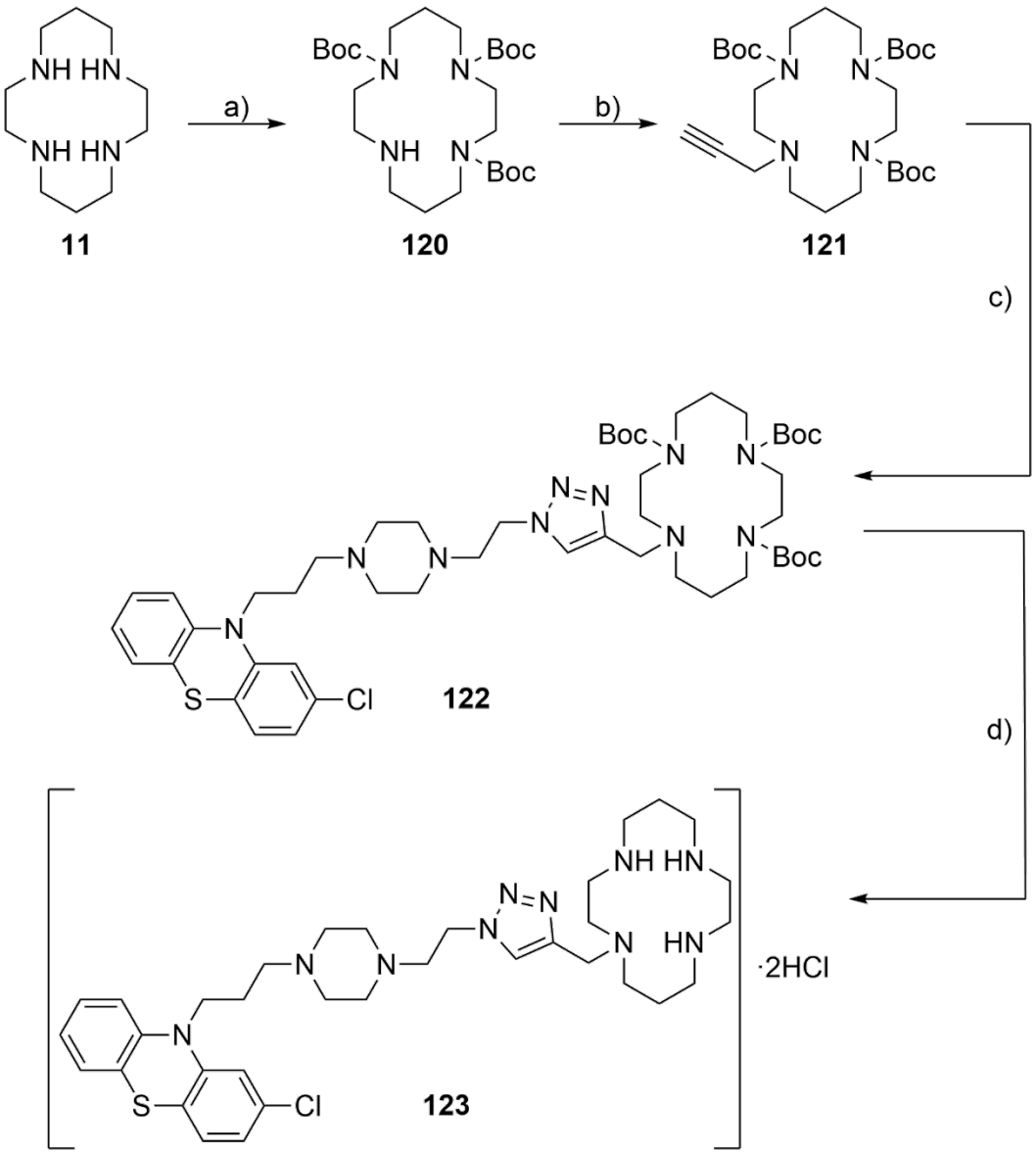

Scheme 4.8: Synthesis of cyclam ligand **123**. Conditions: a) Boc-anhydride, DCM, -15° C to rt, 16 h, 65% yield; b) propargyl bromide, Na_2CO_3, MeCN, reflux, 16 h, 69%; c) **62**, CuI, TBTA, sodium ascorbate, THF/H_2O, reflux, 3 h, 55%; d) HCl/dioxane, rt, 1 h, 69%.

Boc-deprotection using 4 M HCl in dioxane gave the HCl salt **123** of **49** in 69% yield. The metal complexes were then prepared by treatment of this HCl salt **123** with Ambersep 900 OH form to obtain a methanolic solution of the freebase **49**, followed by addition of the desired metal chloride to afford the complexes in yields of 36-44%.

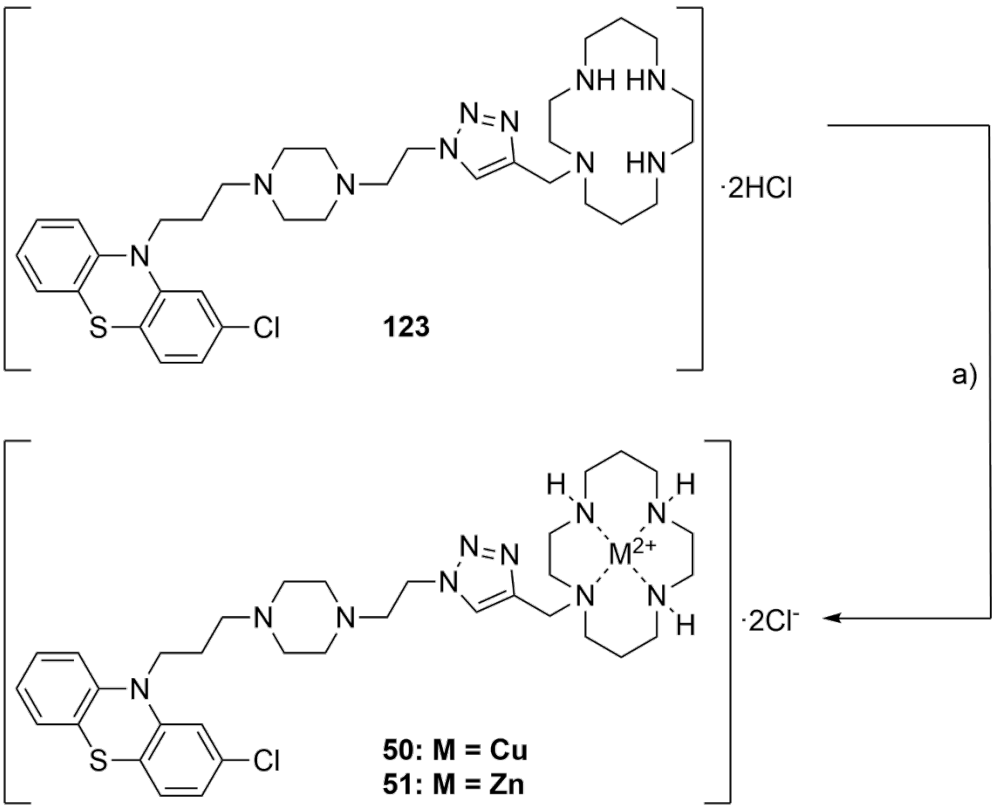

Scheme 4.9: Synthesis of the Cu^{2+} **50** and Zn^{2+} **51** of **49**. Conditions: a) Ambersep 900 OH form, then $CuCl_2 \cdot 2H_2O$ or $ZnCl_2 \cdot 4H_2O$, MeOH, rt, 4 h, **108**: 44%, **109**: 36%.

Synthesis of the cyclam-triacetate ligand **119** began with the alkylation of cyclam using *t*-butyl bromoacetate according to a procedure from Lalli and coworkers.[301] Three equivalents of *t*-butyl bromoacetate were added dropwise to a suspension of **11** and sodium hydrogen carbonate in acetonitrile at 0° C. The mixture was then allowed to warm to room temperature and stirred for 48 hours, which gave **124** in 38% yield. Treatment with propargyl bromide in acetonitrile at room temperature gave **125** in 45% yield, which could be subjected to standard click coupling reaction with **62** to give **126** in 55% yield. The *t*-butyl esters were then cleaved under basic conditions to afford **119** in 79% yield.

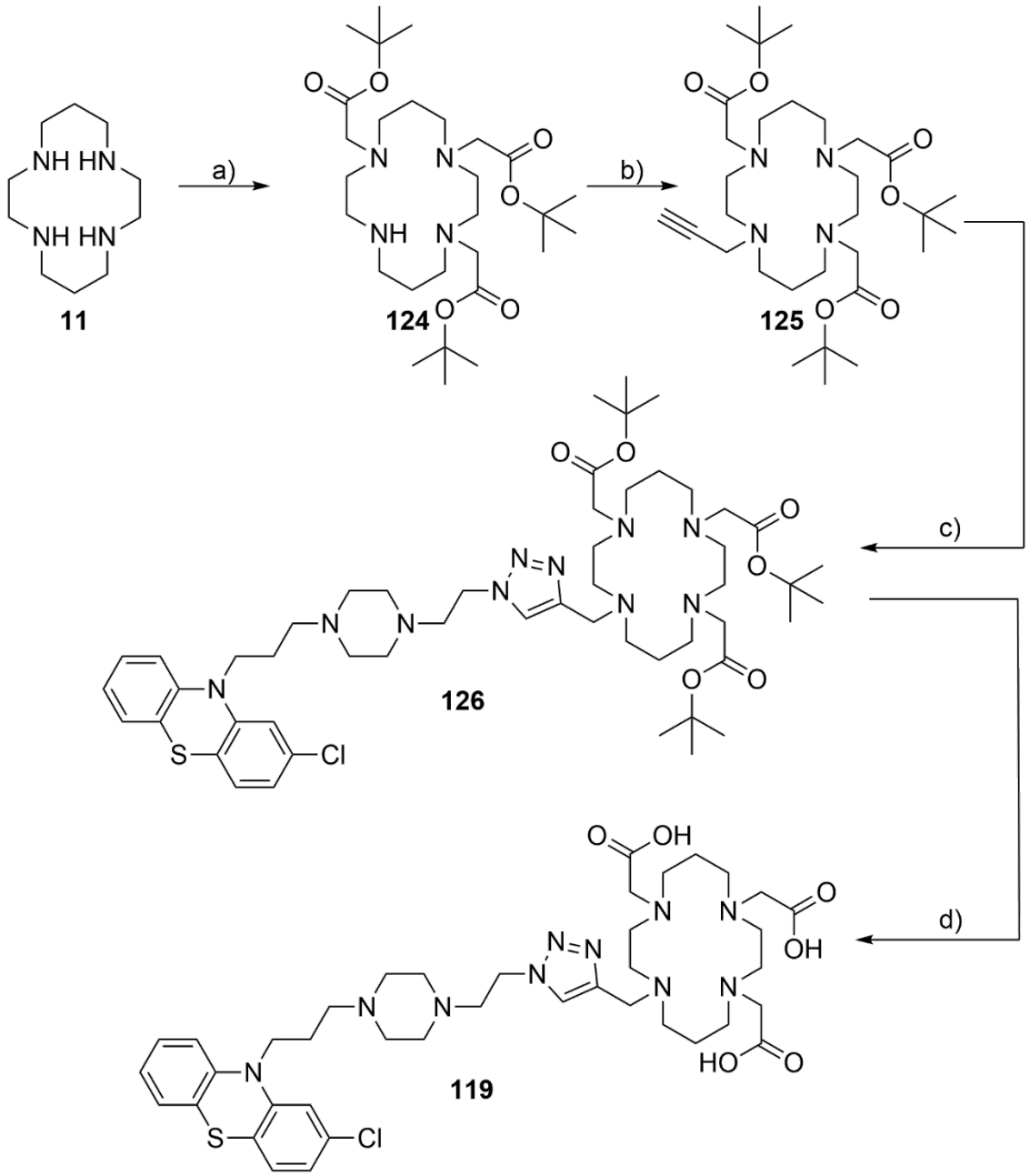

Scheme 4.10: Synthesis of **119** from cyclam. Conditions: a) *t*-butyl bromoacetate, $NaHCO_3$, MeCN, 0° c to rt, 48 h, 38%; b) propargyl bromide, K_2CO_3, MeCN, rt, 16 h, 45%; c) **62**, CuI, TBTA, sodium ascorbate, THF/H_2O, reflux, 55%; d) KOH, THF, reflux, 4 h, 75%.

4.5 Thioflavin T Assays

The lanthanide complexes derived from the cyclen ligand **95** are sufficiently different from the structure of the original bis-perphenazine cyclam probe **58** and its complexes that the anti-aggregation activity needed to be confirmed using ThT assays, before the cyclen derived PRE probes were used in NMR experiments. Thus, the interactions of the following compounds with Aβ were assessed using ThT assays: the single-armed cyclen derived ligand **105**, its transition metal and lanthanide complexes; the single-armed cyclam ligand **123** and its Cu^{2+} **50** and Zn^{2+} **51** complexes; the single-armed, tri-acetate cyclam compound **119**; and the original bis-perhpenazine cyclam compounds **58-60** as positive controls. It was invisaged that the bis-perphenazine complexes derived from **58** would be tested as well, but these proved insoluble in the assay conditions, which also precluded their use as NMR probes. Tested compounds were used at a 10:1 ratio of inhibitor to $A\beta_{42,}$ a ratio that would give a definite indication of their anti-aggregation activity. ThT assay data for these compounds are presented in **Figure 4.11**.

Several contrasting behaviours were observed in the results with these compounds:

- The lead compounds **58-60** behaved as previously reported, maintaining their anti-aggregation activity in these assays, evinced by the complete loss of ThT fluorescence (**Figure 4.11A**).
- The single-armed, unmetallated ligands **49**, **109**, and **115** all caused an apparent increase in aggregation, characterised by a shortening of the lag time and a significantly stronger plateau fluorescence compared to Aβ alone (**Figure 4.11B** and **C**). Shortening of the lag time is a strong indicator that these compounds are still altering the aggregation pathway of $A\beta_{42}$, but ThT assays alone cannot determine which stage of the aggregation process is affected, and whether the resulting aggregates are fibrillar or amorphous.

- Curiously, the Cu^{2+} and Zn^{2+} complexes of **49** (**50** and **51**) and **105** (**116** and **117**) caused a severe reduction in ThT fluorescence (**Figure 4.11 B** and **C**), similar to the behaviour of bis-perphenazine compounds **58-60**. The Mn^{2+} complexes of **49** (**119**) and **105** (**118**), as well as all lanthanide complexes of **105** (**112**, **114**, **115**) caused an increase in fluorescence similar to the unmetallated ligands.

This contrasting influence of the different metals on ThT fluorescence is intriguing. This is not thought to be due to differences in the affinity of the Cu^{2+} and Zn^{2+} complexes with Aβ compared to the unmetallated ligand. While the presence of a coordinating metal ion has been shown to alter the conformation of cyclam complexes in the solid state,[206, 233] the perphenazine-conjugates are thought to be highly flexible in solution, particularly with regard to the orientation of the pendant groups, due to the unconstrained alkyl chains in the perphenazine pendants. Thus, a change of the metal was thought unlikely to cause changes in conformation that enable stronger binding to $A\beta_{42}$.

Instead, we hypothesise that the absence of a ThT signal observed in some of the experiments is due to fluorescence quenching by the complexes, given that metal ions can significantly alter photophysical pathways and cause fluorescence quenching. Investigating this hypothesis further, the UV-Vis spectra of the compounds confirmed that while the metal ion cause slight changes to the UV-Vis spectra, there was no spectral overlap with the absorbance or emission wavelength of ThT (**Figure 4.12**).

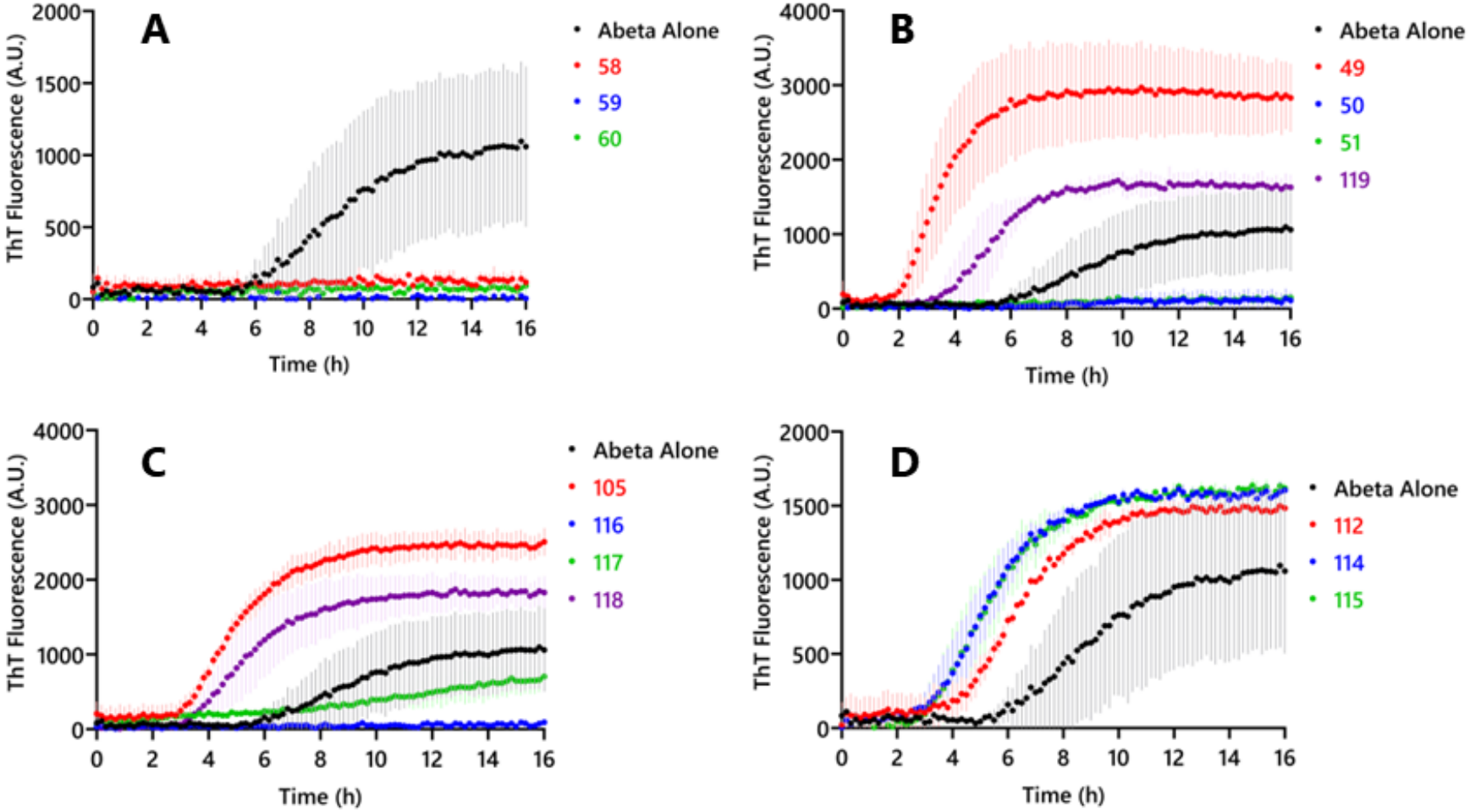

Figure 4.11: Effects of the cyclam control compounds and the cyclen PRE probe compounds on the aggregation of $A\beta_{42}$. 10 μM $A\beta_{42}$ with 1% DMSO against 50 μM compound. **A:** Compounds **58**, **59** and **60**. **B**: Compounds **49**, **50**, **51** and **119**. **C**: Compounds **105**, **116**, **117** and **118**. **D:** Compounds **112**, **114** and **115**.

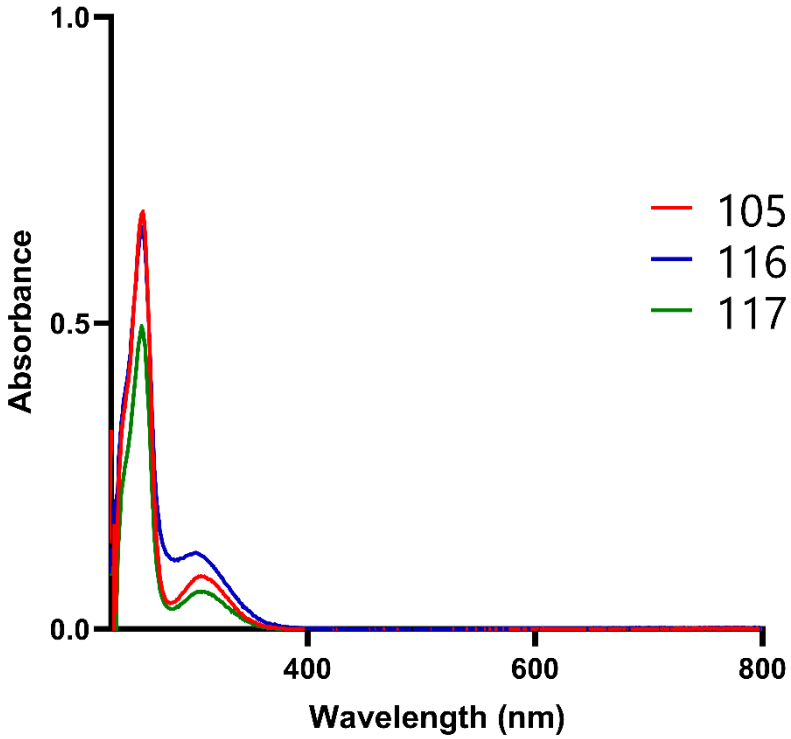

Figure 4.12: The UV-Vis spectra of ligand **105** and its Cu^{2+} **116** and Zn^{2+} **117** complexes. Note the absence of absorbance above 400 nm, which precludes any inner-filter effects with ThT fluorescence.

To confirm whether fluorescence quenching does occur with these probes, fluorescence experiments were performed titrating the unmetallated ligand **105**, the Cu^{2+} complex **116** and the Mn^{2+} complex **118** against assembled $A\beta_{42}$ fibrils incubated with ThT and Stern-Volmer plots were constructed. These experiments were performed batchwise using a platereader, as Aβ fibrils are insoluble and difficult to manipulate in solution.

The kinetics of dynamic quenching, where an excited-state fluorophore is quenched by the collision of a quencher molecule, is described by the Stern-Volmer relationship (**Equation 4.1**).[302]

$$\frac{\phi_0}{\phi} = \frac{\tau_0}{\tau} = 1 + K_{SV}[Q]$$

Equation 4.1: The Stern-Volmer equation, where ϕ_0 and τ_0 are the quantum yield and luminescence lifetime of the fluorophore in the absence of a quencher (Q), ϕ

and τ are the quantum yield and luminescence lifetime in the presence of Q, K_{SV} is the Stern-Volmer constant, which is the product of the kinetic quenching constant k_Q and τ_0.

In most cases the ratio of fluorescence intensity is equal to the ratio of quantum yields in the presence and absence of the quencher. The equivalence of the ratio of quantum yields and the ratio of luminescence lifetimes only holds for dynamic quenching. Static quenching occurs when a non-fluorescent, ground-state adduct forms between the quencher and fluorophore. When the concentration of the unbound fluorophore is negligible compared to that of the adduct, pseudo-Stern-Volmer kinetics are observed (**Equation 4.2**).[302] In other cases of static quenching, deviations from the linear relationship are observed.

$$\frac{I_0}{I} = 1 + K_a[Q]$$

Equation 4.2: Where K_a is the association constant for the formation of the complex and [Q] is equal to the total concentration of the quencher.

The titration demonstrated that the unmetallated ligand **105** and the Mn^{2+} complex **118** cause very mild quenching of ThT fluorescence in the presence of Aβ fibrils (**Figure 4.12**). A straight line can be fitted to the Stern-Volmer plots for these two compounds, which can indicate either dynamic quenching or static quenching, but fluorescence lifetime measurements are required to confirm which mode of quenching is occurring.[302] The Cu^{2+} complex **116** was shown to strongly quench ThT fluorescence (**Figure 4.12**), while the Stern-Volmer plot displays downward curvature. Such a deviation from the Stern-Volmer relationship indicates the formation of an adduct – *i.e.,* static quenching – with a high association constant.[303] However, it is not possible from these current data to determine whether the Cu^{2+} complex **96** is forming an adduct with ThT itself, or with the $A\beta_{42}$ fibrils, to induce this quenching

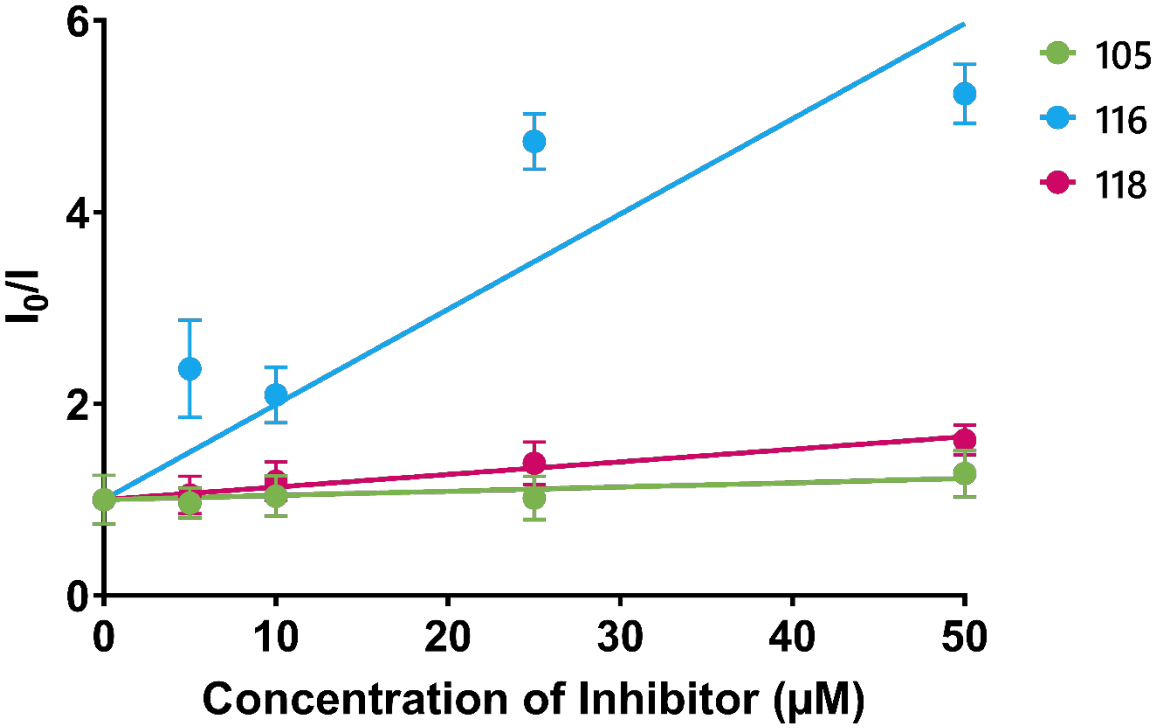

Figure 4.13: Static Stern-Volmer plot of the free ligand **105**, Cu^{2+} complex **116** and Mn^{2+} complex **118** against 10 μM $A\beta_{42}$ and 40 μM ThT in 20 mM NaH_2PO_4. Excitation wavelength: 440 nm. Emission wavelength: 480 nm.

While the Stern-Volmer plots derived from fluorescence intensity measurements provide a good indication of the mode of fluorescence quenching occurring, confirming the quenching mode and elucidating the mechanism requires further experiments. These would include fluorescence lifetime measurements, as well as measuring the redox potentials for both the quenching compounds and fluorescent ThT-$A\beta_{42}$ fibril complex.[302-304] Additionally, the effect of these quenching probes on $A\beta_{42}$ aggregation needs to be investigated further using orthogonal experiments- for example the aggregation could be measured using circular dichroism. Unfortunately, time constraints preclude these further experiments as part of the current study.

4.6 NMR Experiments

ThT assays with the single-armed cyclen ligand **105**, and its complexes, demonstrated that these compounds do interact with $A\beta_{42}$, so these could serve as useful NMR probes to investigate the binding of these complexes to $A\beta_{42}$. Therefore, the ability of Gd^{3+} probe **115** to induce PRE on $A\beta_{42}$ was investigated.

^{15}N-$A\beta_{42}$ was overexpressed and purified by Dr. Sarah Ball using a protocol adapted from Habchi and coworkers[90] and stored in freeze-dried aliquots at -80 °C until required, thawed by standing at room temperature and used immediately. Protein NMR experiments were performed in conjunction with A/Prof Ann Kwan in the School of Life and Environmental Sciences at the University of Sydney.

The concentration of ^{15}N-$A\beta_{42}$ was difficult to determine accurately as the measured absorbance at 280 nm overestimated the protein concentration by approximately twofold when compared to NMR spectra; because of this, the concentration of ^{15}N-$A\beta_{42}$ used in these experiments was estimated from NMR data and is approximate.

The HSQC spectrum of ~10 μM uniformly ^{15}N-labelled $A\beta_{42}$ alone was compared to the spectrum of ^{15}N-labelled Aβ42 in the presence of an equal concentration of the diamagnetic Y^{3+} complex **112** and a spectrum of ^{15}N-labelled $A\beta_{42}$ in the presence of an equal concentration of the paramagnetic Gd^{3+} complex **115**. As expected from the NMR experiments with the original bis-perphenazine compound **58**, no change was observed in the HSQC of $A\beta_{42}$ upon the addition of the diamagnetic complex **112**. Unfortunately, the addition of the paramagnetic complex **115** also did not affect the intensity of any of the signals in the HSQC spectrum compared to the diamagnetic reference.

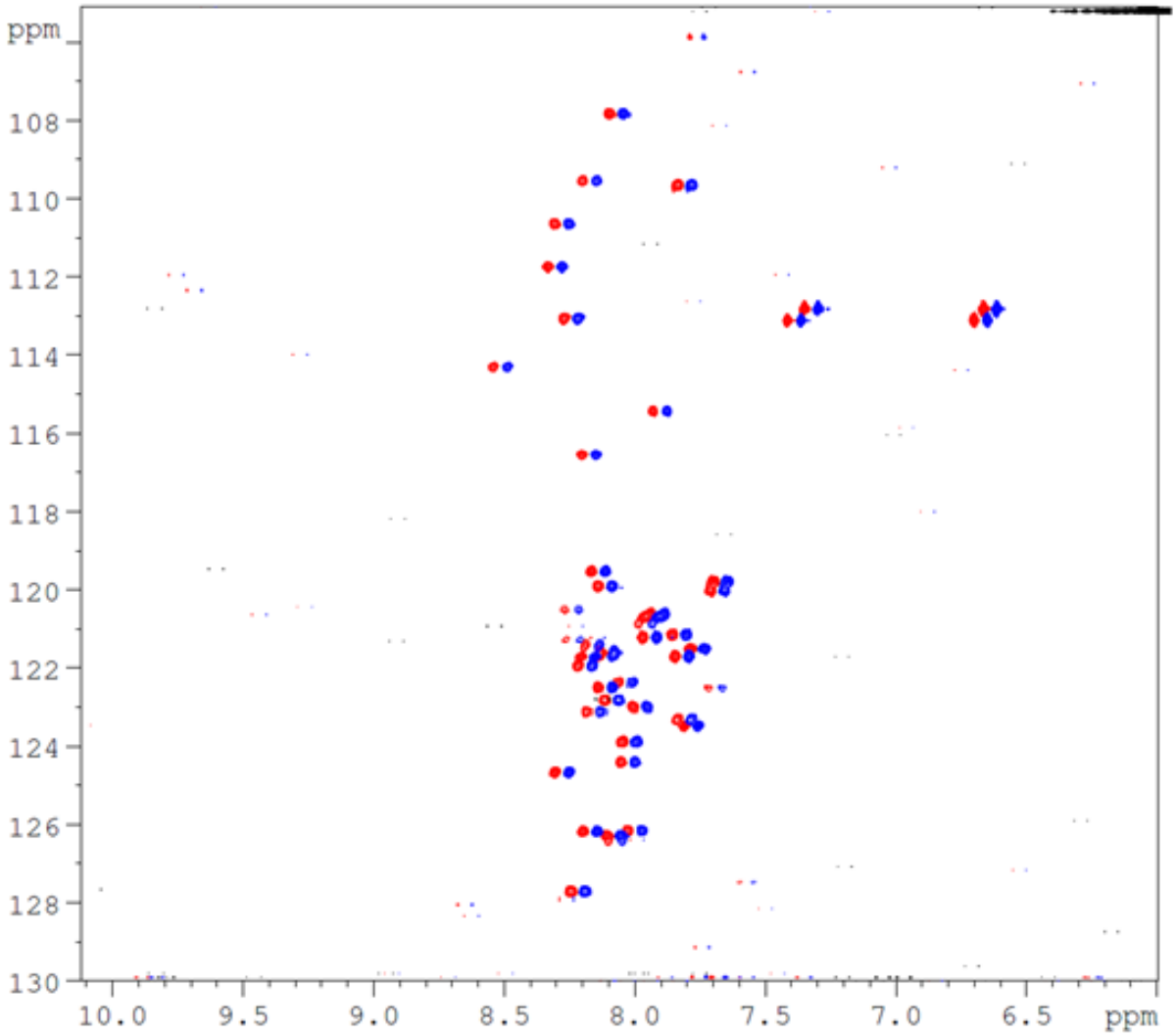

Figure 4.14: Overlay of the ^{15}N-^{1}H HSQC spectra of 10 μM ^{15}N-labelled Aβ$_{42}$ (red) and 1:1 Aβ$_{42}$:**112** (blue). Spectra were recorded in 20 mM NaH_2PO_4, 10% D_2O and 0.1% sodium trimethylsilylpropanesulfonate (DSS) at 600MHz at 4° C. Experiments were performed with the assistance of A/Prof. Ann Kwan.

The apparently similar (lack of) impact of the two metal complexes on the NMR spectra of Aβ$_{42}$ could be due to several reasons. First, it may be that the paramagnetic and diamagnetic compounds do not bind to Aβ$_{42}$ in a specific manner, so at the concentration used the paramagnetic probe **115** is not able to produce PRE on specific residues. In this case, a higher concentration of **115** relative to Aβ$_{42}$ would result in PRE affecting the residues that are predominantly solvent-exposed.[160] Another possibility is that the binding of **115** to Aβ$_{42}$ is much weaker than anticipated, so that at equimolar

concentration of **115** and $A\beta_{42}$, the bound form of $A\beta_{42}$ is only present in such a small proportion (<2%) that it is not detectable using this methods.[305] Alternatively, exchange between **115** and $A\beta_{42}$ may in fact occur at a slower rate than expected, so the PREs cannot be observed for this reason. Or it is possible that **115** interacts with oligomeric species which are not seen in the NMR spectra, rather than the monomeric $A\beta_{42}$.[306]

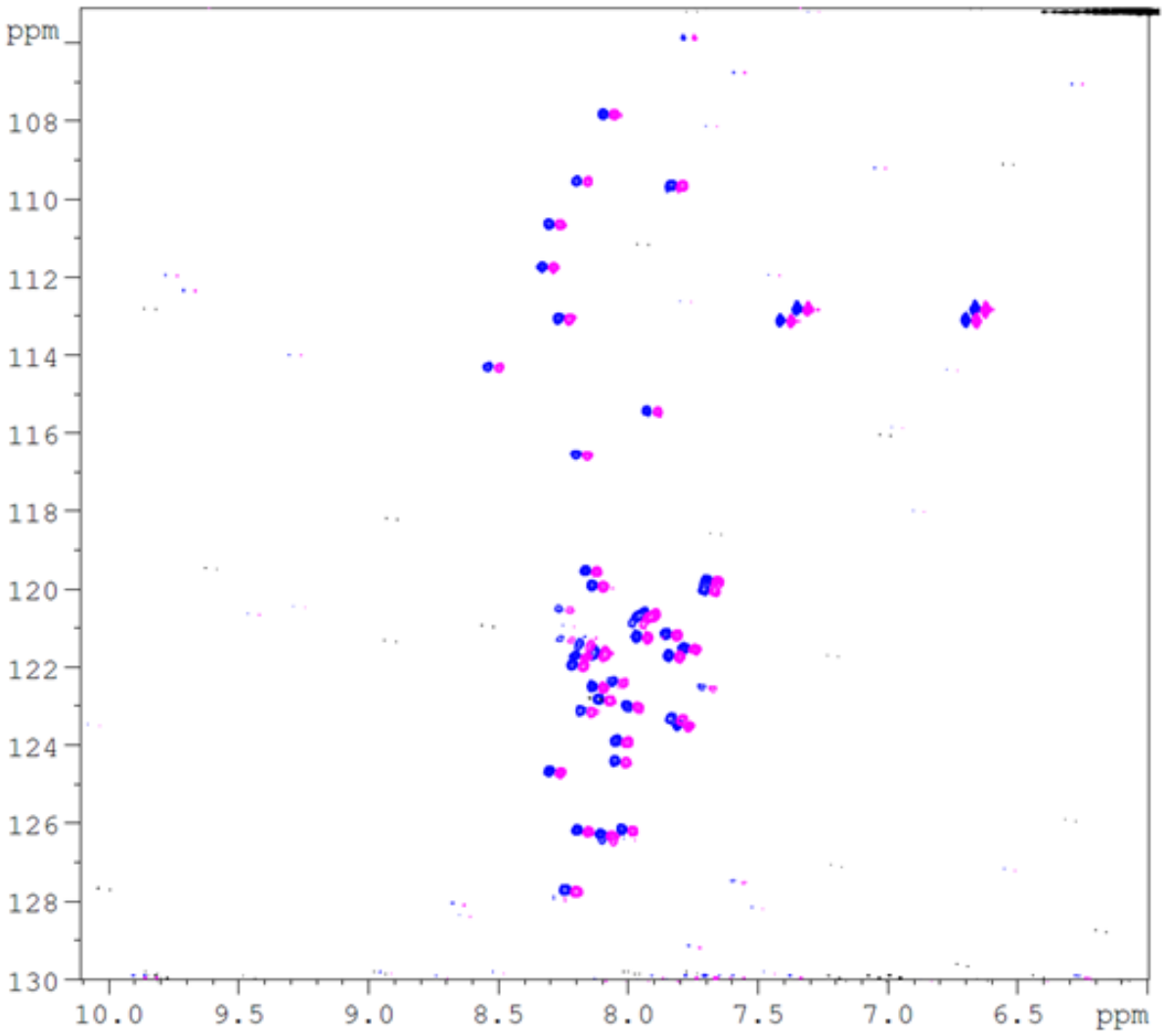

Figure 4.15: Overlay of the ^{15}N-^{1}H HSQC spectra of 1:1 $A\beta_{42}$:**112** (blue) and 1:1 $A\beta_{42}$:**115** (magenta). Spectra were recorded in 20 mM NaH_2PO_4, 10% D_2O and 0.1% (DSS) at 600MHz at 4° C. Experiments were performed with the assistance of A/Prof. Ann Kwan.

Further experiments are required to test these different possibilities, and more fully characterise the interaction between $A\beta_{42}$ and the probes derived from **105**. These

experiments are discussed in further detail in Chapter 5, and could involve the use of a number of different ratios of probe to $A\beta_{42}$, using metals with anisotropic χ tensors to induce PCSs, or the use of alternative NMR experiments that use saturation transfer to measure chemical exchange on longer timescales. Unfortunately, time pressures and constraints on the supply of ^{15}N-labelled $A\beta_{42}$ prevent these experiments from being included in the current study.

4.7 Conclusions

An efficient route to the one-armed cyclen ligand **105** was developed, which could be used to synthesize a series of transition metal and lanthanide complexes with an overall yield of 14-21%. The anti-aggregation activity of these complexes against $A\beta_{42}$ was then assessed using ThT fluorescence assays. An interesting contrast in behaviour was uncovered for these single-armed complexes, with the Cu^{2+} and Zn^{2+} complexes strongly quenching ThT fluorescence, while complexes with other metals, and the ligands themselves, interrupted the aggregation process of $A\beta_{42}$, and resulted in an increase in ThT fluorescence. While these fluorescence assays showed that these compounds can interact with $A\beta_{42}$ and alter aggregation, HSQC NMR experiments with equal ratios of $A\beta_{42}$ and the paramagnetic probe Gd^{3+} complex **115** did not result in the hoped-for PRE manifesting on the spectrum, which meant that further insight into how these complexes interact with $A\beta_{42}$ was not forthcoming.

5. Conclusions and Future Work

5.1 Conclusions

The bis-perphenazine compound **58** and its Cu^{2+} **59** and Zn^{2+} **60** complexes (**Figure 5.1**) have been shown to bind directly to monomeric $A\beta_{42}$ and redirect the assembly of $A\beta_{42}$ from fibrils to amorphous aggregates.[299] These compounds reduce the toxicity caused by $A\beta_{42}$ aggregation in SH-SY5Y cells likely because they prevent the formation of toxic $A\beta_{42}$ oligomers. Small molecules that interact directly with monomeric $A\beta_{42}$ are rare, with few examples reported in the literature,[91] but are key to understanding the role that Aβ plays in the development of AD, and to determine whether targeting Aβ is an effective method for treating AD. The mode of binding **58** to monomeric $A\beta_{42}$ could not be determined by chemical shift analysis in NMR experiments conducted previously. As an alternative approach, paramagnetic probes were envisaged which could induce PRE on the NMR behaviour of Aβ.

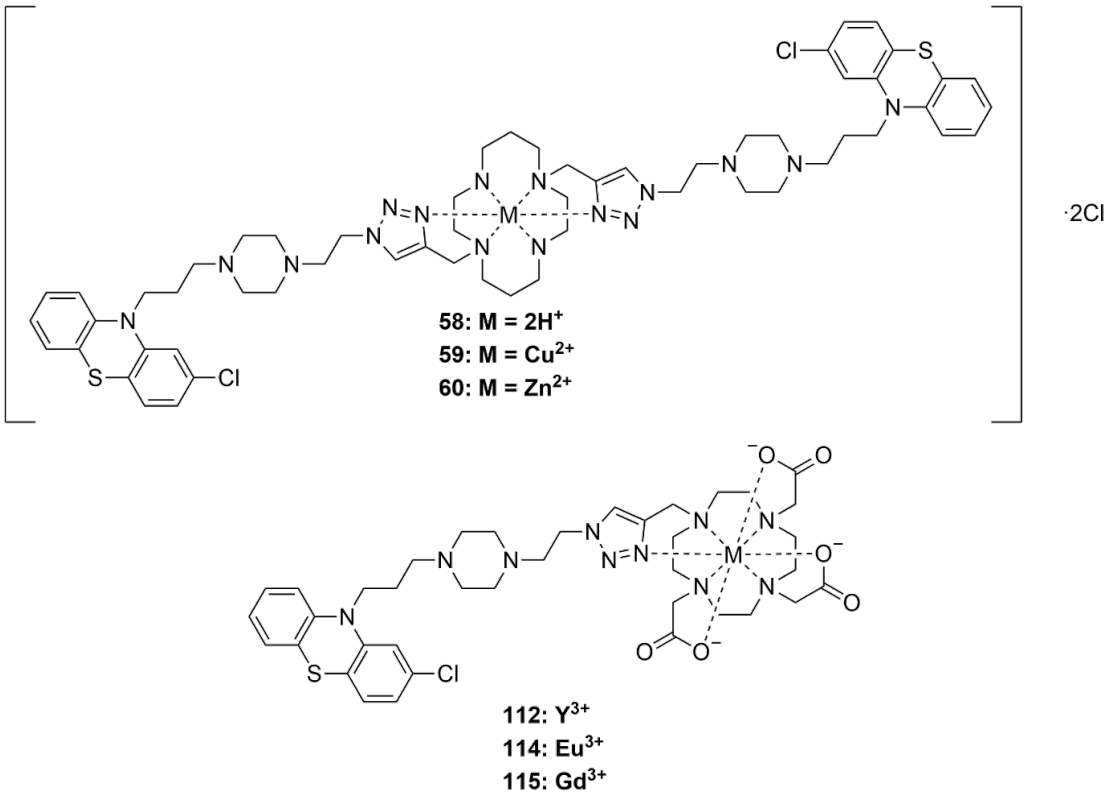

Figure 5.1: Structures of the original bis-perphenazine compounds **58-60**, and the cyclen-lanthanide PRE probes **112**,**114** and **115**.

A wide range of chemistry was directed towards the synthesis of various cyclam- and cyclen-based ligands and metal complexes incorporating 1 or 2 perphenazine pendants and a complement of carboxylate groups. Ultimately, a fruitful route was developed to metal complexes **112**, **114** and **115** (**Figure 5.1**) derived from the cyclen ligand **105** enabling access to the varied paramagnetic effects of lanthanides in complexes that interacted with Aβ. ThT assays confirmed that these modified probes also interacted with Aβ, although some of them were shown to quench the fluorescence of ThT. The ability of the Gd^{3+} complex **115** to induce PRE on $A\beta_{42}$ was assessed using HSQC experiments, however the experiment did not produce meaningful results.

5.2 Future Work

Initial attempts to identify how the family of compounds described in this work interact with $A\beta_{42}$ using intermolecular PREs was unsuccessful. As the next step, titration experiments of the Gd^{3+} complex **115** against $A\beta_{42}$ at a range of concentrations would provide insight into whether the observed absence of PRE arises because the binding of **115** to $A\beta_{42}$ is non-specific,[307] or because the exchange between the bound and unbound state of the probe is occurring too slowly to observe PREs.[306]

One of the key benefits of developing a lanthanide-chelating ligand like **105** is that the one ligand can be used to synthesize probes with a range of magnetic properties arising from the differing magnetic behaviour of different lanthanides. Compounds with anisotrpic χ tensors such as the Eu^{3+} complex **114** can induce PCSs, which opens another way to investigate how these probes bind to $A\beta_{42}$. While these data are more difficult to process, PCSs provide distance and angular information, and can therefore provide a more precise structural picture of the interaction. Moreover, PCS probes are able to provide information on dynamics on timescales up to milliseconds.[308]

If it is the case that the exchange between these probes and $A\beta_{42}$ is too slow for PRE, alternative NMR experiments available to help identify how the probes bind to $A\beta_{42}$.

These include Carr-Purcell-Meiboom-Gill (CPMG) relaxation experiments, which are useful for studying processes in moderate to fast exchange regime, and chemical exchange saturation transfer (CEST) experiments which can be used to study slow-exchange regimes.[309-311] The use of lanthanide probes such as the Eu^{3+} complex **1l4** would complement CEST experiments, as they can be used to enhance sensitivity with paraCEST experiments.[309]

The unexpected results of the ThT fluorescence assays described in Chapter 4 open another area of future investigation. A number of experiments should be performed in order to fully characterise the mechanism of fluorescence quenching. These include fluorescence lifetime measurements, and variable temperature measurements, which are important in confirming whether static or dynamic quenching is occurring.[302]

Fluorescence excitation and emission spectra are needed to deduce whether Förster resonance energy transfer (FRET) or Dexter energy transfer (DET) is occurring. Measuring the reduction and oxidation potentials of the metal complexes and the $A\beta_{42}$-ThT complex should make it possible to ascertain if PET is occurring.[304]

In addition, an orthogonal method to measuring Aβ aggregation, such as circular dichroism, is also needed to confirm if the kinetics of Aβ aggregation occurs as the ThT assays suggest.[63] Together these experiments will determine if the ThT assay is a reliable method for measuring the kinetics of $A\beta_{42}$ aggregation in the presence of exogenous compounds, and whether alternative methods needs to be developed to study the assembly of Aβ under these circumstances.

6. Experimental Procedures

6.1: General Materials and Instrumentation:

Anhydrous solvents were obtained from a PureSolv MD 7 solvent purification system having been passed through anhydrous alumina columns. Commercially available reagents and solvents were purchased from Sigma Aldrich, Merck, Alfa Aesar, Matrix Scientific, Ajax Finechem, Combi-Blocks or Ambeed and were used without purification unless otherwise specified. Automated flash column chromatography was performed using a Biotage Isolera One. Silica chromatography was performed using refillable cartridges obtained from either Biotage or Santai Technologies, packed with silica gel 60 (0.040–0.063 mm) obtained from either Merck or Chemsupply. Reversed-phase chromatography was performed using reusable pre-packed cartridges of C18 silica, obtained from either Biotage or Santai Technologies. Neutral alumina (Brockmann I) was obtained from Sigma-Aldrich and was deactivated by the addition of 5% w/w water prior to use. TLC was performed on Merck silica gel 60 F_{254} pre-coated aluminium plates (0.2 mm) and visualised with UV (254 and 365 nm) followed by staining with potassium permanganate.

Melting points were recorded on an Optimelt 100 automated melting point apparatus and are uncorrected. Infrared spectra were recorded on a Bruker ALPHA FT-IR spectrophotometer (ZnSe or diamond ATR) using OPUS software. Low resolution mass spectrometry was recorded on a Bruker amazon SL mass spectrometer using electrospray ionization. LRMS measurements are reported with observed mass-to-charge ratios and their assignment. High resolution mass spectrometry was performed on a Bruker 7T fourier-transform ion cyclotron resonance using ESI. Nuclear Magnetic Resonance spectroscopy on small molecules was carried out on either a Bruker AVANCE 300 (^{1}H at 300 MHz, ^{13}C at 75 MHz) or a Bruker AVANCE III 500 (^{1}H at 500 MHz, ^{13}C at 126 MHz). NMR experiments on $A\beta_{42}$ were carried out on a Bruker AVANCE III HD spectrometer

(600 MHz). Spectra obtained were processed using MestReNova v 12.0.0-20080. Deuterated solvents were obtained from either Cambridge Isotope Laboratories or Sigma-Aldrich. Spectra were referenced to either TMS or residual solvent peaks.

6.2: General Synthetic Procedures:

Safety note: Sodium azide and organic azides are potentially explosive and all samples should be handled with caution. At no point should halogenated solvents be used in any procedure involving sodium azide.

General Synthetic Procedure A: CuAAC "Click" reaction using TBTA.

Copper iodide (0.1 equiv.), TBTA(0.1 equiv.) and sodium ascorbate (1.5 equiv.) were placed in a three-neck flask and the vessel was flushed with N_2. A degassed mixture of 4:1 THF:water (3 mM) was added to the flask and the mixture was stirred under N_2 for 30 min, resulting in a homogeneous, yellow solution. To this solution was added a solution of the desired alkyne (1 equiv., 0.3 M) and azide (1.1–2.2 equiv., 0.3–0.6 M) and the mixture was heated to 75° C. The mixture was stirred under N_2 until the reaction was complete by TLC, typically 3–4 h. The mixture was allowed to cool to rt under N_2 and quickly added to a separatory funnel containing EtOAc and a mixture of equal parts EDTA (50 mM) in NH_3/NH_4Cl buffer (2 M, pH 9.5) and brine. The aqueous phase was collected, and the organic phase washed twice more with an identical buffer/brine mixture. The organic phase was dried over magnesium sulfate and concentrated under reduced pressure to give the crude product.

General Synthetic Procedure B: Base-mediated *tert*-butyl ester deprotection.[281]

To a solution of the *tert*-butyl ester in THF (0.07 M) was added powdered KOH (25 equiv.) and the mixture was heated to reflux and stirred for 4 h. The mixture was neutralized with 1 M aqueous HCl and the THF was removed under reduced pressure. The crude product in water was loaded directly onto a reversed-phase cartridge for purification *via*

automated flash column chromatography (gradient 10% MeOH in water to 100%). The fractions containing the desired product were lyophilised to give the product as a powder.

General Synthetic Procedure C: Acid mediated *tert*-butyl ester deprotection using TFA.[284]

The *tert*-butyl ester was dissolved in a 1:1 mixture of DCM and TFA (0.05 M) and stirred at rt for 36 h. The mixture was concentrated under reduced pressure. Residual TFA was removed by dissolving the residue in toluene (10 mL) and concentrating under reduced pressure, repeating the process three times. The residue was then dissolved in a minimal amount of methanol and the product precipitated by diluting 5-fold with diethyl ether. The solid was washed with diethyl ether (3 × 5 mL) and dried *in vacuo* to afford the product as the TFA salt.

General Synthetic Procedure D: Acid-mediated Boc deprotection using HCl in dioxane.[246]

To the Boc-protected amine was added an excess of HCl in dioxane (4 M) at 0° C. The mixture was warmed to rt and stirred for up to 1 h. The mixture was concentrated under reduced pressure to give a solid. The crude product was purified *via* reversed-phase automated flash column chromatography (gradient of 10% MeOH in water to 100% MeOH). The fractions containing the desired product were lyophilised to afford the product as the HCl salt.

6.3: Synthetic Procedures

1,4,8,11-Tetraazatricyclo[9.3.1.14,8]hexadecane[238] 64

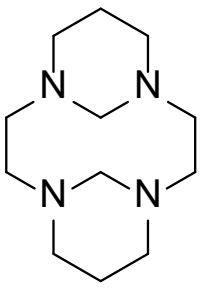

To a solution of cyclam (0.954 g) in water (60 mL) was added formaldehyde (37% in water, 0.9 mL) at 0 °C and the mixture was stirred for 1 h. The solid was isolated *via* vacuum filtration, washed with ice-cold water (20 mL) and dried in vacuo to give the product as a white powder (0.888 g, 83%). **m.p.**: 106–108 °C (lit = 106–108 °C). **^{1}H NMR** (300 MHz, Chloroform-d): δ 5.43 (d, 2H, 10.8), 3.15 (d, 4H, 9.66), 2.94–2.76 (m, 6), 2.71–2.53 (m, 4H), 2.46–2.19 (m, 6H), 1.18 (d, 2H, *J* 13.3). **LRMS** (ESI+): *m/z* 224.91 $[M+H]^+$. Spectroscopic data were in agreement with literature values. [238]

Di-tert-butyl 4,11-di(prop-2-yn-1-yl)-1,4,8,11-tetraazacyclotetradecane-1,8-dicarboxylate[235] 61

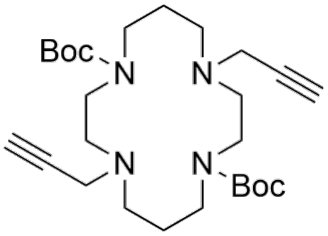

To a solution of bridged cyclam (0.967 g, 4.318 mmol) in acetonitrile (40 mL) was added propargyl bromide (80% in toluene, 1.6 mL, 14.72 mmol) and the mixture was stirred at rt overnight. The solids were isolated via vacuum filtration, washed with acetonitrile (20 mL) and dried briefly in vacuo. The solids were suspended in NaOH (2.5 M, 40 mL) and MeOH (40 mL) and stirred at rt for 3 h. This was followed by the addition of a solution of Boc anhydride (2.1 mL, 9.141 mmol) in methanol (6.0 mL) and the mixture was stirred at rt overnight. Another portion of Boc anhydride (1.1 mL, 4.570 mmol) in methanol (3.0 mL) and the mixture was stirred for 4 h. The resulting precipitate was isolated *via* vacuum filtration, washed with water (3 × 10 mL) and dried in a desiccator overnight to give a white powder (1.046 g, 88%). **m.p.** 149–152 °C(lit. 153-155 °C). **^{1}H NMR** (300 MHz, Chloroform-d): 3.48–3.21 (m, 12H), 2.72–2.59 (m, 4H), 2.58–2.46 (m, 4H), 1.78–1.65 (m, 4H), 1.46 (s, 18H). **LRMS** (ESI+): *m/z* 477.36 $[M+H]^+$. Spectroscopic data were in agreement with literature.[235]

10-(3-(4-(2-Azidoethyl)piperazin-1-yl)propyl)-2-chloro-10H-phenothiazine[299] 62

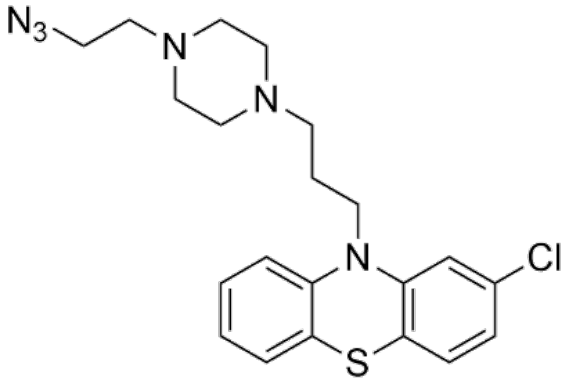

To an oven-dried three neck flask was added perphenazine (1.076 g, 2.606 mmol) and the vessel was flushed with N_2. To this was added anhydrous THF (5 mL), followed by DPPA (0.62 mL, 2.884 mmol) and DBU (0.43 mL, 2.966 mmol) and the mixture was heated to 50° C and stirred overnight. The reaction was cooled to rt, diluted with brine (50 mL) and extracted with toluene (3 × 50 mL). The combined extracts were dried over magnesium sulfate and concentrated under reduced pressure to give an amber oil. The oil was purified via flash column chromatography (basic alumina, 10% EtOAc in hexanes) to give the product as a yellow oil (0.7644 g, 68%). **^{1}HNMR** (500 MHz, Chloroform-d): 1.19 (qn, 2H, *J*6.85), 2.39–2.53 (m, 8H), 2.55 (t, 2H, *J*6.3), 3.31 (t, 2H, *J* 6.75 hz)), 3.87 (t, 2H, *J* 6.70 hz), 6.84–6.93 (m, 4H), 6.98 (d, 1H, *J* 8.1), 7.06–7.16 (m, 2). **^{13}CNMR** (500 MHz, Chloroform-d): 24.21, 45.32, 48.20, 53.17, 55.40, 57.08, 115.81, 122.22, 122.87, 123.48, 124.74, 127.41, 127.49, 127.86, 133.20, 144.49, 146.47. **FTIR** (ATR) ν_{max}/cm^{-1}: 2940, 2809, 2097, 1566, 1455, 1407, 1279, 1242, 1158, 1140, 1033. **LRMS** (ESI+): *m/z* 429.19 $[M+H]^+$ **HRMS** (ESI+): *m/z* calc. for $C_{21}H_{26}ClN_6S^+$ 429.16227 $[M+H]^+$, found 429.16195.

10-(3-(4-(2-Azidoethyl)piperazin-1-yl)propyl)-2-chloro-10H-phenothiazine 62 (Alternative procedure).

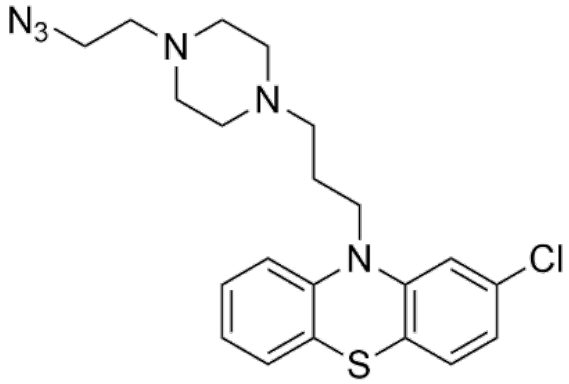

To an oven-dried flask was added a solution of perphenazine (5.024 g, 12.44 mmol) in anhydrous THF (30 mL), followed by triethylamine (1.9 mL, 13.63 mmol). The flask was cooled to 0 °C and mesyl chloride (1.1 mL, 14.21 mmol) was added dropwise. The mixture was allowed to warm to rt and stirred for 3 h. The mixture was diluted with ethyl acetate (40 mL) and washed with water (60 mL). The aqueous phase was extracted twice more with ethyl acetate (40 mL). The combined organic extracts were dried over magnesium sulfate and concentrated under reduced pressure to give a beige foam. The foam was dissolved in anhydrous DMF (50 mL) and to this solution was added sodium azide (1.275 g, 16.61 mmol). The mixture was heated to 60º C and stirred overnight. The solution was diluted with toluene (100 mL) and washed with water (300 mL). The aqueous phase was extracted twice more with toluene (100 mL), and the combined organic extracts were washed with water (5 × 50 mL), followed by brine (150 mL). The organic extracts were dried over magnesium sulfate and concentrated under reduced pressure to give the product as a yellow gum (4.148 g, 78%).

Di-tert-butyl 4,11-bis((1-(2-(4-(3-(2-chloro-10H-phenothiazin-10-yl)propyl)piperazin-1-yl)ethyl)-1H-1,2,3-triazol-4-yl)methyl)-1,4,8,11-tetraazacyclotetradecane-1,8-dicarboxylate[299] 72

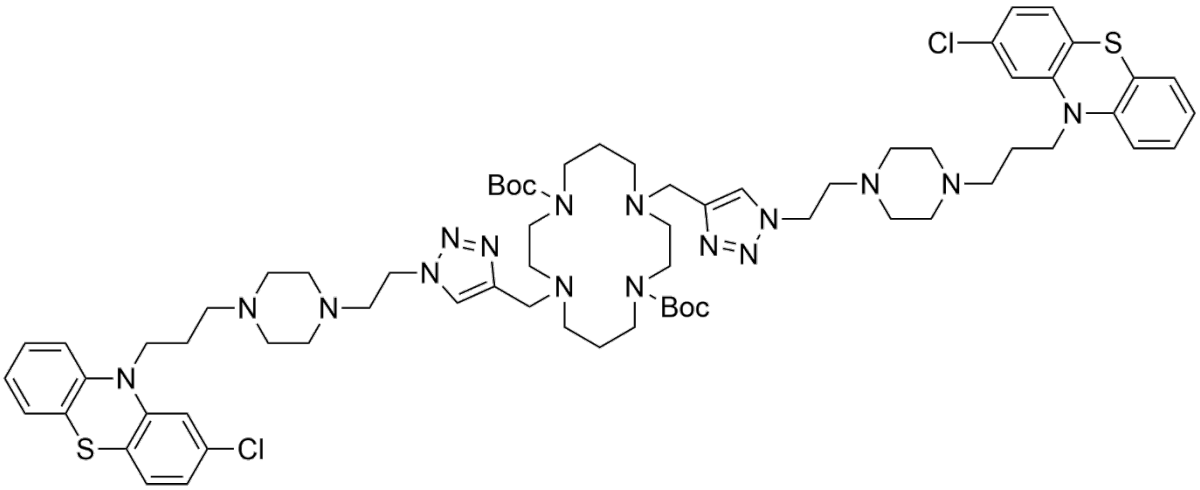

Prepared according to General Synthetic Procedure A using **64** (0.096 g, 0.202 mmol) and **62** (2.1 equiv, 0.180 g, 0.420 mmol). The crude product was purified *via* reversed-phase column chromatography (10% MeOH/H_2O to 100% MeOH) to give the product as a white solid. (0.212 g, 78%). **^{1}H NMR** (500 MHz, Chloroform-d): δ 7.54 (s, 2H), 7.13 (ddd, *J* = 14.8, 7.5, 1.5 Hz, 4H), 7.06 – 6.81 (m, 10H), 4.42 (t, *J* = 6.5 Hz, 4H), 3.89 (t, *J* = 6.8 Hz, 4H), 3.76 (s, 4H), 3.34 (s, 8H), 2.79 (t, *J* = 6.5 Hz, 4H), 2.62–2.54 (m, 4H), 2.46 (dd, *J* = 12.5, 5.6 Hz, 24H), 1.92 (p, *J* = 7.0 Hz, 4H), 1.77–1.71 (m, 8H), 1.39 (s, 18H). **^{13}C NMR** (125 MHz, Chloroform-d): δ 146.46, 144.45, 133.22, 127.90, 127.52, 127.45, 124.81, 123.56, 122.94, 122.28, 115.87, 79.29, 70.62, 65.84, 57.47, 55.32, 53.16, 52.85, 47.56, 45.21, 28.47, 26.51, 24.04, 15.27. **LRMS** (ESI+): 1333.76 $[M+H]^+$. **HRMS** (ESI+): *m/z calc.* for $C_{68}H_{96}Cl_2N_{16}O_4S_2^{2+}$ 667.33040 $[M+2H]^{2+}$, found 667.32932. **FTIR** (ATR) ν_{max}/cm^{-1}: 2936, 2808 1682, 1566.

(1,8-Bis((1-(2-(4-(3-(2-chloro-10H-phenothiazin-10-yl)propyl)piperazin-1-yl)ethyl)-1H-1,2,3-triazol-4-yl)methyl)-1,4,8,11-tetraazacyclotetradecane[299] 58

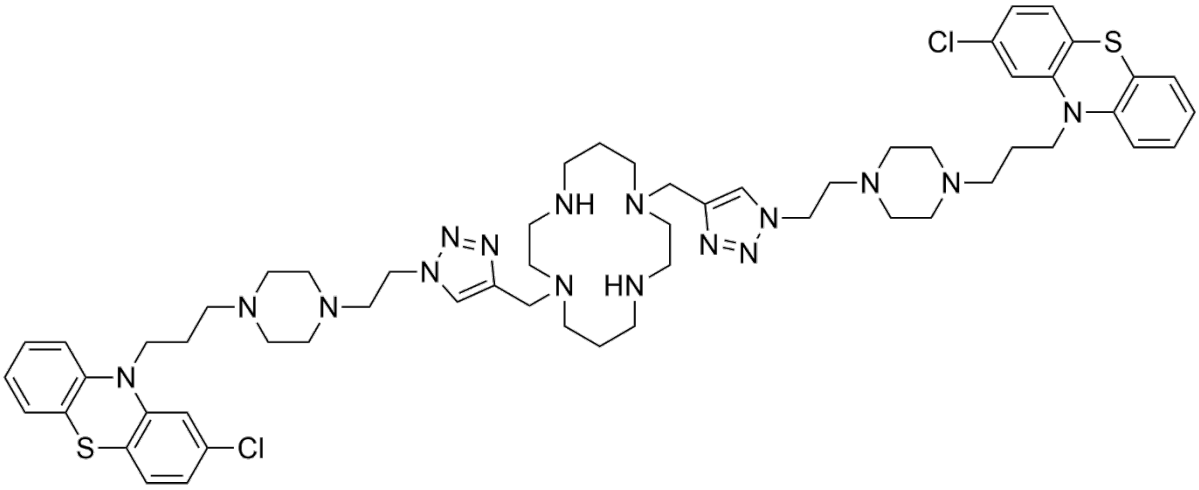

Prepared according to General Synthetic Procedure D using Boc-protected bis-perphenazine cyclam **72** (0.200 g, 0.150 mmol). The product was obtained as a white powder (0.150 g, 83%). For characterisation by NMR, the product was converted to the freebase *via* passage through an ion exchange column (Ambersep 900 OH form). **^{1}H NMR** (500 MHz, Chloroform-d) δ 7.67 (s, 2H), 7.13–6.99 (m, 4H), 6.98–6.73 (m, 10H), 4.33 (t, *J* = 6.5 Hz, 4H), 3.81 (t, *J* = 6.8 Hz, 4H), 3.71 (s, 4H), 2.67 (dt, *J* = 11.3, 5.9 Hz, 20H), 2.37 (td, *J* = 16.5, 7.2 Hz, 24H), 1.85 (dd, *J* = 14.1, 7.1 Hz, 4H). **^{13}C NMR** (125 MHz, DMSO-d6): 145.90, 143.17, 142.25, 133.0, 128.20, 127.92, 127.65, 125.74, 124.23, 123.59, 123.05, 122.50, 116.58, 115.67, 60.31, 55.29, 54.05, 52.99, 50.17, 48.52, 44.83, 43.26, 21.80, 21.00. **LRMS** (ESI+): 1133.61 $[M+H]^+$. **HRMS** (ESI+): *m*/*z* calc. for $C_{58}H_{79}Cl_2N_{16}S_2^+$ 1133.54866, $[M+H]^+$, found 1133.54823. **FTIR** (ATR) ν_{max}/cm^{-1}: 2968, 2801, 2186, 1682, 1566.

[Cu(58)]Cl_2 59 [299]

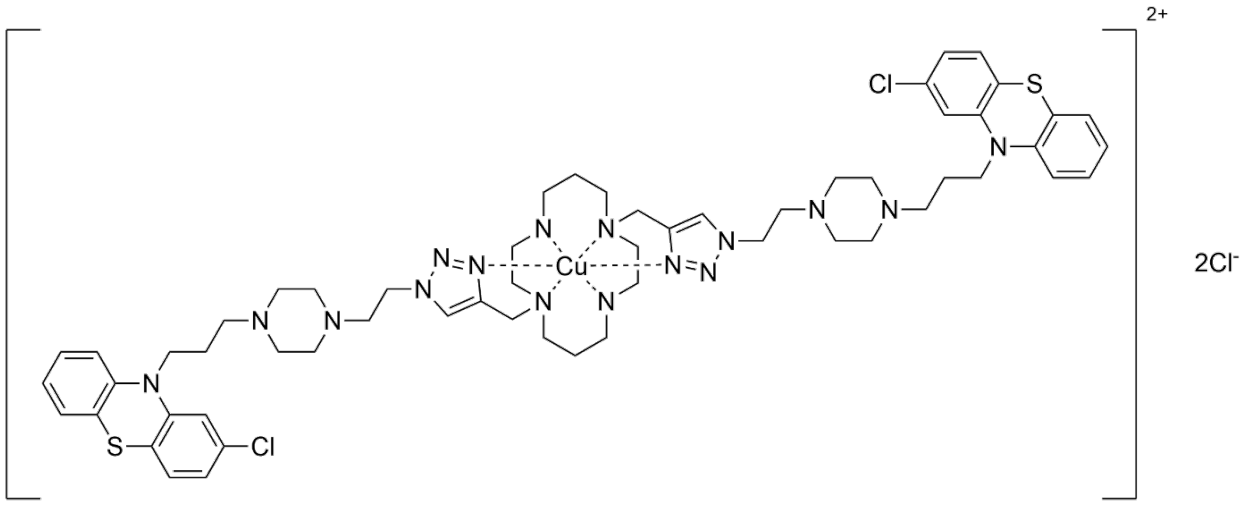

A solution of bis-perphenazine cyclam **58** (0.053 g, 0.044 mmol) in methanol (3.0 mL) was added to a suspension of Ambersep 900 hydroxide form resin (~80 mg) in methanol (5.0 mL) that had been pre-swollen for 30 min. The mixture was stirred at rt for 30 min and filtered. Copper(II) chloride dihydrate (0.010 g, 0.056 mmol) was added to the filtrate and the mixture stirred at rt for 4 h. The solution was concentrated under reduced pressure to a volume of ~1 mL and diethyl ether (~5 mL) was added, resulting in the precipitation of a blue powder. This precipitation was repeated twice and the resulting solid was lyophilised to give a light blue powder (0.049 g, 87%). **LRMS** (ESI+): 1232.53 $[M\text{-}Cl^-]^+$. **HRMS** (ESI+): *m/z* calc. for $C_{58}H_{78}Cl_3CuN_{16}S_2^+$ 1167.51078 $[M\text{-}Cl]^+$, found 1167.51100. **FTIR** (ATR) ν_{max}/cm^{-1}: 2937, 2814, 1565, 1455, 1082.

[Zn(58)]Cl_2 60 [299]

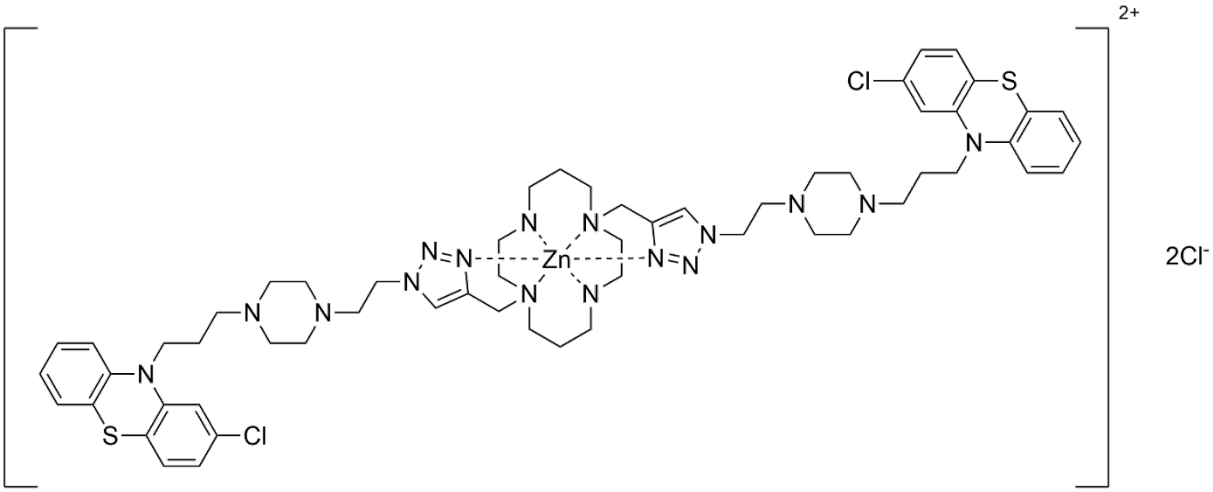

A solution of bis-perphenazine cyclam **58** (0.051 g, 0.043 mmol) in methanol (3.0 mL) was added to a suspension of Ambersep 900 hydroxide form resin (~80 mg) in methanol (5.0 mL) that had been pre-swollen for 30 min. The mixture was stirred at rt for 30 min and filtered. Zinc(II) chloride (0.007 g, 0.054 mmol) was added to the filtrate and the mixture stirred at rt for 4 h. The solution was concentrated under reduced pressure to a volume of ~1 mL and diethyl ether (~5 mL) was added, resulting in the precipitation of a blue powder. This precipitation was repeated twice and the resulting solid was lyophilised to give a light blue powder (0.046 g, 86%). **LRMS** (ESI+): 1233.56 $[M\text{-}Cl^-]^+$. **HRMS** (ESI+): *m/z* calc. for $C_{58}H_{78}Cl_3N_{16}S_2Zn^+$ $[M\text{-}Cl]^+$ 1231.43883, found 1231.44012. **FTIR** (ATR) ν_{max}/cm^{-1}: 2927, 2870, 2815, 1564, 1455, 1072.

Di-*tert*-butyl 2,2'-(4,11-di(prop-2-yn-1-yl)-1,4,8,11-tetraazacyclotetradecane-1,8-diyl)diacetate 75

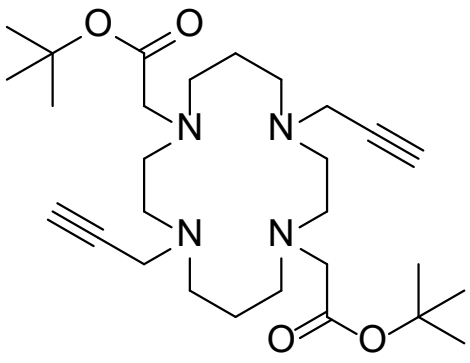

To a solution of bridged cyclam **64** (1.472 g, 6.562 mmol) in acetonitrile (80 mL) was added propargyl bromide (80% in toluene, 2.5 mL, 22.45 mmol) and the mixture stirred at rt overnight. The solids were isolated *via* vacuum filtration and resuspended in methanol (50mL) and NaOH (2.5 M, 50 mL) and stirred at rt for 3 h. The volatiles were removed under reduced pressure and the residue was extracted with DCM (3 x 50 mL). The combined organic extracts were dried over $MgSO_4$ and concentrated under reduced pressure. The residue was dissolved in DMF (30 mL) and sodium carbonate (2.067 g, 19.50 mmol) was added. A solution of *tert*-butyl bromoacetate (2.13 mL, 14.43 mmol) in DMF (20 mL) was added dropwise over 30 min and the mixture was stirred for an additional 2 h. The solids were removed *via* vacuum filtration and the filtrate was diluted with water (50 mL). The solution was allowed to stand overnight, and the resulting crystals were isolated *via* vacuum filtration to give the product as white needles (2.115 g, 64%). **^{1}H NMR** (500 MHz, Chloroform-d) δ 3.45 (t, J = 2.8 Hz, 4H), 3.25 (d, J = 2.8 Hz, 4H), 2.72 (h, J = 6.4, 5.4 Hz, 8H), 2.59 (ddd, J = 21.5, 7.6, 5.3 Hz, 8H), 2.16 (q, J = 2.8, 2.3 Hz, 2H), 1.60 (h, J = 6.9 Hz, 4H), 1.46 (d, J = 3.3 Hz, 18H). **^{13}C NMR** (126 MHz, Chloroform-d) δ 170.96, 80.62, 78.98, 72.66, 56.47, 51.18, 50.60, 50.38, 49.81, 42.54, 28.21, 25.06. **LRMS** (ESI+): m/z 505.42 $[M+H]^+$ **HRMS** (ESI+): m/z calc. for $C_{28}H_{49}N_4O_4^+$ $[M+H]^+$ 505.37483, found: 505.37480 $[M+H]^+$ **FTIR** (ATR) ν_{max}/cm^{-1} 2910, 2815, 1734.

Di-*tert*-butyl 2,2'-(4,11-bis((1-(2-(4-(3-(2-chloro-10H-phenothiazin-10-yl)propyl)piperazin-1-yl)ethyl)-1H-1,2,3-triazol-4-yl)methyl)-1,4,8,11-tetraazacyclotetradecane-1,8-diyl)diacetate 80

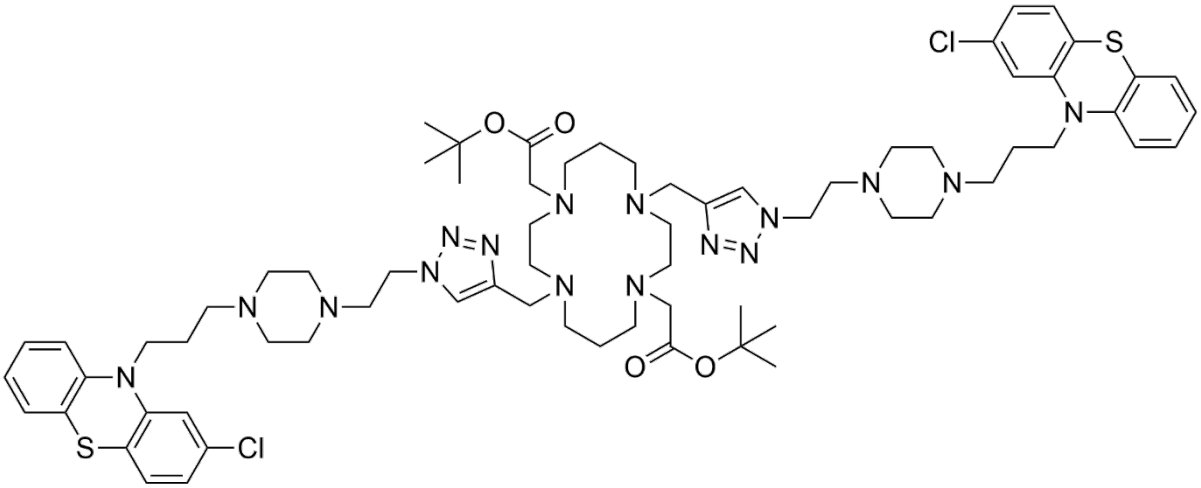

Prepared according to General Synthetic Procedure A using *t*-butyl protected bis-propargyl cyclam **75** (0.993 g, 1.967 mmol) and perphenazine azide **62** (2.2 equiv, 1.902 g, 4.444 mmol). The product was purified by dissolving in a minimal amount of DCM (5.0 mL) and precipitating with diethyl ether (20 mL). The solids were isolated *via* vacuum filtration and washed with ice-cold diethyl ether (3 × 10 mL) to give the product as a white powder (2.167 g, 79%). **^{1}H NMR** (500 MHz, Chloroform-d) δ 7.57 (s, 2H), 7.16–7.08 (m, 4H), 6.99 (d, *J* = 8.1 Hz, 2H), 6.93–6.82 (m, 7H), 4.41 (t, *J* = 6.5 Hz, 4H), 3.89 (t, *J* = 6.8 Hz, 4H), 3.76 (s, 4H), 3.19 (s, 4H), 2.77 (dt, *J* = 16.1, 6.2 Hz, 9H), 2.67 (t, *J* = 6.7 Hz, 4H), 2.63 – 2.27 (m, 31H), 1.91 (p, *J* = 6.9 Hz, 4H), 1.69–1.59 (m, 4H), 1.41 (s, 18H). **^{13}C NMR** (126 MHz, Chloroform-d) δ 170.94, 146.49, 144.52, 133.19, 127.86, 127.49, 127.41, 123.00, 122.87, 122.21, 115.84, 115.80, 80.64, 57.58, 56.55, 55.36, 53.27, 53.17, 51.49, 50.95, 50.88, 49.44, 47.60, 45.27, 28.23, 24.71, 24.28. **LRMS** (ESI+): *m*/z 1363.74 $[M+H]^+$. **HRMS** (ESI+): *m*/*z* calc. for $C_{70}H_{100}Cl_2N_{16}O_4S_2^{2+}$ 681.34605 $[M+2H]^{2+}$, found 681.34627. **FTIR** (ATR) ν_{max}/cm^{-1}: 3119, 3072, 2967, 2941, 2804, 1724, 1591, 1565.

2,2'-(4,11-Bis((1-(2-(4-(3-(2-chloro-10H-phenothiazin-10-yl)propyl)piperazin-1-yl)ethyl)-1H-1,2,3-triazol-4-yl)methyl)-1,4,8,11-tetraazacyclotetradecane-1,8-diyl)diacetic acid 74

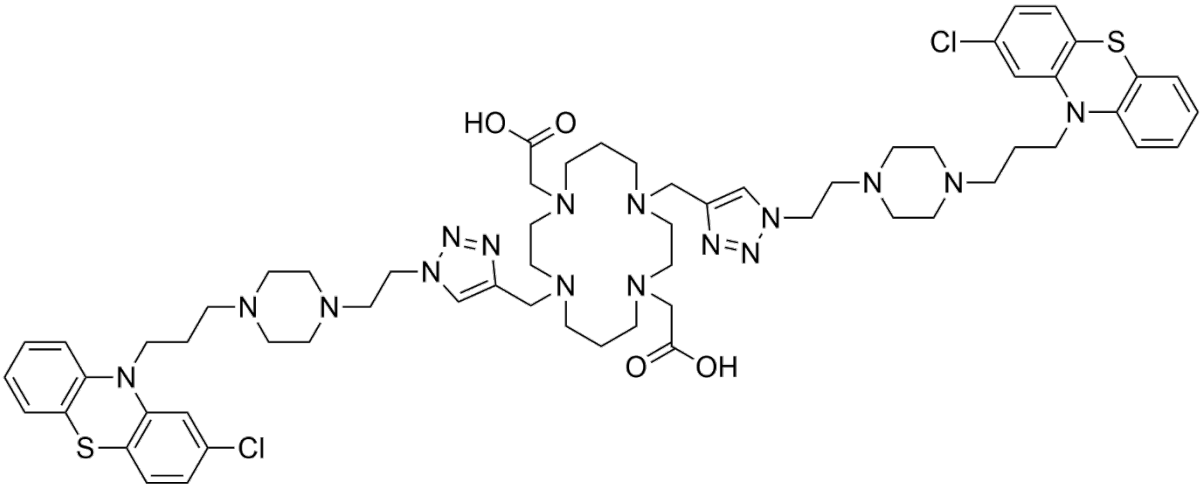

Prepared according to General Synthetic Procedure B using *t*-butyl protected bis-perphenazine cyclam **80** (0.200 g, 0.147 mmol). The product was obtained as an off-white powder (0.141 g, 76%). **^{1}H NMR** (500 MHz, 333K, DMSO-d6): 7.99 (s, 2H), 7.24–7.17 (m, 4H), 7.13–7.10 (m, 4H), 7.06–7.01 (m, 4H), 6.98–6.92 (m, 4H), 4.45–4.39 (m, 4H), 3.96–3.90 (m, 4H), 3.81 (s, 4H), 3.15 (s, 4H), 2.85–2.74 (m, 8H), 2.74–2.69 (m, 4H), 2.67–2.61 (m, 4H), 2.58–2.52 (m, 4H), 2.44–2.34 (m, 12 H), 2.30 (bs, 8H), 1.81–1.68 (m, 8H). **^{13}C NMR** (125 MHz, Chloroform-d): 146.85, 144.30, 133.25, 128.06, 127.61, 125.58, 124.80, 123.57, 123.05, 122.39, 115.93, 58.09, 57.32, 55.38, 54.18, 53.22, 52.97, 52.18, 49.36, 47.85, 47.01, 45.32, 24.28, 23.37. **LRMS** (ESI+): *m/z* 1251.81 $[M+H]^+$. **HRMS** (ESI+): *m/z* calc. for $C_{62}H_{83}Cl_2N_{16}O_4S_2^+$ 1249.55962 $[M+H]^+$, found 1249.55933. **FTIR** (ATR) ν_{max}/cm^{-1}: 3310, 1723, 1642, 1567.

[Zn(74)] 81

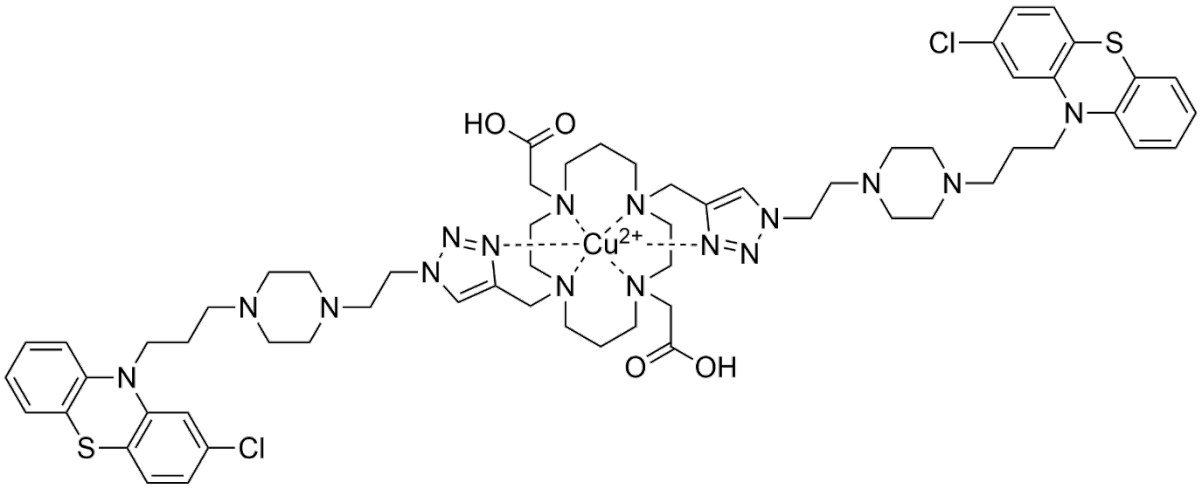

To a solution of bis-perphenazine cyclam **74** (0.210 g, 0.168 mmol) in methanol (3.0 mL) was added a solution of copper chloride dihydrate (0.035 g, 0.206 mmol) in methanol (2.0 mL) and the mixture was heated to reflux overnight. The mixture was cooled to rt, resulting in the formation of dark green crystals that were isolated via centrifugation and washed with ice-cold methanol (3 × 5mL). The crystals were dried in vacuo to a constant weight (0.139 g, 59%). **LRMS** (ESI+): *m*/*z* 1310.57 $[M-H]^+$. **HRMS** (ESI+): *m*/*z* calc. for $C_{62}H_{81}Cl_2CuN_{16}O_4S_2^+$ 1310.47357 $[M-H]^+$, found 1310.47779. **FTIR** (ATR) ν_{max}/cm^{-1} : 3355, 2946, 1590, 1566.

[Zn(74)] 82

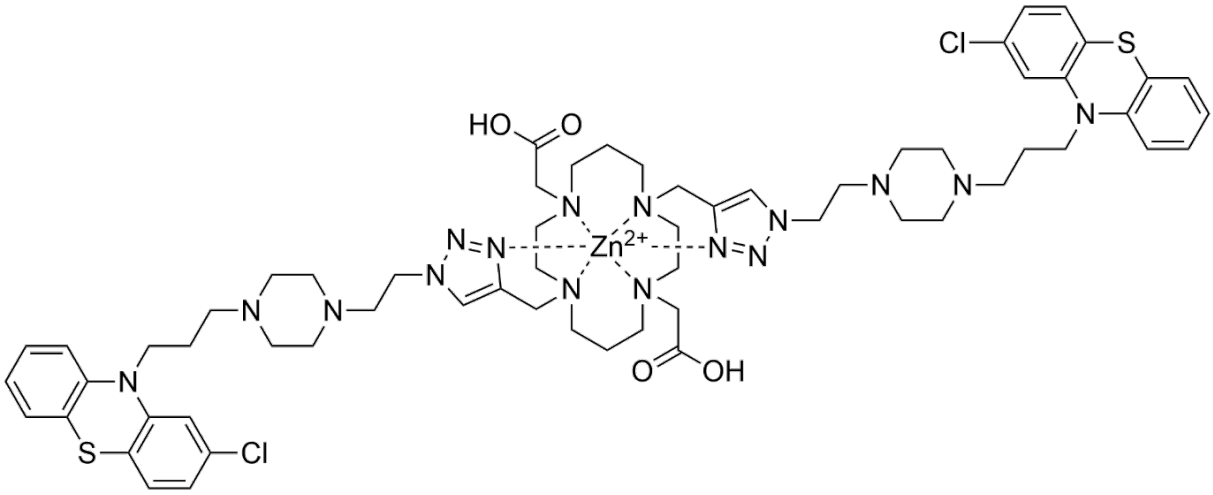

To a solution of bis-perphenazine cyclam **74** (0.101 g, 0.081 mmol) in ethanol (1.0 mL) was added a solution of $ZnCl_2$ (0.011g, 0.081 mmol) in ethanol (1.0 mL) and the mixture was stirred at rt overnight. The solid was isolated via centrifugation, washed with ice-

cold ethanol (3 × 3 mL) and diethyl ether (3 × 3 mL) and lyophilised to give the product as an off-white powder (0.048 g, 45%). **LRMS** (ESI+): *m*/*z* 657.70 $[M]^{2+}$. **HRMS** (ESI+): *m*/*z* calc. for $C_{62}H_{82}Cl_2N_{16}O_4S_2Zn^{2+}$ 657.24186 $[M]^{2+}$, found: 657.24186. **FTIR** (ATR) ν_{max}/cm^{-1}: 3380, 3261, 2965, 2863, 1590, 1567.

[Mn(74)] 83

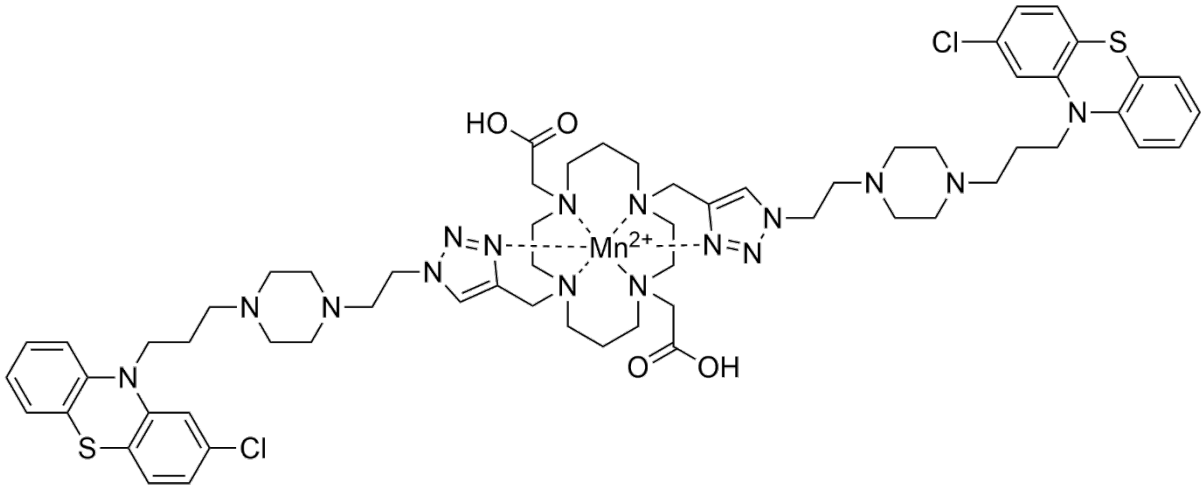

To a solution of bis-perphenazine cyclam **74** (0.067 g, 0.050 mmol) in methanol (1.0 mL) was added a solution of $MnCl_2{\cdot}4H_2O$ (0.012g, 0.062 mmol) in ethanol (1.0 mL) and the mixture was stirred at rt overnight. The mixture was concentrated under reduced pressure to half its volume and diluted with diethyl ether (3.0 mL) to precipitate the crude product. The solid was triturated with diethyl ether containing a few drops of methanol (3 × 2mL) and dried *in vacuo* to give the product as a yellow solid (0.038 g, 57%). **LRMS** (ESI+): *m*/*z* 651.74 $[M]^{2+}$. **HRMS** (ESI+): *m*/*z* calc. for $C_{62}H_{82}Cl_2MnN_{16}O_4S_2^{2+}$ 651.74464 $[M]^{2+}$, found: 651.74492. **FTIR** (ATR) ν_{max}/cm^{-1}: 3380, 3261, 2965, 2863, 1590, 1567.

Dibenzyl 1,4,7,10-tetraazacyclododecane-1,7-dicarboxylate 86[286]

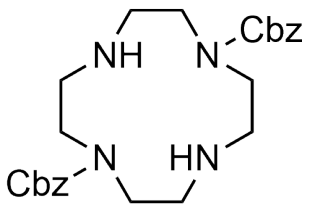

Cyclen (2.528 g, 14.68 mmol) was dissolved in water (18 mL) and the pH adjusted to ~3 with aqueous HCl (10 M, ~3 mL). The solution was diluted with dioxane (15 mL) and a solution of benzyl chloroformate (5.3 mL, 37.28 mmol) in dioxane (15 mL) was added dropwise over 24–36 h at rt. The pH of the reaction was monitored throughout the addition, and was adjusted to 3 periodically with the addition of aqueous NaOH (2.5 M). The mixture was allowed to stir for an additional 3 h at rt after the addition was complete. The mixture was then concentrated under reduced pressure to give a yellow oil. To this was added aqueous Na_2CO_3 (sat., 50 mL) and the mixture was extracted with diethyl ether (3 × 50 mL). The combined organic extracts were washed with brine (50 mL), dried over $MgSO_4$ and concentrated under reduced pressure to give the product as a colourless oil (5.469 g, 85%). **^{1}H NMR** (300 MHz, Chloroform-d) δ 7.44–7.28 (m, 10H), 5.16 (s, 4H), 3.57–3.36 (m, 8H), 2.98–2.62 (m, 8H). **LRMS** (ESI+): *m/z* 441.22 $[M+H]^+$ **FTIR** (ATR) ν_{max}/cm^{-1}: 3195, 3030, 2930, 2825, 2248, 2064, 1961, 1690, 1585. Spectroscopic data were in agreement with literature.

Dibenzyl 4,10-bis(2-(*tert*-butoxy)-2-oxoethyl)-1,4,7,10-tetraazacyclododecane-1,7-dicarboxylate 87[287]

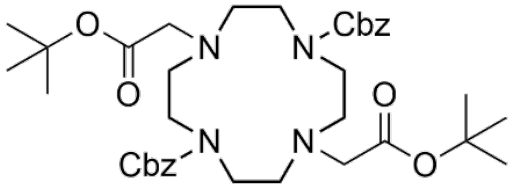

To a solution of protected cyclen **86** (2.834 g, 6.432 mmol) in anhydrous acetonitrile (25 mL) was added sodium carbonate (1.732 g, 16.338 mmol) and *tert*-butyl bromoacetate (2.0 mL, 13.64 mmol). The mixture was heated to 50° C and stirred overnight under N_2. The mixture was allowed to cool and the solids removed *via* vacuum filtration. The filtrate was concentrated under reduced pressure to give the crude product, which was purified *via* automated flash column chromatography (silica, 2%

MeOH in DCM) to give the product as an off-white foam (3.196 g, 74%). **^{1}H NMR** (300 MHz, Chloroform-d) δ 7.45–7.24 (m, 10H), 5.12 (s, 4H), 3.16–3.52 (m, 12H), 2.87 (s, 8H), 1.43 (s, 18H). **LRMS** (ESI+): *m/z* 669.38 $[M+H]^+$ **FTIR** (ATR) ν_{max}/cm^{-1}: 2976, 2932, 1730, 1694. Spectroscopic data were in agreement with literature.

Di-*tert*-butyl 2,2'-(1,4,7,10-tetraazacyclododecane-1,7-diyl)diacetate 88[286]

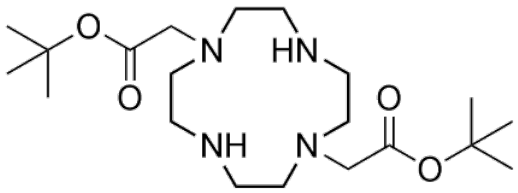

To a solution of **87** (2.545 g, 3.810 mmol) in methanol (15 mL) was added 10% Pd/C (0.126 g) and the mixture was placed under an atmosphere of H_2. The solution was stirred for 3 h before celite (~0.5 g) was added and allowed to stir for 30 min. The solids were then removed *via* vacuum filtration over a pad of celite and the filtrate was concentrated under reduced pressure. The residue was dissolved in diethyl ether (10 mL) and syringe filtered to remove residual celite, then concentrated under reduced pressure to give the product as an orange oil (1.3864g, 91%). **^{1}H NMR** (300 MHz, Chloroform-d) δ 3.31 (s, 4H), 2.81 (m, 8H), 2.61 (t, *J* = 5.1 Hz, 8H), 1.46 (s, 18H). **LRMS** (ESI+): *m/z* 401.29 $[M+H]^+$. **FTIR** (ATR) ν_{max}/cm^{-1}: 3298, 2974, 2930, 2820, 1726. Spectroscopic data were in agreement with literature.

Di-*tert*-butyl 2,2'-(4,10-di(prop-2-yn-1-yl)-1,4,7,10-tetraazacyclododecane-1,7-diyl)diacetate 85[288]

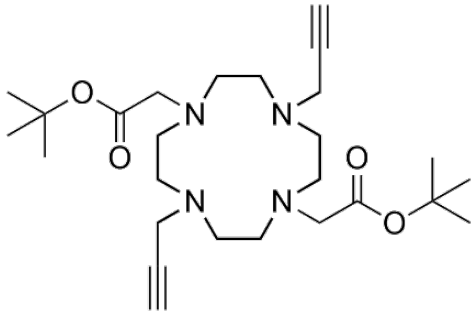

To a solution of **88** (1.386 g, 3.461 mmol) in acetonitrile (20 mL) was added sodium carbonate (1.772 g, 16.72 mmol) and propargyl bromide (80 wt% in toulene, 830 µL, 7.612 mmol). The mixture was heated to 50° C and stirred for 48 h. The solids were removed *via* vacuum filtration and the filtrate was concentrated under reduced pressure to give the crude product as an orange oil, which was recrystallised from boiling isopropanol to give the product as white needles (1.151 g, 70%). **^{1}H NMR** (300 MHz, Chloroform-d) δ 4.18–4.09 (m, 2H), 3.47 (s, 2H), 3.39–3.16 (m, 11H), 2.83–3.10 (m, 4H), 2.60 (d, *J* = 10.8 Hz, 2H), 2.39 (dtd, *J* = 10.2, 7.5, 6.9, 2.8 Hz, 3H), 2.17 – 2.11 (m, 2H), 1.49 (d, *J* = 9.3 Hz, 18H). **LRMS** (ESI+): *m*/*z* 477.32 $[M+H]^+$. **FTIR** (ATR) ν_{max}/cm^{-1}: 3294, 2975, 2930, 2819, 1724, 1654. Spectroscopic data were in agreement with literature.

Tri-tert-butyl 2,2',2''-(1,4,7,10-tetraazacyclododecane-1,4,7-triyl)triacetate 92[284]

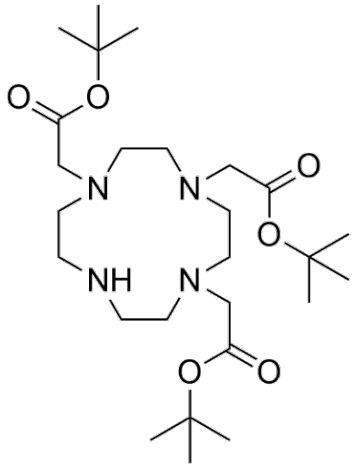

To a supsension of cyclen (1.783 g, 10.318 mmol) and sodium hydrogen carbonate (2.775 g, 33.03 mmol) in acetonitrile (60 mL) was added *tert*-butyl bromoacetate (4.9 mL, 33.20 mmol) dropwise over 30 min at 0 °C. The mixture was allowed to warm to rt and was stirred for 48 h. The solids were removed *via* vacuum filtration and the filtrate was concentrated under reduced pressure at 30 °C to give an off-white solid. This solid was triturated with ice-cold toluene (80 mL) to give a white solid (2.757 g, 52%)**. ^{1}H NMR** (300 MHz, Chloroform-d) δ 10.03 (s, 1H), 3.38 (s, 4H), 3.30 (s, 2H), 3.11 (t, *J* = 4.9 Hz, 4H), 3.03–2.79 (m, 12H), 1.46 (d, *J* = 2.0 Hz, 27H). **LRMS** (ESI+): *m*/*z* 515.40 $[M+H]^+$.

FTIR (ATR) ν_{max}/cm^{-1}: 2974, 2943, 2851, 2734, 1727, 1716, 1574. Spectroscopic data were in agreement with literature.

2-Azidoethyl methanesulfonate 93[294]

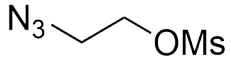

Safety note: 2-azidoethylmethanesulfonate has an C/N ratio of <3, making it potentially explosive. Neat samples should be handled with caution and stored under N_2 in the freezer. At no point should the isolation of 2-azidoethanol be attempted.

To a solution of 2-bromoethanol (2.004 g, 16.04 mmol) in anhydrous DMF (7.0 mL) was added sodium azide (2.686 g, 41.32 mmol) and the mixture was stirred at 60 °C for 24 h. The mixture was allowed to cool to rt and was diluted with THF (30 mL). The resulting precipitate was removed *via* vacuum filtration over a pad of celite. The filtrate was cooled to 0 °C and triethylamine (4.47 mL, 32.07 mmol) was added to the mixture, followed by the dropwise addition of mesyl chloride (2.48 mL, 32.04 mmol). The mixture was allowed to warm to rt and was stirred overnight. The volatiles were removed under reduced pressure and the mixture was diluted with ethyl acetate (40 mL) and water (40 mL). The organic layer was collected, and the aqueous phase was extracted with ethyl acetate (2 × 40 mL). The combined organic extracts were washed with brine, dried over magnesium sulfate and concetrated under reduced pressure to give the product as a yellow oil (1.775 g, 67%). **^{1}H NMR** (300 MHz, Chloroform-d) δ 4.42–4.27 (m, 2H), 3.60 (t, *J* = 5.0 Hz, 2H), 3.09 (s, 3H). **^{13}C NMR** (75 MHz, Chloroform-d) δ 67.54, 49.87, 37.76. **FTIR** (ATR) ν_{max}/cm^{-1}: 2098, 1659. Spectroscopic data were in agreement with literature.

Tri-tert-butyl 2,2',2''-(10-(2-azidoethyl)-1,4,7,10-tetraazacyclododecane-1,4,7-triyl)triacetate 91[288]

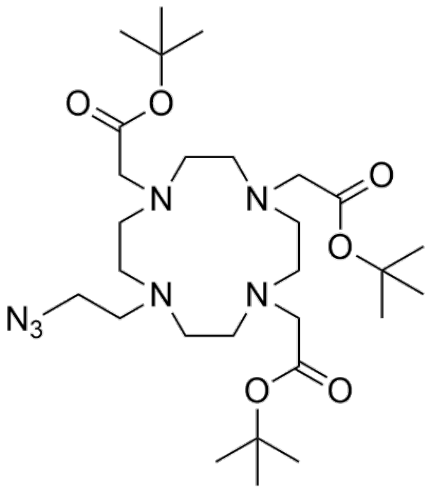

To a solution of **92** (0.204 g, 0.397 mmol) in acetonitrile (10 mL) was added potassium carbonate (0.218 g, 1.58 mmol) and **93** (0.198 g, 1.200 mmol) and the mixture was stirred at 50 °C overnight. The solids were removed *via* vacuum filtration and the filtrate was concentrated under reduced pressure to give a brown oil. The crude product was purified *via* automated flash column chromatography (alumina, 4% MeOH in DCM) to give the pure product as an orange oil (0.107 g, 46%). **^{1}H NMR** (300 MHz, Chloroform-d) δ 4.41–4.32 (m, 2H), 3.61 (t, *J* = 5.0 Hz, 2H), 3.44 (d, *J* = 6.1 Hz, 2H), 3.31 (s, 4H), 3.10 (d, *J* = 1.0 Hz, 2H), 2.99 (t, *J* = 6.0 Hz, 2H), 2.92 – 2.62 (m, 12H), 1.46 (d, *J* = 2.3 Hz, 27H). **LRMS** (ESI+): *m*/*z* 584.43 $[M+H]^+$. **FTIR** (ATR) ν_{max}/cm^{-1}: 3410, 2976, 2932, 2824, 2101, 1716. Spectroscopic data were in agreement with literature.

2,2'-(4,10-Di(prop-2-yn-1-yl)-1,4,7,10-tetraazacyclododecane-1,7-diyl)diacetic acid 98[288]

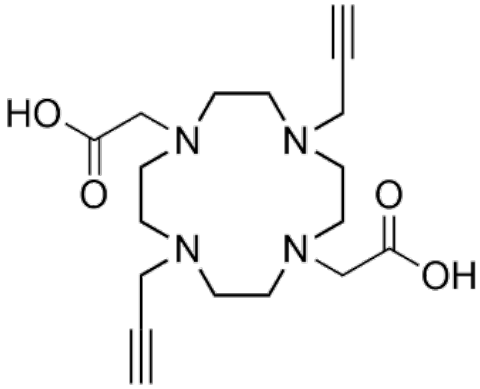

Prepared according to General Synthetic Procedure C using **80** (0.105 g, 0.221 mmol). The product was afforded as an off-white solid (0.116 g, 90%).**^{1}H NMR** (300 MHz, Deuterium Oxide) δ 3.83 (s, 4H), 3.70 (s, 4H), 3.43–3.02 (m, 16H), 2.77 (s, 2H). **LRMS** (ESI+): *m/z* 365.19 $[M+H]^+$. **FTIR** (ATR) ν_{max}/cm^{-1}: 3661, 3423, 3281, 2980, 2865, 2844, 2105, 1676. Spectroscopic data were in agreement with literature.

2,2'-(4,11-Di(prop-2-yn-1-yl)-1,4,8,11-tetraazacyclotetradecane-1,8-diyl)diacetic acid 99

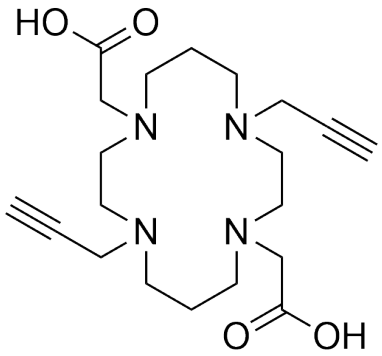

Prepared according to General Synthetic Procedure C using (0.105 g, 0.221 mmol). The product was afforded as an off-white solid (0.116 g, 90%).**^{1}H NMR** (500 MHz, Methanol-d4) δ 4.66 (s, 3H), 4.06 (s, 4H), 3.59 (d, *J* = 15.1 Hz, 4H), 3.44 – 3.35 (m, 8H), 3.16 (d, *J* = 5.5 Hz, 5H), 3.01 (d, *J* = 6.3 Hz, 4H), 2.01 (dt, *J* = 15.4, 7.6 Hz, 4H). **^{13}C NMR** (126 MHz, Methanol-d4) δ 173.67, 161.05, 157.74, 117.59, 115.27, 113.51, 79.10, 71.87, 53.63, 52.17, 51.54, 50.68, 41.84, 26.95, 21.57. **LRMS** (ESI+): *m/z* 393.24 $[M+H]^+$. **HRMS** (ESI+): *m/z* calc. for $C_{20}H_{33}N_4O_4^+$ 393.24963 $[M+H]^+$, found 393.24987. **FTIR** (ATR) ν_{max}/cm^{-1}: 3310, 1723, 1642, 1567.

(1-(2-(4-(3-(2-Chloro-10H-phenothiazin-10-yl)propyl)piperazin-1-yl)ethyl)-1H-1,2,3-triazol-4-yl)methanol 100

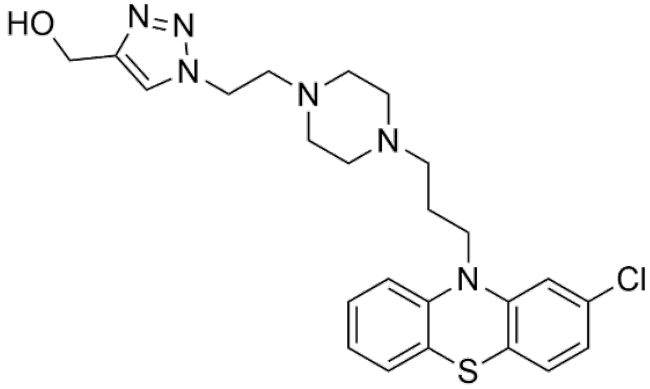

To a two-necked flask was added copper iodide (0.045 g, 0.234 mmol) and sodium ascorbate (0.495 g, 2.500 mmol), and the vessel was flushed with nitrogen. To this was added a solution of **62** (1.000 g, 2.331 mmol) in degassed THF (2.4 mL), and the mixture was diluted with another addition of degassed THF (10 mL). To this was added DIPEA (0.45 mL, 2.583 mmol) and propargyl alcohol (0.15 mL, 2.601 mmol), resulting in a beige precipitate. The mixture was stirred at rt for 1 h, resulting in a bright yellow solution. The mixture was diluted with ethyl acetate (40 mL) and washed with a mixture of brine (20 mL) and a solution of EDTA in NH_4Cl/NH_4OH buffer (50 mM, pH 9, 20 mL) three times. The combined aqueous washes were back extracted with ethyl acetate (3 × 40 mL) and the combined organic extracts were washed with brine (100 mL) and concentrated under reduced pressure to give the crude product as an orange oil. The oil was dissolved in hot acetonitrile (5 mL) and sonicated to precipitate the pure product as a white powder (0.912 g, 81%). **^{1}H NMR** (500 MHz, Chloroform-d) δ 7.67 (s, 1H), 7.18–7.08 (m, 2H), 7.00 (d, *J* = 8.1 Hz, 1H), 6.92 (td, *J* = 7.5, 1.2 Hz, 1H), 6.87 (ddd, *J* = 8.1, 5.4, 1.6 Hz, 2H), 6.84 (d, *J* = 2.1 Hz, 1H), 4.76 (s, 2H), 4.42 (t, *J* = 6.3 Hz, 2H), 3.89 (t, *J* = 6.8 Hz, 2H), 2.78 (t, *J* = 6.3 Hz, 2H), 2.46 (dd, *J* = 12.9, 5.9 Hz, 7H), 1.91 (p, *J* = 7.0 Hz, 2H). **^{13}C NMR** (126 MHz, Chloroform-d) δ 147.61, 146.47, 144.48, 133.18, 127.87, 127.49, 127.41, 124.75, 123.49, 122.89, 122.34, 122.22, 115.84, 115.80, 57.42, 56.32, 55.31, 53.13, 53.03, 47.51, 45.25, 24.19. **LRMS** (ESI+): *m/z* 485.19 $[M+H]^+$. **HRMS** (ESI+): *m/z* calc. for

$C_{24}H_{29}ClN_6OS$ 485.18848 $[M+H]^+$, found 485.18857. **FTIR** (ATR) ν_{max}/cm^{-1}: 3302, 2900, 2874, 2810, 2780, 1591, 1567.

Tri-tert-butyl 2,2',2''-(10-(prop-2-yn-1-yl)-1,4,7,10-tetraazacyclododecane-1,4,7-triyl)triacetate 107[284]

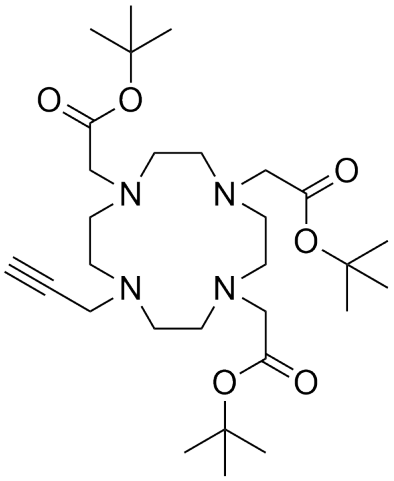

To a suspension of **92** (1.003g, 1.952 mmol) and potassium carbonate (0.582 g, 4.210 mmol) in acetonitrile (25 mL) was added propagyl bromide (0.25 mL, 2.348 mmol) at 0 °C, the mixture was then allowed to warm to rt and was stirred overnight. The solids were removed *via* vacuum filtration and the filtrate was concentrated under reduced pressure to give the crude product as a beige foam. This was purified *via* automated flash column chromatography (silica, 4% MeOH in DCM) to give the product as a white foam (0.776 g, 72%). **^{1}H NMR** (300 MHz, Chloroform-d) δ 3.35–3.25 (m, 3H), 3.25–2.45 (m, 18H), 2.35 (dd, *J* = 14.3, 6.8 Hz, 3H), 2.14 (t, *J* = 2.3 Hz, 1H), 1.46 (d, *J* = 13.7 Hz, 27H). **^{13}C NMR** (75 MHz, Chloroform-d) δ 178.03, 177.74, 175.82, 86.63, 86.46, 85.81, 85.74, 83.71, 81.53, 61.30, 60.77, 57.13, 54.97, 53.62, 50.78, 47.48, 33.09, 33.06, 32.92, 32.78. **LRMS** (ESI+): *m/z* 553.44 $[M+H]^+$. Spectroscopic data were in agreement with literature.

2,2',2''-(10-(Prop-2-yn-1-yl)-1,4,7,10-tetraazacyclododecane-1,4,7-triyl)triacetic acid[284] 106

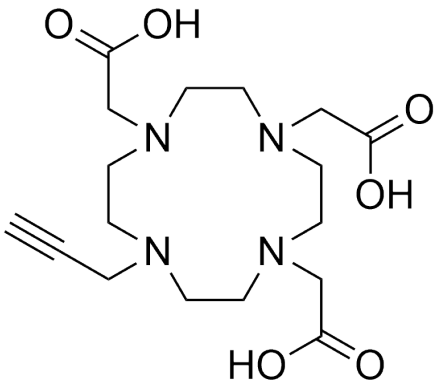

Prepared according to General Synthetic Procedure C using **107** (0.504 g, 0.912 mmol). The product as the TFA salt was afforded as a white solid (0.478 g, 85%). **^{1}H NMR** (300 MHz, Methanol-d4) δ 3.88 (d, *J* = 25.3 Hz, 6H), 3.58 (s, 2H), 3.49–3.26 (m, 8H), 3.16 (s, 8H), 2.92 (d, *J* = 2.3 Hz, 1H). **LRMS** (ESI+): *m/z* 385.18 $[M+H]^+$ **FTIR** (ATR) ν_{max}/cm^{-1}**:** 3464, 3427, 3296, 3275, 3110, 2868, 1670. Spectroscopic data were in agreement with literature.

[Y(106)] 109

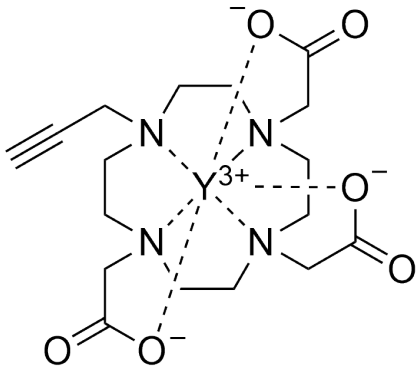

To a solution of **106** (0.102 g, 0.167 mmol) in methanol (5.0 mL) was added yttrium triflate (0.102 g, 0.191 mmol) and the mixture was stirred at 50 °C for 48 h. The mixture was concentrated under reduced pressure and the solids were dissolved in deionized water (1 mL). The pH was ad*J*usted to ~8 by the addition of 1 M NaOH (1 drop) and the resulting solids were removed *via* centrifugation. The supernatant was syringe filtered and desalted using reversed-phase column chromatography. The fraction containing

the product was lyophilised to give the product as an off-white solid (0.057 g, 72%). **LRMS** (MALDI): *m/z* 471.068 $[M+H]^+$. **FTIR** (ATR) ν_{max}/cm^{-1}: 3341, 3114, 2837, 1613.

[Eu(106)] 110

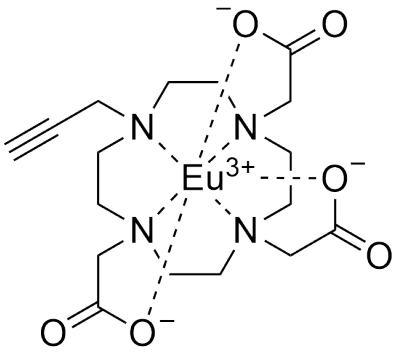

To a solution of **106** (0.110 g, 0.180 mmol) in methanol (5.0 mL) was added europium triflate (0.124 g, 0.208 mmol) and the mixture was stirred at 50 °C for 48 h. The mixture was concentrated under reduced pressure and the solids were dissolved in deionized water (1 mL). The pH was adjusted to ~8 by the addition of 1 M NaOH (1 drop) and the resulting solids were removed *via* centrifugation. The supernatant was syringe filtered and desalted using reversed-phase column chromatography. The fraction containing the product was lyophilised to give the product as an off-white solid (0.063 g, 66%). **LRMS** (MALDI): *m/z* 535.118 $[M+H]^+$. **FTIR** (ATR) ν_{max}/cm^{-1}: 3218, 2950, 2837 1597, 1552.

[Gd(106)] 111

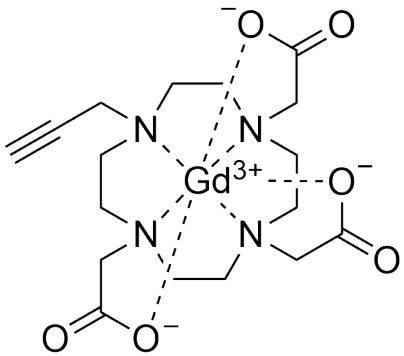

To a solution of **106** (0.096 g, 0.156 mmol) in methanol (5.0 mL) was added gadolinium triflate (0.111 mg, 0.183 mmol) and the mixture was stirred at 50 °C for 48 h. The mixture was concentrated under reduced pressure and the solids were dissolved in deionized water (1 mL). The pH was adjusted to ~8 by the addition of 1 M NaOH (1 drop) and the

resulting solids were removed *via* centrifugation. The supernatant was syringe filtered and desalted using reversed-phase column chromatography. The fraction containing the product was lyophilised to give the product as an off-white solid (0.059 g, 70%). **LRMS** (MALDI): *m/z* 540.078 $[M+H]^+$. **FTIR** (ATR) ν_{max}/cm^{-1}: 3261, 2869, 1683, 1575.

Tri-tert-butyl 2,2',2''-(10-((1-(2-(4-(3-(2-chloro-10H-phenothiazin-10-yl)propyl)piperazin-1-yl)ethyl)-1H-1,2,3-triazol-4-yl)methyl)-1,4,7,10-tetraazacyclododecane-1,4,7-triyl)triacetate 113

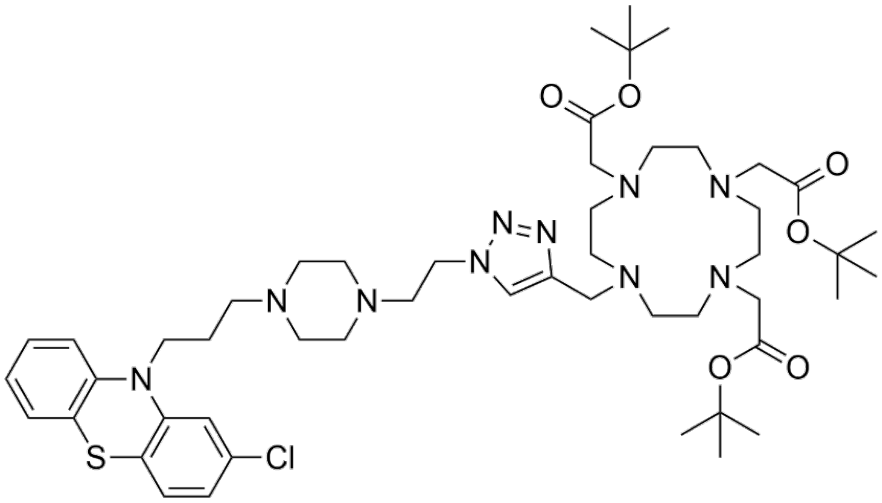

To a solution of **100** (0.504 g, 1.039 mmol) in anhydrous DCM (10 mL) was added triethylamine (0.22 mL, 1.58 mmol) and mesyl chloride (0.12 mL, 1.550 mmol) and the mixture was stirred at rt overnight. The mixture was diluted with DCM (20 mL) and washed with water (3 × 30 mL), followed by brine. The organic phase was dried over magnesium sulfate and concentrated under reduced pressure to give an amber oil. This was dissolved in DMF (10 mL), and caesium carbonate (0.347 g, 1.065 mmol) was added, followed by **92** (0.481 g, 0.994 mmol). The mixture was heated to 50 °C and stirred overnight. The mixture was diluted with ethyl acetate (50 mL) and aqueous lithium chloride (5%, 50 mL). The organic layer was collected, and the aqueous phase washed with ethyl acetate (2 × 50 mL). The combined organic layers were then washed with water (5 × 50 mL), followed by brine (70 mL) and dried over magnesium sulfate. The solution was then concentrated under reduced pressure to give the crude product as an

off-white foam. This was dissolved in 5% MeOH in DCM and passed through a plug of alumina (Brockmann grade III). The filtrate was concentrated under reduced pressure to give the pure product as a slightly yellow solid (0.637 g, 65%). **^{1}H NMR** (500 MHz, Acetonitrile-d3, 323K) δ 7.72 (s, 1H), 7.22 (ddt, *J* = 9.6, 7.6, 2.0 Hz, 1H), 7.13 (dt, *J* = 8.0, 2.0 Hz, 1H), 7.10 – 6.91 (m, 5H), 4.42 (t, *J* = 6.1 Hz, 2H), 3.95 (t, *J* = 6.7 Hz, 2H), 3.63 (s, 2H), 3.38 (d, *J* = 11.4 Hz, 0H), 3.30 (d, *J* = 2.6 Hz, 1H), 3.21 – 2.11 (m, 32H), 1.84 (p, *J* = 6.8 Hz, 2H), 1.50 (dd, *J* = 19.2, 2.0 Hz, 27H). **^{13}C NMR** (126 MHz, Acetonitrile-d3) δ 173.51, 172.92, 145.02, 128.43, 128.27, 127.77, 124.87, 123.54, 122.61, 116.85, 116.48, 82.20, 57.59, 56.40, 56.18, 55.27, 53.66, 53.24, 49.98, 48.36, 47.78, 45.40, 27.96, 27.87, 24.22, 1.40, 1.23. **LRMS** (ESI+): *m*/*z* 1003.58 $[M+Na]^+$. **HRMS** (ESI+): *m*/*z* calc. for $C_{50}H_{77}ClN_{10}NaO_6S^+$ 1003.53438 $[M+Na]^+$, found: 1003.53290 $[M+Na]^+$. **FTIR** (ATR) ν_{max}/cm^{-1}: 3367, 2974, 2817, 1726, 1669, 1592, 1565.

2,2',2''-(10-((1-(2-(4-(3-(2-Chloro-10H-phenothiazin-10-yl)propyl)piperazin-1-yl)ethyl)-1H-1,2,3-triazol-4-yl)methyl)-1,4,7,10-tetraazacyclododecane-1,4,7-triyl)triacetic acid 105

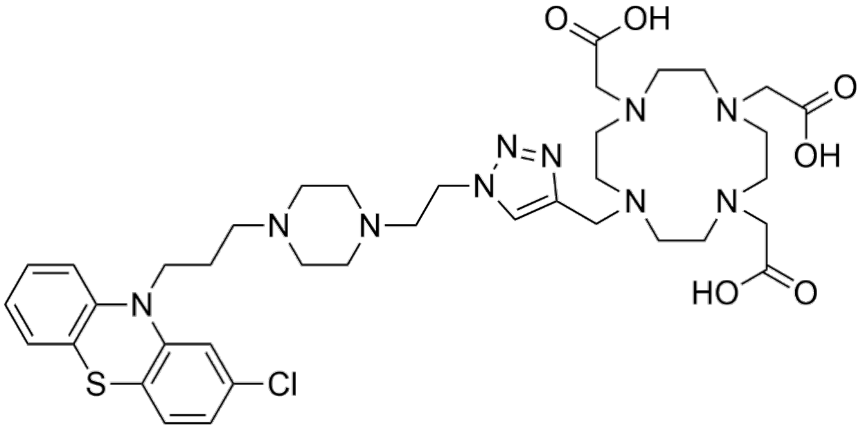

Prepared according to General Synthetic Procedure B using **113** (0.490 g, 0.500 mmol). The product was obtained as a pearlescent, off-white solid (0.217 g, 64%). **^{1}H NMR** (500 MHz, Methanol-d4) δ 8.29 (s, 1H), 7.10 (t, *J* = 7.8 Hz, 1H), 7.01 (d, *J* = 7.6 Hz, 1H), 6.98 – 6.78 (m, 5H), 4.54 (t, *J* = 5.2 Hz, 2H), 3.89 (t, *J* = 6.3 Hz, 2H), 3.78 (s, 2H), 3.35 (d, *J* = 28.4 Hz, 12H), 3.19 (d, *J* = 19.5 Hz, 8H), 2.94 – 2.75 (m, 15H), 2.71 (t, *J* = 7.5 Hz, 2H), 1.93

(p, *J* = 7.0 Hz, 2H). **^{13}C NMR** (126 MHz, CH_3OD) δ 175.63, 146.68, 144.48, 143.89, 133.06, 127.77, 127.45, 127.13, 125.19, 124.30, 122.93, 122.18, 116.14, 115.86, 56.56, 55.98, 55.65, 53.86, 51.47, 51.01, 50.14, 49.57, 45.36, 44.12, 22.52. **LRMS** (ESI+): *m/z* 813.36 $[M+H]^+$. **HRMS** (ESI+): *m/z* calc. for $C_{38}H_{54}ClN_{10}O_6S^+$ 813.36404 $[M+H]^+$, found 813.36315 $[M+H]^+$. **FTIR** (ATR) ν_{max}/cm^{-1}: 3367, 2950, 2826, 1625, 1592, 1566.

[Y(105)] 112

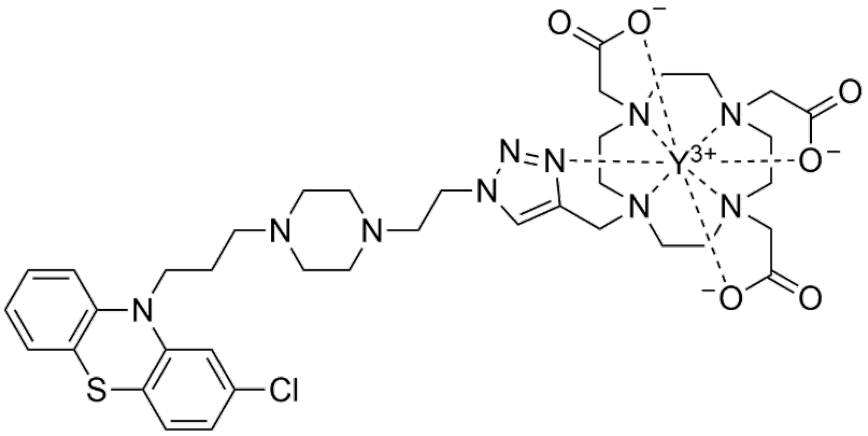

To a solution of **105** (0.020 g, 0.025 mmol) in methanol (2.0 mL) was added yttrium triflate (0.015 mg, 0.029 mmol) and the mixture was stirred at 50 °C for 48 h. The mixture was concentrated under reduced pressure and the solids were dissolved in deionized water (1.0 mL). The pH was adjusted to ~8 by the addition of 1 M NaOH (1 drop) and the resulting solids were removed *via* centrifugation. The supernatant was syringe filtered and desalted using reversed-phase column chromatography. The fraction containing the product was lyophilised to give the product as an off-white solid (0.024 mg, 99%). **LRMS** (ESI+): *m/z* 899.16 $[M+H]^+$. **HRMS** (ESI+): *m/z* calc. for $C_{38}H_{51}ClN_{10}NaO_6SY^{2+}$ 461.11737 $[M+2H]^{2+}$, found 461.11828. **FTIR** (ATR) ν_{max}/cm^{-1}: 3401, 2872, 1606.

[Gd(105)] 114

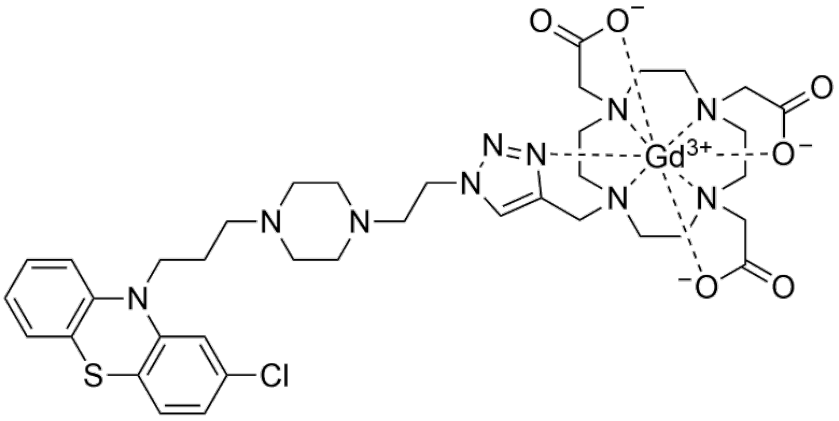

To a solution of **105** (0.022 g, 0.027 mmol) in methanol (2.0 mL) was added gadolinium triflate (0.015 g, 0.030 mmol) and the mixture was stirred at 50 °C for 48 h. The mixture was concentrated under reduced pressure and the solids were dissolved in deionized water (1.0 mL). The pH was adjusted to ~8 by the addition of 1 M NaOH (1 drop) and the resulting solids were removed *via* centrifugation. The supernatant was syringe filtered and desalted using reversed-phase column chromatography. The fraction containing the product was lyophilised to give the product as an off-white solid (0.022 g, 86%). **LRMS** (ESI+): *m/z* 968.21 $[M+H]^+$. **HRMS** (ESI+): *m/z* calc. for $C_{38}H_{51}ClGdN_{10}NaO_6S^{2+}$ $[M+H+Na]^{2+}$, 495.62645, found 495.62740. **FTIR** (ATR) ν_{max}/cm^{-1}: 3429, 2863, 1601.

[Eu(105)] 115

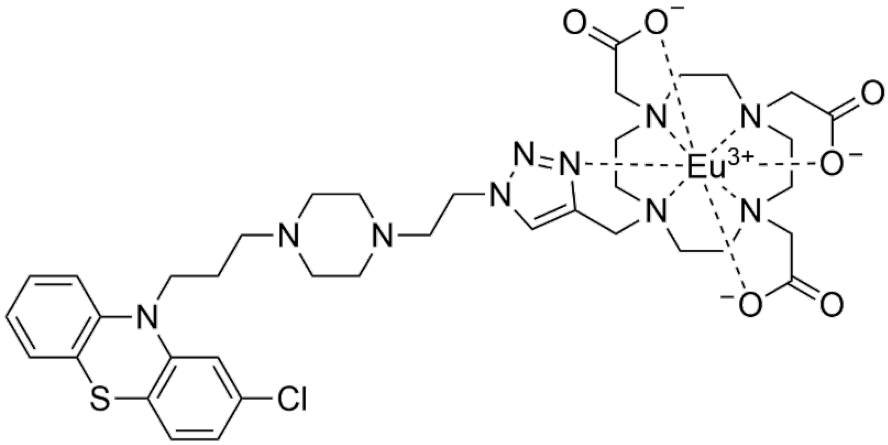

To a solution of **105** (0.020 g, 0.024 mmol) in methanol (2.0 mL) was added europium triflate (0.017 mg, 0.029 mmol) and the mixture was stirred at 50 °C for 48 h. The

mixture was concentrated under reduced pressure and the solids were dissolved in deionized water (1.0 mL). The pH was adjusted to ~8 by the addition of 1 M NaOH (1 drop) and the resulting solids were removed *via* centrifugation. The supernatant was syringe filtered and desalted using reversed-phase column chromatography. The fraction containing the product was lyophilised to give the product as an off-white solid (0.020 g, 87%). **LRMS** (ESI+): *m*/*z* 963.22. **HRMS** (ESI+): *m*/*z* calc. for $C_{38}H_{51}ClEuN_{10}NaO_6S^{2+}$ 963.26019 $[M+H+Na]^{2+}$, found 963.26195. **FTIR** (ATR) ν_{max}/cm^{-1}: 3439, 2856, 1601.

[Cu(105)] 116

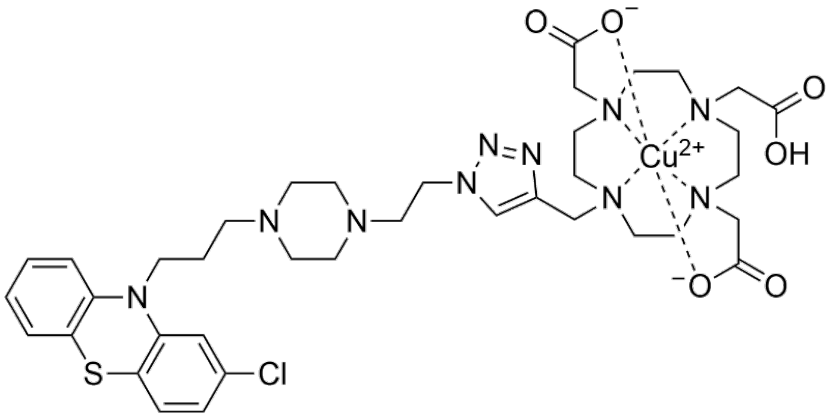

To a solution of **105** (0.023 g, 0.028 mmol) in methanol (2.0 mL) was added copper(II) chloride dihydrate (0.006 mg, 0.034 mmol) and the mixture was stirred at 50 °C overnight. The resulting blue solution was concentrated under reduced pressure. The solids were dissolved in methanol (~0.5 mL) and a few drops of water, and were precipitated by the addition of diethyl ether (8.0 mL). The resulting blue-green solid was washed with diethyl ether (2 × 4 mL) and dried *in vacuo* to give the product (0.018 mg, 75%). **LRMS** (ESI+): *m*/*z* 874.25 $[M+H]^+$. **HRMS** (ESI+): *m*/*z* calc. for $C_{38}H_{52}ClCuN_{10}O_6S^+$ 874.27710, found 874.27747. **FTIR** (ATR) ν_{max}/cm^{-1}: 3410, 3373, 2942, 2866, 1725, 1589, 1566.

[Zn(105)] 117

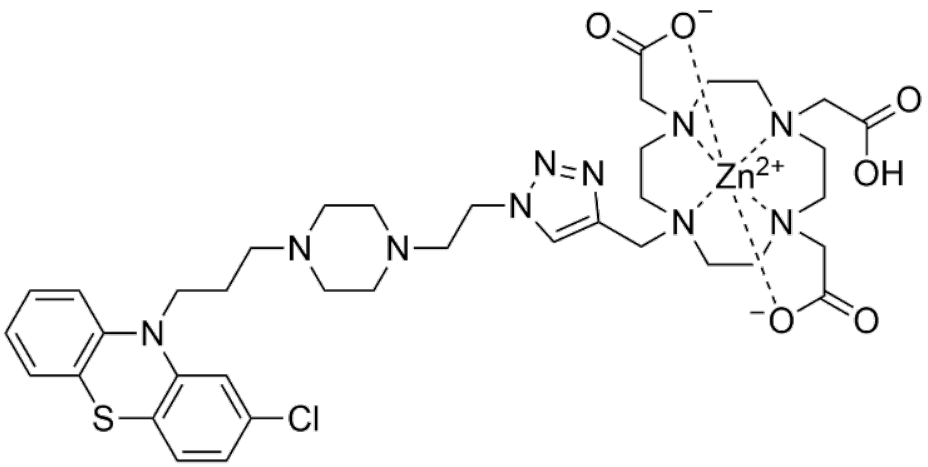

To a solution of **105** (0.020 g, 0.025 mmol) in methanol (2.0 mL) was added zinc chloride (0.005 g, 0.039 mmol) and the mixture was stirred at 50 °C overnight. The resulting white mixture was concentrated under reduced pressure. The solids were dissolved in methanol (~0.5 mL) and a few drops of water, and were precipitated by the addition of diethyl ether (8.0 mL). The resulting white solid was washed with diethyl ether (2 × 4 mL) and dried *in vacuo* to give the product (0.016 g, 74%). **LRMS** (ESI+): *m/z* 875.22 $[M+H]^+$. **HRMS** (ESI+): *m/z* calc. for $C_{38}H_{52}ClN_{10}O_6SZn^+$ 875.27665 $[M+H]^+$, found 875.27696. **FTIR** (ATR) ν_{max}/cm^{-1}: 3377, 2966, 2865, 1736, 1590.

[Mn(105)] 118

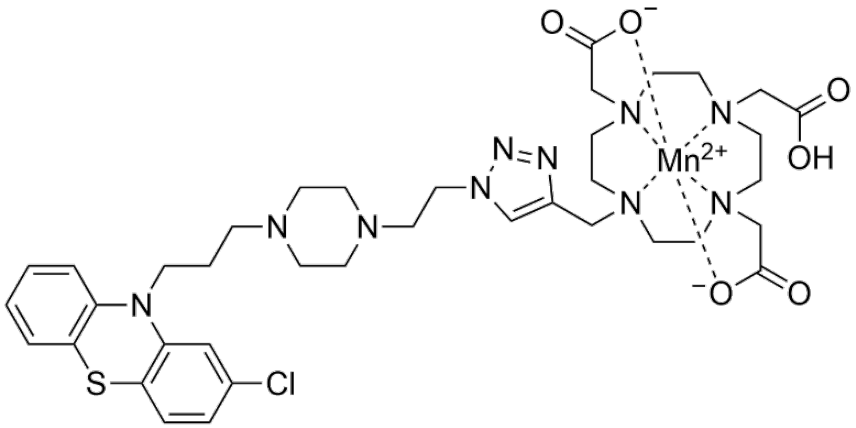

To a solution of **105** (0.028 mg, 0.034 mmol) in methanol (2.0 mL) was added manganese(II) chloride dihydrate (0.008 mg, 0.048 mmol) and the mixture was stirred at 50 °C overnight. The resulting yellow mixture was concentrated under reduced pressure. The solids were dissolved in methanol (~0.5 mL) and a few drops of water,

and were precipitated by the addition of diethyl ether (8.0 mL). The resulting yellow solid was washed with diethyl ether (2 × 4 mL) and dried *in vacuo* to give the product (0.020 g, 68%). **LRMS** (ESI+): *m/z* 866.25 $[M+H]^+$. **HRMS** (ESI+): *m/z* calc. for $C_{38}H_{52}ClMnN_{10}O_6S^+$ 866.28555 $[M+H]^+$, found 866.28810. **FTIR** (ATR) ν_{max}/cm^{-1}: 3369, 2952, 2861, 1584.

Tri-tert-butyl 11-(prop-2-yn-1-yl)-1,4,8,11-tetraazacyclotetradecane-1,4,8-tricarboxylate 121[230]

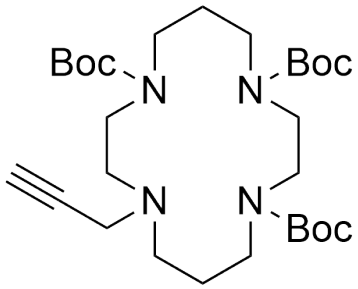

To a solution of tri-Boc cyclam **120** (0.450 g, 0.899 mmol) in acetonitrile (25 mL) was added sodium carbonate (0.384 g, 3.63 mmol) and propagyl bromide (0.16 mL, 1.10 mmol). The mixture was heated to reflux and stirred overnight. The solids were removed *via* vacuum filtration and the filtrate was concentrated under reduced pressure to give an orange oil. The crude product was purified *via* automated flash column chromatography (silica, 5% MeOH in DCM) to give the product as an off-white solid (0.336 g, 69%). **^{1}H NMR** (300 MHz, Chloroform-d) δ 3.34 (dt, *J* = 18.1, 9.0 Hz, 1lH), 2.67 (t, *J* = 5.3 Hz, 1H), 2.51 (t, *J* = 6.0 Hz, 1H), 2.21 – 2.13 (m, 1H), 1.88 (d, *J* = 9.7 Hz, 1H), 1.81 – 1.63 (m, 3H), 1.46 (d, *J* = 1.8 Hz, 27H). **LRMS** (ESI+): *m/z* 539.39 $[M+H]^+$. **FTIR** (ATR) ν_{max}/cm^{-1}: 2972, 2937, 1720, 1592, 1567.

Tri-tert-butyl 11-((1-(2-(4-(3-(2-chloro-10H-phenothiazin-10-yl)propyl)piperazin-1-yl)ethyl)-1H-1,2,3-triazol-4-yl)methyl)-1,4,8,11-tetraazacyclotetradecane-1,4,8-tricarboxylate 122

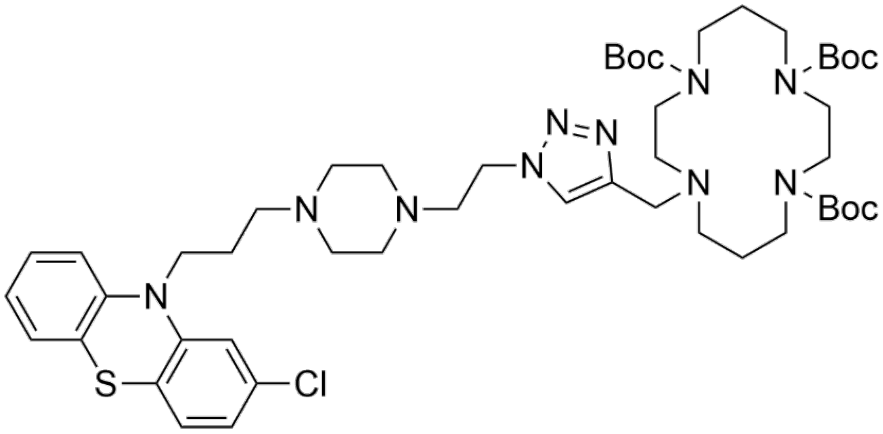

Prepared according to General Synthetic Procedure A using **121** (0.318 g, 0.590 mmol) and **62** (1.2 equiv, 0.304 g, 0.708 mmol). The crude product was then purified *via* automated flash column chromatography (reversed-phase, gradient of 10% MeOH in water to 100% MeOH)) and the fractions containing the product were lyophilized to give a white powder (0.316 g, 55%). **^{1}H NMR** (500 MHz, Chloroform-d) δ 7.50 (s, 1H), 7.17–7.04 (m, 2H), 6.99 (d, *J* = 8.1 Hz, 1H), 6.96 – 6.81 (m, 4H), 4.40 (t, *J* = 6.4 Hz, 2H), 3.90 (t, *J* = 6.8 Hz, 2H), 3.78 (s, 2H), 3.34 (tq, *J* = 14.0, 7.0, 5.9 Hz, 12H), 2.79 (t, *J* = 6.4 Hz, 2H), 2.62 (t, *J* = 5.5 Hz, 2H), 2.44 (tdd, *J* = 14.8, 7.0, 2.9 Hz, 12H), 1.91 (p, *J* = 7.0 Hz, 4H), 1.72 (h, *J* = 6.5, 6.1 Hz, 2H), 1.64 – 1.34 (m, 27H). **^{13}C NMR** (126 MHz, Chloroform-d) δ 146.49, 144.52, 133.20, 127.87, 127.50, 127.41, 124.76, 123.50, 122.89, 122.22, 115.85, 115.80, 79.51, 77.30, 77.05, 76.79, 57.52, 55.35, 53.26, 53.19, 53.15, 50.75, 47.60, 45.27, 28.54, 28.50, 24.28. **LRMS** (ESI+): *m/z* 967.57 $[M+H]^+$. **HRMS** (ESI+): *m/z* calc. for $C_{49}H_{76}ClN_{10}O_6S^+$ 967.53530 $[M+H]^+$, found 967.53531. **FTIR** (ATR) ν_{max}/cm^{-1}: 2971, 2936, 2812, 1720, 1592, 1567.

1-((1-(2-(4-(3-(2-Chloro-10H-phenothiazin-10-yl)propyl)piperazin-1-yl)ethyl)-1H-1,2,3-triazol-4-yl)methyl)-1,4,8,11-tetraazacyclotetradecan-1-ium 49

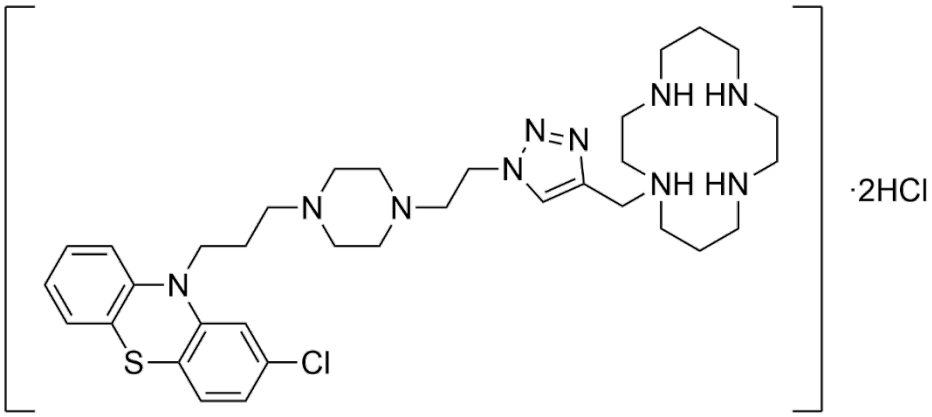

Prepared according to General Synthetic Procedure D using **122** (0.094 g, 0.097 mmol). The product as the HCl salt was obtained as a white powder (0.045 mg, 69%). The compound was converted to the freebase by passage through an ion exchange column (Ambersep 900 OH form) for characterization by NMR. **^{1}H NMR** (500 MHz, Chloroform-d) δ 7.50 (s, 1H), 7.11–7.02 (m, 2H), 6.94 (d, *J* = 8.1 Hz, 1H), 6.89–6.76 (m, 5H), 4.35 (t, *J* = 6.4 Hz, 2H), 3.83 (t, *J* = 6.8 Hz, 3H), 2.73–2.54 (m, 11H), 2.54–2.27 (m, 18H), 1.92–1.74 (m, 6H), 1.63 (p, *J* = 5.4 Hz, 2H). **^{13}C NMR** (126 MHz, Chloroform-d) δ 145.48, 143.51, 142.34, 132.19, 126.86, 126.49, 126.39, 123.77, 122.50, 122.10, 121.87, 121.22, 114.84, 114.78, 76.26, 76.21, 76.00, 75.75, 56.60, 54.37, 53.55, 52.22, 52.19, 51.33, 49.67, 48.42, 48.27, 47.94, 47.14, 46.59, 46.14, 45.36, 44.25, 28.09, 25.12, 23.25, 0.00. **LRMS** (ESI+): *m/z* 667.38 $[M+H]^+$. **HRMS** (ESI+): *m/z* calc. for $C_{34}H_{52}ClN_{10}S^+$ 667.37802 $[M+H]^+$, found 667.37768. **FTIR** (ATR) ν_{max}/cm^{-1}: 3380, 2959, 2843, 1636, 1591, 1566.

[Cu(49)]Cl_2 50

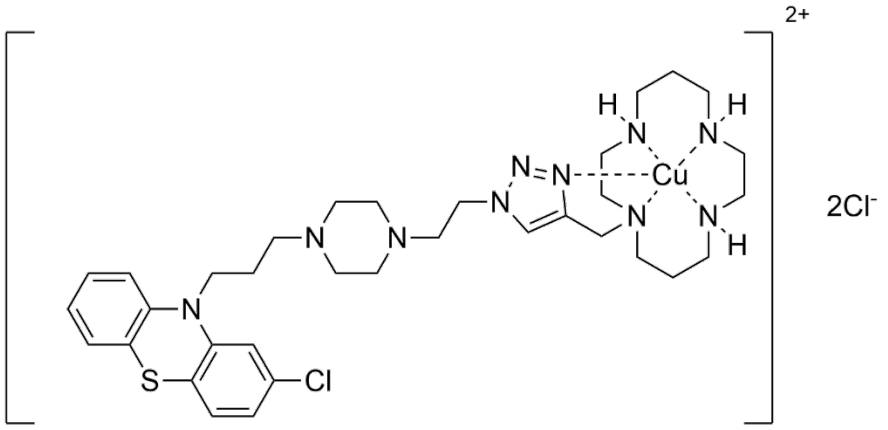

A solution of **123** (0.012 g, 0.016 mmol) in methanol (1.0 mL) was added to a suspension of Ambersep 900 hydroxide form resin (~50 mg) in methanol (2.0 mL) that had been pre-swollen for 30 min. The mixture was stirred at rt for 30 min and filtered. Copper(II) chloride dihydrate (0.003 g, 0.016 mmol) was added to the filtrate and the mixture stirred at rt for 4 h. The solution was concentrated under reduced pressure to a volume of ~1 mL and diethyl ether (~5 mL) was added, resulting in the precipitation of a blue-green powder. This was repeated twice and the solid was dried *in vacuo* to give a blue-green powder (0.006 g, 44%). **LRMS** (ESI+): *m/z* 364.63 $[M+H]^+$. **HRMS** (ESI+): *m/z* calc. for $C_{34}H_{51}Cl_2CuN_{10}S^+$ 766.26569 $[M-Cl]^+$, found 766.26641 **FTIR** (ATR) ν_{max}/cm^{-1}: 3372, 2939, 2876, 2817, 1661, 1590, 1566.

[Zn(105)]Cl_2 51

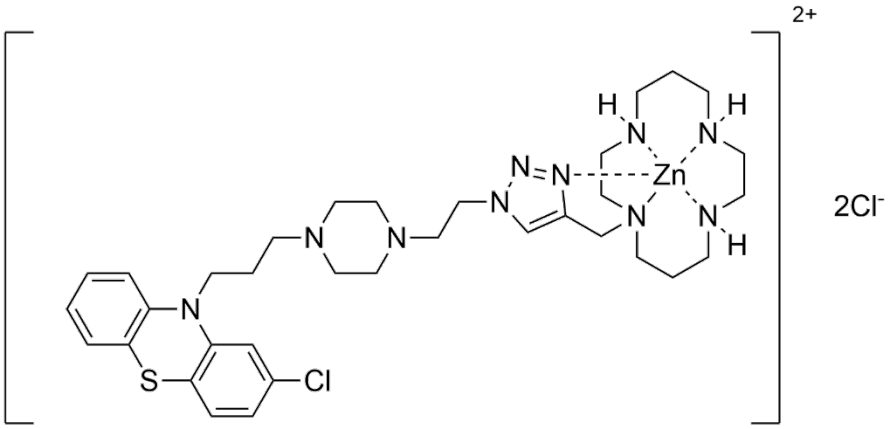

A solution of **49** (0.012 mg, 0.016 mmol) in methanol (1.0 mL) was added to a suspension of Ambersep 900 hydroxide form resin (~50 mg) in methanol (2.0 mL) that had been pre-swollen for 30 min. The mixture was stirred at rt for 30 min and filtered.

Copper(II) chloride dihydrate (0.003 mg, 0.021 mmol) was added to the filtrate and the mixture stirred at rt for 4 h. The solution was concentrated under reduced pressure to a volume of ~1 mL and diethyl ether (~5 mL) was added, resulting in the precipitation of a white. This was repeated twice and the resulting solid was dried *in vacuo* to give a white powder (0.005 g, 36%). **LRMS** (ESI+): *m/z* 366.11[M+H]$^+$. **HRMS** (ESI+): *m/z* calc. for $C_{34}H_{51}Cl_2N_{10}SZn^+$ 767.26524 [M-Cl]$^+$, found 767.26526. **FTIR**: 3369. 2930, 2874, 2801, 1659, 1594, 1562.

Tri-tert-butyl 2,2',2''-(11-(prop-2-yn-1-yl)-1,4,8,11-tetraazacyclotetradecane-1,4,8-triyl)triacetate 124[301]

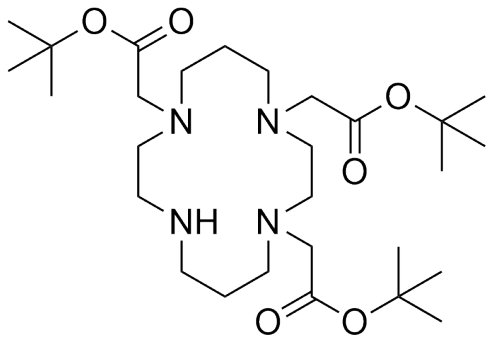

To a suspension of cyclam (0.499 g, 2.492 mmol) and sodium hydrogen carbonate (0.338 g, 4.023 mmol) in acetonitrile (50 mL) was added dropwise *tert*-butyl bromoacetate (1.10 mL, 7.510 mmol) over 30 min at 0° C. The mixture was allowed to warm to rt and was stirred for 48 h. The solids were removed *via* vacuum filtration and the filtrate was concentrated under reduced pressure at 30° C to give a grey gum. The crude product was purified *via* automated flash column chromatography (5% MeOH in DCM) to afford the product as a colourless foam (0.511 g, 38%). **^{1}H NMR** (300 MHz, Acetonitrile-d3) δ 3.24 (d, *J* = 25.3 Hz, 6H), 2.66 (ddt, *J* = 22.7, 11.7, 4.5 Hz, 12H), 2.32 (bs, 5H), 1.60 (dtd, *J* = 17.0, 11.2, 4.9 Hz, 4H), 1.46 (d, *J* = 1.2 Hz, 27H). **LRMS** (ESI+): *m/z* 543.41 [M+H]$^+$. **FTIR** (ATR) ν_{max}/cm^{-1}**:** 2959, 2868, 2709, 1725. Spectroscopic data was in agreement with literature.

Tri-tert-butyl 2,2',2''-(11-(prop-2-yn-1-yl)-1,4,8,11-tetraazacyclotetradecane-1,4,8-triyl)triacetate 125

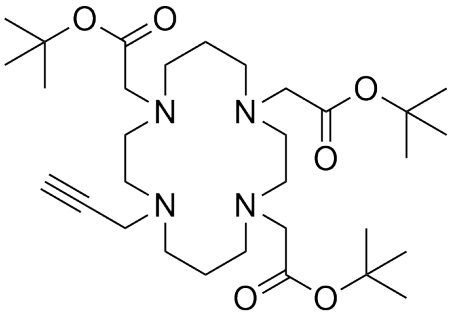

To a solution of **124** (0.484 g, 0.891 mmol) in acetonitrile (15 ml) was added potassium carbonate (0.138 g, 0.996 mmol) and propargyl bromide (0.12 mL, 1.08 mmol) and the mixture was stirred at rt for 24 h. The solids were removed *via* vacuum filtration and the filtrate was concentrated under reduced pressure at 30 °C to give an orange oil. The crude product was purified *via* automated flash column chromatography (6% MeOH in DCM) to give the product as a yellow oil (0.231 g, 45%). **^{1}H NMR** (500 MHz, Acetonitrile-d3) δ 3.57 (d, *J* = 2.4 Hz, 2H), 3.33 (s, 2H), 3.25 (d, *J* = 13.6 Hz, 4H), 2.77–2.64 (m, 16H), 2.11–2.08 (m, 1H), 1.62 (dq, *J* = 12.8, 6.4 Hz, 4H), 1.50 – 1.38 (m, 27H). **^{13}C NMR** (126 MHz, CD3CN) δ 207.67, 207.52, 207.46, 207.40, 207.35, 171.33, 171.13, 117.86, 81.27, 81.21, 78.80, 78.54, 78.28, 74.83, 56.53, 56.41, 56.18, 51.72, 51.28, 50.64, 42.31, 30.99, 30.50, 30.41, 30.31, 30.25, 30.16, 30.10, 30.00, 29.90, 29.85, 29.75, 29.69, 29.60, 27.98, 24.84, 24.40, 1.39, 1.23, 1.06, 0.90, 0.74, 0.57, 0.40. **LRMS** (ESI+): *m/z* 581.44 $[M+H]^+$. **HRMS** (ESI+): *m/z* calc. for $C_{31}H_{57}N_4O_6^+$ 581.42726 $[M+H]^+$, found 581.42753. **FTIR** (ATR) ν_{max}/cm^{-1}: 2975, 2931, 2819, 1720.

Tri-tert-butyl 2,2',2''-(11-((1-(2-(4-(3-(2-chloro-10H-phenothiazin-10-yl)propyl)piperazin-1-yl)ethyl)-1H-1,2,3-triazol-4-yl)methyl)-1,4,8,11-tetraazacyclotetradecane-1,4,8-triyl)triacetate 126

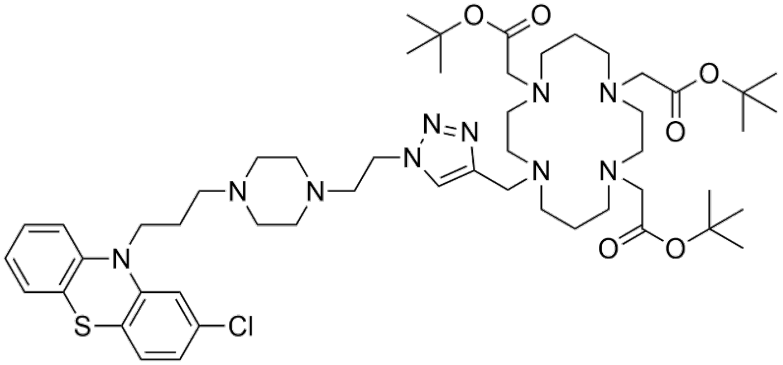

Prepared according to General Synthetic Procedure A using **125** (0.101 g, 0.173 mmol) and **62** (1.2 equiv, 0.092 g, 0.215 mmol). The crude product was then purified *via* automated flash column chromatography (reversed-phase, gradient of 10% MeOH in water to 100% MeOH)) and the fractions containing the product were lyophilized to give a white powder (0.316 g, 55%). **^{1}H NMR** (500 MHz, Chloroform-d) δ 7.59 (s, 1H), 7.17–7.08 (m, 2H), 7.00 (d, *J* = 8.1 Hz, 1H), 6.94 – 6.82 (m, 4H), 4.42 (t, *J* = 6.5 Hz, 2H), 3.90 (t, *J* = 6.8 Hz, 2H), 3.77 (s, 2H), 3.46 (s, 1H), 3.26 (d, *J* = 4.6 Hz, 4H), 3.20 (s, 2H), 2.82–2.63 (m, 14H), 2.59–2.38 (m, 14H), 1.92 (p, *J* = 6.8 Hz, 3H), 1.72 – 1.58 (m, 4H), 1.51 – 1.38 (m, 27H). **^{13}C NMR** (126 MHz, Chloroform-d) δ 171.05, 171.00, 146.48, 145.10, 144.51, 133.18, 127.85, 127.47, 127.40, 124.73, 123.47, 123.01, 122.86, 122.20, 115.83, 115.80, 80.61, 77.32, 77.07, 76.81, 57.58, 56.55, 56.50, 56.41, 55.36, 53.26, 53.15, 51.30, 51.17, 51.01, 50.83, 49.43, 47.59, 45.26, 28.22, 25.28, 24.82, 24.27. **LRMS** (ESI+): *m/z* 1009.67 $[M+H]^+$. **HRMS** (ESI+): *m/z* calc. for $C_{52}H_{82}ClN_{10}O_6S^+$ 1009.58226 $[M+H]^+$, found 1009.58230. **FTIR**: 3460, 2973, 2814, 2362, 1725, 1592, 1567.

2,2',2''-(11-((1-(2-(4-(3-(2-Chloro-10H-phenothiazin-10-yl)propyl)piperazin-1-yl)ethyl-1H-1,2,3-triazol-4-yl)methyl)-1,4,8,11-tetraazacyclotetradecane-1,4,8-triyl)triacetic acid 119

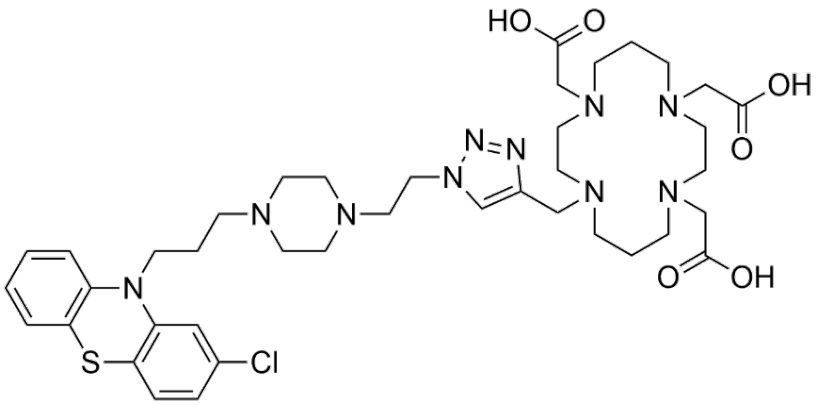

Prepared according to General Synthetic Procedure B using **126** (0.064 g, 0.064 mmol). The product was obtained as an off-white solid (0.043 g, 79%). **^{1}H NMR** (500 MHz, DMSO-d6) δ 8.10–7.97 (m, 1H), 7.21 (t, *J* = 7.8 Hz, 1H), 7.13 (dd, *J* = 8.2, 6.1 Hz, 2H), 7.10 – 7.02 (m, 2H), 6.96 (t, *J* = 7.4 Hz, 2H), 4.43 (q, *J* = 7.5, 7.0 Hz, 2H), 3.93 (t, *J* = 6.7 Hz, 2H), 3.86 (s, 2H), 3.29 (d, *J* = 4.3 Hz, 3H), 3.22 (s, 1H), 2.96 – 2.88 (m, 4H), 2.88–2.77 (m, 4H), 2.73 (t, *J* = 6.3 Hz, 2H), 2.68 (s, 2H), 2.57 (q, *J* = 6.3 Hz, 2H), 2.51 (q, *J* = 2.4, 1.9 Hz, 2H), 2.47–2.31 (m, 13H), 1.87–1.61 (m, 4H). **^{13}C NMR** (126 MHz, DMSO) δ 146.71, 144.37, 132.91, 128.51, 128.27, 127.65, 123.62, 123.45, 122.91, 122.51, 116.75, 116.17, 65.38, 57.31, 54.87, 53.09, 52.57, 44.97, 40.49, 40.33, 40.16, 39.99, 39.83, 39.66, 39.49, 23.80, 15.63. **LRMS** (ESI+): *m/z* 841.43 $[M+H]^+$. **HRMS** (ESI+): *m/z* calc. for $C_{40}H_{58}ClN_{10}O_6S^+$ 841.39445 $[M+H]^+$, found 841.39388. **FTIR** (ATR) ν_{max}/cm^{-1}: 3410, 3373, 2942, 2866, 1725, 1589, 1566.

6.4: Biological procedures

Preparation of synthetic Aβ$_{42}$:

Aβ$_{42}$ stocks were prepared from synthetic Aβ$_{42}$ according to Taylor and coworkers.[312] All solutions were kept on ice during the sample preparation. The freeze-dried peptide was resuspended in cold 50 mM NaOH to an approximate concentration of 1 mg/mL.

The peptide was dissolved by gently rotating the tube, preventing the introduction of air bubbles. The protein was transferred to a low-binding microcentrifuge tube and sonicated in ice-water for 5 min. The solution was then filtered through a 0.22 μm spin filter at 10000 rcf. The concentration was determined from the A_{280} measured using a Nanodrop. The peptide was diluted to 500 μM and 50 μL aliquots were prepared in low-binding microcentrifuge tubes, snap frozen in liquid nitrogen and stored at -80 C until required.

Thioflavin T fluorescence Assays:

$A\beta_{42}$ was prepared in triplicate in non-binding 96-well half area plates (Corning 3881) in 20 mM NaH_2PO_4 pH 7.4, 40 μM ThT, 1% DMSO and 50 μM compound to a final volume of 80 μL and final concentration of 5 μM. Plate preparation was performed at 4° C to minimize aggregation. Samples were incubated at 37° C in a POLARstar Omega microplate reader (BMG Labtech), with excitation at 440 nm and the fluorescence emission recorded at 480 nm under quiescent conditions. Stock solutions of compounds were prepared at 5 mM in DMSO.

Fluorescence titrations:

Fluorescence titrations were performed in a non-binding 96-well half area plate (corning 3881. $A\beta_{42}$ was prepared in 20 mM NaH_2PO_4 pH 7.4, 40 μM ThT, 1% DMSO to a final volume of 80 μL and final concentration of 5 μM. Samples were incubated at 37° C in a POLARstar Omega microplate reader (BMG Labtech), with excitation at 440 nm and the fluorescence emission recorded at 480 nm under quiescent conditions. Once the plateau of ThT fluorescence had been reached, a solution of the compound in DMSO was added to a final concentration of 5, 10, 25 or 50 μM and a final volume of 90 μL and the fluorescence was measured.

NMR Experiments Using ^{15}N-labelled $A\beta_{42}$

^{15}N-labelled Aβ_{42} was expressed by Sarah Ball according to the procedure by Habchi and coworkers and stored in freeze-dried aliquots at -80 °C until required.[90] The freeze-dried peptide was thawed by standing at room temperature, suspended in 10 mM NaOH to approximately 2 mg/mL and sonicated for 1 min in ice-water to dissolve the peptide. The peptide was diluted with 20 mM NaH_2PO_4 pH 6.6 to a volume of 1.5 mL and the concentration was determined from the A_{280} measured *via* Nanodrop. The peptide was diluted to a concentration of approximately 10 μM in NMR buffer consisting of 20 mM NaH_2PO_4 pH 7.0, 10% D_2O, 1% DSS, 0.1% d_6-DMSO for NMR experiments. ^{1}H-^{15}N heteronuclear single quantum coherence (HSQC) experiments were recorded overnight at 4 °C for 240 scans with a spectral width of 25 ppm (^{15}N offset at 117.5 ppm) with either 10 μM **112**, **115** or Aβ_{42} alone.

7. References

1. Anfinsen, C.B., *Principles that Govern the Folding of Protein Chains.* Science, 1973. **181**(4096): p. 223-230.
2. Kauzmann, W., *Some Factors in the Interpretation of Protein Denaturation11The preparation of this article has been assisted by a grant from the National Science Foundation*, in *Advances in Protein Chemistry*, C.B. Anfinsen, et al., Editors. 1959, Academic Press. p. 1-63.
3. Chiti, F. and C.M. Dobson, *Protein Misfolding, Amyloid Formation, and Human Disease: A Summary of Progress Over the Last Decade.* Annual Review of Biochemistry, 2017. **86**(1): p. 27-68.
4. Englander, S.W., L. Mayne, and M.M.G. Krishna, *Protein folding and misfolding: mechanism and principles.* Quarterly Reviews of Biophysics, 2007. **40**(4): p. 1-41.
5. Serpell, L.C., et al., *The protofilament substructure of amyloid fibrils11Edited by F. E. Cohen.* Journal of Molecular Biology, 2000. **300**(5): p. 1033-1039.
6. Fitzpatrick, A.W.P., et al., *Atomic structure and hierarchical assembly of a cross-β amyloid fibril.* Proceedings of the National Academy of Sciences, 2013. **110**(14): p. 5468-5473.
7. Sunde, M., et al., *Common core structure of amyloid fibrils by synchrotron X-ray diffraction11Edited by F. E. Cohen.* Journal of Molecular Biology, 1997. **273**(3): p. 729-739.
8. Fändrich, M. and C.M. Dobson, *The behaviour of polyamino acids reveals an inverse side chain effect in amyloid structure formation.* The EMBO Journal, 2002. **21**(21): p. 5682-5690.
9. Baldwin, A.J., et al., *Metastability of Native Proteins and the Phenomenon of Amyloid Formation.* Journal of the American Chemical Society, 2011. **133**(36): p. 14160-14163.
10. Hardy, J. and D. Allsop, *Amyloid deposition as the central event in the aetiology of Alzheimer's disease.* Trends in Pharmacological Sciences, 1991. **12**: p. 383-388.
11. Beyreuther, K. and C.L. Masters, *Amyloid Precursor Protein (APP) and BZA4 Amyloid in the Etiology of Alzheimer's Disease: Precursor-Product Relationships in the Derangement of Neuronal Function.* Brain Pathology, 1991. **1**(4): p. 241-251.
12. Hardy, J. and G. Higgins, *Alzheimer's disease: the amyloid cascade hypothesis.* Science, 1992. **256**(5054): p. 184-185.
13. Ballatore, C., V.M.Y. Lee, and J.Q. Trojanowski, *Tau-mediated neurodegeneration in Alzheimer's disease and related disorders.* Nature Reviews Neuroscience, 2007. **8**(9): p. 663-672.
14. Berriman, J., et al., *Tau filaments from human brain and from in vitro assembly of recombinant protein show cross-β structure.* Proceedings of the National Academy of Sciences, 2003. **100**(15): p. 9034-9038.
15. Spillantini, M.G. and M. Goedert, *Tau pathology and neurodegeneration.* The Lancet Neurology, 2013. **12**(6): p. 609-622.
16. de Lau, L.M.L. and M.M.B. Breteler, *Epidemiology of Parkinson's disease.* The Lancet Neurology, 2006. **5**(6): p. 525-535.

17. Gibb, W.R. and A.J. Lees, *The relevance of the Lewy body to the pathogenesis of idiopathic Parkinson's disease.* Journal of Neurology, Neurosurgery & Psychiatry, 1988. **51**(6): p. 745-752.
18. McKinley, M.P., D.C. Bolton, and S.B. Prusiner, *A protease-resistant protein is a structural component of the Scrapie prion.* Cell, 1983. **35**(1): p. 57-62.
19. Collinge, J., et al., *Molecular analysis of prion strain variation and the aetiology of 'new variant' CJD.* Nature, 1996. **383**(6602): p. 685-690.
20. Brown, P., et al., *Iatrogenic Creutzfeldt–Jakob disease at the millennium.* Neurology, 2000. **55**(8): p. 1075-1081.
21. Imran, M. and S. Mahmood, *An overview of human prion diseases.* Virology Journal, 2011. **8**(1): p. 559.
22. Liberski, P.P. and P. Brown, *Kuru: Its ramifications after fifty years.* Experimental Gerontology, 2009. **44**(1): p. 63-69.
23. Buchanan, J.A., et al., *Functional Amyloids: Where Supramolecular Amyloid Assembly Controls Biological Activity or Generates New Functionality.* Journal of Molecular Biology, 2023. **435**(11): p. 167919.
24. Fowler, D.M., et al., *Functional amyloid – from bacteria to humans.* Trends in Biochemical Sciences, 2007. **32**(5): p. 217-224.
25. Chapman, M.R., et al., *Role of Escherichia coli Curli Operons in Directing Amyloid Fiber Formation.* Science, 2002. **295**(5556): p. 851-855.
26. Wang, X., et al., *Gatekeeper residues in the major curlin subunit modulate bacterial amyloid fiber biogenesis.* Proceedings of the National Academy of Sciences, 2010. **107**(1): p. 163-168.
27. Dueholm, M.S., et al., *Functional amyloid in Pseudomonas.* Molecular Microbiology, 2010. **77**(4): p. 1009-1020.
28. Romero, D., et al., *Amyloid fibers provide structural integrity to Bacillus subtilis biofilms.* Proceedings of the National Academy of Sciences, 2010. **107**(5): p. 2230-2234.
29. Taglialegna, A., et al., *Staphylococcal Bap Proteins Build Amyloid Scaffold Biofilm Matrices in Response to Environmental Signals.* PLOS Pathogens, 2016. **12**(6): p. e1005711.
30. Kaur, G., et al., *Mycobacterium tuberculosis CarD, an essential global transcriptional regulator forms amyloid-like fibrils.* Scientific Reports, 2018. **8**(1): p. 10124.
31. Alteri, C.J., et al., *Mycobacterium tuberculosis produces pili during human infection.* Proceedings of the National Academy of Sciences, 2007. **104**(12): p. 5145-5150.
32. Wösten, H.A.B., et al., *How a fungus escapes the water to grow into the air.* Current Biology, 1999. **9**(2): p. 85-88.
33. Wessels, J.G.H., *Hydrophobins: Proteins that Change the Nature of the Fungal Surface*, in *Advances in Microbial Physiology*, R.K. Poole, Editor. 1996, Academic Press. p. 1-45.
34. Aimanianda, V., et al., *Surface hydrophobin prevents immune recognition of airborne fungal spores.* Nature, 2009. **460**(7259): p. 1117-1121.
35. Claessen, D., et al., *A novel class of secreted hydrophobic proteins is involved in aerial hyphae formation in Streptomyces coelicolor by forming amyloid-like fibrils.* Genes & Development, 2003. **17**(14): p. 1714-1726.

36. Lacroute, F., *Non-Mendelian Mutation Allowing Ureidosuccinic Acid Uptake in Yeast.* Journal of Bacteriology, 1971. **106**(2): p. 519-522.
37. Cox, B.S., *Ψ, A cytoplasmic suppressor of super-suppressor in yeast.* Heredity, 1965. **20**(4): p. 505-521.
38. Wickner, R., *[URE3] as an altered URE2 protein: evidence for a prion analog in Saccharomyces cerevisiae.* Science, 1994. **264**(5158): p. 566-569.
39. Cox, B.S., M.F. Tuite, and C.S. McLaughlin, *The ψ factor of yeast: A problem in inheritance.* Yeast, 1988. **4**(3): p. 159-178.
40. True, H.L. and S.L. Lindquist, *A yeast prion provides a mechanism for genetic variation and phenotypic diversity.* Nature, 2000. **407**(6803): p. 477-483.
41. Shorter, J. and S. Lindquist, *Prions as adaptive conduits of memory and inheritance.* Nature Reviews Genetics, 2005. **6**(6): p. 435-450.
42. Daskalov, A., W. Dyrka, and S.J. Saupe, *Theme and variations: evolutionary diversification of the HET-s functional amyloid motif.* Scientific Reports, 2015. **5**(1): p. 12494.
43. Tharp, W.G. and I.N. Sarkar, *Origins of amyloid-β.* BMC Genomics, 2013. **14**(1): p. 290.
44. Tyan, S.-H., et al., *Amyloid precursor protein (APP) regulates synaptic structure and function.* Molecular and Cellular Neuroscience, 2012. **51**(1): p. 43-52.
45. Hoe, H.-S., H.-K. Lee, and D.T.S. Pak, *The Upside of APP at Synapses.* CNS Neuroscience & Therapeutics, 2012. **18**(1): p. 47-56.
46. Barnham, K.J., et al., *Structure of the Alzheimer's Disease Amyloid Precursor Protein Copper Binding Domain: A REGULATOR OF NEURONAL COPPER HOMEOSTASIS.* Journal of Biological Chemistry, 2003. **278**(19): p. 17401-17407.
47. Duce, J.A., et al., *Iron-Export Ferroxidase Activity of β-Amyloid Precursor Protein Is Inhibited by Zinc in Alzheimer's Disease.* Cell, 2010. **142**(6): p. 857-867.
48. Swomley, A.M., et al., *Abeta, oxidative stress in Alzheimer disease: Evidence based on proteomics studies.* Biochimica et Biophysica Acta (BBA) - Molecular Basis of Disease, 2014. **1842**(8): p. 1248-1257.
49. Haass, C., *Take five—BACE and the γ-secretase quartet conduct Alzheimer's amyloid β-peptide generation.* The EMBO Journal, 2004. **23**(3): p. 483-488.
50. Jarrett, J.T. and P.T. Lansbury, *Seeding "one-dimensional crystallization" of amyloid: A pathogenic mechanism in Alzheimer's disease and scrapie?* Cell, 1993. **73**(6): p. 1055-1058.
51. Hardy, J. and D.J. Selkoe, *The Amyloid Hypothesis of Alzheimer's Disease: Progress and Problems on the Road to Therapeutics.* Science, 2002. **297**(5580): p. 353-356.
52. Benilova, I., E. Karran, and B. De Strooper, *The toxic Aβ oligomer and Alzheimer's disease: an emperor in need of clothes.* Nature Neuroscience, 2012. **15**(3): p. 349-357.
53. Zempel, H., et al., *Aβ Oligomers Cause Localized Ca²⁺ Elevation, Missorting of Endogenous Tau into Dendrites, Tau Phosphorylation, and Destruction of Microtubules and Spines.* The Journal of Neuroscience, 2010. **30**(36): p. 11938-11950.
54. Wang, X., et al., *Amyloid-β-Derived Diffusible Ligands Cause Impaired Axonal Transport of Mitochondria in Neurons.* Neurodegenerative Diseases, 2010. **7**(1-3): p. 56-59.

55. Walsh, D.M., et al., *Naturally secreted oligomers of amyloid β protein potently inhibit hippocampal long-term potentiation in vivo.* Nature, 2002. **416**(6880): p. 535-539.
56. Jin, M., et al., *Soluble amyloid β-protein dimers isolated from Alzheimer cortex directly induce Tau hyperphosphorylation and neuritic degeneration.* Proceedings of the National Academy of Sciences, 2011. **108**(14): p. 5819-5824.
57. Shankar, G.M., et al., *Amyloid-β protein dimers isolated directly from Alzheimer's brains impair synaptic plasticity and memory.* Nature Medicine, 2008. **14**(8): p. 837-842.
58. Lambert, M.P., et al., *Diffusible, nonfibrillar ligands derived from Aβ_{1–42} are potent central nervous system neurotoxins.* Proceedings of the National Academy of Sciences, 1998. **95**(11): p. 6448-6453.
59. Jarrett, J.T., E.P. Berger, and P.T. Lansbury, *The carboxy terminus of the .beta. amyloid protein is critical for the seeding of amyloid formation: Implications for the pathogenesis of Alzheimer's disease.* Biochemistry, 1993. **32**(18): p. 4693-4697.
60. Ferrone, F., *[17] Analysis of protein aggregation kinetics*, in *Methods in Enzymology*. 1999, Academic Press. p. 256-274.
61. Morris, A.M., M.A. Watzky, and R.G. Finke, *Protein aggregation kinetics, mechanism, and curve-fitting: A review of the literature.* Biochimica et Biophysica Acta (BBA) - Proteins and Proteomics, 2009. **1794**(3): p. 375-397.
62. Lee, J., et al., *Amyloid-β forms fibrils by nucleated conformational conversion of oligomers.* Nature Chemical Biology, 2011. **7**(9): p. 602-609.
63. Arosio, P., T.P.J. Knowles, and S. Linse, *On the lag phase in amyloid fibril formation.* Physical Chemistry Chemical Physics, 2015. **17**(12): p. 7606-7618.
64. Michaels, T.C.T., et al., *Dynamics of oligomer populations formed during the aggregation of Alzheimer's Aβ42 peptide.* Nature Chemistry, 2020. **12**(5): p. 445-451.
65. Tycko, R. and R.B. Wickner, *Molecular Structures of Amyloid and Prion Fibrils: Consensus versus Controversy.* Accounts of Chemical Research, 2013. **46**(7): p. 1487-1496.
66. Tycko, R., *Physical and structural basis for polymorphism in amyloid fibrils.* Protein Science, 2014. **23**(11): p. 1528-1539.
67. Antzutkin, O.N., et al., *Supramolecular Structural Constraints on Alzheimer's β-Amyloid Fibrils from Electron Microscopy and Solid-State Nuclear Magnetic Resonance.* Biochemistry, 2002. **41**(51): p. 15436-15450.
68. Ehrnhoefer, D.E., et al., *EGCG redirects amyloidogenic polypeptides into unstructured, off-pathway oligomers.* Nature Structural & Molecular Biology, 2008. **15**(6): p. 558-566.
69. Paravastu, A.K., et al., *Molecular structural basis for polymorphism in Alzheimer's β-amyloid fibrils.* Proceedings of the National Academy of Sciences, 2008. **105**(47): p. 18349-18354.
70. Shewmaker, F., R.P. McGlinchey, and R.B. Wickner, *Structural Insights into Functional and Pathological Amyloid.* Journal of Biological Chemistry, 2011. **286**(19): p. 16533-16540.
71. Iadanza, M.G., et al., *A new era for understanding amyloid structures and disease.* Nature Reviews Molecular Cell Biology, 2018. **19**(12): p. 755-773.

72. Sawaya, M.R., et al., *Atomic structures of amyloid cross-β spines reveal varied steric zippers.* Nature, 2007. **447**(7143): p. 453-457.
73. Colvin, M.T., et al., *Atomic Resolution Structure of Monomorphic Aβ42 Amyloid Fibrils.* Journal of the American Chemical Society, 2016. **138**(30): p. 9663-9674.
74. Gremer, L., et al., *Fibril structure of amyloid-β(1–42) by cryo–electron microscopy.* Science, 2017. **358**(6359): p. 116-119.
75. Doody, R.S., et al., *A Phase 3 Trial of Semagacestat for Treatment of Alzheimer's Disease.* New England Journal of Medicine, 2013. **369**(4): p. 341-350.
76. Coric, V., et al., *Targeting Prodromal Alzheimer Disease With Avagacestat: A Randomized Clinical Trial.* JAMA Neurology, 2015. **72**(11): p. 1324-1333.
77. Muntimadugu, E., et al., *Intranasal delivery of nanoparticle encapsulated tarenflurbil: A potential brain targeting strategy for Alzheimer's disease.* European Journal of Pharmaceutical Sciences, 2016. **92**: p. 224-234.
78. Wong, G.T., et al., *Chronic treatment with the gamma-secretase inhibitor LY-411,575 inhibits beta-amyloid peptide production and alters lymphopoiesis and intestinal cell differentiation.* J Biol Chem, 2004. **279**(13): p. 12876-82.
79. Atri, A., *Current and Future Treatments in Alzheimer's Disease.* Semin Neurol, 2019. **39**(2): p. 227-240.
80. The Lancet, N., *Solanezumab: too late in mild Alzheimer's disease?* The Lancet Neurology, 2017. **16**(2): p. 97.
81. Vandenberghe, R., et al., *Bapineuzumab for mild to moderate Alzheimer's disease in two global, randomized, phase 3 trials.* Alzheimer's Research & Therapy, 2016. **8**(1): p. 18.
82. van Dyck, C.H., et al., *Lecanemab in Early Alzheimer's Disease.* New England Journal of Medicine, 2022. **388**(1): p. 9-21.
83. Budd Haeberlein, S., et al., *Two Randomized Phase 3 Studies of Aducanumab in Early Alzheimer's Disease.* The Journal of Prevention of Alzheimer's Disease, 2022. **9**(2): p. 197-210.
84. Miller, Y., B. Ma, and R. Nussinov, *Polymorphism in Alzheimer Aβ Amyloid Organization Reflects Conformational Selection in a Rugged Energy Landscape.* Chemical Reviews, 2010. **110**(8): p. 4820-4838.
85. Liang, C., et al., *Kinetic Intermediates in Amyloid Assembly.* Journal of the American Chemical Society, 2014. **136**(43): p. 15146-15149.
86. Cohen, S.I.A., et al., *Proliferation of amyloid-β42 aggregates occurs through a secondary nucleation mechanism.* Proceedings of the National Academy of Sciences, 2013. **110**(24): p. 9758-9763.
87. Arosio, P., et al., *Chemical kinetics for drug discovery to combat protein aggregation diseases.* Trends in Pharmacological Sciences, 2014. **35**(3): p. 127-135.
88. Cohen, S.I.A., et al., *A molecular chaperone breaks the catalytic cycle that generates toxic Aβ oligomers.* Nature Structural & Molecular Biology, 2015. **22**(3): p. 207-213.
89. Aprile, F.A., et al., *Selective targeting of primary and secondary nucleation pathways in Aβ42 aggregation using a rational antibody scanning method.* Science Advances, 2017. **3**(6): p. e1700488.

90. Habchi, J., et al., *Systematic development of small molecules to inhibit specific microscopic steps of Aβ42 aggregation in Alzheimer's disease.* Proceedings of the National Academy of Sciences, 2017. **114**(2): p. E200-E208.
91. Heller, G.T., et al., *Small-molecule sequestration of amyloid-β as a drug discovery strategy for Alzheimer's disease.* Science Advances, 2020. **6**(45): p. eabb5924.
92. Löhr, T., et al., *A Small Molecule Stabilizes the Disordered Native State of the Alzheimer's Aβ Peptide.* ACS Chemical Neuroscience, 2022. **13**(12): p. 1738-1745.
93. Heller, G.T., P. Sormanni, and M. Vendruscolo, *Targeting disordered proteins with small molecules using entropy.* Trends in Biochemical Sciences, 2015. **40**(9): p. 491-496.
94. McColl, G., et al., *Utility of an improved model of amyloid-beta (Aβ1-42) toxicity in Caenorhabditis elegansfor drug screening for Alzheimer's disease.* Molecular Neurodegeneration, 2012. **7**(1): p. 57.
95. Kametani, F. and M. Hasegawa, *Reconsideration of Amyloid Hypothesis and Tau Hypothesis in Alzheimer's Disease.* Frontiers in Neuroscience, 2018. **12**.
96. Webster, S.J., et al., *Using mice to model Alzheimer's dementia: an overview of the clinical disease and the preclinical behavioral changes in 10 mouse models.* Frontiers in Genetics, 2014. **5**.
97. Burley, S.K., et al., *Protein Data Bank (PDB): The Single Global Macromolecular Structure Archive*, in *Protein Crystallography: Methods and Protocols*, A. Wlodawer, Z. Dauter, and M. Jaskolski, Editors. 2017, Springer New York: New York, NY. p. 627-641.
98. Davis, A.M., S.J. Teague, and G.J. Kleywegt, *Application and Limitations of X-ray Crystallographic Data in Structure-Based Ligand and Drug Design.* Angewandte Chemie International Edition, 2003. **42**(24): p. 2718-2736.
99. Blundell, T.L., H. Jhoti, and C. Abell, *High-throughput crystallography for lead discovery in drug design.* Nature Reviews Drug Discovery, 2002. **1**(1): p. 45-54.
100. Wallin, E. and G. von Heijne, *Genome-wide analysis of integral membrane proteins from eubacterial, archaean, and eukaryotic organisms.* Protein Sci, 1998. **7**(4): p. 1029-38.
101. Overington, J.P., B. Al-Lazikani, and A.L. Hopkins, *How many drug targets are there?* Nature Reviews Drug Discovery, 2006. **5**(12): p. 993-996.
102. Hauser, A.S., et al., *Trends in GPCR drug discovery: new agents, targets and indications.* Nature Reviews Drug Discovery, 2017. **16**(12): p. 829-842.
103. Rawlings, Andrea E., *Membrane proteins: always an insoluble problem?* Biochemical Society Transactions, 2016. **44**(3): p. 790-795.
104. Tate, C.G., *Practical Considerations of Membrane Protein Instability during Purification and Crystallisation*, in *Heterologous Expression of Membrane Proteins: Methods and Protocols*, I. Mus-Veteau, Editor. 2010, Humana Press: Totowa, NJ. p. 187-203.
105. Laskowski, R.A., *Structural Quality Assurance*, in *Structural Bioinformatics*. 2003. p. 273-303.
106. Scheeff, E.D. and J.L. Fink, *Fundamentals of Protein Structure*, in *Structural Bioinformatics*. 2003. p. 15-39.
107. Brünger, A.T., *X-ray crystallography and NMR reveal complementary views of structure and dynamics.* Nature structural biology, 1997. **4 Suppl**: p. 862-865.

108. Uversky, V.N., *Functional roles of transiently and intrinsically disordered regions within proteins.* The FEBS Journal, 2015. **282**(7): p. 1182-1189.
109. Wright, P.E. and H.J. Dyson, *Intrinsically unstructured proteins: re-assessing the protein structure-function paradigm.* Journal of Molecular Biology, 1999. **293**(2): p. 321-331.
110. Jakob, U., R. Kriwacki, and V.N. Uversky, *Conditionally and Transiently Disordered Proteins: Awakening Cryptic Disorder To Regulate Protein Function.* Chemical Reviews, 2014. **114**(13): p. 6779-6805.
111. McNeil, B.W.J. and N.R. Thompson, *X-ray free-electron lasers.* Nature Photonics, 2010. **4**(12): p. 814-821.
112. Spence, J., *XFELs for structure and dynamics in biology.* IUCrJ, 2017. **4**(4): p. 322-339.
113. Henderson, R. and B.C. Clarke, *Cryo-protection of protein crystals against radiation damage in electron and X-ray diffraction.* Proceedings of the Royal Society of London. Series B: Biological Sciences, 1990. **241**(1300): p. 6-8.
114. Boutet, S., et al., *High-Resolution Protein Structure Determination by Serial Femtosecond Crystallography.* Science, 2012. **337**(6092): p. 362-364.
115. Neutze, R., et al., *Potential for biomolecular imaging with femtosecond X-ray pulses.* Nature, 2000. **406**(6797): p. 752-757.
116. Kühlbrandt, W., *Cryo-EM enters a new era.* eLife, 2014. **3**: p. e03678.
117. Murata, K. and M. Wolf, *Cryo-electron microscopy for structural analysis of dynamic biological macromolecules.* Biochimica et Biophysica Acta (BBA) - General Subjects, 2018. **1862**(2): p. 324-334.
118. Nogales, E., *The development of cryo-EM into a mainstream structural biology technique.* Nature Methods, 2016. **13**(1): p. 24-27.
119. Yip, K.M., et al., *Atomic-resolution protein structure determination by cryo-EM.* Nature, 2020. **587**(7832): p. 157-161.
120. Shi, D., et al., *Three-dimensional electron crystallography of protein microcrystals.* eLife, 2013. **2**: p. e01345.
121. Hattne, J., et al., *MicroED data collection and processing.* Acta Crystallographica Section A, 2015. **71**(4): p. 353-360.
122. Shi, D., et al., *The collection of MicroED data for macromolecular crystallography.* Nature Protocols, 2016. **11**(5): p. 895-904.
123. Senior, A.W., et al., *Improved protein structure prediction using potentials from deep learning.* Nature, 2020. **577**(7792): p. 706-710.
124. Varadi, M. and S. Velankar, *The impact of AlphaFold Protein Structure Database on the fields of life sciences.* PROTEOMICS, 2023. **23**(17): p. 2200128.
125. Laurents, D.V., *AlphaFold 2 and NMR Spectroscopy: Partners to Understand Protein Structure, Dynamics and Function.* Frontiers in Molecular Biosciences, 2022. **9**.
126. Lindorff-Larsen, K. and B.B. Kragelund, *On the Potential of Machine Learning to Examine the Relationship Between Sequence, Structure, Dynamics and Function of Intrinsically Disordered Proteins.* Journal of Molecular Biology, 2021. **433**(20): p. 167196.
127. Ruff, K.M. and R.V. Pappu, *AlphaFold and Implications for Intrinsically Disordered Proteins.* Journal of Molecular Biology, 2021. **433**(20): p. 167208.

128. Kwan, A.H., et al., *Macromolecular NMR spectroscopy for the non-spectroscopist.* The FEBS Journal, 2011. **278**(5): p. 687-703.
129. Wüthrich, K., et al., *Sequential resonance assignments as a basis for determination of spatial protein structures by high resolution proton nuclear magnetic resonance.* Journal of Molecular Biology, 1982. **155**(3): p. 311-319.
130. Clore, G.M. and A.M. Gronenborn, *Applications of three- and four-dimensional heteronuclear NMR spectroscopy to protein structure determination.* Progress in Nuclear Magnetic Resonance Spectroscopy, 1991. **23**(1): p. 43-92.
131. Wüthrich, K., M. Billeter, and W. Braun, *Polypeptide secondary structure determination by nuclear magnetic resonance observation of short proton-proton distances.* Journal of Molecular Biology, 1984. **180**(3): p. 715-740.
132. Pardi, A., M. Billeter, and K. Wüthrich, *Calibration of the angular dependence of the amide proton-Cα proton coupling constants, 3JHNα, in a globular protein: Use of 3JHNα for identification of helical secondary structure.* Journal of Molecular Biology, 1984. **180**(3): p. 741-751.
133. Cavalli, A., et al., *Protein structure determination from NMR chemical shifts.* Proceedings of the National Academy of Sciences, 2007. **104**(23): p. 9615-9620.
134. Nabuurs, S.B., et al., *Traditional Biomolecular Structure Determination by NMR Spectroscopy Allows for Major Errors.* PLOS Computational Biology, 2006. **2**(2): p. e9.
135. Svergun, D.I., *Restoring Low Resolution Structure of Biological Macromolecules from Solution Scattering Using Simulated Annealing.* Biophysical Journal, 1999. **76**(6): p. 2879-2886.
136. Tjandra, N. and A. Bax, *Direct Measurement of Distances and Angles in Biomolecules by NMR in a Dilute Liquid Crystalline Medium.* Science, 1997. **278**(5340): p. 1111-1114.
137. Fleming, K., et al., *Cellulose Crystallites: A New and Robust Liquid Crystalline Medium for the Measurement of Residual Dipolar Couplings.* Journal of the American Chemical Society, 2000. **122**(21): p. 5224-5225.
138. Clore, G.M., M.R. Starich, and A.M. Gronenborn, *Measurement of Residual Dipolar Couplings of Macromolecules Aligned in the Nematic Phase of a Colloidal Suspension of Rod-Shaped Viruses.* Journal of the American Chemical Society, 1998. **120**(40): p. 10571-10572.
139. Rückert, M. and G. Otting, *Alignment of Biological Macromolecules in Novel Nonionic Liquid Crystalline Media for NMR Experiments.* Journal of the American Chemical Society, 2000. **122**(32): p. 7793-7797.
140. Tolman, J.R., et al., *Nuclear magnetic dipole interactions in field-oriented proteins: information for structure determination in solution.* Proceedings of the National Academy of Sciences, 1995. **92**(20): p. 9279-9283.
141. Pintacuda, G., et al., *Site-specific Labelling with a Metal Chelator for Protein-structure Refinement.* Journal of Biomolecular NMR, 2004. **29**(3): p. 351-361.
142. Häussinger, D., J.-r. Huang, and S. Grzesiek, *DOTA-M8: An Extremely Rigid, High-Affinity Lanthanide Chelating Tag for PCS NMR Spectroscopy.* Journal of the American Chemical Society, 2009. **131**(41): p. 14761-14767.
143. Graham, B., et al., *DOTA-Amide Lanthanide Tag for Reliable Generation of Pseudocontact Shifts in Protein NMR Spectra.* Bioconjugate Chemistry, 2011. **22**(10): p. 2118-2125.

144. Ikegami, T., et al., *Novel Techniques for Weak Alignment of Proteins in Solution Using Chemical Tags Coordinating Lanthanide Ions.* Journal of Biomolecular NMR, 2004. **29**(3): p. 339-349.
145. Prudêncio, M., et al., *A Caged Lanthanide Complex as a Paramagnetic Shift Agent for Protein NMR.* Chemistry – A European Journal, 2004. **10**(13): p. 3252-3260.
146. Vlasie, M.D., et al., *Long-Range-Distance NMR Effects in a Protein Labeled with a Lanthanide–DOTA Chelate.* Chemistry – A European Journal, 2007. **13**(6): p. 1715-1723.
147. Donaldson, L.W., et al., *Structural Characterization of Proteins with an Attached ATCUN Motif by Paramagnetic Relaxation Enhancement NMR Spectroscopy.* Journal of the American Chemical Society, 2001. **123**(40): p. 9843-9847.
148. Battiste, J.L. and G. Wagner, *Utilization of Site-Directed Spin Labeling and High-Resolution Heteronuclear Nuclear Magnetic Resonance for Global Fold Determination of Large Proteins with Limited Nuclear Overhauser Effect Data.* Biochemistry, 2000. **39**(18): p. 5355-5365.
149. Bertini, I., et al., *Magnetic Susceptibility Tensor Anisotropies for a Lanthanide Ion Series in a Fixed Protein Matrix.* Journal of the American Chemical Society, 2001. **123**(18): p. 4181-4188.
150. Alsaadi, B.M., F.J.C. Rossotti, and R.J.P. Williams, *Electron relaxation rates of lanthanide aquo-cations.* Journal of the Chemical Society, Dalton Transactions, 1980(11): p. 2147-2150.
151. Granot, J., *Paramagnetic relaxation in dipolar-coupled homonuclear spin systems.* Journal of Magnetic Resonance (1969), 1982. **49**(2): p. 257-270.
152. Solomon, I., *Relaxation Processes in a System of Two Spins.* Physical Review, 1955. **99**(2): p. 559-565.
153. Gottstein, D., et al., *Requirements on Paramagnetic Relaxation Enhancement Data for Membrane Protein Structure Determination by NMR.* Structure, 2012. **20**(6): p. 1019-1027.
154. Furuita, K., et al., *Utilization of paramagnetic relaxation enhancements for high-resolution NMR structure determination of a soluble loop-rich protein with sparse NOE distance restraints.* Journal of Biomolecular NMR, 2015. **61**(1): p. 55-64.
155. Clore, G.M. and J. Iwahara, *Theory, Practice, and Applications of Paramagnetic Relaxation Enhancement for the Characterization of Transient Low-Population States of Biological Macromolecules and Their Complexes.* Chemical Reviews, 2009. **109**(9): p. 4108-4139.
156. Iwahara, J. and G.M. Clore, *Detecting transient intermediates in macromolecular binding by paramagnetic NMR.* Nature, 2006. **440**(7088): p. 1227-1230.
157. Spreitzer, E., S. Usluer, and T. Madl, *Probing Surfaces in Dynamic Protein Interactions.* Journal of Molecular Biology, 2020. **432**(9): p. 2949-2972.
158. Li, Y., et al., *Membrane topology of NS2B of dengue virus revealed by NMR spectroscopy.* Biochimica et Biophysica Acta (BBA) - Biomembranes, 2015. **1848**(10, Part A): p. 2244-2252.

159. Gong, Z., et al., *Protein Structural Ensembles Visualized by Solvent Paramagnetic Relaxation Enhancement.* Angewandte Chemie International Edition, 2017. **56**(4): p. 1002-1006.
160. Kooshapur, H., C.D. Schwieters, and N. Tjandra, *Conformational Ensemble of Disordered Proteins Probed by Solvent Paramagnetic Relaxation Enhancement (sPRE).* Angewandte Chemie International Edition, 2018. **57**(41): p. 13519-13522.
161. Phillips, W.D., et al., *Proton Magnetic Resonance Studies of Chromatium High-Potential Iron Protein.* Proceedings of the National Academy of Sciences, 1970. **67**(2): p. 682-687.
162. McConnell, H.M. and R.E. Robertson, *Isotropic Nuclear Resonance Shifts.* The Journal of Chemical Physics, 1958. **29**(6): p. 1361-1365.
163. Bertini, I., et al., *Experimentally exploring the conformational space sampled by domain reorientation in calmodulin.* Proceedings of the National Academy of Sciences, 2004. **101**(18): p. 6841-6846.
164. Allegrozzi, M., et al., *Lanthanide-Induced Pseudocontact Shifts for Solution Structure Refinements of Macromolecules in Shells up to 40 Å from the Metal Ion.* Journal of the American Chemical Society, 2000. **122**(17): p. 4154-4161.
165. Yagi, H., et al., *Three-Dimensional Protein Fold Determination from Backbone Amide Pseudocontact Shifts Generated by Lanthanide Tags at Multiple Sites.* Structure, 2013. **21**(6): p. 883-890.
166. Zhuang, T., et al., *Structure determination of a Galectin-3–carbohydrate complex using paramagnetism-based NMR constraints.* Protein Science, 2008. **17**(7): p. 1220-1231.
167. John, M., et al., *Structure Determination of Protein–Ligand Complexes by Transferred Paramagnetic Shifts.* Journal of the American Chemical Society, 2006. **128**(39): p. 12910-12916.
168. Balogh, E., et al., *NMR Second Site Screening for Structure Determination of Ligands Bound in the Hydrophobic Pocket of HIV-1 gp41.* Journal of the American Chemical Society, 2009. **131**(8): p. 2821-2823.
169. Brath, U., et al., *Paramagnetic Ligand Tagging To Identify Protein Binding Sites.* Journal of the American Chemical Society, 2015. **137**(35): p. 11391-11398.
170. Morss, L.R., *Chapter 122 Comparative thermochemical and oxidation-reduction properties of lanthanides and actinides*, in *Handbook on the Physics and Chemistry of Rare Earths*. 1994, Elsevier. p. 239-291.
171. Freeman, A.J. and R.E. Watson, *Theoretical Investigation of Some Magnetic and Spectroscopic Properties of Rare-Earth Ions.* Physical Review, 1962. **127**(6): p. 2058-2075.
172. Brewer, L., *Systematics of the Properties of the Lanthanides*, in *Systematics and the Properties of the Lanthanides*, S.P. Sinha, Editor. 1983, Springer Netherlands: Dordrecht. p. 17-69.
173. Sorace, L. and D. Gatteschi, *Electronic Structure and Magnetic Properties of Lanthanide Molecular Complexes*, in *Lanthanides and Actinides in Molecular Magnetism*. 2015. p. 1-26.
174. Bünzli, J.-C.G. and S.V. Eliseeva, *Basics of Lanthanide Photophysics*, in *Lanthanide Luminescence: Photophysical, Analytical and Biological Aspects*, P. Hänninen and H. Härmä, Editors. 2011, Springer Berlin Heidelberg: Berlin, Heidelberg. p. 1-45.

175. Judd, B.R., *Optical Absorption Intensities of Rare-Earth Ions.* Physical Review, 1962. **127**(3): p. 750-761.
176. Carnall, W.T., P.R. Fields, and K. Rajnak, *Electronic Energy Levels in the Trivalent Lanthanide Aquo Ions. I. Pr3+, Nd3+, Pm3+, Sm3+, Dy3+, Ho3+, Er3+, and Tm3+.* The Journal of Chemical Physics, 2003. **49**(10): p. 4424-4442.
177. Carnall, W.T., P.R. Fields, and K. Rajnak, *Spectral Intensities of the Trivalent Lanthanides and Actinides in Solution. II. Pm3+, Sm3+, Eu3+, Gd3+, Tb3+, Dy3+, and Ho3+.* The Journal of Chemical Physics, 2003. **49**(10): p. 4412-4423.
178. Judd, B.R., *Hypersensitive Transitions in f-Electron Systems*, in *Lanthanide and Actinide Chemistry and Spectroscopy*. 1980, AMERICAN CHEMICAL SOCIETY. p. 267-274.
179. Ofelt, G.S., *Intensities of Crystal Spectra of Rare-Earth Ions.* The Journal of Chemical Physics, 2004. **37**(3): p. 511-520.
180. Weissman, S.I., *Intramolecular Energy Transfer The Fluorescence of Complexes of Europium.* The Journal of Chemical Physics, 2004. **10**(4): p. 214-217.
181. Marckmann, P., et al., *Nephrogenic Systemic Fibrosis: Suspected Causative Role of Gadodiamide Used for Contrast-Enhanced Magnetic Resonance Imaging.* Journal of the American Society of Nephrology, 2006. **17**(9).
182. Cheong, B.Y. and R. Muthupillai, *Nephrogenic systemic fibrosis: a concise review for cardiologists.* Tex Heart Inst J, 2010. **37**(5): p. 508-15.
183. Shannon, R.D., *Revised effective ionic radii and systematic studies of interatomic distances in halides and chalcogenides.* Acta Crystallographica Section A, 1976. **32**(5): p. 751-767.
184. Kumar, K., C.A. Chang, and M.F. Tweedle, *Equilibrium and kinetic studies of lanthanide complexes of macrocyclic polyamino carboxylates.* Inorganic Chemistry, 1993. **32**(5): p. 587-593.
185. Sherry, A.D., P. Caravan, and R.E. Lenkinski, *Primer on gadolinium chemistry.* Journal of Magnetic Resonance Imaging, 2009. **30**(6): p. 1240-1248.
186. Chaves, S., R. Delgado, and J.J.R.F. Da Silva, *The stability of the metal complexes of cyclic tetra-aza tetra-acetic acids.* Talanta, 1992. **39**(3): p. 249-254.
187. Izatt, R.M., et al., *Thermodynamic and kinetic data for macrocycle interactions with cations and anions.* Chemical Reviews, 1991. **91**(8): p. 1721-2085.
188. Kodama, M. and E. Kimura, *Equilibria of complex formation between several bivalent metal ions and macrocyclic tri- and penta-amines.* Journal of the Chemical Society, Dalton Transactions, 1978(9): p. 1081-1085.
189. Delgado, R. and J.J.R.F. da Silva, *Metal complexes of cyclic tetra-azatetra-acetic acids.* Talanta, 1982. **29**(10): p. 815-822.
190. Smith, R.M. and A.E. Martell, *Critical stability constants, enthalpies and entropies for the formation of metal complexes of aminopolycarboxylic acids and carboxylic acids.* Science of The Total Environment, 1987. **64**(1): p. 125-147.
191. Busch, D.H. and N.A. Stephenson, *Molecular organization, portal to supramolecular chemistry: Structural analysis of the factors associated with molecular organization in coordination and inclusion chemistry, including the coordination template effect.* Coordination Chemistry Reviews, 1990. **100**: p. 119-154.
192. Abedini, A. and D.P. Raleigh, *A critical assessment of the role of helical intermediates in amyloid formation by natively unfolded proteins and*

polypeptides. Protein Engineering, Design and Selection, 2009. **22**(8): p. 453-459.
193. Hancock, R.D. and A.E. Martell, *Ligand design for selective complexation of metal ions in aqueous solution.* Chemical Reviews, 1989. **89**(8): p. 1875-1914.
194. Cacheris, W.P., S.K. Nickle, and A.D. Sherry, *Thermodynamic study of lanthanide complexes of 1,4,7-triazacyclononane-N,N',N''-triacetic acid and 1,4,7,10-tetraazacyclododecane-N,N',N'',N'''-tetraacetic acid.* Inorganic Chemistry, 1987. **26**(6): p. 958-960.
195. Clarke, E.T. and A.E. Martell, *Stabilities of the alkaline earth and divalent transition metal complexes of the tetraazamacrocyclic tetraacetic acid ligands.* Inorganica Chimica Acta, 1991. **190**(1): p. 27-36.
196. Loncin, M.F., J.F. Desreux, and E. Merciny, *Coordination of lanthanides by two polyamino polycarboxylic macrocycles: formation of highly stable lanthanide complexes.* Inorganic Chemistry, 1986. **25**(15): p. 2646-2648.
197. Ling Wu, S. and W. DeW. Horrocks, *Direct determination of stability constants of lanthanide ion chelates by laser-excited europium(III) luminescence spectroscopy: application to cyclic and acyclic aminocarboxylate complexes.* Journal of the Chemical Society, Dalton Transactions, 1997(9): p. 1497-1502.
198. Hancock, R.D. and G.J. McDougall, *The macrocyclic effect in tetraaza-macrocyclic ligands.* Advances in Molecular Relaxation and Interaction Processes, 1980. **18**(2): p. 99-108.
199. Cabbiness, D.K. and D.W. Margerum, *Macrocyclic effect on the stability of copper(II) tetramine complexes.* Journal of the American Chemical Society, 1969. **91**(23): p. 6540-6541.
200. Häfliger, H. and T.A. Kaden, *Metal Complexes of Macrocyclic Ligands. XII. A Complexone-like Tetraazamacrocycle.* Helvetica Chimica Acta, 1979. **62**(3): p. 683-688.
201. Chang, C.A., et al., *Ligand Preorganization in Metal Ion Complexation: Molecular Mechanics/Dynamics, Kinetics, and Laser-Excited Luminescence Studies of Trivalent Lanthanide Complex Formation with Macrocyclic Ligands TETA and DOTA.* Inorganic Chemistry, 2001. **40**(14): p. 3448-3455.
202. Akkaya, E.U., M.E. Huston, and A.W. Czarnik, *Chelation-enhanced fluorescence of anthrylazamacrocycle conjugate probes in aqueous solution.* Journal of the American Chemical Society, 1990. **112**(9): p. 3590-3593.
203. El Majzoub, A., et al., *(Benzimidazolylmethyl)cyclen: A Potential Sensitive Fluorescent PET Chemosensor for Zinc.* European Journal of Inorganic Chemistry, 2007. **2007**(32): p. 5087-5097.
204. Kimura, E., et al., *A macrocyclic zinc(II) fluorophore as a detector of apoptosis.* Proceedings of the National Academy of Sciences, 2003. **100**(7): p. 3731-3736.
205. Tamanini, E., et al., *A Synthetically Simple, Click-Generated Cyclam-Based Zinc(II) Sensor.* Inorganic Chemistry, 2009. **48**(1): p. 319-324.
206. Tamanini, E., et al., *Cyclam-Based "Clickates": Homogeneous and Heterogeneous Fluorescent Sensors for Zn(II).* Inorganic Chemistry, 2010. **49**(8): p. 3789-3800.
207. Aulsebrook, M.L., et al., *The synthesis of luminescent lanthanide-based chemosensors for the detection of zinc ions.* Tetrahedron, 2014. **70**(29): p. 4367-4372.

208. Roger, M., et al., *Lanthanide Complexes with Heteroditopic Ligands as Fluorescent Zinc Sensors.* European Journal of Inorganic Chemistry, 2014. **2014**(6): p. 1072-1081.
209. Comby, S., et al., *New Trick for an Old Ligand! The Sensing of Zn(II) Using a Lanthanide Based Ternary Yb(III)-cyclen-8-hydroxyquinoline System As a Dual Emissive Probe for Displacement Assay.* Inorganic Chemistry, 2012. **51**(19): p. 10158-10168.
210. Winnett, M.R., et al., *Time-Resolved Terbium-Based Probe for the Detection of Zinc(II) Ions: Investigation of the Formation of a Luminescent Ternary Complex.* Inorganic Chemistry, 2020. **59**(1): p. 118-127.
211. Santos-Figueroa, L.E., et al., *Highly Selective Fluorescence Detection of Hydrogen Sulfide by Using an Anthracene-Functionalized Cyclam–CuII Complex.* European Journal of Inorganic Chemistry, 2014. **2014**(1): p. 41-45.
212. Aulsebrook, M.L., et al., *A luminogenic lanthanide-based probe for the highly selective detection of nanomolar sulfide levels in aqueous samples.* Chemical Communications, 2017. **53**(36): p. 4911-4914.
213. Wrobel, A.T., et al., *A Fast and Selective Near-Infrared Fluorescent Sensor for Multicolor Imaging of Biological Nitroxyl (HNO).* Journal of the American Chemical Society, 2014. **136**(12): p. 4697-4705.
214. Butler, S.J., *Quantitative determination of fluoride in pure water using luminescent europium complexes.* Chemical Communications, 2015. **51**(54): p. 10879-10882.
215. Smith, D.G., et al., *Evidence for the optical signalling of changes in bicarbonate concentration within the mitochondrial region of living cells.* Chemical Communications, 2011. **47**(26): p. 7347-7349.
216. Pal, R., D. Parker, and L.C. Costello, *A europium luminescence assay of lactate and citrate in biological fluids.* Organic & Biomolecular Chemistry, 2009. **7**(8): p. 1525-1528.
217. Lauffer, R.B., *Paramagnetic metal complexes as water proton relaxation agents for NMR imaging: theory and design.* Chemical Reviews, 1987. **87**(5): p. 901-927.
218. Zhang, S., et al., *PARACEST Agents: Modulating MRI Contrast via Water Proton Exchange.* Accounts of Chemical Research, 2003. **36**(10): p. 783-790.
219. Lancelot, E., J.-S. Raynaud, and P. Desché, *Current and Future MR Contrast Agents: Seeking a Better Chemical Stability and Relaxivity for Optimal Safety and Efficacy.* Investigative Radiology, 2020. **55**(9).
220. Czeyda-Pommersheim, F., et al., *Contrast Agents for MR Imaging.* Magnetic Resonance Imaging Clinics of North America, 2017. **25**(4): p. 705-711.
221. Kanal, E., *Gadolinium based contrast agents (GBCA): Safety overview after 3 decades of clinical experience.* Magnetic Resonance Imaging, 2016. **34**(10): p. 1341-1345.
222. Li, W.-h., S.E. Fraser, and T.J. Meade, *A Calcium-Sensitive Magnetic Resonance Imaging Contrast Agent.* Journal of the American Chemical Society, 1999. **121**(6): p. 1413-1414.
223. Major, J.L., et al., *The synthesis and in vitro testing of a zinc-activated MRI contrast agent.* Proceedings of the National Academy of Sciences, 2007. **104**(35): p. 13881-13886.

224. Tu, C., R. Nagao, and A.Y. Louie, *Multimodal Magnetic-Resonance/Optical-Imaging Contrast Agent Sensitive to NADH.* Angewandte Chemie International Edition, 2009. **48**(35): p. 6547-6551.
225. Ward, K.M., A.H. Aletras, and R.S. Balaban, *A New Class of Contrast Agents for MRI Based on Proton Chemical Exchange Dependent Saturation Transfer (CEST).* Journal of Magnetic Resonance, 2000. **143**(1): p. 79-87.
226. Chauvin, T., et al., *Detection of Enzymatic Activity by PARACEST MRI: A General Approach to Target a Large Variety of Enzymes.* Angewandte Chemie International Edition, 2008. **47**(23): p. 4370-4372.
227. Hammell, J., et al., *Eu(III) Complexes as Anion-Responsive Luminescent Sensors and Paramagnetic Chemical Exchange Saturation Transfer Agents.* Inorganic Chemistry, 2011. **50**(11): p. 4857-4867.
228. Ren, J., et al., *Imaging the tissue distribution of glucose in livers using a PARACEST sensor.* Magnetic Resonance in Medicine, 2008. **60**(5): p. 1047-1055.
229. Ratnakar, S.J., et al., *A Frequency-Selective pH-Responsive paraCEST Agent.* Angewandte Chemie International Edition, 2020. **59**(48): p. 21671-21676.
230. Yu, M., et al., *A Fluorescent "Allosteric Scorpionand" Complex Visualizes a Biological Recognition Event.* ChemBioChem, 2013. **14**(2): p. 224-229.
231. Lau, Y.H., et al., *A Click Fluorophore Sensor that Can Distinguish CuII and HgII via Selective Anion-Induced Demetallation.* Chemistry – A European Journal, 2011. **17**(10): p. 2850-2858.
232. Wong, J.K.H., et al., *Synthesis and Evaluation of 1,8-Disubstituted-Cyclam/Naphthalimide Conjugates as Probes for Metal Ions.* ChemistryOpen, 2016. **5**(4): p. 375-385.
233. Lau, Y.H., et al., *Molecular Switches for any pH: A Systematic Study of the Versatile Coordination Behaviour of Cyclam Scorpionands.* Chemistry – A European Journal, 2018. **24**(7): p. 1573-1585.
234. Yu, M., et al., *Nontoxic Metal–Cyclam Complexes, a New Class of Compounds with Potency against Drug-Resistant Mycobacterium tuberculosis.* Journal of Medicinal Chemistry, 2016. **59**(12): p. 5917-5921.
235. Spain, M., et al., *Antitubercular Bis-Substituted Cyclam Derivatives: Structure–Activity Relationships and in Vivo Studies.* Journal of Medicinal Chemistry, 2018. **61**(8): p. 3595-3608.
236. Wu, W.-h., et al., *Sequestration of Copper from β-Amyloid Promotes Selective Lysis by Cyclen-Hybrid Cleavage Agents *.* Journal of Biological Chemistry, 2008. **283**(46): p. 31657-31664.
237. Yu, M., et al., *Neuroprotective peptide–macrocycle conjugates reveal complex structure–activity relationships in their interactions with amyloid β†.* Metallomics, 2014. **6**(10): p. 1931-1940.
238. Royal, G., et al., *New Synthesis of trans-Disubstituted Cyclam Macrocycles – Elucidation of the Disubstitution Mechanism on the Basis of X-ray Data and Molecular Modeling.* European Journal of Organic Chemistry, 1998. **1998**(9): p. 1971-1975.
239. Treitler, D.S. and S. Leung, *How Dangerous Is Too Dangerous? A Perspective on Azide Chemistry.* The Journal of Organic Chemistry, 2022. **87**(17): p. 11293-11295.

240. Delhaye, L., et al., *Removal of Reaction Solvent by Extractive Workup: Survey of Water and Solvent Co-extraction in Various Systems.* Organic Process Research & Development, 2007. **11**(1): p. 160-164.
241. Mitsunobu, O. and M. Yamada, *Preparation of Esters of Carboxylic and Phosphoric Acid via Quaternary Phosphonium Salts.* Bulletin of the Chemical Society of Japan, 1967. **40**(10): p. 2380-2382.
242. Shi, M., *Functionalised Azamacrocycles for Modulating Amyloid Aggregation*, in *School of Chemistry*. 2020, University of Sydney: Sydney. p. 104.
243. Fürst, A. and F. Koller, *Über Steroide und Sexualhormone. Ein neuer Weg zur Herstellung der α-Oxyde von Cholesterin und trans-Dehydro-androsteron.* Helvetica Chimica Acta, 1947. **30**(6): p. 1454-1460.
244. Liang, L. and D. Astruc, *The copper(I)-catalyzed alkyne-azide cycloaddition (CuAAC) "click" reaction and its applications. An overview.* Coordination Chemistry Reviews, 2011. **255**(23): p. 2933-2945.
245. Davide Castelvecchi, H.L., *Chemists who invented revolutionary 'click' reactions win Nobel.* Nature, 2022. **610**: p. 242-243.
246. Han, G., M. Tamaki, and V.J. Hruby, *Fast, efficient and selective deprotection of the tert-butoxycarbonyl (Boc) group using HCl/dioxane (4 m).* The Journal of Peptide Research, 2001. **58**(4): p. 338-341.
247. Underberg, W.J.M., *Oxidative Degradation of Pharmaceutically Important Phenothiazines III: Kinetics and Mechanism of Promethazine Oxidation.* Journal of Pharmaceutical Sciences, 1978. **67**(8): p. 1133-1138.
248. Reinke, A.A. and J.E. Gestwicki, *Insight into Amyloid Structure Using Chemical Probes.* Chemical Biology & Drug Design, 2011. **77**(6): p. 399-411.
249. Levine Iii, H., *Thioflavine T interaction with synthetic Alzheimer's disease β-amyloid peptides: Detection of amyloid aggregation in solution.* Protein Science, 1993. **2**(3): p. 404-410.
250. Stsiapura, V.I., et al., *Computational Study of Thioflavin T Torsional Relaxation in the Excited State.* The Journal of Physical Chemistry A, 2007. **111**(22): p. 4829-4835.
251. Groenning, M., *Binding mode of Thioflavin T and other molecular probes in the context of amyloid fibrils—current status.* Journal of Chemical Biology, 2010. **3**(1): p. 1-18.
252. Harel, M., et al., *Crystal Structure of Thioflavin T Bound to the Peripheral Site of Torpedo californica Acetylcholinesterase Reveals How Thioflavin T Acts as a Sensitive Fluorescent Reporter of Ligand Binding to the Acylation Site.* Journal of the American Chemical Society, 2008. **130**(25): p. 7856-7861.
253. Sen, P., et al., *Interactions of thioflavin T with serum albumins: Spectroscopic analyses.* Spectrochimica Acta Part A: Molecular and Biomolecular Spectroscopy, 2009. **74**(1): p. 94-99.
254. Ruschak, A.M. and A.D. Miranker, *Fiber-dependent amyloid formation as catalysis of an existing reaction pathway.* Proceedings of the National Academy of Sciences, 2007. **104**(30): p. 12341-12346.
255. House, E., et al., *Aluminium, iron, zinc and copper influence the in vitro formation of amyloid fibrils of Aβ 42 in a manner which may have consequences for metal chelation therapy in Alzheimer's disease.* Journal of Alzheimer's Disease, 2004. **6**: p. 291-301.

256. Lee, M.-C., et al., *Zinc ion rapidly induces toxic, off-pathway amyloid-β oligomers distinct from amyloid-β derived diffusible ligands in Alzheimer's disease.* Scientific Reports, 2018. **8**(1): p. 4772.
257. Mold, M., et al., *Copper prevents amyloid-β1–42 from forming amyloid fibrils under near-physiological conditions in vitro.* Scientific Reports, 2013. **3**(1): p. 1256.
258. Meisl, G., et al., *Molecular mechanisms of protein aggregation from global fitting of kinetic models.* Nature Protocols, 2016. **11**(2): p. 252-272.
259. Krishtal, J., et al., *In situ fibrillizing amyloid-beta 1-42 induces neurite degeneration and apoptosis of differentiated SH-SY5Y cells.* PLOS ONE, 2017. **12**(10): p. e0186636.
260. Poppe, L., et al., *Different Modes of Inhibitor Binding to Prolyl Hydroxylase by Combined Use of X-ray Crystallography and NMR Spectroscopy of Paramagnetic Complexes.* Journal of the American Chemical Society, 2009. **131**(46): p. 16654-16655.
261. Pintacuda, G., et al., *Angular dependence of dipole-dipole-Curie-spin cross-correlation effects in high-spin and low-spin paramagnetic myoglobin***. Journal of Biomolecular NMR, 2003. **27**(2): p. 115-132.
262. Gueron, M., *Nuclear relaxation in macromolecules by paramagnetic ions: a novel mechanism.* Journal of Magnetic Resonance (1969), 1975. **19**(1): p. 58-66.
263. Bertini, I., et al., *Cross Correlation between the Dipole–Dipole Interaction and the Curie Spin Relaxation: The Effect of Anisotropic Magnetic Susceptibility.* Journal of Magnetic Resonance, 2001. **152**(1): p. 103-108.
264. Pintacuda, G., A. Kaikkonen, and G. Otting, *Modulation of the distance dependence of paramagnetic relaxation enhancements by CSA×DSA cross-correlation.* Journal of Magnetic Resonance, 2004. **171**(2): p. 233-243.
265. Pandya, D.N., et al., *Revival of TE2A; a better chelate for Cu(II) ions than TETA?* Chemical Communications, 2010. **46**(20): p. 3517-3519.
266. Boswell, C.A., et al., *Relationship between reduction potential and in vivo stability of copper-azamacrocycle complexes.* Journal of Labelled Compounds and Radiopharmaceuticals, 2001. **44**(S1): p. S770-S772.
267. Heroux, K.J., et al., *The long and short of it: the influence of N-carboxyethyl versusN-carboxymethyl pendant arms on in vitro and in vivo behavior of copper complexes of cross-bridged tetraamine macrocycles.* Dalton Transactions, 2007(21): p. 2150-2162.
268. Shokeen, M. and C.J. Anderson, *Molecular Imaging of Cancer with Copper-64 Radiopharmaceuticals and Positron Emission Tomography (PET).* Accounts of Chemical Research, 2009. **42**(7): p. 832-841.
269. Maiti, B.K., et al., *Designed Metal-ATCUN Derivatives: Redox- and Non-redox-Based Applications Relevant for Chemistry, Biology, and Medicine.* iScience, 2020. **23**(12): p. 101792.
270. Chan, T.R., et al., *Polytriazoles as Copper(I)-Stabilizing Ligands in Catalysis.* Organic Letters, 2004. **6**(17): p. 2853-2855.
271. Rodionov, V.O., et al., *Benzimidazole and Related Ligands for Cu-Catalyzed Azide–Alkyne Cycloaddition.* Journal of the American Chemical Society, 2007. **129**(42): p. 12696-12704.

272. Soriano del Amo, D., et al., *Biocompatible Copper(I) Catalysts for in Vivo Imaging of Glycans.* Journal of the American Chemical Society, 2010. **132**(47): p. 16893-16899.
273. Wang, W., et al., *Sulfated ligands for the copper(I)-catalyzed azide-alkyne cycloaddition.* Chem Asian J, 2011. **6**(10): p. 2796-802.
274. Lima, L.M.P., et al., *Monopicolinate Cyclen and Cyclam Derivatives for Stable Copper(II) Complexation.* Inorganic Chemistry, 2012. **51**(12): p. 6916-6927.
275. Woodin, K.S., et al., *Kinetic Inertness and Electrochemical Behavior of Copper(II) Tetraazamacrocyclic Complexes: Possible Implications for in Vivo Stability.* European Journal of Inorganic Chemistry, 2005. **2005**(23): p. 4829-4833.
276. Uzal-Varela, R., et al., *On the dissociation pathways of copper complexes relevant as PET imaging agents.* Journal of Inorganic Biochemistry, 2022. **236**: p. 111951.
277. *Protection for the Hydroxyl Group, Including 1,2- and 1,3-Diols*, in *Protective Groups in Organic Synthesis*. 1999. p. 17-245.
278. Mehta, A., et al., *Improved efficiency and selectivity in peptide synthesis: Use of triethylsilane as a carbocation scavenger in deprotection of t-butyl esters and t-butoxycarbonyl-protected sites.* Tetrahedron Letters, 1992. **33**(37): p. 5441-5444.
279. Kaul, R., et al., *Selective tert-Butyl Ester Deprotection in the Presence of Acid Labile Protecting Groups with Use of ZnBr2.* The Journal of Organic Chemistry, 2004. **69**(18): p. 6131-6133.
280. Marcantoni, E., et al., *Selective Deprotection of N-Boc-Protected tert-Butyl Ester Amino Acids by the CeCl3·7H2O–NaI System in Acetonitrile.* The Journal of Organic Chemistry, 2001. **66**(12): p. 4430-4432.
281. Paul, S. and R.R. Schmidt, *A New Base Mediated Method for the Cleavage of tert-Butyl Esters.* Synlett, 2002. **2002**(07): p. 1107-1108.
282. Filali, E., G.C. Lloyd-Jones, and D.A. Sale, *Cleavage of tert-Butyl Benzoates with NaH in DMF: Comments on the -Mechanism and a Simple and Safe Alternative Procedure.* Synlett, 2009. **2009**(02): p. 205-208.
283. Jauregui, M., et al., *Changing the local coordination environment in mono- and bi- nuclear lanthanide complexes through "click" chemistry.* Dalton Transactions, 2009(32): p. 6283-6285.
284. Junker, A.K.R., et al., *Kinetically Inert Lanthanide Complexes as Reporter Groups for Binding of Potassium by 18-crown-6.* Inorganic Chemistry, 2016. **55**(23): p. 12299-12308.
285. Tropiano, M., et al., *Reversible Luminescence Switching of a Redox-Active Ferrocene–Europium Dyad.* Journal of the American Chemical Society, 2011. **133**(31): p. 11847-11849.
286. Kovacs, Z. and A.D. Sherry, *pH-Controlled Selective Protection of Polyaza Macrocycles.* Synthesis, 1997. **1997**(07): p. 759-763.
287. Hirayama, T., et al., *Selective labeling of tag-fused protein by tryptophan-sensitized luminescence of a terbium complex.* Chemical Communications, 2009(22): p. 3196-3198.
288. Szíjjártó, C., E. Pershagen, and K.E. Borbas, *Functionalisation of lanthanide complexes via microwave-enhanced Cu(i)-catalysed azide–alkyne cycloaddition.* Dalton Transactions, 2012. **41**(25): p. 7660-7669.

289. Delgado, R., et al., *Metal complexes of cyclen and cyclam derivatives useful for medical applications: a discussion based on thermodynamic stability constants and structural data.* Dalton Transactions, 2007(26): p. 2734-2745.
290. Aime, S., M. Botta, and G. Ermondi, *NMR study of solution structures and dynamics of lanthanide(III) complexes of DOTA.* Inorganic Chemistry, 1992. **31**(21): p. 4291-4299.
291. Do-Thanh, C.-L., M.M. Rowland, and M.D. Best, *Fluorescent bis-cyclen tweezer receptors for inositol (1,4,5)-trisphosphate.* Tetrahedron, 2011. **67**(21): p. 3803-3808.
292. Hein, J.E. and V.V. Fokin, *Copper-catalyzed azide–alkyne cycloaddition (CuAAC) and beyond: new reactivity of copper(i) acetylides.* Chemical Society Reviews, 2010. **39**(4): p. 1302-1315.
293. Ahlquist, M. and V.V. Fokin, *Enhanced Reactivity of Dinuclear Copper(I) Acetylides in Dipolar Cycloadditions.* Organometallics, 2007. **26**(18): p. 4389-4391.
294. Nulwala, H., et al., *N-Vinyltriazoles: A New Functional Monomer Family through Click Chemistry.* Macromolecules, 2010. **43**(12): p. 5474-5477.
295. Mundy, B.P. and C.A. Stewart, *Phosphorus(III) Bromide*, in *Encyclopedia of Reagents for Organic Synthesis (EROS)*. 2008.
296. Taschner, M.J. and V.R. Krishnamurthy, *Triphenylphosphine–Carbon Tetrabromide*, in *Encyclopedia of Reagents for Organic Synthesis (EROS)*. 2019. p. 1-4.
297. Roux, M.-C., R. Paugam, and G. Rousseau, *Evaluation of exo-endo Ratios in the Halolactonization of ω-Unsaturated Acids.* The Journal of Organic Chemistry, 2001. **66**(12): p. 4304-4310.
298. Yoshida, Y., et al., *Facile and Practical Methods for the Sulfonylation of Alcohols Using Ts(Ms)Cl and Me2N(CH2)nNMe2 as a Key Base.* Synthesis, 1999. **1999**(09): p. 1633-1636.
299. Ball, S.R., et al., *Perphenazine–Macrocycle Conjugates Rapidly Sequester the Aβ42 Monomer and Prevent Formation of Toxic Oligomers and Amyloid.* ACS Chemical Neuroscience, 2023. **14**(1): p. 87-98.
300. Jiang, X., *Design and Synthesis of Multi-Armed Cyclams as Novel Chemical Probes for Studying Amyloid-β (Aβ) Aggregation*, in *School of Chemistry*. 2016, University of Sydney.
301. Lalli, D., et al., *Combination of solid-state NMR and 1H NMR relaxometry for the study of intercalated saponite clays with the macrocyclic derivatives of Gd(iii) and Y(iii).* Dalton Transactions, 2020. **49**(20): p. 6566-6571.
302. Genovese, D., et al., *Static quenching upon adduct formation: a treatment without shortcuts and approximations.* Chemical Society Reviews, 2021. **50**(15): p. 8414-8427.
303. Heinlein, T., et al., *Photoinduced Electron Transfer between Fluorescent Dyes and Guanosine Residues in DNA-Hairpins.* The Journal of Physical Chemistry B, 2003. **107**(31): p. 7957-7964.
304. Doose, S., H. Neuweiler, and M. Sauer, *Fluorescence Quenching by Photoinduced Electron Transfer: A Reporter for Conformational Dynamics of Macromolecules.* ChemPhysChem, 2009. **10**(9-10): p. 1389-1398.

305. Tang, C., R. Ghirlando, and G.M. Clore, *Visualization of Transient Ultra-Weak Protein Self-Association in Solution Using Paramagnetic Relaxation Enhancement.* Journal of the American Chemical Society, 2008. **130**(12): p. 4048-4056.
306. Fawzi, N.L., et al., *Kinetics of Amyloid β Monomer-to-Oligomer Exchange by NMR Relaxation.* Journal of the American Chemical Society, 2010. **132**(29): p. 9948-9951.
307. Yagi, H., et al., *Tunable paramagnetic relaxation enhancements by [Gd(DPA)3]3– for protein structure analysis.* Journal of Biomolecular NMR, 2010. **47**(2): p. 143-153.
308. Hass, M.A.S., et al., *Validation of a Lanthanide Tag for the Analysis of Protein Dynamics by Paramagnetic NMR Spectroscopy.* Journal of the American Chemical Society, 2010. **132**(29): p. 9952-9953.
309. Ma, R.S., et al., *Determination of pseudocontact shifts of low-populated excited states by NMR chemical exchange saturation transfer.* Physical Chemistry Chemical Physics, 2016. **18**(20): p. 13794-13798.
310. Vallurupalli, P., G. Bouvignies, and L.E. Kay, *Studying "Invisible" Excited Protein States in Slow Exchange with a Major State Conformation.* Journal of the American Chemical Society, 2012. **134**(19): p. 8148-8161.
311. Fawzi, N.L., et al., *Atomic-resolution dynamics on the surface of amyloid-β protofibrils probed by solution NMR.* Nature, 2011. **480**(7376): p. 268-272.
312. Taylor, A.I.P., et al., *Simple, Reliable Protocol for High-Yield Solubilization of Seedless Amyloid-β Monomer.* ACS Chemical Neuroscience, 2023. **14**(1): p. 53-71.

Appendix

Appendix 1: Selected NMR Spectra

Processed ^{1}H and ^{13}C NMR spectra of compounds which have not been published elsewhere are shown. Each spectrum was taken on a Bruker AVANCE III 500 spectrometer. The proposed structure of the compound is superimposed on each spectrum. The ^{1}H spectrum of some molecules was acquired at 333 K in order to reduce peak broadening, and is indicated in the figure legend.

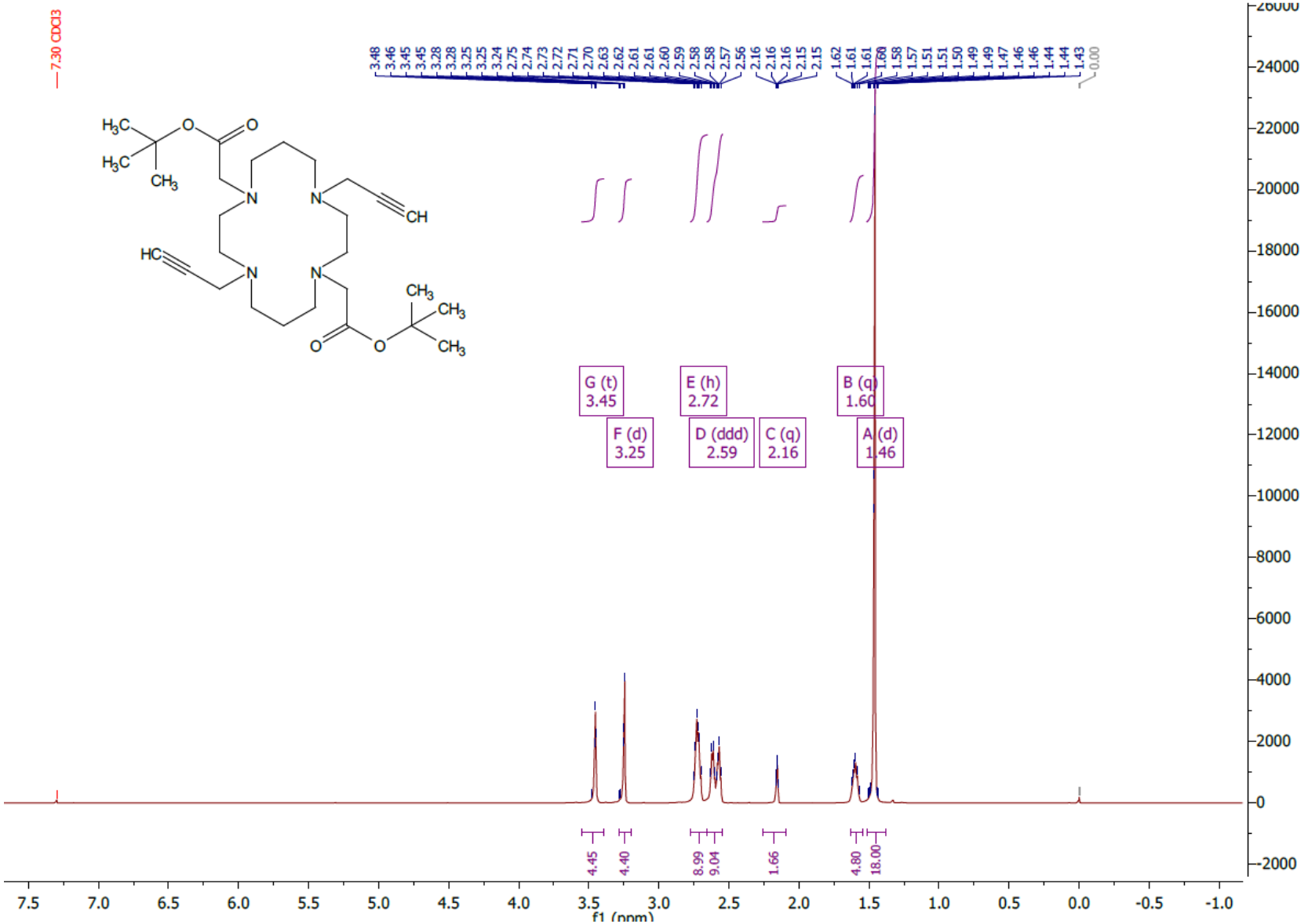

Appendix 1.1 ^{1}H NMR spectrum of **75**. Solvent: Chloroform-d.

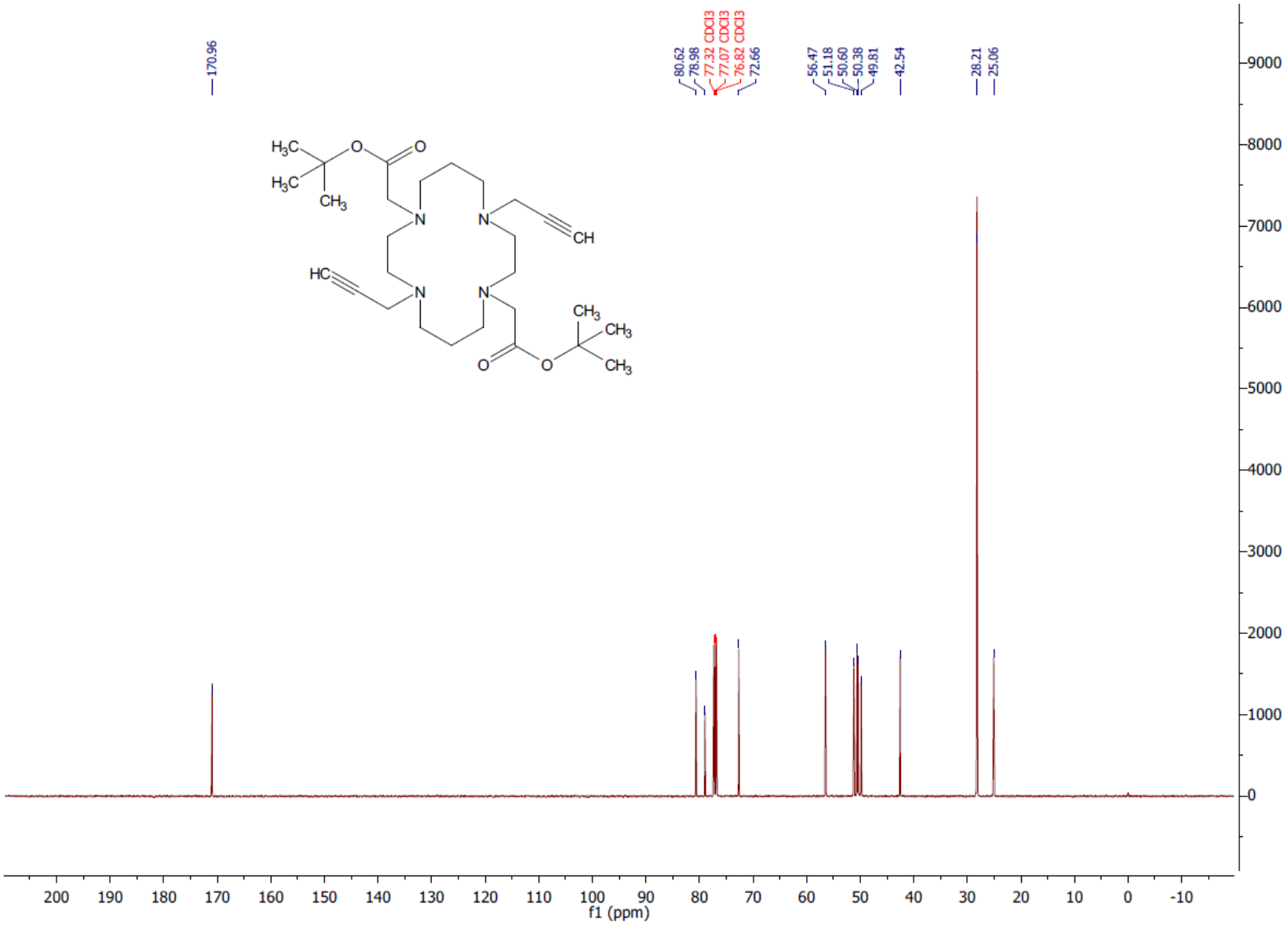

Appendix 1.2 ^{13}C NMR spectrum of **75**. Solvent: Chloroform-d.

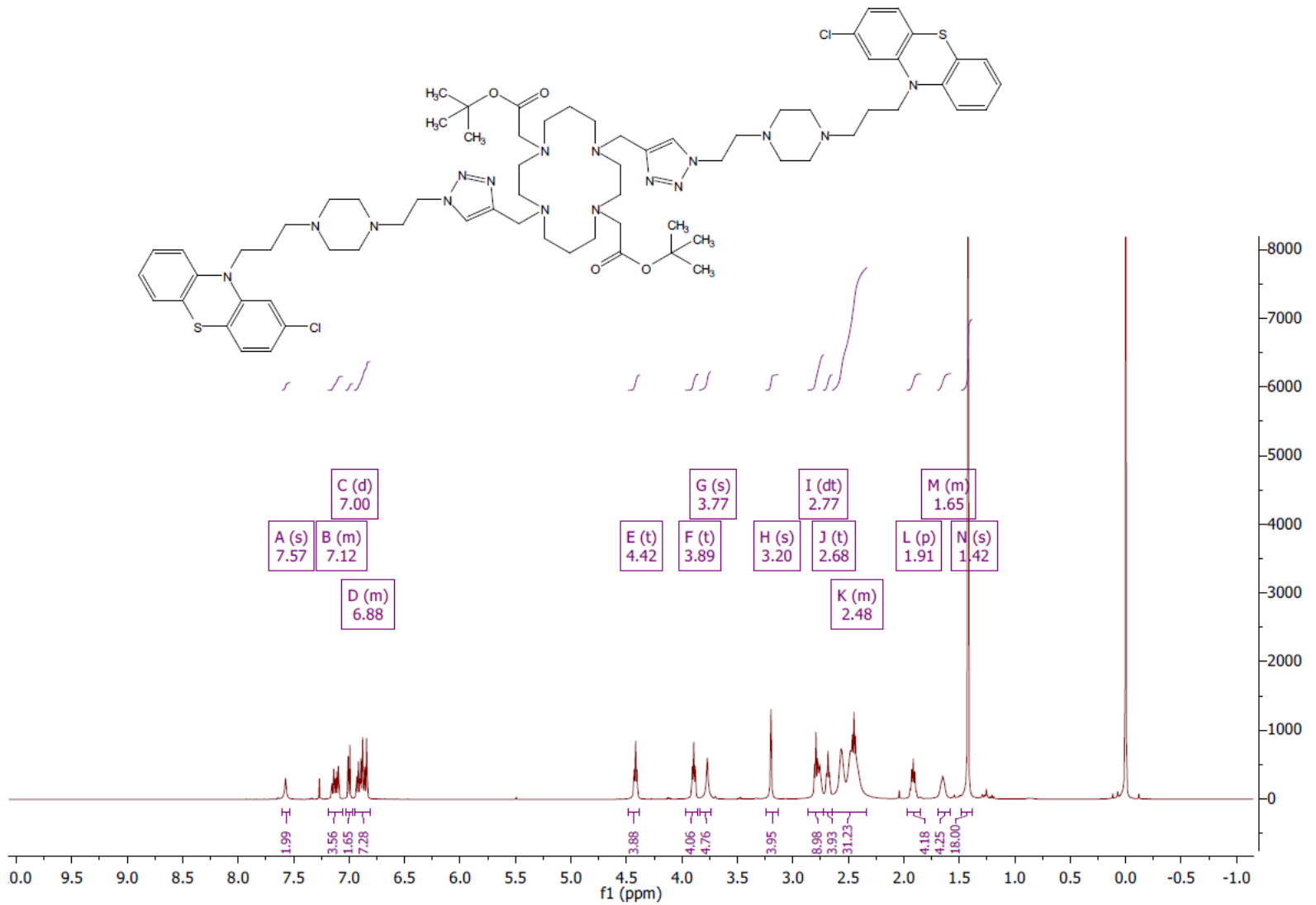

Appendix 1.3 ^{1}H NMR spectrum of **80**. Solvent: Chloroform-d

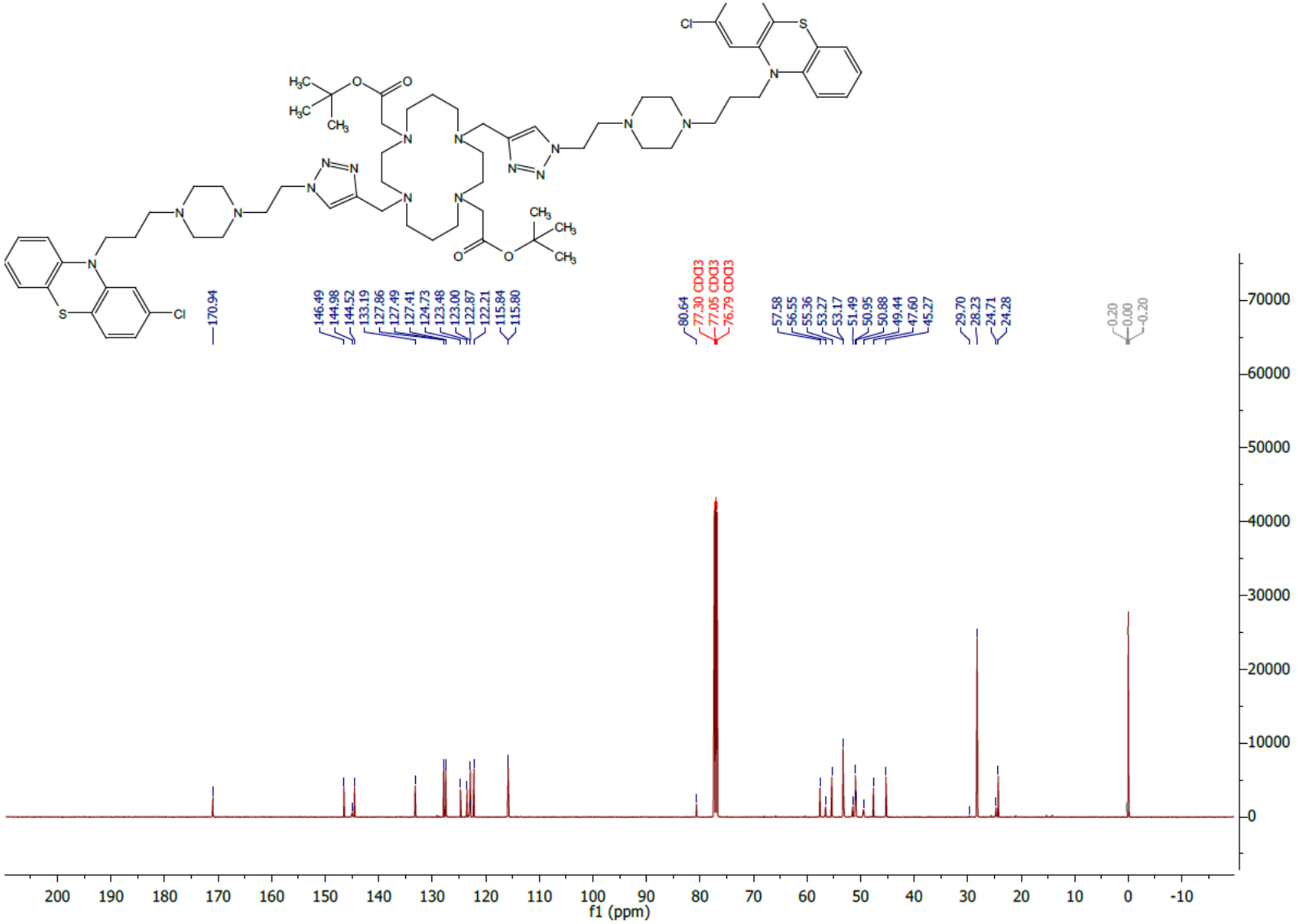

Appendix 1.4 ^{13}C NMR spectrum of **80**. Solvent: Chloroform-d.

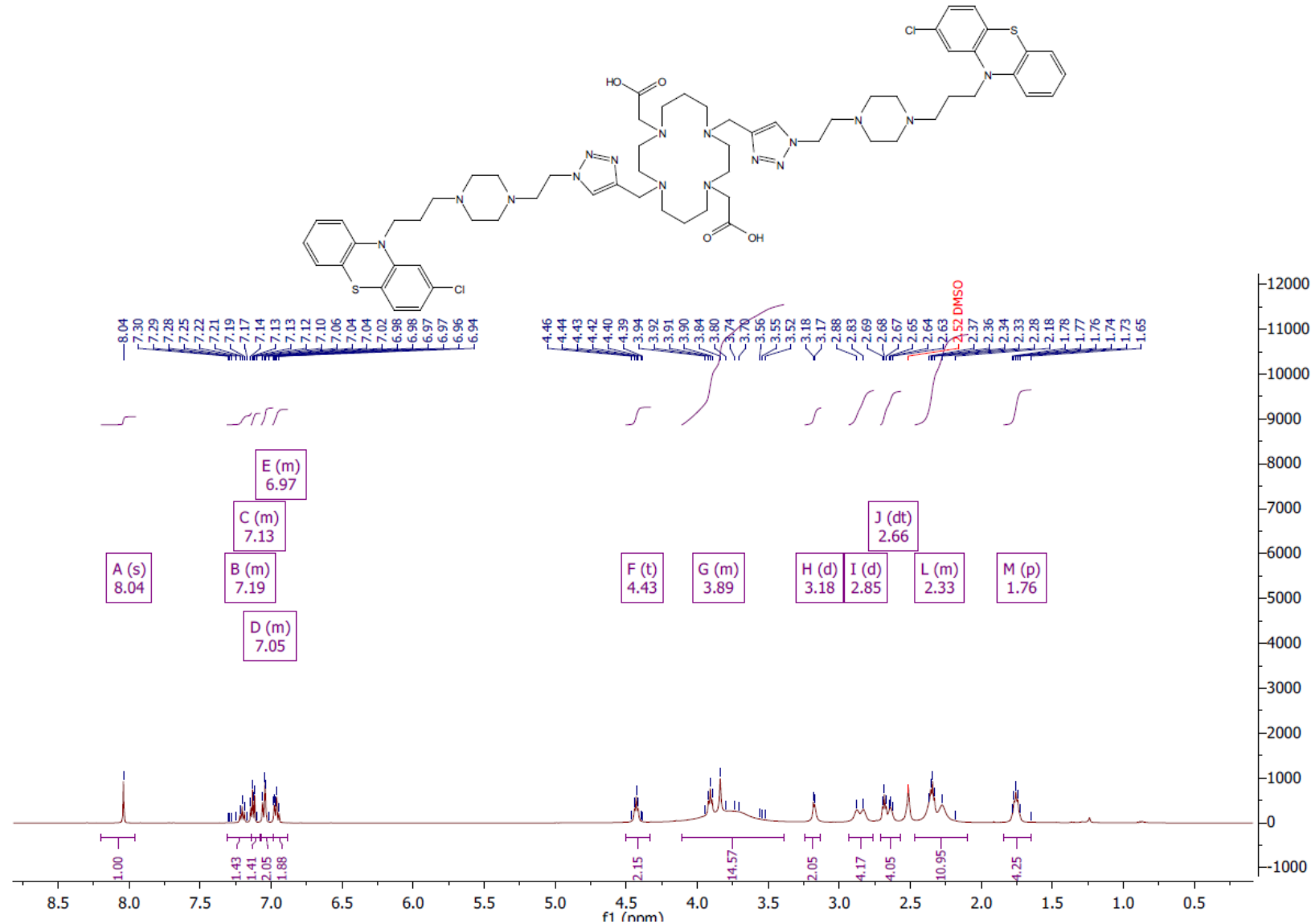

Appendix 1.5. ^{1}H NMR spectrum of **74**. Solvent: DMSO-d_6, 333K.

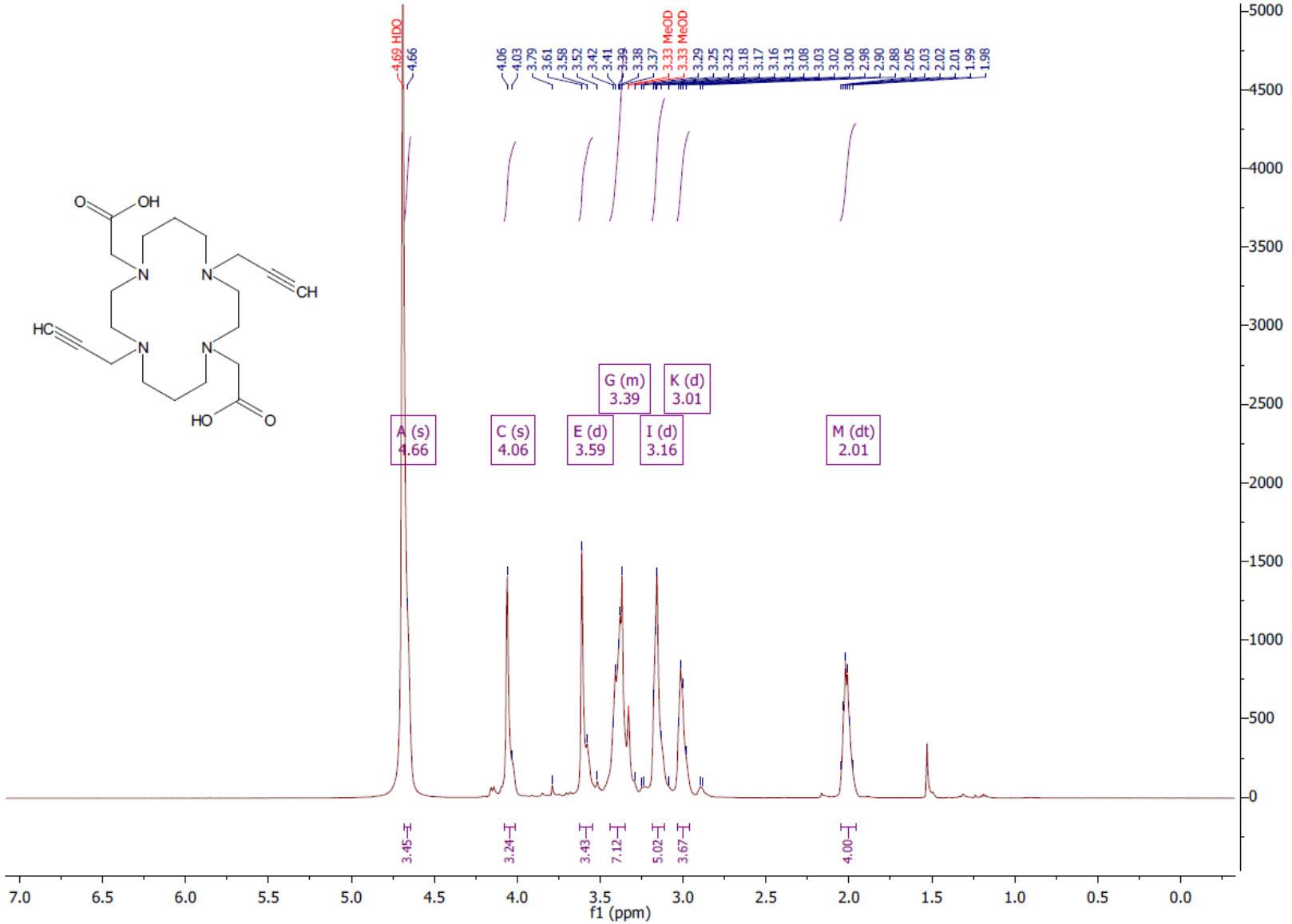

Appendix 1.6 ^{1}H NMR spectrum of **99.** Solvent: methanol-d_4.

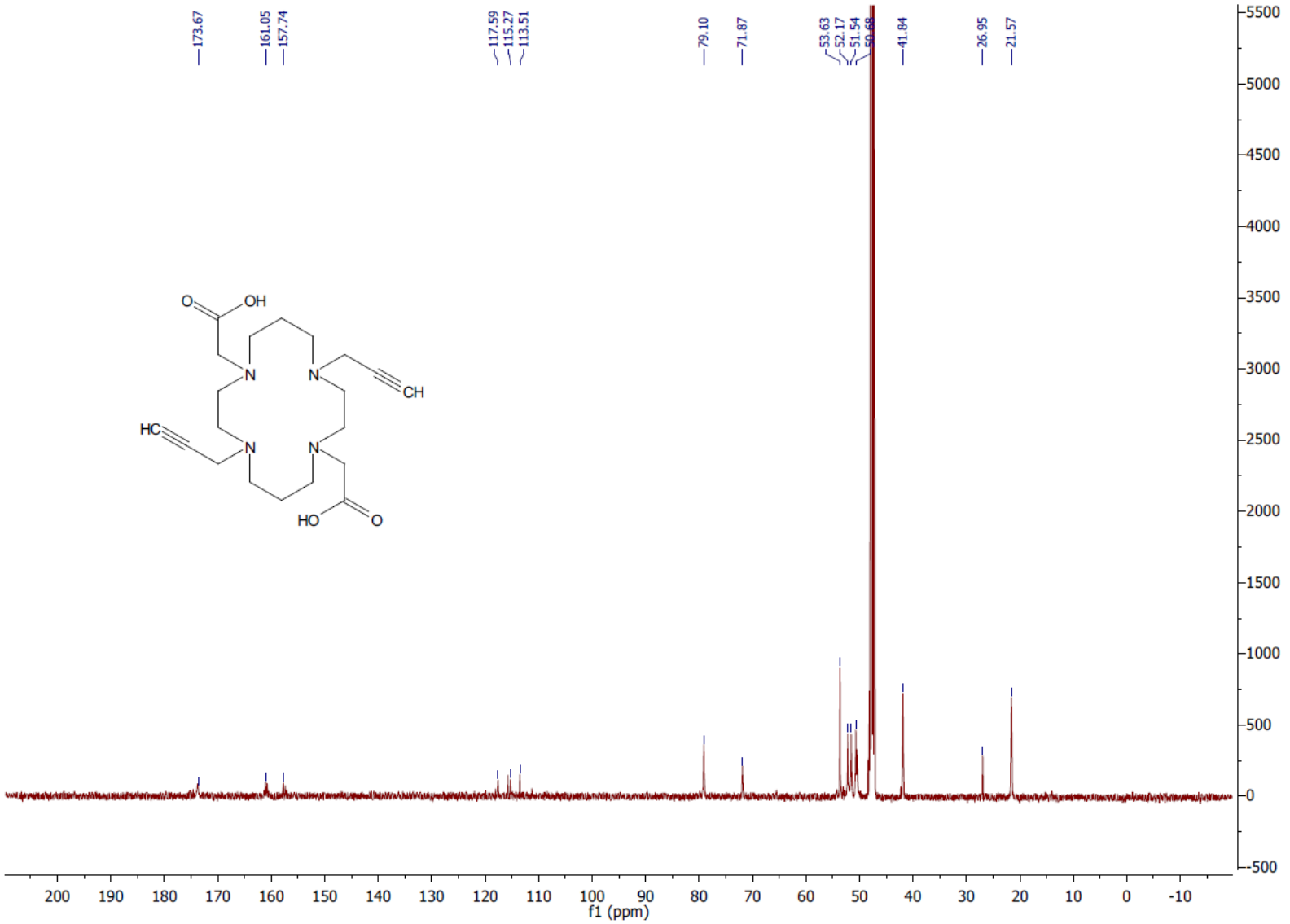

Appendix 1.7 ^{13}C NMR Spectrum of **99**. Solvent: methanol-d_4

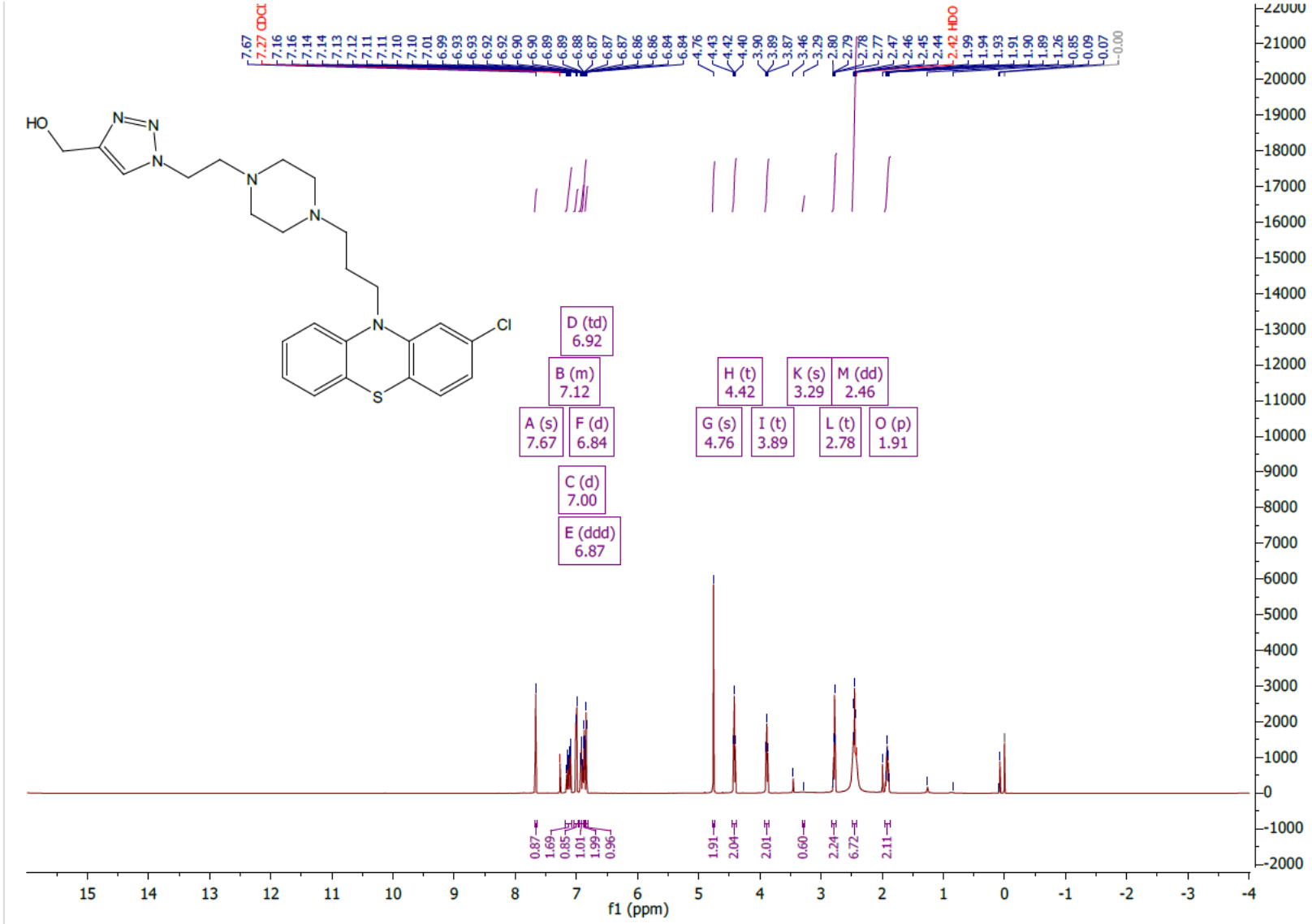

Appendix 1.8 ^{1}H NMR spectrum of **100**. Solvent: Chloroform-d

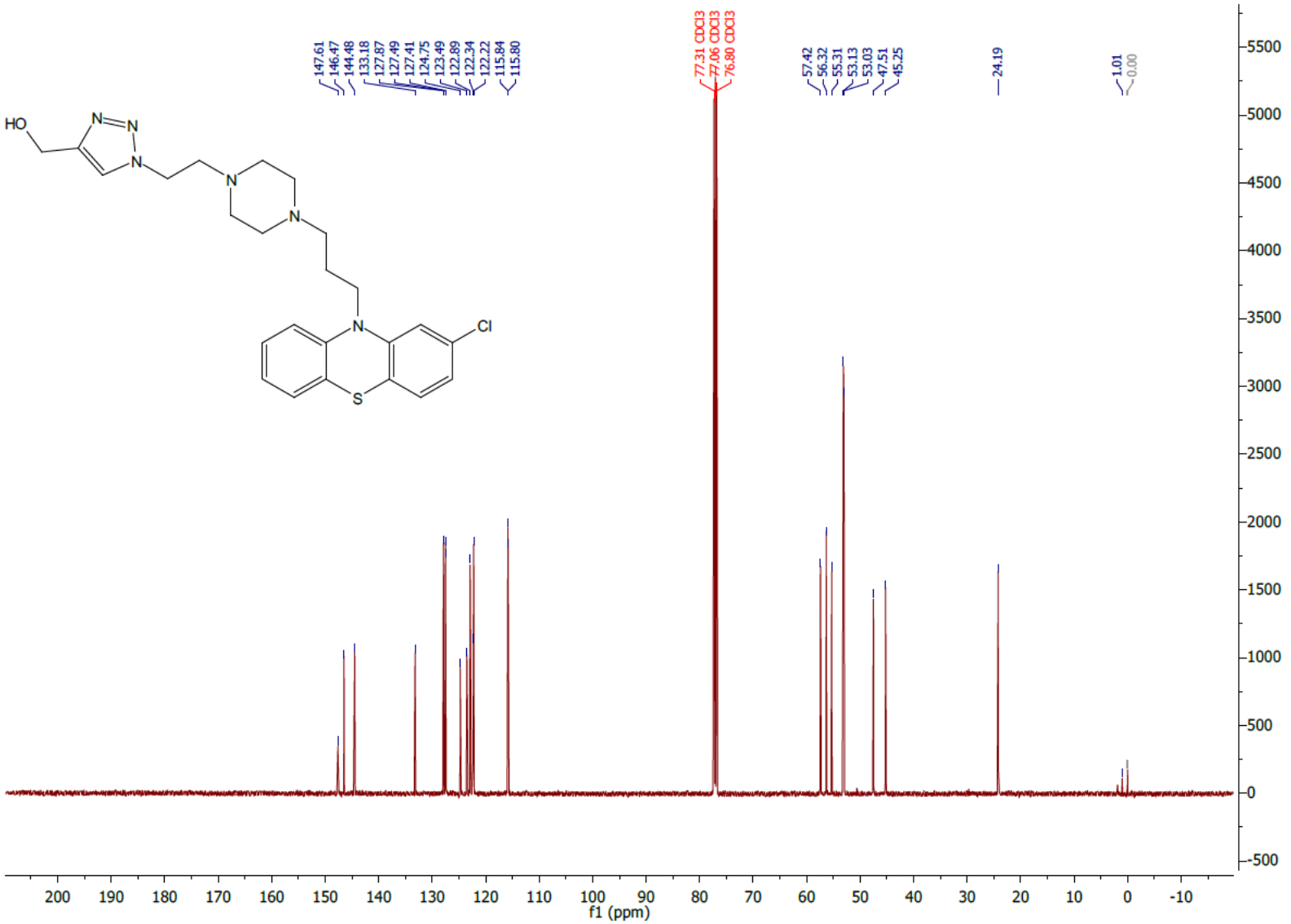

Appendix 1.9 ^{13}C NMR spectrum of **100**. Solvent: Chloroform-d

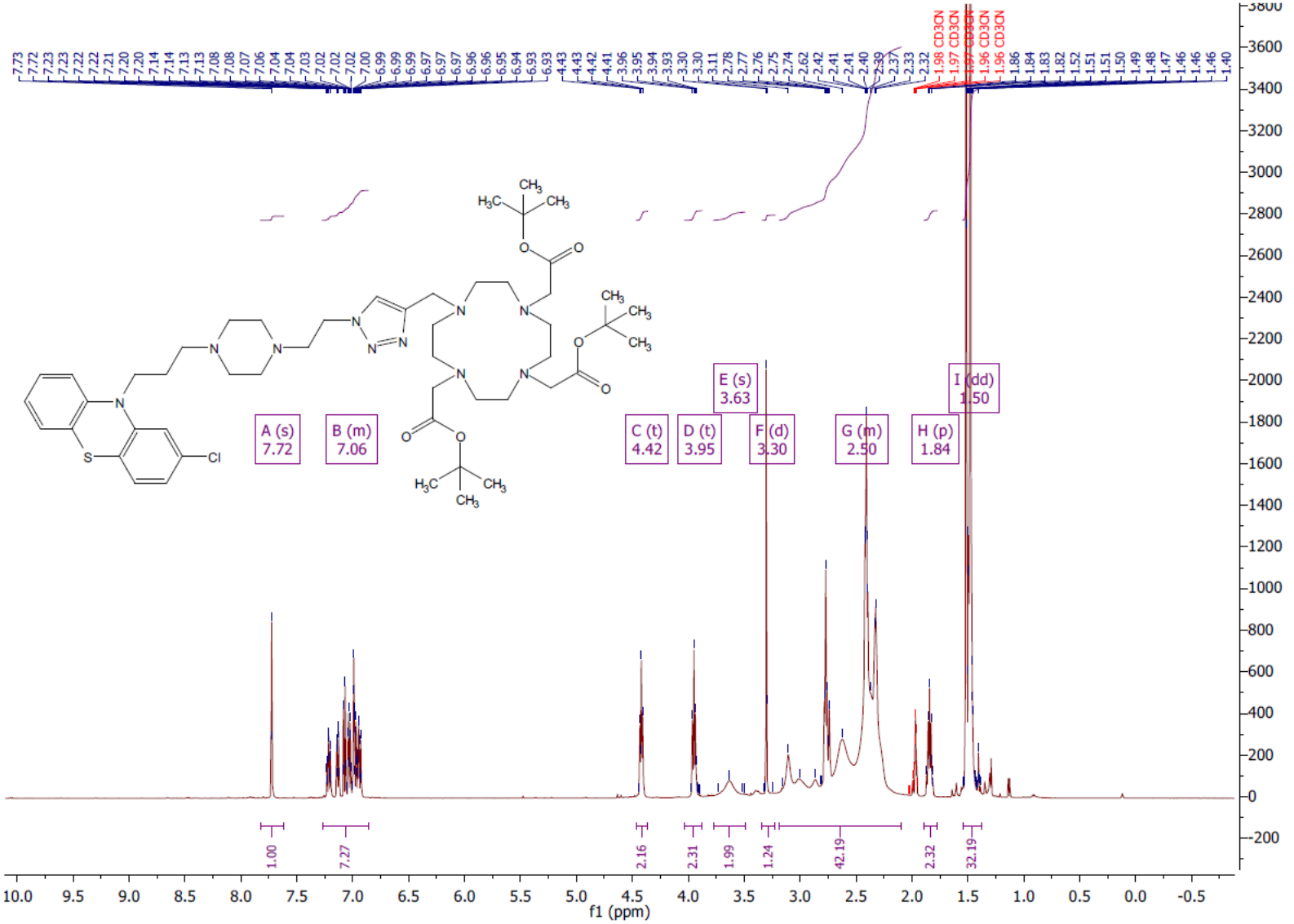

Appendix 1.10 ^{1}H NMR spectrum of **113**. Solvent: acetonitrile-d_3

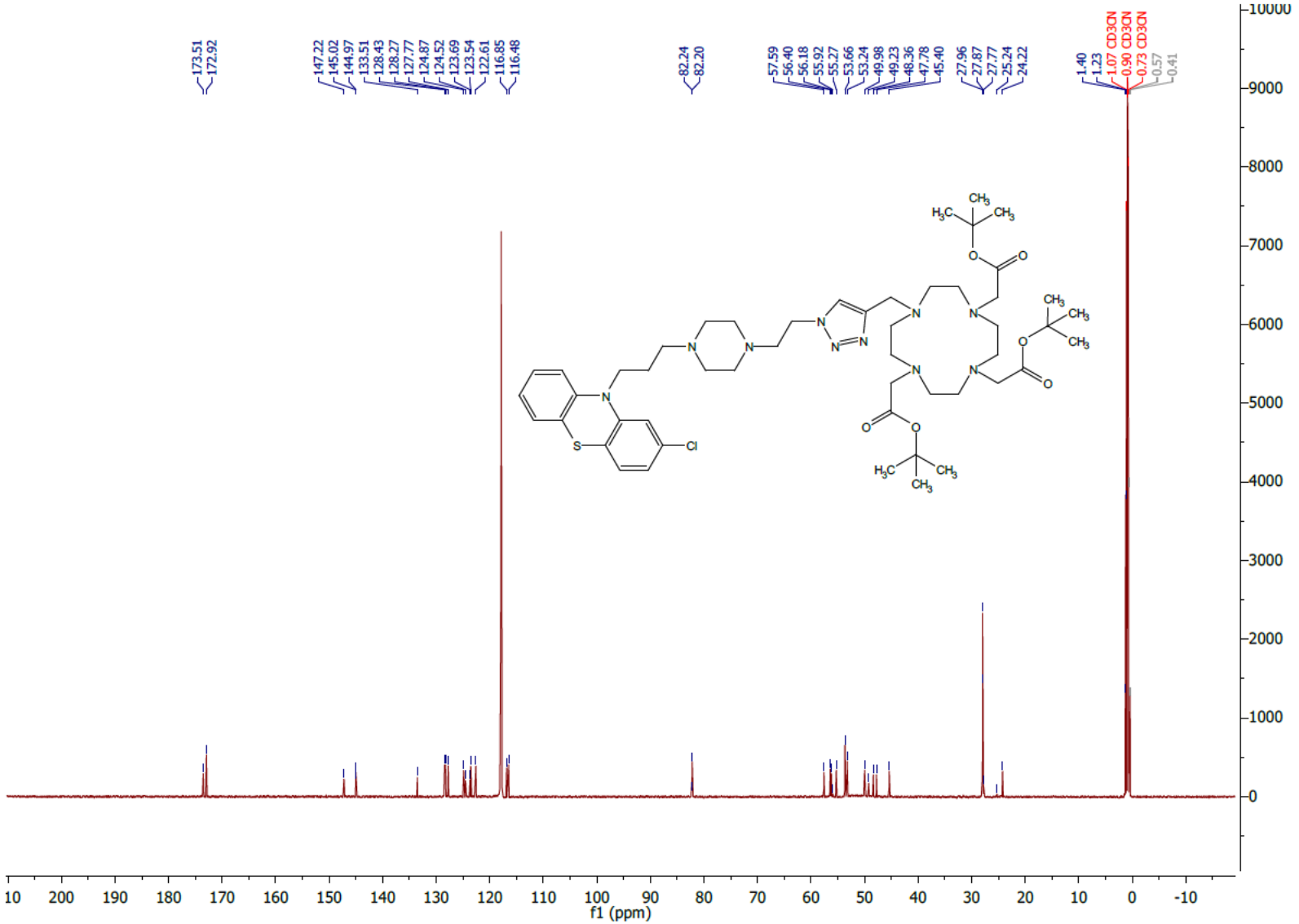

Appendix 1.11 ^{13}C NMR spectrum of **113**. Solvent: acetonitrile-d_3.

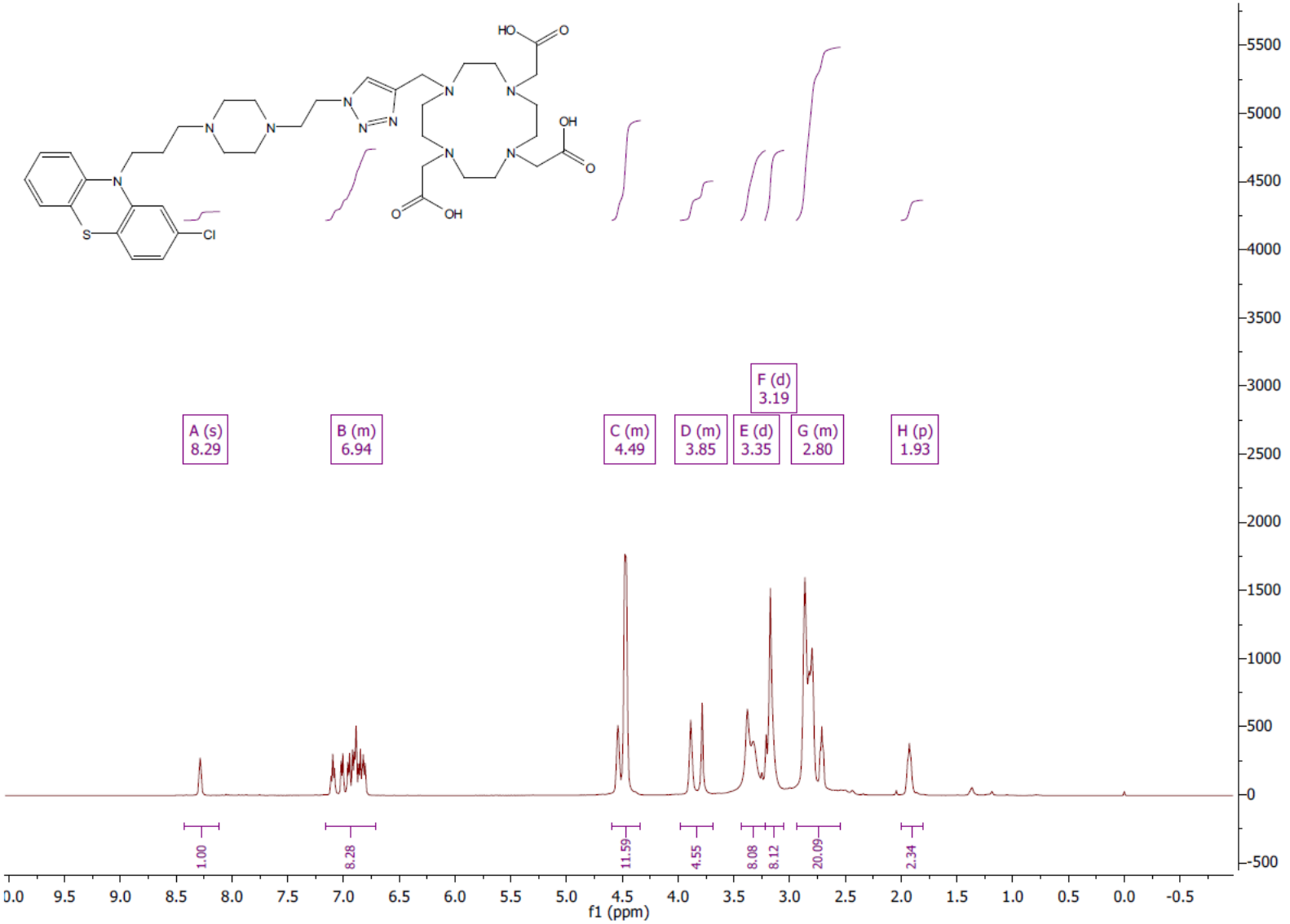

Appendix 1.12 ^{1}H NMR spectrum of **105**. Solvent: methanol-d_4

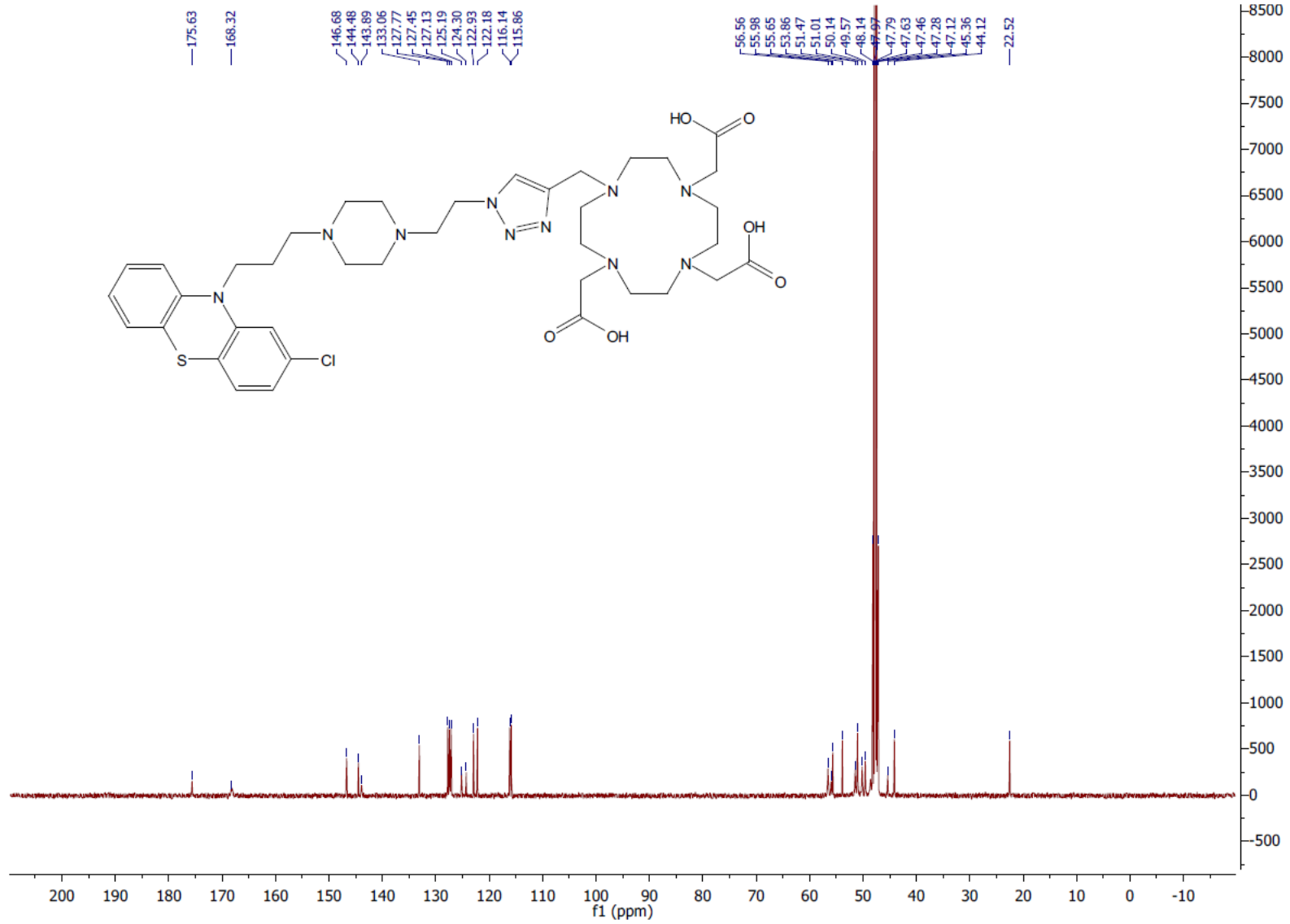

Appendix 1.13 ^{13}C NMR spectrum of **105**. Solvent: methanol-d_4.

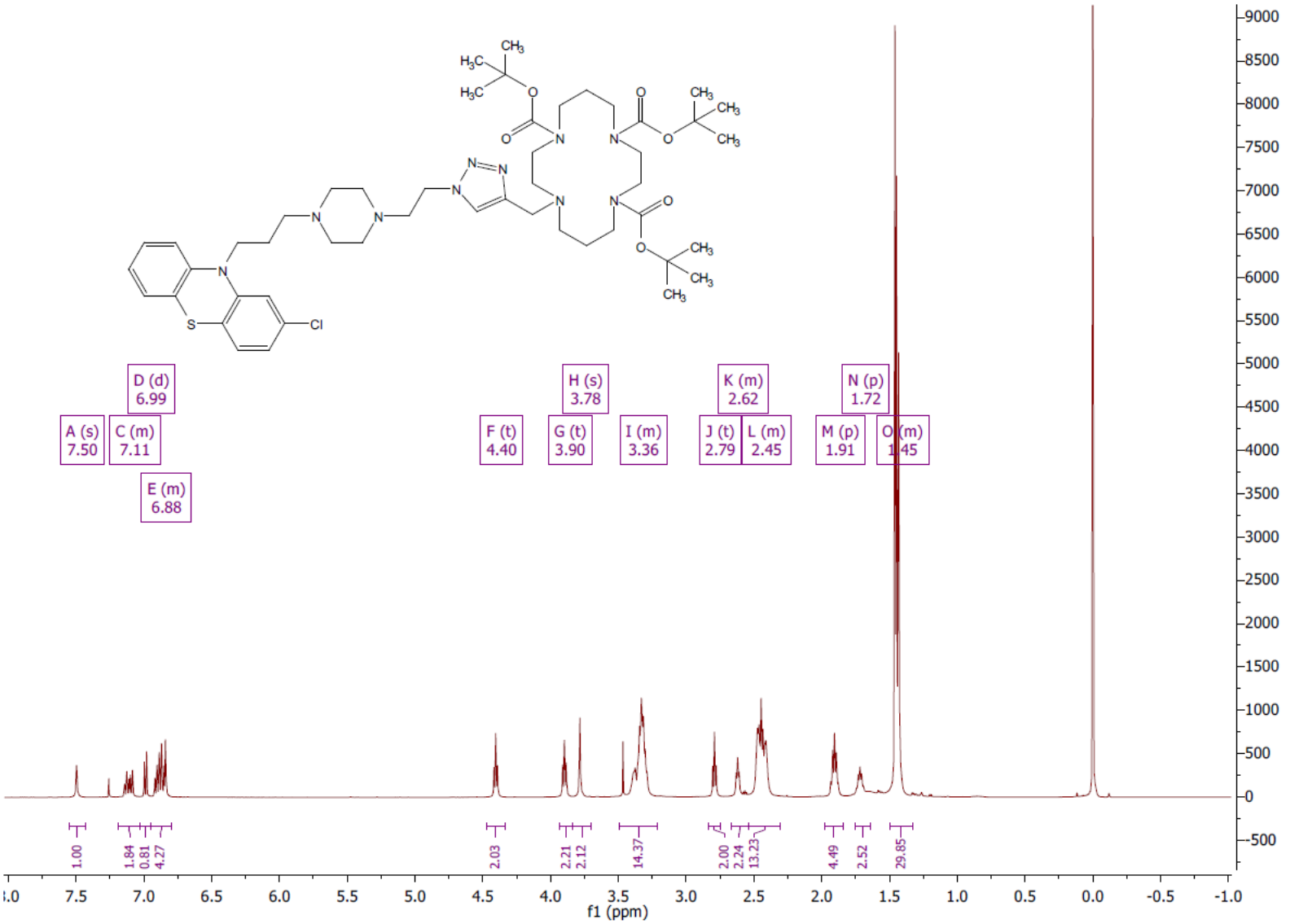

Appendix 1.14 ^{1}H NMR spectrum of **122**. Solvent: Chloroform-d

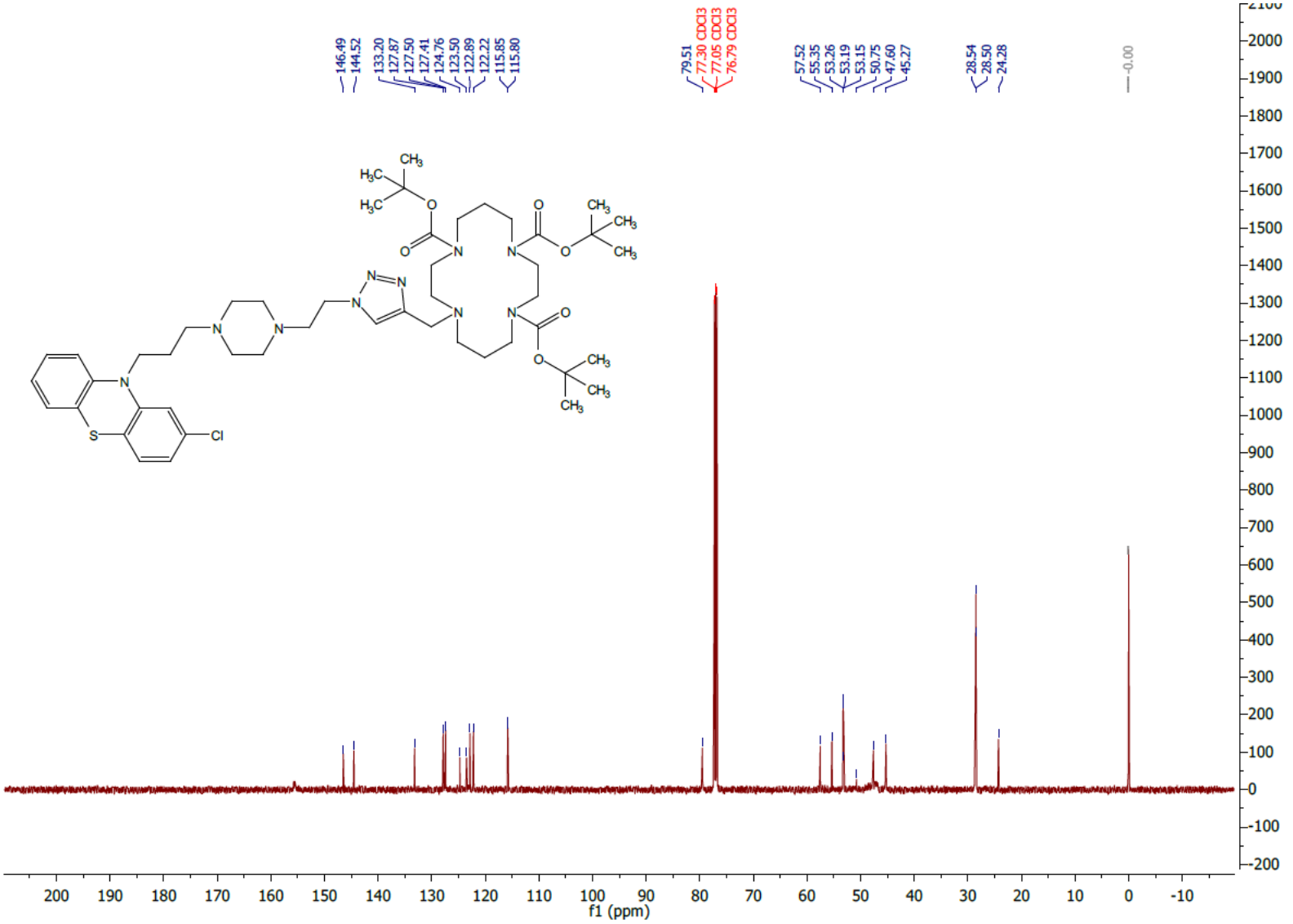

Appendix 1.15 ^{13}C NMR spectrum of **122**. Solvent: Chloroform-d.

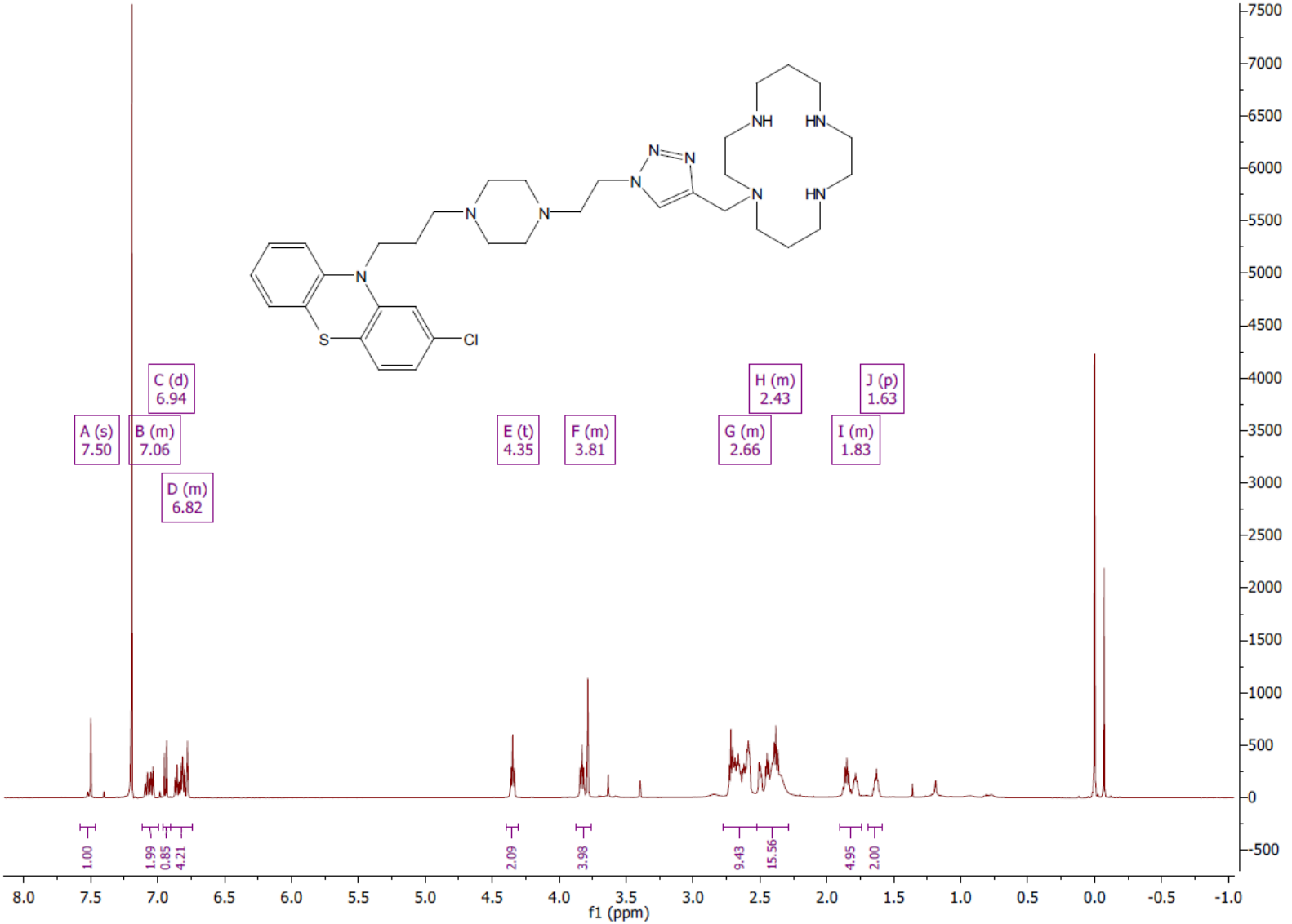

Appendix 1.16 ^{1}H NMR spectrum of **49**. Solvent: Chloroform-d.

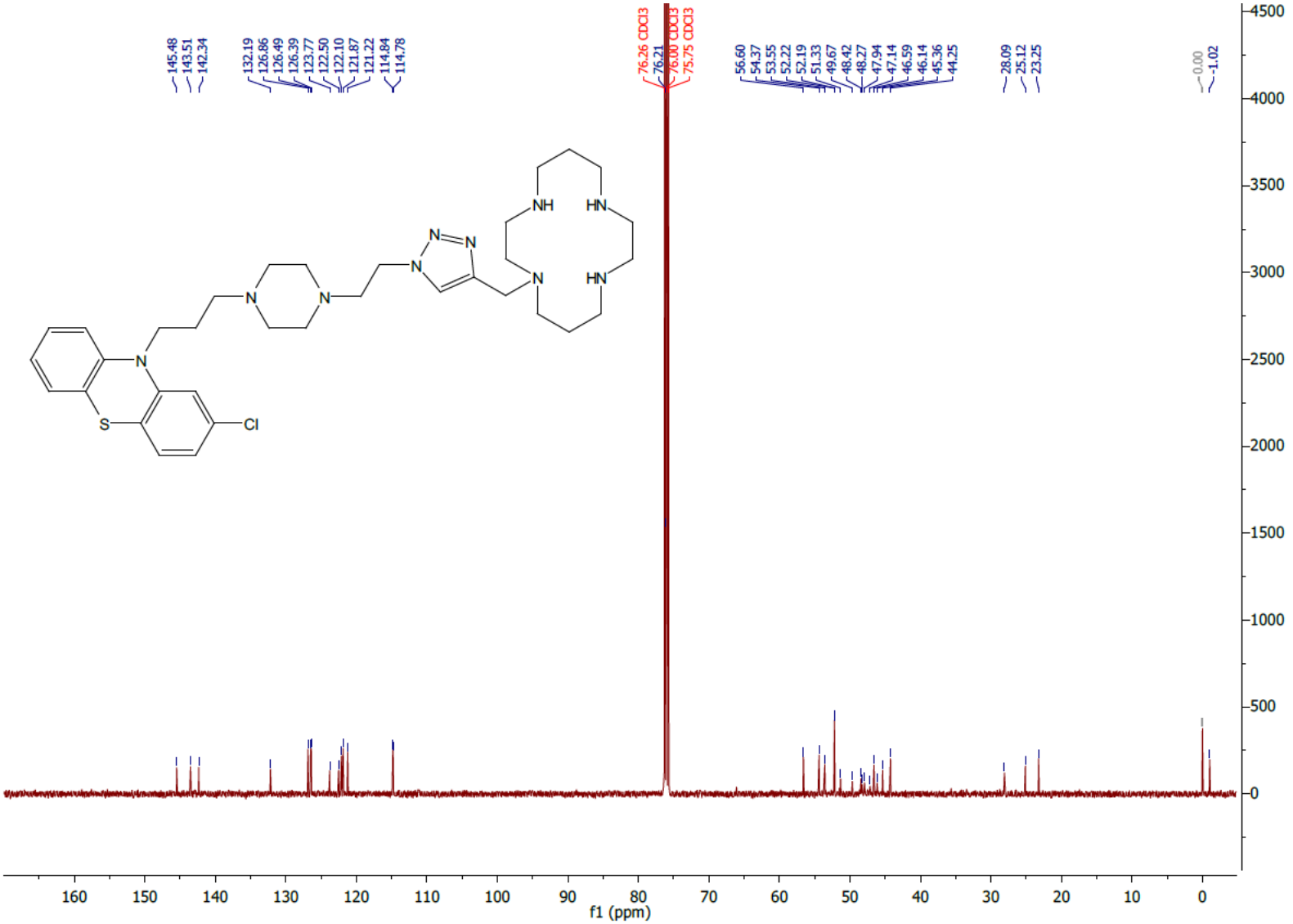

Appendix 1.17: ^{13}C NMR spectrum of **49**. Solvent: Chloroform-d.

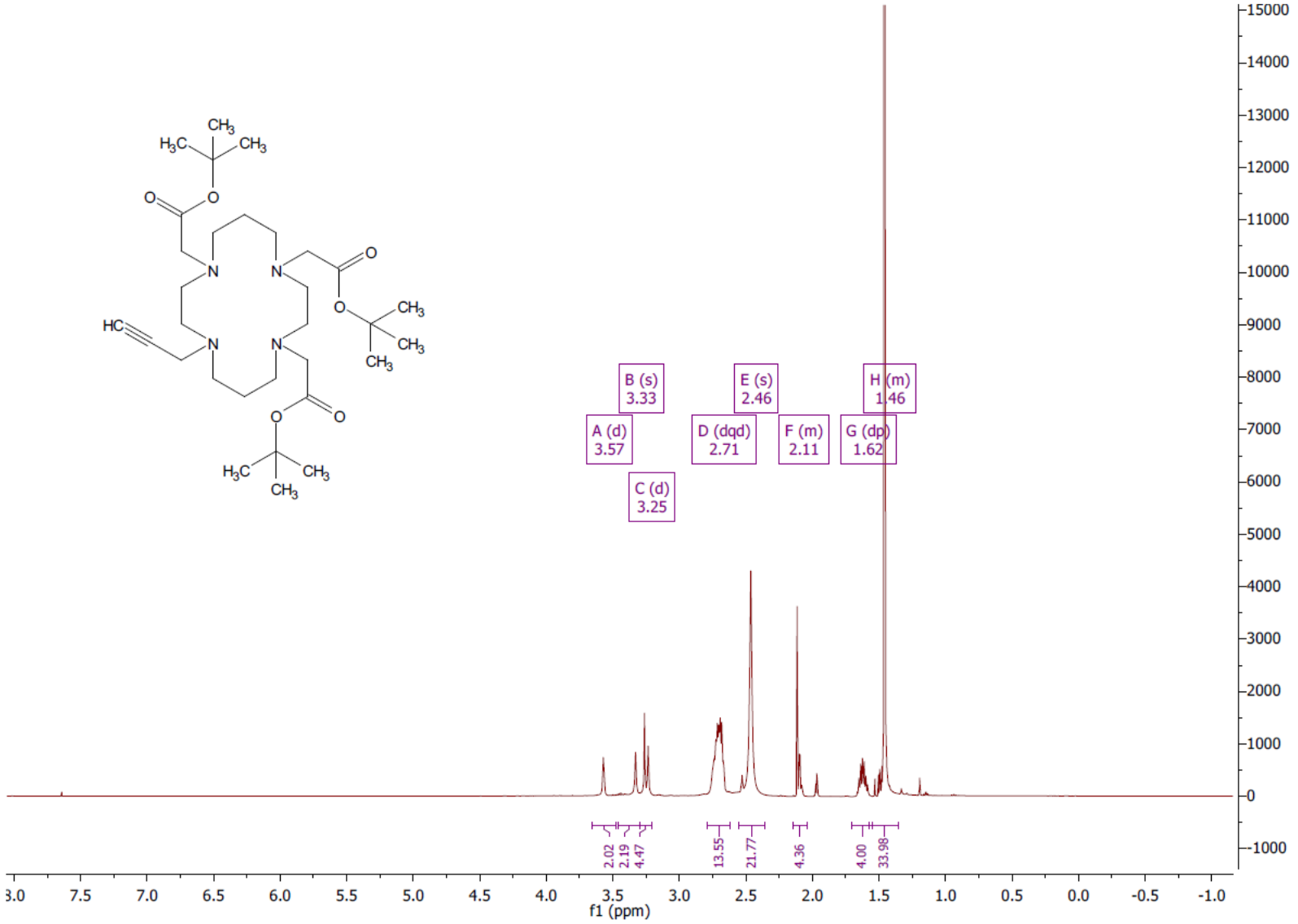

Appendix 1.18: ^{1}H NMR spectrum of **125**. Solvent acetonitrile-d_4.

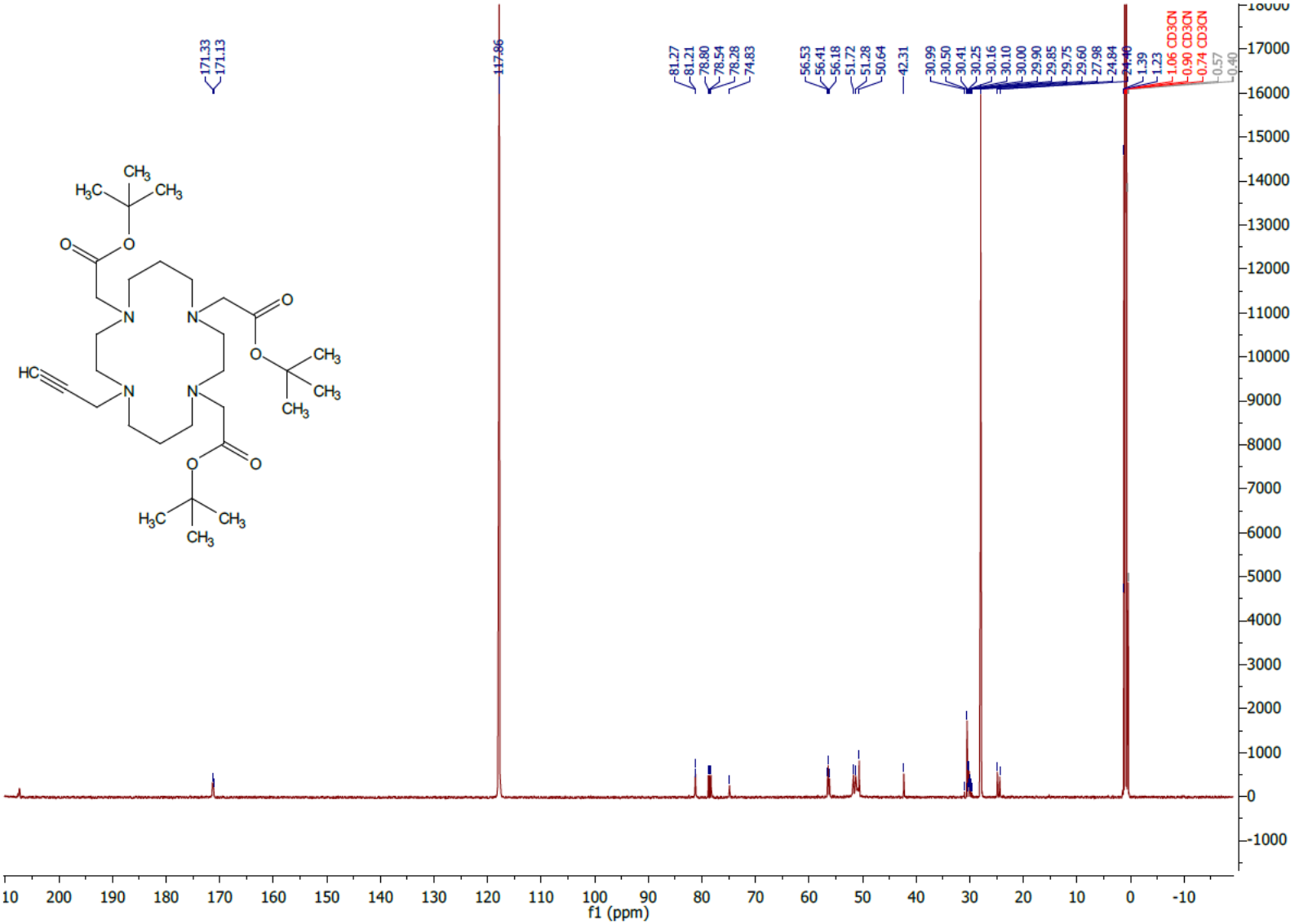

Appendix 1.19: ^{13}C NMR spectrum of **125**. Solvent: acetonitrile-*d*$_4$.

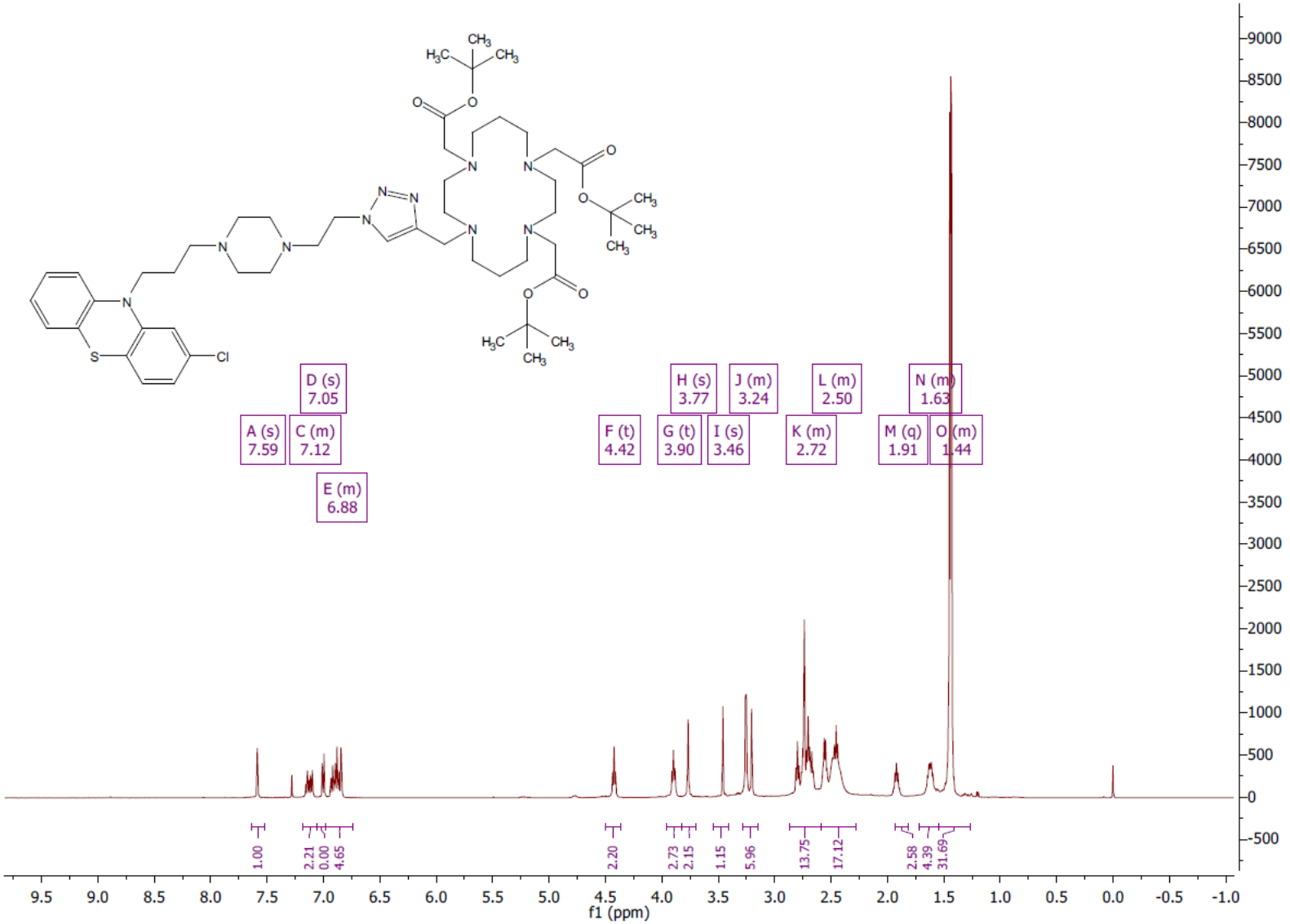

Appendix 1.20: ^{1}H NMR spectrum of **126**. Solvent: Chloroform-d.

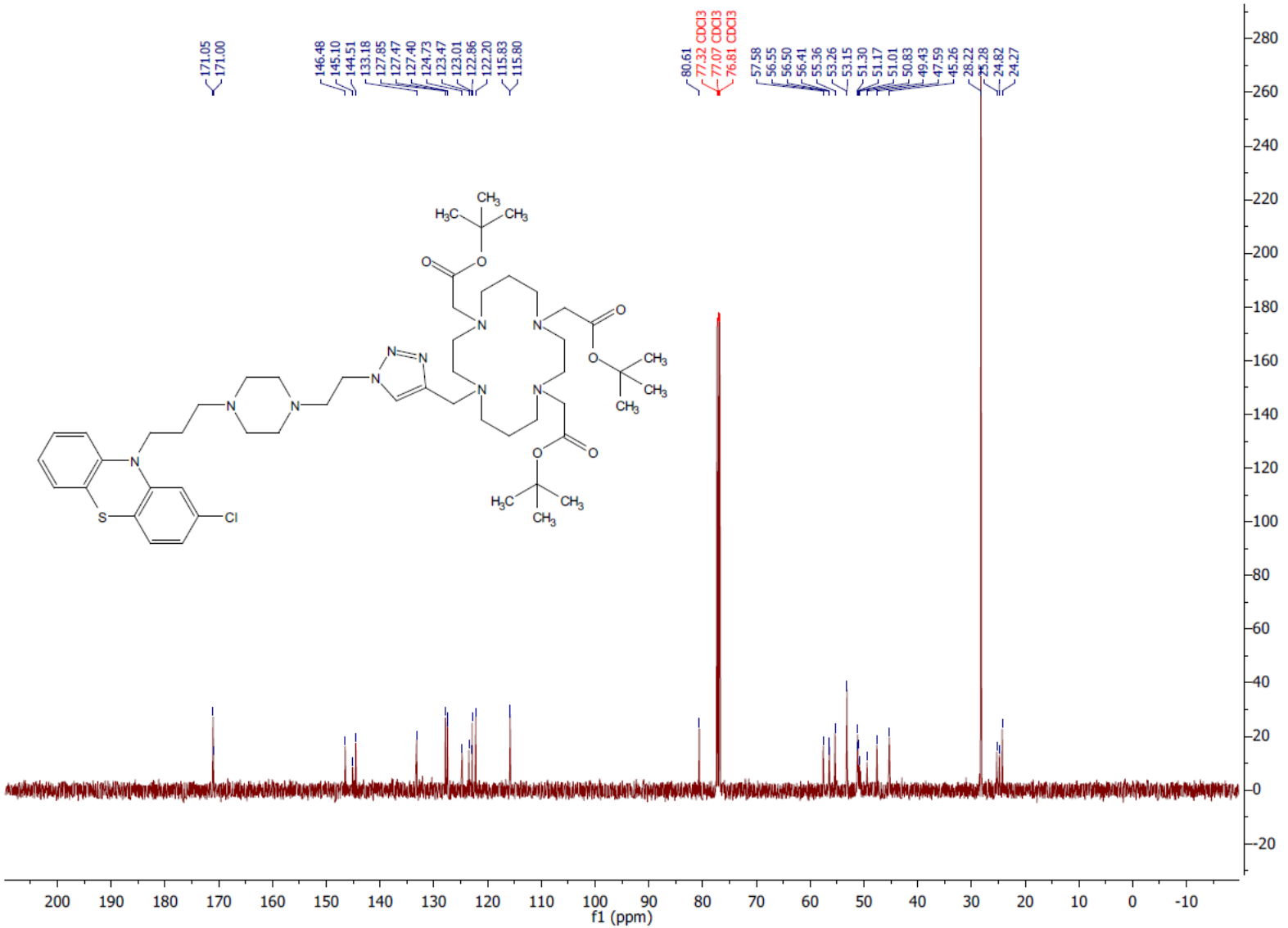

Appendix 1.21: ^{13}C NMR spectrum of **126**. Solvent: Chloroform-d.

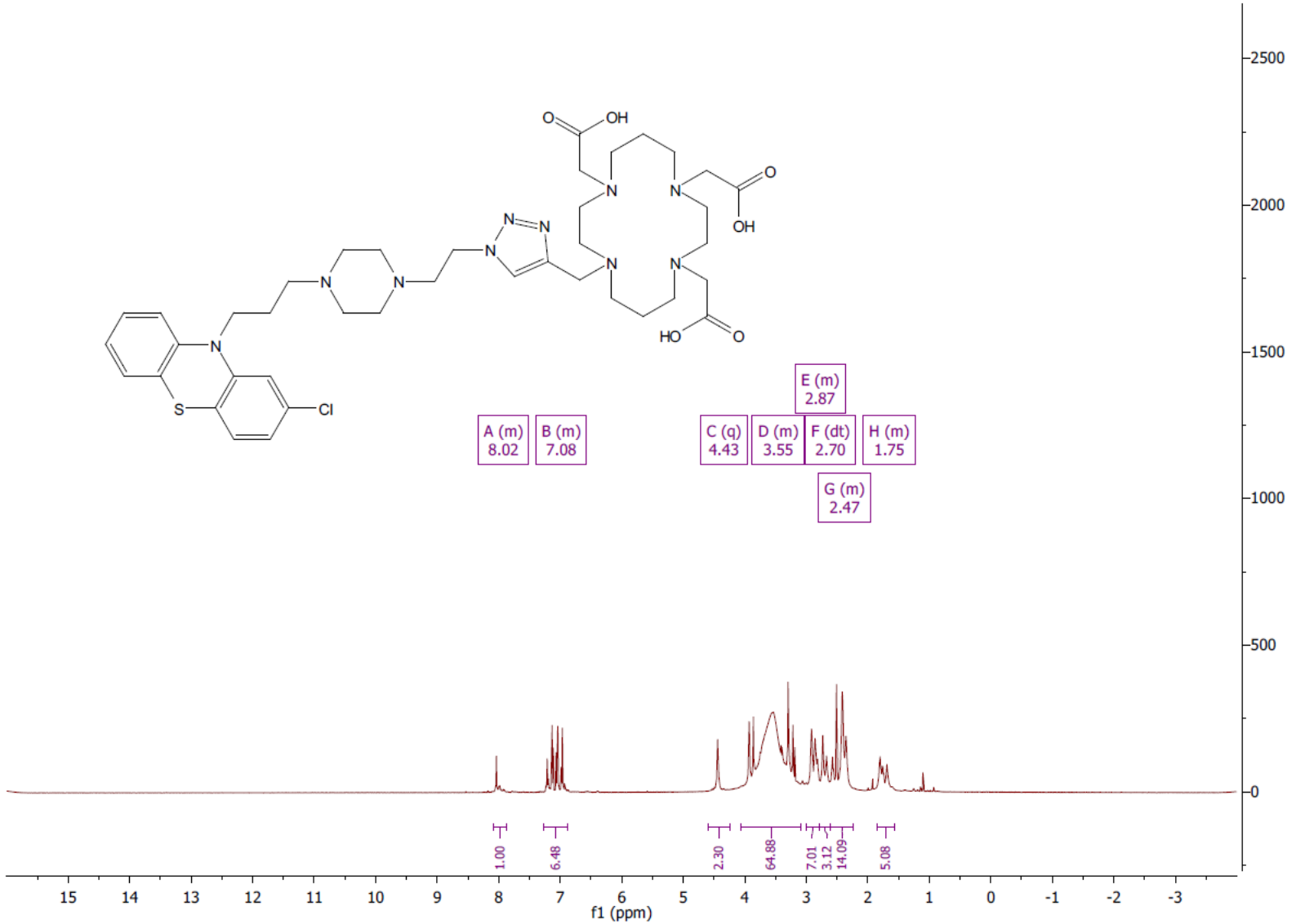

Appendix 1.22: ^{1}H NMR Spectrum of **119**. Solvent: DMSO-d_6

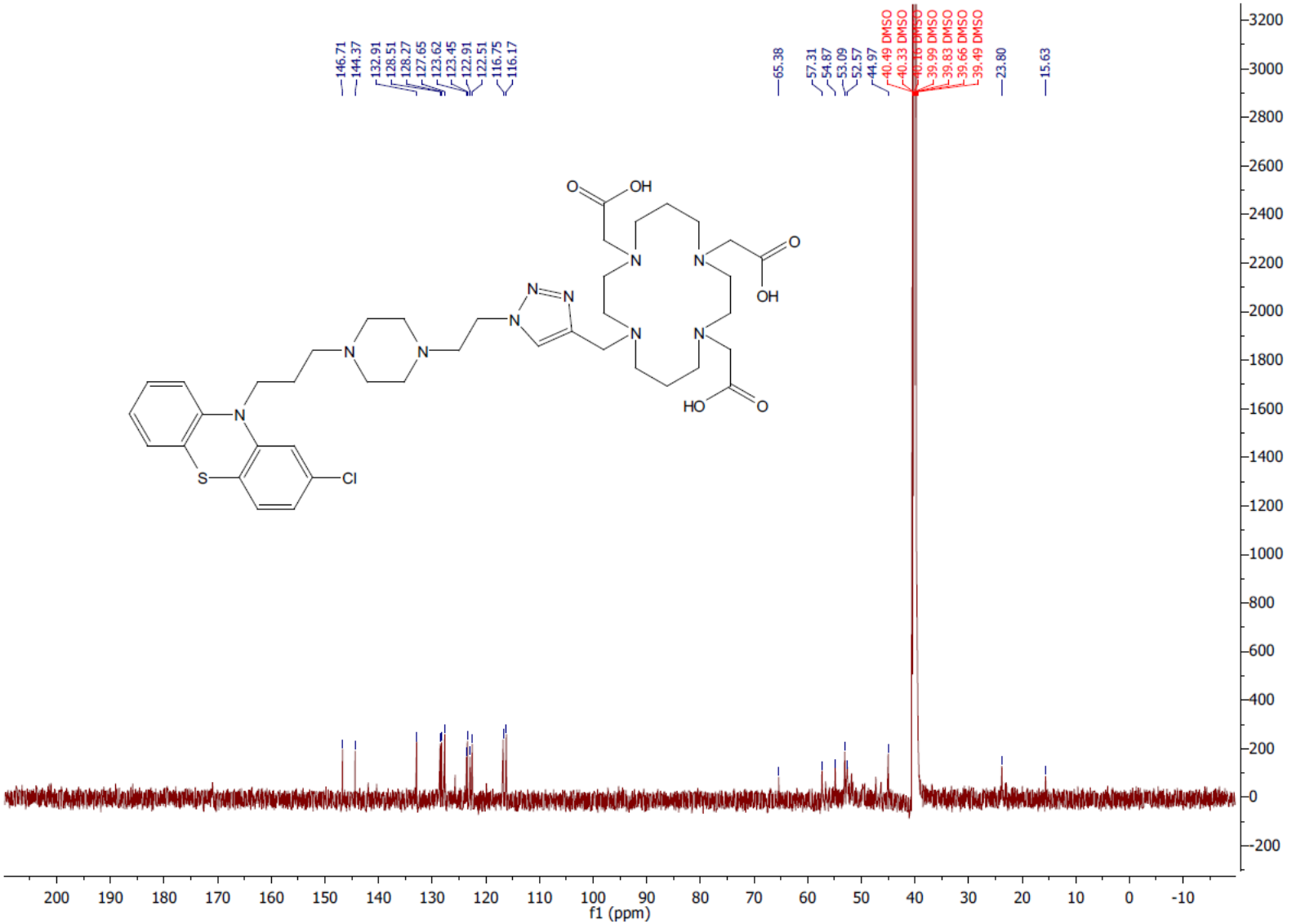

Appendix 1.23: ^{13}C NMR spectrum of **119**. Solvent: DMSO-d_6.